SPACE WEATHER PREDICTION: CHALLENGES AND PROSPECTS

EDITED BY: Nandita Srivastava, Marilena Mierla and Jie Zhang
PUBLISHED IN: Frontiers in Astronomy and Space Sciences

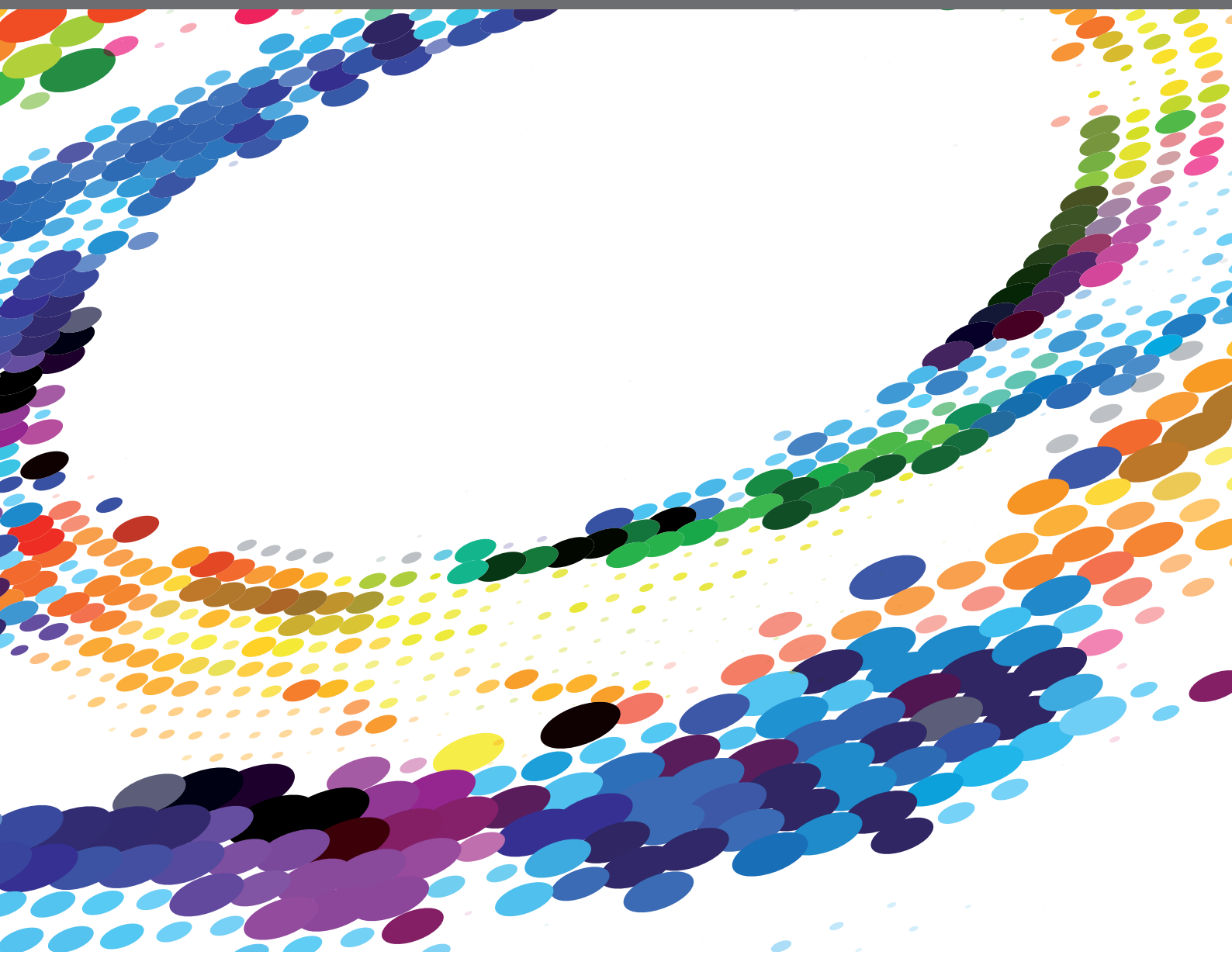

frontiers Research Topics

ISSN 1664-8714
ISBN 978-2-88974-280-6
DOI 10.3389/978-2-88974-280-6

About Frontiers

Frontiers is more than just an open-access publisher of scholarly articles: it is a pioneering approach to the world of academia, radically improving the way scholarly research is managed. The grand vision of Frontiers is a world where all people have an equal opportunity to seek, share and generate knowledge. Frontiers provides immediate and permanent online open access to all its publications, but this alone is not enough to realize our grand goals.

Frontiers Journal Series

The Frontiers Journal Series is a multi-tier and interdisciplinary set of open-access, online journals, promising a paradigm shift from the current review, selection and dissemination processes in academic publishing. All Frontiers journals are driven by researchers for researchers; therefore, they constitute a service to the scholarly community. At the same time, the Frontiers Journal Series operates on a revolutionary invention, the tiered publishing system, initially addressing specific communities of scholars, and gradually climbing up to broader public understanding, thus serving the interests of the lay society, too.

Dedication to Quality

Each Frontiers article is a landmark of the highest quality, thanks to genuinely collaborative interactions between authors and review editors, who include some of the world's best academicians. Research must be certified by peers before entering a stream of knowledge that may eventually reach the public - and shape society; therefore, Frontiers only applies the most rigorous and unbiased reviews.
Frontiers revolutionizes research publishing by freely delivering the most outstanding research, evaluated with no bias from both the academic and social point of view. By applying the most advanced information technologies, Frontiers is catapulting scholarly publishing into a new generation.

What are Frontiers Research Topics?

Frontiers Research Topics are very popular trademarks of the Frontiers Journals Series: they are collections of at least ten articles, all centered on a particular subject. With their unique mix of varied contributions from Original Research to Review Articles, Frontiers Research Topics unify the most influential researchers, the latest key findings and historical advances in a hot research area! Find out more on how to host your own Frontiers Research Topic or contribute to one as an author by contacting the Frontiers Editorial Office: frontiersin.org/about/contact

SPACE WEATHER PREDICTION: CHALLENGES AND PROSPECTS

Topic Editors:
Nandita Srivastava, Physical Research Laboratory, India
Marilena Mierla, Royal Observatory of Belgium, Belgium
Jie Zhang, George Mason University, United States

Citation: Srivastava, N., Mierla, M., Zhang, J., eds. (2022). Space Weather Prediction: Challenges and Prospects. Lausanne: Frontiers Media SA.
doi: 10.3389/978-2-88974-280-6

Table of Contents

frontiers in Astronomy and Space Sciences

EDITORIAL
published: 17 December 2021
doi: 10.3389/fspas.2021.818878

Editorial: Space Weather Prediction: Challenges and Prospects

Nandita Srivastava[1]*, *Marilena Mierla*[2,3] *and Jie Zhang*[4]

[1]Udaipur Solar Observatory, Physical Research Laboratory, Udaipur, India, [2]Solar–Terrestrial Centre of Excellence, Royal Observatory of Belgium, Brussels, Belgium, [3]Institute of Geodynamics of the Romanian Academy, Bucharest, Romania, [4]Department of Physics and Astronomy, George Mason University, Fairfax, VA, United States

Keywords: space weather, coronal mass ejections, stealth CMEs, geomagnetic storm, flux rope

Editorial on the Research Topic

Space Weather Prediction: Challenges and Prospects

Coronal mass ejections (CMEs), launched from the Sun are known to be the main drivers of space weather. Earth-directed CMEs can produce severe impacts upon their arrival at the Earth by compressing the magnetosphere and reconnecting with the Earth's magnetic field. Although space weather studies carried out in the last 2 decades have improved our understanding of solar drivers, i.e., CMEs and flares, however accurate prediction of the space weather impact of a given CME still eludes us.

Considerable progress has been achieved by researchers for estimation of arrival times with the development of semi-empirical/analytical models (Drag-Based Model); numerical simulations and Magnetohydrodynamic models (e.g., ENLIL, EUHFORIA), combined with observational techniques, such as interplanetary scintillation, wide-angle heliospheric imaging, and radio waves. However, there is no model developed yet that can accurately predict the arrival times and the geoeffectiveness of CMEs.

CMEs are considered to propagate as magnetic flux ropes from the Sun to the Earth so that the magnetic field of the CME can be predicted at any point in the inner heliosphere. However, due to the lack of the CME magnetic field observations close to the Sun, estimating the magnetic field orientation of the CME at 1 AU is a major problem for forecasting. Furthermore, the impact of a single CME on the Earth's magnetosphere can be predicted to some extent with reliability. However, in the case of multiple CMEs, they may merge to form "complex ejecta," often resulting in severe space weather effects.

In this research topic, several important contributions related to prediction of space weather impact of CMEs i.e. arrival time and geoeffectiveness have been included. In addition, research contributions related to the early evolution of CMEs i.e., magnetic flux ropes; the initial width distributions of slow and fast CMEs which play an important role in impacting space weather conditions have been reported.

The research topic also includes an in-depth review by Vourlidas based on solar observations from a plethora of space missions, modelling efforts and on what has kept us holding back actionable medium term (hours to days) forecasting of space weather. The paper assesses 2 decades of research on solar drivers i.e., flux ropes observations in EUV and visible wavelengths from SOHO and SDO missions; multi-view point imaging of the Sun and tracking of the Earth-bound eruptions by twin STEREO spacecraft. The paper further highlights the bottle-necks in space weather forecasting and the current research gaps which include uncovering the magnetic configuration of the pre-eruptive structure; formation and dynamics of CMEs in the lower corona; propagation of CMEs in the interplanetary medium and its interaction with the ambient solar wind and CME-CME interaction.

OPEN ACCESS

Edited and reviewed by:
Scott William McIntosh, National Center for Atmospheric Research (UCAR), United States

***Correspondence:**
Nandita Srivastava
nandita@prl.res.in

Specialty section:
This article was submitted to Stellar and Solar Physics, a section of the journal Frontiers in Astronomy and Space Sciences

Received: *20 November 2021*
Accepted: *24 November 2021*
Published: *17 December 2021*

Citation:
Srivastava N, Mierla M and Zhang J (2021) Editorial: Space Weather Prediction: Challenges and Prospects. Front. Astron. Space Sci. 8:818878. doi: 10.3389/fspas.2021.818878

One of the main challenges for Space Weather prediction is understanding the coronal magnetic configuration of the pre-eruptive structure and how it leads to eruption which would help prediction of flares/CMEs. Inspite of several studies (Green et al., 2018), we are far from closing this challenge as the eruptions are magnetically driven and originate in the corona, where magnetic field measurement is difficult. A new approach is reported in this Research Topic by Kilpua et al. who implemented a fully data-driven and time-dependent magnetofrictional method (TMFM) developed by Pomoell et al. (2019), to model the early evolution of the flux rope using photospheric vector magnetograms as its sole boundary conditions. The method self-consistently produces a coherent flux rope and derives key magnetic properties such as twist, helicity, and axial magnetic flux. The axial magnetic flux value obtained from TMFM are in good agreement with observations, thereby promising a reliable space-weather forecast.

The Research Topic addresses a major challenge faced by the space weather forecasters due to Stealth CMEs which originate at higher altitudes in the corona, in regions with weaker magnetic fields and leave no signatures on the disk. To address this issue, have studied four stealth CMEs on which several image processing techniques were applied *viz*. image differencing, wavelets packets equalization, multi-scale Gaussian normalization and geometric techniques involving latitude projection, triangulation, GCS. The analysis shows that the main factor contributing to "stealthiness" is the spatial extent of the eruption rather than the altitude from which a CME lifts off. It is found that difference images with large temporal separations (12 h) revealed the clearest eruptive signatures. This technique proves to be promising for the early detection of stealth CMEs which can adversely impact the space weather.

An important parameter to predict is the time of arrival of CMEs which can be estimated from MHD modelling, numerical simulations and empirical tools. An example is the analytical drag based model (DBM) which is a simple and quick tool for heliospheric propagation of CMEs and CME arrival time prediction. In this research topic, Dumbović et al. provide an extensive overview of the assumptions, applications, and performance of the five sequentially developed DBM models for improved CME arrival time estimates. Out of these, three models basically differ on the assumed different initial geometries of CMEs. The other two approaches are based on ensemble models which provide an improved probability of arrival and confidence interval of the arrival time and speed. These lead to better predictions as they rely on a large number of computationally inexpensive DBM runs.

Understanding the propagation of CMEs before they arrive at the Earth is quite crucial for space weather prediction. This is achieved by studying the kinematical properties of CMEs using coronagraphic and heliospheric imaging observations, specifically by estimating the CME width. Research work reported here by Pant et al. shows that the width distribution of slow and fast CMEs follow different power law distributions that can be related to different types of source regions, *viz*. eruptive prominences and active regions; suggestive of different mechanisms involved in the width expansion of slow and fast CMEs originating from different sources.

Besides the arrival time estimates, one also needs to forecast if the Earth directed CMEs will be geo-effective. Besliu-Ionescu and Mierla report the results of an updated logistic regression model implemented on 2796 CMEs observed during solar cycle 24 for predicting their geoeffectivess. The model was trained 75% of these events and validated for the remaining 25%. The model successfully predicted 98% of the events from the training set, and 98% of the events from the validation set. The study suggests that the model depends on CME properties derived close to the Sun and for robust analysis, one needs to incorporate the evolution of the CMEs in their heliospheric journey.

Solar Cycle 24 (SC24) was the weakest cycle in the last few decades and although solar wind reached its lowest values ever measured (McComas et al., 2013), the cosmic ray background reached record values. Weaker geomagnetic storms were recorded in SC24 (Manoharan et al., 2018) although the CME rate was largely the same (Lamy et al., 2017). The absence of strong events owes to the lower rate of fast and/or wide CMEs in SC24 (Gopalswamy et al., 2020). To understand the contribution of the heliospheric state on the expansion behavior of ICMEs, Mishra et al. estimated the dimensions of ICME structures at 1 AU during SC 23 and 24. They reported a decrease in the radial sizes of ICMEs at 1 AU in SC24 and also that the reduced heliospheric pressure in SC24 is compensated by the reduced magnetic content inside CMEs. Further, the average dimension of sheaths in both cycles is found to be equal, which is unexpected as the ICMEs in SC23 are stronger than that in cycle SC24. The study also highlights that one should consider the propagation and expansion speeds of the CMEs relative to the ambient solar wind speeds.

Lastly, future prospects in space weather prediction that are envisaged, have been emphasized by Vourlidas. These include the importance of coronal magnetic measurements; recording of uninterrupted observations from the solar surface to about 15 solar radii, and enhancing the capability of heliospheric imaging. Further, a more technological challenge to be addressed is planning an off -ecliptic heliospheric imaging. These efforts are expected to impact research and forecasting of space weather significantly.

AUTHOR CONTRIBUTIONS

All authors listed have made a substantial, direct, and intellectual contribution to the work and approved it for publication.

REFERENCES

Gopalswamy, N., Akiyama, S., and Yashiro, S. (2020). The State of the Heliosphere Revealed by Limb-Halo Coronal Mass Ejections in Solar Cycles 23 and 24. *Astrophysical J. Lett.* 897, L1. doi:10.3847/2041-8213/ab9b7b

Green, L. M., Török, T., Vršnak, B., Manchester, W., and Veronig, A. (2018). The Origin, Early Evolution and Predictability of Solar Eruptions. *Space Sci. Rev.* 214, 46. doi:10.1007/s11214-017-0462-5

Lamy, P., Floyd, O., Quémerais, E., Boclet, B., and Ferron, S. (2017). Coronal Mass Ejections and Solar Wind Mass Fluxes Over the Heliosphere During Solar Cycles 23 and 24 (1996–2014). *J. Geophys. Res. Space Phys.* 122, 50–62. doi:10.1002/2016JA022970

Manoharan, P. K., Mahalakshmi, K., Johri, A., Jackson, B. V., Ravikumar, D., Kalyanasundaram, K., et al. (2018). Current State of Reduced Solar Activity: Intense Space Weather Events in the Inner Heliosphere. *Sun and Geosphere.* 13, 135–143. doi:10.31401/SunGeo.2018.02.03

McComas, D. J., Angold, N., Elliott, H. A., Livadiotis, G., Schwadron, N. A., Skoug, R. M., et al. (2013). Weakest Solar Wind of the Space Age and the Current "Mini" Solar Maximum. *Astrophys. J.* 779, 2. doi:10.1088/0004-637X/779/1/2

Pomoell, J., Lumme, E., and Kilpua, E. (2019). Time-Dependent Data-Driven Modeling of Active Region Evolution Using Energy-Optimized Photospheric Electric fields. *Sol. Phys.* 294, 41. doi:10.1007/s11207-019-1430-x

Conflict of Interest: The authors declare that the research was conducted in the absence of any commercial or financial relationships that could be construed as a potential conflict of interest.

Publisher's Note: All claims expressed in this article are solely those of the authors and do not necessarily represent those of their affiliated organizations, or those of the publisher, the editors and the reviewers. Any product that may be evaluated in this article, or claim that may be made by its manufacturer, is not guaranteed or endorsed by the publisher.

frontiers in Astronomy and Space Sciences

ORIGINAL RESEARCH
published: 30 March 2021
doi: 10.3389/fspas.2021.631582

Estimating the Magnetic Structure of an Erupting CME Flux Rope From AR12158 Using Data-Driven Modeling

Emilia K. J. Kilpua, Jens Pomoell, Daniel Price, Ranadeep Sarkar and Eleanna Asvestari*

Department of Physics, University of Helsinki, Helsinki, Finland

We investigate here the magnetic properties of a large-scale magnetic flux rope related to a coronal mass ejection (CME) that erupted from the Sun on September 12, 2014 and produced a well-defined flux rope in interplanetary space on September 14–15, 2014. We apply a fully data-driven and time-dependent magnetofrictional method (TMFM) using Solar Dynamics Observatory (SDO) magnetograms as the lower boundary condition. The simulation self-consistently produces a coherent flux rope and its ejection from the simulation domain. This paper describes the identification of the flux rope from the simulation data and defining its key parameters (e.g., twist and magnetic flux). We define the axial magnetic flux of the flux rope and the magnetic field time series from at the apex and at different distances from the apex of the flux rope. Our analysis shows that TMFM yields axial magnetic flux values that are in agreement with several observational proxies. The extracted magnetic field time series do not match well with *in-situ* components in direct comparison presumably due to interplanetary evolution and northward propagation of the CME. The study emphasizes also that magnetic field time-series are strongly dependent on how the flux rope is intercepted which presents a challenge for space weather forecasting.

Keywords: magnetic fields, solar wind, corona, coronal mass ejection, flux ropes, space weather

OPEN ACCESS

Edited by:
Jie Zhang,
George Mason University,
United States

Reviewed by:
Chaowei Jiang,
Harbin Institute of Technology,
Shenzhen, China
Jiajia Liu,
Queen's University Belfast,
United Kingdom

****Correspondence:***
Emilia K. J. Kilpua
emilia.kilpua@helsinki.fi

Specialty section:
This article was submitted to Stellar and Solar Physics, a section of the journal Frontiers in Astronomy and Space Sciences

Received: *20 November 2020*
Accepted: *24 February 2021*
Published: *30 March 2021*

Citation:
Kilpua EKJ, Pomoell J, Price D, Sarkar R and Asvestari E (2021) Estimating the Magnetic Structure of an Erupting CME Flux Rope From AR12158 Using Data-Driven Modeling. Front. Astron. Space Sci. 8:631582. doi: 10.3389/fspas.2021.631582

1. INTRODUCTION

Coronal mass ejections (CMEs; e.g., Webb and Howard, 2012) are huge eruptions of plasma and magnetic field from the Sun that are connected to the strongest space weather effects at Earth (e.g., Zhang et al., 2004, 2007; Huttunen et al., 2005; Richardson and Cane, 2012; Kilpua et al., 2017b). Their intrinsic configuration is a magnetic flux rope, a coherent structure formed of bundles of helical magnetic field lines that wind about a common axis (e.g., Chen, 2017; Green et al., 2018). Flux ropes are also regularly identified in interplanetary counterparts of CMEs (ICMEs; e.g., Kilpua et al., 2017a), although, due to distortions and interactions during propagation and large crossing distances far from the flux rope axis not all ICMEs observed *in situ* include one (e.g., Cane et al., 1997; Jian et al., 2006; Kilpua et al., 2011). The presence of a flux rope in an ICME is featured by a smoothly rotating magnetic field direction over a large angle on time-scales of about a day, enhanced magnetic field magnitude, and depressed proton temperature and plasma beta. A solar wind structure fulfilling such observational signatures is typically called a "magnetic cloud" (e.g., Burlaga et al., 1981; Klein and Burlaga, 1982). Several studies have shown that ICMEs that embed flux ropes/magnetic clouds are most likely to be geoeffective (Kilpua et al., 2017b, and references therein), because they can provide sustained periods of strongly southward interplanetary magnetic

field that is a key requirement for the generation of intense geomagnetic storms (e.g., Dungey, 1961; Vasyliunas, 1975; Gonzalez et al., 1994; Pulkkinen, 2007).

Predicting the magnetic structure of CME flux ropes has thus received a substantial interest in the space weather forecasting community and the so-called "B_Z problem" or "B_Z challenge" is one of the most critical issues toward accurate long-lead time forecasting (e.g., Kilpua et al., 2019; Vourlidas et al., 2019; Tsurutani et al., 2020). Firstly, it is currently difficult to extract the information of the *intrinsic* magnetic structure of CME flux ropes from remote-sensing observation or through modeling in a routine manner. Secondly, the magnetic structure of the CME flux rope may be dramatically altered during its propagation in the corona and interplanetary space (e.g., Manchester et al., 2017; Kilpua et al., 2019), affecting therefore the magnetic field vectors that finally impinge the Earth. The nature of the interactions between the CME flux rope with the ambient solar wind and other CMEs depends strongly on the intrinsic magnetic structure of flux rope (e.g., Lugaz et al., 2013). The intrinsic flux rope properties can give early warning of the potential space weather consequences, but most importantly it provides critical information for constraining flux ropes in a variety of semi-empirical and first-principle models describing the propagation and evolution of CMEs in the corona and heliosphere, such as ForeCAT and FIDO (Kay et al., 2013, 2017), 3DCORE (Möstl et al., 2018), INFROS (Sarkar et al., 2020), Enlil (Odstrcil et al., 2004), EUropean Heliospheric FORecasting Information Asset (EUHFORIA; Pomoell and Poedts, 2018), and SUSANOO-CME (Shiota and Kataoka, 2016). Although first-principle models are so-far routinely run with only cone-model CMEs for space weather forecasting purposes, for example EUHFORIA is now actively tested with magnetized CMEs to give improved predictions and more realistic information on the effect of CME interactions (Scolini et al., 2019, 2020; Verbeke et al., 2019). The intrinsic magnetic field structure of a CME flux rope can be estimated using indirect observational proxies that combine characteristics of structures in the solar atmosphere related to the erupting CME, such as filament details, flare ribbons, and sigmoids (e.g., Palmerio et al., 2017, 2018; Gopalswamy et al., 2018, and references therein). The magnetic flux enclosed within the flux rope can be estimated e.g., by determining the poloidal flux added during the reconnection related to the CME release process from the techniques based on post-eruption arcades (PEAs) and flare ribbons (e.g., Gopalswamy et al., 2017; Kazachenko et al., 2017) and the toroidal flux from coronal dimming (e.g., Webb et al., 2000; Gopalswamy et al., 2018). Dimming is a temporary and localized reduction in the coronal EUV or X-ray emission and marks the plasma evacuated by the CME eruption. It can be divided into a "core dimming" and "secondary dimming" regions. The core dimming regions mark the footpoints of the ejected flux rope, which can be a pre-existing one or newly formed during the eruption or developed due to the magnetic flux added to the pre-existing one via magnetic reconnection (Dissauer et al., 2018b). Therefore, half of the unsigned magnetic flux underlying the twin core dimming regions provide the estimation of total toroidal flux of the erupting flux rope. On the other hand, the "secondary dimming" regions are formed due to the expansion of the CME and the overlying magnetic field that evacuate the plasma behind the ejected flux rope.

Another approach to derive the flux rope structure low in the corona is the data-driven modeling that takes advantage of the observations of the photosphere, which are currently routinely available from the Earth's viewpoint. While simulations that use a full time-dependent magnetohydrodynamic (MHD) approach would be the most realistic option currently in use (e.g., Jiang et al., 2016), they are computationally expensive and, furthermore, not all boundary conditions needed are available from observations.

From a space weather forecasting perspective, a faster approach is to neglect plasma effects and use a non-linear force free field (NLFFF; Wiegelmann and Sakurai, 2012; James et al., 2018) approximation, i.e., it is assumed that electric currents and magnetic fields are parallel to each other and related by a scalar function that varies in space. The force-free assumption is generally justified in the low corona, in particular above active regions, where the plasma beta is low (e.g., Gary, 2001; Bourdin, 2017). The drawback in the NLFFF approach is however that it is static and does not describe the dynamics of the eruption.

We apply here the time-dependent magnetofrictional method (TMFM) (for its first application, see van Ballegooijen et al., 2000). In the magnetofrictional method (Yang et al., 1986) a friction term is added to the MHD momentum equation. When low beta and quasi-static situation is assumed, the plasma velocity is proportional to the Lorentz force. The Lorentz force drives the dynamics of the system. In non-timedependent case the system relaxes toward a force-free state, while when the boundary conditions are evolved in time the fully force-free state is not reached. TMFM is therefore capable of modeling quasi-static accumulation of free magnetic energy. We note that due to the low-beta constraint this approach is suited for modeling the formation and early evolution of the solar flux rope. Several studies have now demonstrated that TMFM can describe the formation and in some cases also the lift-off of coronal structures (e.g., Cheung and DeRosa, 2012; Fisher et al., 2015; Yardley et al., 2018; Pomoell et al., 2019; Price et al., 2019, 2020).

In this paper we investigate the eruptive flux rope on September 12, 2014. This event has been analyzed in previous studies by Vemareddy et al. (2016), Zhao et al. (2016), and Duan et al. (2017) by performing NLFFF extrapolation of the photospheric magnetic field. We instead apply TMFM (Pomoell et al., 2019), i.e., our simulation is fully data-driven and time-dependent allowing it to model the formation and early evolution of the flux rope using photospheric vector magnetograms as its sole boundary conditions. We describe the scheme to extract the flux rope from the simulation data and to derive its key magnetic properties (such as a twist map, helicity sign, and axial magnetic flux). The obtained twist and axial magnetic fluxes are compared to the observationally derived values to assess the performance of the model. We also make the lineouts through the TMFM flux rope to arrive at a prediction for the magnetic field time series at Earth. To our knowledge this is the first study to investigate the sensitivity of how the magnetic field time-series extracted from a data-driven coronal flux rope depends on the

point the flux rope is crossed and also to compare them directly to *in-situ* observations.

The paper is organized as follows: In section 2 we describe the used data and the magnetofrictional method, including electric field inversion to obtained boundary conditions for the simulation. In section 3 we give the overview of the event. Section 4 describes the method to identify the flux rope from the simulation and calculate the important parameters, while in section 5 we compare estimated axial magnetic flux in the flux rope and magnetic field line-outs to observations. Finally in section 6 we discuss and summarize our results, including a discussion of challenges associated with this approach for space weather forecasting purposes.

2. DATA AND METHODS

2.1. Spacecraft Data

Our simulation approach uses photospheric electric fields derived from phospheric vector magnetograms as the boundary condition. In this study the magnetograms used are provided by the Helioseismic and Magnetic Imager (HMI; Scherrer et al., 2012) onboard the Solar Dynamics (SDO; Pesnell et al., 2012) as full-disk vector magnetograms at 720 s temporal resolution. The magnetogram time series are processed for the simulation using the method developed in Lumme et al. (2017), and described in detail e.g., in Pomoell et al. (2019) and Price et al. (2019). The key steps in short are to remove bad and spurious (temporal flips in the azimuth) pixels, interpolate the data-gaps, smooth the magnetograms spatially and temporally, and rebin the data to lower resolution. The magnetograms were also made to smoothly approach zero at the boundaries and the total signed flux was balanced using a multiplicative method.

To investigate the CME propagation direction we examined the white-light images from the coronagraphs of the Large Angle Spectrometric Coronagraph (LASCO; Brueckner et al., 1995) onboard the Solar and Heliospheric Observatory (SOHO; Domingo et al., 1995) and Sun Earth Connection Coronal and Heliospheric Investigation (SECCHI; Howard et al., 2008) package onboard the Solar Terrestrial Relations Observatory (STEREO; Kaiser et al., 2008).

The observational determination of the magnetic fluxes enclosed by the flux rope using the Post-Eruptive Arcades (PEA), flare ribbon and dimming analysis was based on the Extreme UltraViolet (EUV) images from the Atmospheric Imaging Assembly (AIA; Lemen et al., 2012) onboard SDO as well as SDO/HMI magnetograms. The AIA/EUV images were also used to visually compare the magnetic field morphology in the model to observational features of eruptive coronal structures.

The *in-situ* plasma and magnetic field observations analyzed here were obtained from the Wind spacecraft (Ogilvie and Desch, 1997). The magnetic field data comes from the Magnetic Field Investigation (MFI; Lepping et al., 1995) instrument and the plasma data from the Solar Wind Experiment (SWE; Ogilvie et al., 1995) instrument. We also use suprathermal electron observations from the Three-Dimensional Plasma and Energetic Particle Investigation (3DP; Lin et al., 1995) onboard Wind and ion charge state data (1-h resolution) from the Solar Wind Ion Composition Spectrometer (SWICS; Gloeckler et al., 1998) instrument onboard the Advanced Composition Explorer (ACE; Stone et al., 1998) spacecraft. Both Wind and ACE were located at Lagrangian point L1 at the time of this study.

2.2. Magnetofrictional Method and Electric Field Boundary Conditions

We use in this study a time-dependent magnetofrictional method (TMFM) that is described in detail in Pomoell et al. (2019). The electric field comes from the resistive Ohm's law where for the resistivity we use a constant value of $200 \times 10^6\ m^2\ s^{-1}$. In TMFM a frictional term $-\nu\mathbf{v}$ is added to the MHD momentum equation and the method assumes quasi-static and low-beta situation that is applicable in the low corona where the magnetic forces dominate (Gary, 2001; Bourdin, 2017). This means that the pressure gradient can be ignored so that the momentum equation can be replaced by the magnetofrictional velocity prescription $\mathbf{v} = \frac{1}{\nu}\frac{\mu_0 \mathbf{J}\times\mathbf{B}}{B^2}$, where $\mathbf{J}$ is the current density, for details see also e.g., van Ballegooijen et al. (2000) and Cheung and DeRosa (2012). The frictional coefficient is held constant through the simulation with the value $1 \times 10^{-11}\ s\ m^{-2}$, except at the inner boundary where the $1/\nu$ term smoothly approaches zero. The magnetofrictional velocity is then used to evolve the magnetic field according to Faraday's law.

Photospheric electric field constitutes the driving lower boundary condition to TMFM. We invert the electric field from the photospheric magnetogram time-series (see section 2.1) using the ELECTRIC field Inversion Toolkit (ELECTRICIT; Lumme et al., 2017). The process divides the electric field to its inductive ($\mathbf{E}_I$) and non-inductive ($-\nabla\psi$) components, where the former is calculated straightforwardly from Faraday's law and the latter can be constrained e.g., using the *ad-hoc* optimization method described also in Lumme et al. (2017). Several previous works have indicated that the inclusion of the non-inductive electric field component is paramount for the full determination of the electric field (e.g., Schuck, 2008; Kazachenko et al., 2014; Fisher et al., 2015; Lumme et al., 2017) and thus for obtaining the flux ropes and their eruption in the simulation (e.g., Cheung and DeRosa, 2012; Pomoell et al., 2019).

The functional form for the non-inductive potential ψ we use in this study is the "U"-assumption following Cheung et al. (2015) expressed as follows:

$$\nabla_h^2 \psi = -U\mu_0 J_z = -U(\nabla \times \mathbf{B}) \cdot \hat{\mathbf{z}} \tag{1}$$

In the above, U is a free parameter and J_z the vertical current density. U has units of velocity and it can be considered in an idealized setting to represent the vertical velocity by which the twisted magnetic flux tube emerges through the photosphere. The boundary conditions at the top and sides are open so that magnetic flux can pass through the domain (see details from Pomoell et al., 2019).

3. EVENT OVERVIEW

The CME of interest erupted from the Sun in the evening of September 10, 2014. It originated from Active Region (AR) 12158

which at this time was located at N15E02, i.e., very close to the visible solar disk center. The left panel of **Figure 1** shows the SDO 193 193 Å image of the Sun at the time of the eruption. In the LASCO catalog (https://cdaw.gsfc.nasa.gov/CME_list/) the CME was listed as a full halo (angular width 360°) with the first appearance in the C2 field of view (FOV) at 18:00 UT and with a linear speed of 1,267 km/s. This CME was also detected by the STEREO-B spacecraft with the first appearance in the COR1 FOV at 17:45 UT and in the COR2 FOV at 18:10 UT (STEREO-A did not have data at this time). **Figure 2** shows the coronagraph images from LASCO/C3 and STEREO-B/COR2 at 18:54 UT featuring the CME. At this time STEREO-B was located at the Heliographic (HEEQ) longitude of −160.8°, i.e., almost on the other side of the Sun than the Earth. STEREO-A was also located near the far side of the Sun and its data was not available for this period of time. The CME was accompanied by an X1.6-class solar flare that peaked on September 10 at 17:10 UT. Both LASCO and STEREO coronagraph data indicate that the CME was headed in a northward direction.

A few days later a clear interplanetary CME was detected in the near-Earth solar wind. **Figure 3** shows the leading shock on September 12, 15:17 UT as an abrupt jump in the magnetic field magnitude and plasma parameters. The shock is followed by a turbulent sheath and an ejecta. The ejecta showed classical magnetic cloud signatures indicative of a flux rope configuration, i.e., enhanced magnetic field magnitude (**Figure 3A**), smooth rotation of the field direction (**Figure 3B**) and depressed plasma beta (**Figure 3E**). The figure also shows several general ICME signatures (e.g., Zurbuchen and Richardson, 2006; Kilpua et al., 2017a, and references therein) including low magnetic field variability, declining speed profile from front to trailing edge, enhanced oxygen charge ratio O^{+7}/O^{+6} and average iron charge ratio $\langle Q_{Fe} \rangle$ (**Figure 3F**) as well as bi-directional suprathermal electrons (**Figure 3G**) during the ejecta. The leading edge of the ejecta occurred on September 12, 21:25 UT and the trailing edge on September 14, 01:45 UT. This end time is selected to coincide at the point where the declining speed ends, plasma beta increases and compositional signatures start to cease. This end time also matches the end time reported in the Richardson and Cane ICME list (http://www.srl.caltech.edu/ACE/ASC/DATA/level3/icmetable2.htm, Richardson and Cane, 2010).

The *in situ* observations in **Figure 3** suggest that the shock of the ICME discussed above intercepted a weak previous ICME. This previous ICME drove a shock, observed on September 11, at 22:49 UT, but the ejecta signatures are not clear, suggesting that Wind made only a glancing encounter. The weak ICME is likely associated with an eruption that occurred early on Sep 9, 2014 from the same AR 12158 with the first appearance in the LASCO field of view at 00:06 UT. The September 9 CME was also a full halo and had a linear speed of 920 km/s. The signatures of the preceding CME are however much weaker and also as indicated by the Space Weather Database Of Notifications, Knowledge, Information (DONKI; https://kauai.ccmc.gsfc.nasa.gov/DONKI/) run (data not shown) the Earth intercepted the September 9, 2014 CME only through its very western and southern flanks. The September 10 CME was in turn encountered clearly more centrally, however also toward its southern part consistent with the coronagraph observations suggesting the propagation north from the ecliptic plane. We therefore conclude that the flux rope in the strong ICME did not have a significant interference from the earlier ICME.

4. SIMULATION AND FLUX ROPE IDENTIFICATION/PARAMETERS

4.1. Simulation Setup

The magnetogram data, used as input to the electric field inversion, is most reliable when the active region is not too close to the limb. AR 12158 was fully visible from the eastern solar limb by September 5 noon and it was leaving the visible disk (but still fully seen) on September 16 noon. The period when the AR was within $\sim 50^\circ$ from the disk center extends from September 7, $\sim$ 0 UT to September 14, $\sim$ 0 UT. We selected to perform the electric field inversion for this temporal window. The spatial region selected for the inversion is shown in **Figure 1**. Note that we opted to not apply a masking to the magnetic field data since it yielded the smallest flux imbalance in the dataset (see **Supplementary Figure 1**).

The temporal evolution of the photospheric energy and helicity injections as provided by the inversion result are shown in **Supplementary Figures 2, 3**. The electric fields shown in the figures were inverted using the optimal value of U (70 m/s, pink dashed line) and twice the optimal value of U (140 m/s, blue solid line). The reference value from DAVE4VM is shown as the black curve. There is a very good agreement with the optimized U curve and the DAVE4VM curve in terms of the energy injection during the whole simulation, but the helicity injection is overestimated, in particular toward the end of the simulation. Our previous works indicate that helicity injection needs to typically be greatly overestimated to obtain the eruption in the simulation, and thus optimized U typically gives too little helicity to produce the flux rope, see discussion, e.g., in Pomoell et al. (2019).

The simulation was conducted for the twice of the value of optimized U since it yielded the clearest flux rope that ejected from the simulation domain. In our previous studies also (e.g., Price et al., 2020) we have obtained a clear flux rope with the U-assumption.

4.2. Flux Rope Identification

To identify the portion of the domain in the simulation that consists of the flux rope we assume that it consist of highly twisted magnetic field lines that are rooted in the photosphere. The twist value T_w is a measure of the number of turns that the two infinitesimally close magnetic field lines make about each other and it is defined as $T_w = \frac{1}{4\pi} \int ds \, \frac{\mu_0 J_\parallel}{B}$ (see e.g., Berger and Prior, 2006; Liu et al., 2016, and references therein). In this definition $J_\parallel$ is the electric current density parallel to the magnetic field and ds is the increment of the arc length along the field line. We define the flux rope to consist of the field lines that have $|T_w| > 1$ with a constant sign within a coherent region (similar to e.g., Liu et al., 2016; Duan et al., 2019).

In our simulation a coherent structure of negative T_w was seen to form in the lower part of the simulation domain on September

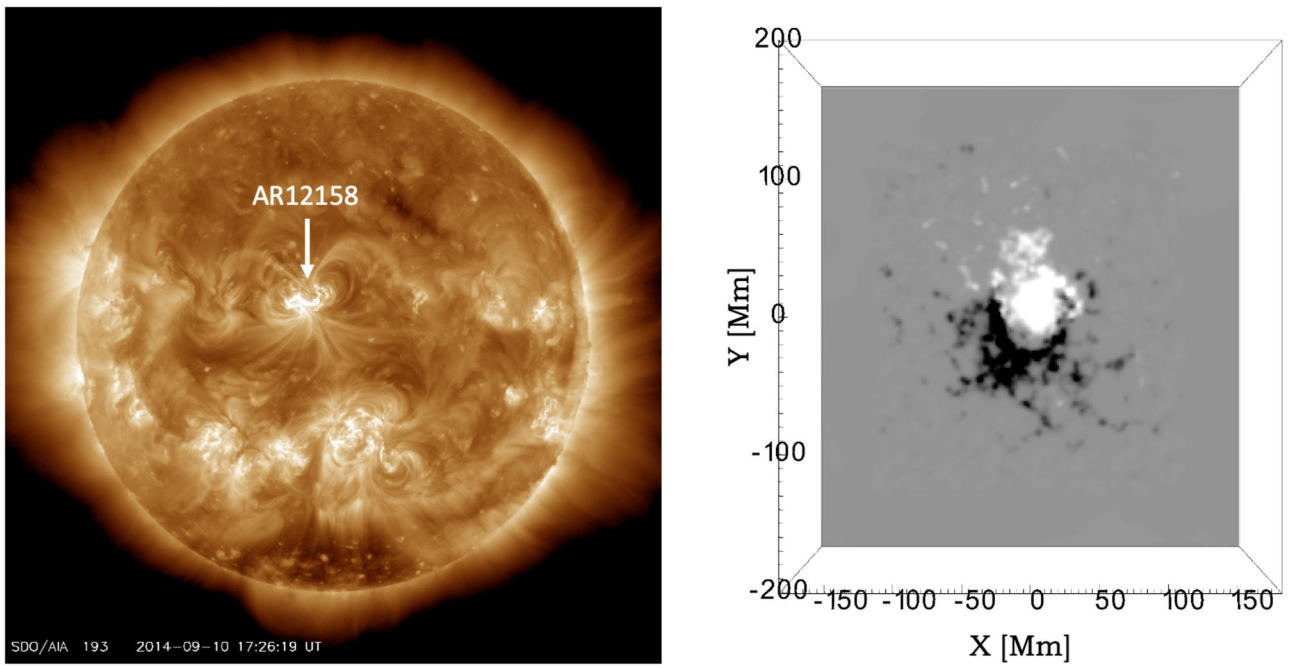

FIGURE 1 | (Left) Extreme Ultraviolet images at 193 Å (Left) taken by SDO/AIA on September 10 2014, 17:10 UT at the early phase of the eruption. The AR12158 is bounded by a white box and it shows the eruptive structure. **(Right)** Simulation domain shown for the approximately same time. In the *Z*-direction the domain extends to 150 Mm. The magnetic field in the magnetogram is saturated to ±300 Gauss.

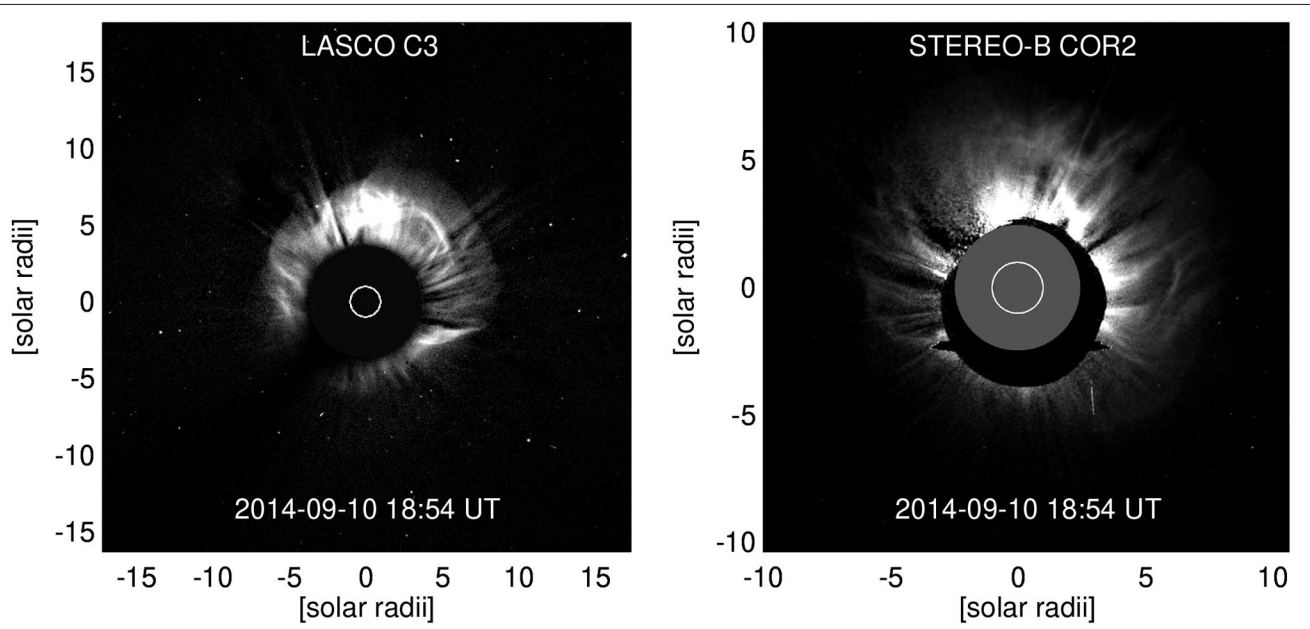

FIGURE 2 | CME morphology as observed by LASCO C3 **(left)** and STEREO COR2 **(right)**.

9, around 8 UT that then grows in size when the time progresses. The coherent $T_w < -1$ structure starts to rise early on September 11 and reaches the upper part of the domain early September 13. The structure also expands as it rises. The snapshots from the twist map and T_w contours in the YZ-plane (placed at $X = 0$) of the simulation are shown in **Figure 4** taken in steps of 24 h. See also the full movie from **Supplementary Material**. The movie and snapshots show that higher T_w regions ($T_w < -1.5$ and

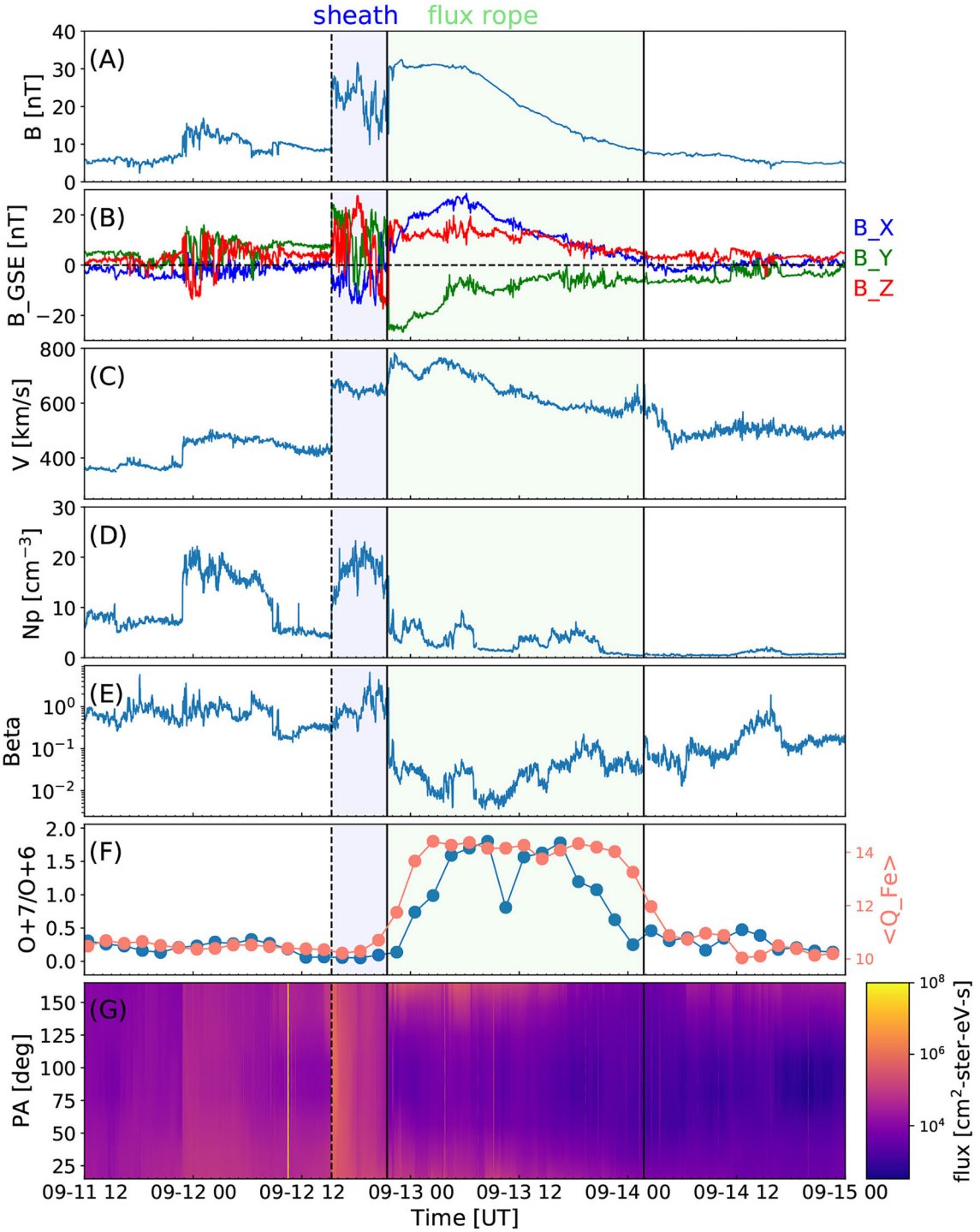

FIGURE 3 | The solar wind *in-situ* measurements recorded at the Earth's Lagrangian point L1. The panels show, from top to bottom: **(A)** magnetic field magnitude, **(B)** magnetic field components in GSE coordinates (blue: B_x, green: B_y, red: B_z), **(C)** speed, **(D)** density, **(E)** plasma beta, **(F)** oxygen charge state ratio and the average iron charge state, and **(G)** pitch angle spectrogram of suprathermal 255 eV electrons. The magnetic field and plasma data are from the Wind spacecraft with 1-min resolution, while the 2-h charge state data are from the ACE spacecraft. The suprathermal electron measurements are from Wind. The vertical line marks the shock. The sheath is indicated by the green shaded region and FR by purple-shaded region.

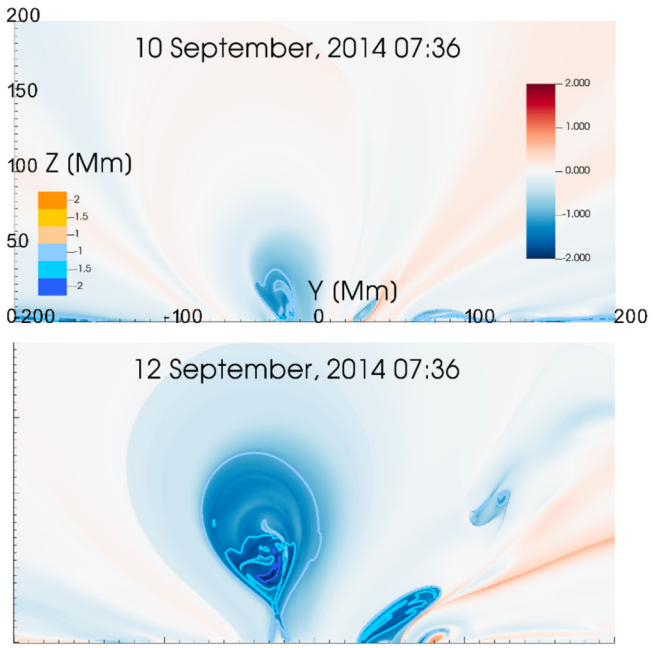

FIGURE 4 | Snapshots of twist number (T_w) maps and T_w countours from the TMFM simulation in steps of 24 h. The colorbar on left shows the contour value with blue colors depicting negative twist contours and orange colors positive twist contours. T_w is a measure of how many turns two field lines that are infinitesimally close make about each other. The colorbar on right shows the T_w map values (blue colors indicate negative T_w, red positive, saturated at ±2).

$T_w < -2$ contours) form already when the flux rope is still close to the bottom of the simulation domain. These higher T_w region expand with the expanding and rising flux rope, but there is no general drastic increase in T_w.

Figure 5 shows three snapshots from the simulation in the steps of 24 h. In the upper panels the vertical plane of the twist value map and contours are shown in the background while these have been removed in the bottom panels. The field lines that pass through the $T_w < -1$ contours are drawn and they clearly form a twisted flux rope.

In **Figure 6**, a set of field lines identified by the above method are drawn and visualized in a view from the top (Right) together with SDO/AIA 131 Å (Middle) EUV images. The time selected is September 10, at 17:10 UT, i.e., when the CME took place at the Sun and the flux rope was still residing close to the bottom of the simulation domain. Here the field lines going through the highest $|T_w|$ core ($T_w < -1.5$) very close to the bottom of the simulation domain are shown with pink and those above which cross within the $T_w < -1.0$ contour (but $T_w > -1.5$) are shown with green (different hues of pink and green represent different individual field lines). Both sets of field lines are traced starting from the strong magnetic field region of positive polarity, but they connect to negative polarities in slightly different regions. The higher lying green lines end to the stronger negative polarity region, while the lower lying pink field lines end to a bit weaker negative field region a bit further away.

The flux rope field lines from TMFM simulation match visually well with EUV observations in **Figure 6**. Both feature a clear inverse S-shaped sigmoid that is considered as a proxy of a flux rope with a negative sign of magnetic helicity (e.g., Rust and Kumar, 1996; Green and Kliem, 2009; Palmerio et al., 2017). The negative helicity sign is also consistent with the "hemispheric rule" (Bothmer and Schwenn, 1998; Pevtsov and Balasubramaniam, 2003) suggesting that magnetic structures on the Sun, including flux ropes, in the northern hemisphere should have a preference for negative helicity, while in the southern hemisphere the dominant helicity is positive. We also note that close to the apex of the TMFM flux rope structure, the field lines run predominantly in a direction that is approximately parallel to the photospheric polarity inversion line.

In the following analysis we will focus on the time when the flux rope had risen close to the top of the simulation domain on September 13, 07:36 UT. This time corresponds to the last times shown in **Figures 4**, **5** showing the twist value map and twist contours. The flux rope has higher T_w inner part and lower T_w outer part in absolute sense.

4.3. Flux Rope Axis and Apex

For deriving the axial flux and magnetic field cuts through the flux rope the key features that are needed to be identified from the simulation data are the axis of the flux rope and its apex.

The axis of the flux rope is defined using the following scheme: Firstly, for the selected time, we computed the twist value T_w for all closed field lines that passed through the plane close to the photosphere, here the plane $Z = R_\odot + 20$ Mm was

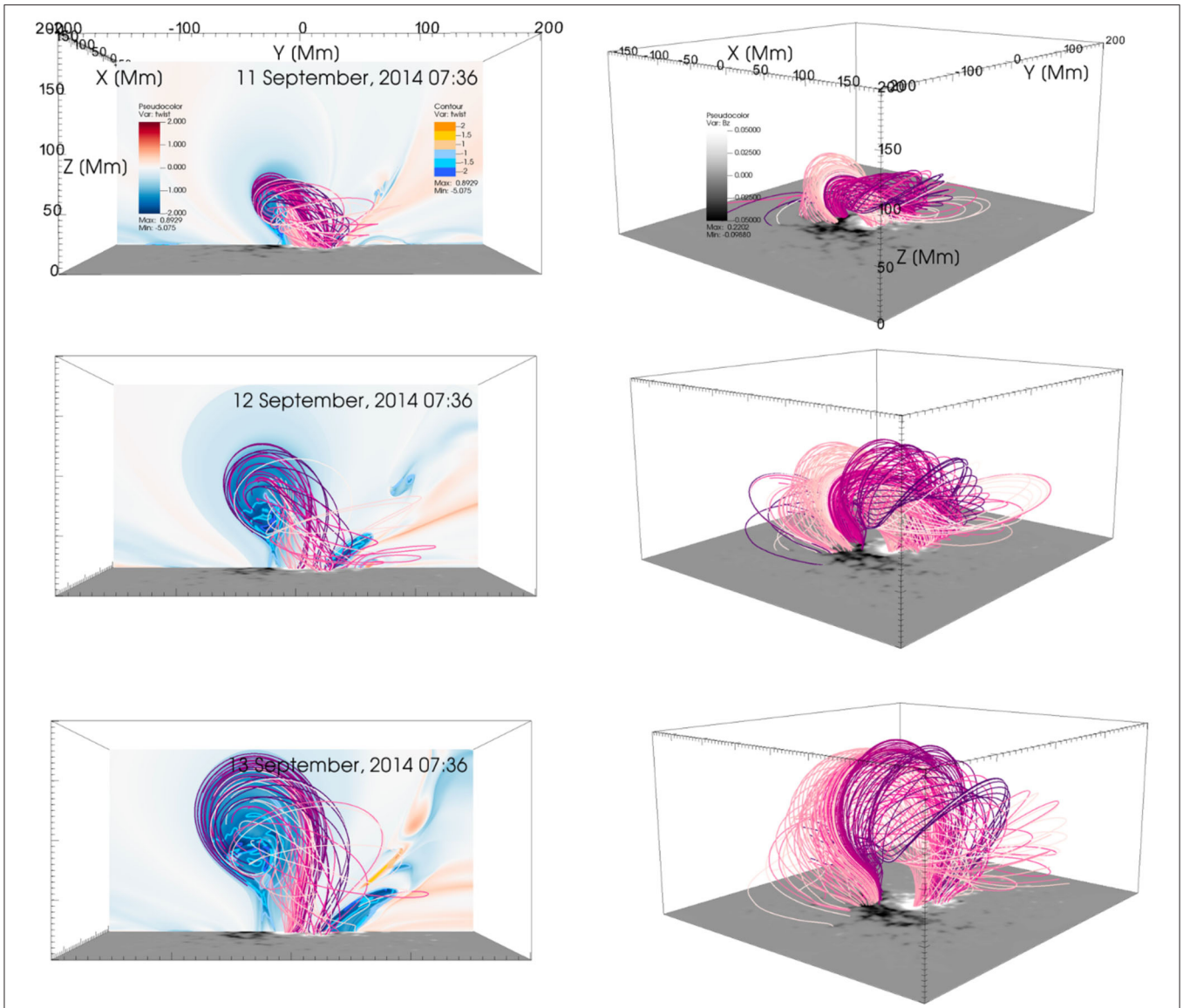

FIGURE 5 | Snapshots from the simulation from 07:36 UT on 11 September, 2014 to 07:36 UT on 13 September with a cadence of 24 h between each snapshot. The top panels show the flux rope field lines where $Tw < -1$ (different colors depicting different field lines). The flux rope is intercepted with a *Tw* plane that also shows the contours of Tw. The top panels show the flux rope from a different angle without a slice of Tw and contours. The lower boundary is shown by the B_z on the bottom surface in all plots. The colorbars are same as in **Figure 3**.

used, and that had a twist number $T_w \leq -1$. Then one of the footpoints of the flux rope was selected, e.g., let's assume that it is the positive polarity foot-point, and all points for which the radial magnetic field component $B_r < 0$ were removed from the twist map. The resulting map therefore consists of a set of points locating the highly-twisted field lines associated with the positive-polarity foot-point of the flux rope. According to Liu et al. (2016) the spatial variations of T_w can be used to locate the flux rope axis. The authors show that the axis is found as the local extremum, either peak, or a dip, in the T_w map (see also Duan et al., 2019, for example this approach). This method gives thus the coordinates for the axis in the selected plane and those can be used as the seed to draw the axis. For this case, the axis was found as the local minimum. The determination of the axis using T_w, as discussed in Liu et al. (2016), is not straightforward and not a suitable approach for all cases. In this case a local extremum was identified and we note that field lines clearly appear to wind about the common axis found by this method (see **Figures 5**, **9**).

The apex of the flux rope is defined here as the point on the axis with the largest Z value. On September 13, 07:36 UT the apex is located at $(X, Y, Z) = (14.3, -41.8, 137.0)$ Mm.

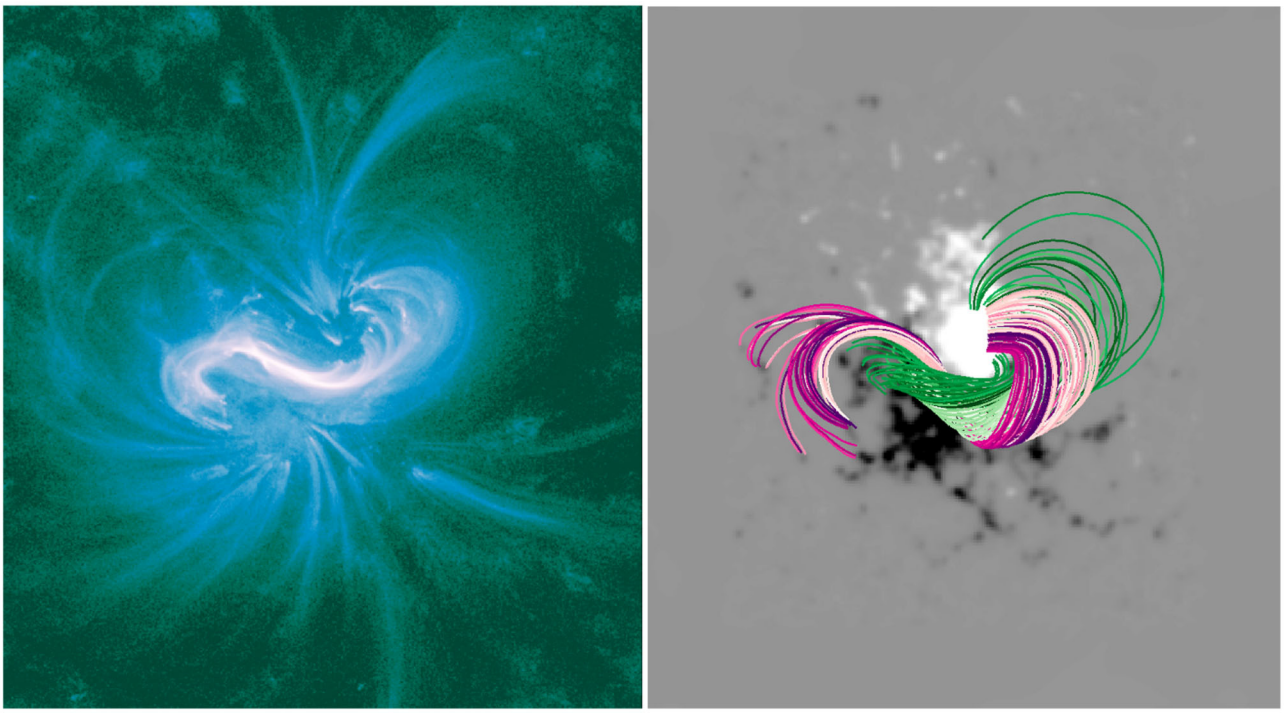

FIGURE 6 | The left panels shows the Extreme Ultraviolet image at 131 Å wavelength taken by SDO/AIA on September 10 2014, 17:10 UT at the early phase of the eruption showing a clear reversed S-shaped sigmoid. The right panel shows a snapshot from the TMFM simulation featuring flux rope field lines with almost at matching time at 17:36 UT. The pink field lines are those intercepting the highest twist $T_w < -1.5$ contour and green field lines those that intercept the $-1.5 < T_w < -1$ contour. The magnetic field is saturated to ±300 Gauss.

4.4. Axial Magnetic Flux

In the simulation the axial flux (or toroidal) within the flux rope is computed as $\phi_T = \int_A \mathbf{B} \cdot d\mathbf{A}$, where $\mathbf{A}$ is the area of integration in a plane normal to the flux rope axis. Note that the extent of the flux rope is determined to the flux rope identification scheme described in section 4.2.

The results are shown in **Table 1**. The values are calculated for three different increments in steps of 30 Mm along the axis to the both sides of the apex. **Table 1** shows that the fluxes determined from the TMFM flux rope vary between 3.8×10^{21}–4.1×10^{21} Mx and are thus very consistent to within 4%. Since magnetic flux should be constant through the flux rope this gives further support that the axis and extent of the flux rope are robustly determined. We also checked the axial flux at two earlier times on September 12 at and September 11 at 07:36 UT. The values are 4.0×10^{21} and 3.6×10^{21} Mx.

5. COMPARISON TO OBSERVATIONS

In this section we compare the axial magnetic fluxes in the flux rope identified from the performed TMFM simulation (section 4.4) with the magnetic fluxes estimated using different observational methods as well as defined lineouts through the flux rope to investigate how much they vary with distance from the apex and compare the result to *in-situ* observations.

5.1. Comparison of Axial Magnetic Flux to Observational Proxies

We estimate both the axial and poloidal fluxes in the flux rope using various observational methods that were briefly described in the Introduction. Firstly, we estimate the reconnection flux using both the post-eruptive arcades (PEA) and flare ribbon methods (See the Introduction). These methods give the reconnection flux that can be interpreted as the poloidal flux added to the flux rope via magnetic reconnection during its eruption (see the Introduction). The panels (A) and (B) in **Figure 7** illustrate the flare ribbons as seen in AIA 1,600 Å image and the radial component of HMI magnetogram with cumulative flare ribbon area overlying the positive and negative magnetic field polarities depicted with the red and blue regions, respectively. The panels (C) and (D) show the PEA and the HMI magnetogram where the PEA area is delimited with a dashed red box. In order to select the end boundaries of the elongated area underlying the post-eruption arcades, we have followed the extent of the flare ribbons so that we can get rid of the projection effect that may arise due to the presence of post-eruption loops at the end boundaries. The PEAs were very well-formed in this case and their inclination follows roughly that of the EUV sigmoid and PIL, and thus the axis of the TMFM flux rope. **Table 1** shows that both flare ribbon and PEA methods give poloidal fluxes of similar orders of magnitude, $\approx 6 \times 10^{21}$ Mx.

TABLE 1 | Magnetic flux in the flux rope as determined from the TMFM method and from different observational methods (see text for details).

Method	Flux (Mx)
TMFM run (toroidal)	
Apex-90 Mm	3.9×10^{21}
Apex-60 Mm	3.8×10^{21}
Apex-30 Mm	4.0×10^{21}
Apex	4.0×10^{21}
Apex+30 Mm	4.1×10^{21}
Apex+60 Mm	3.9×10^{21}
Apex+90 Mm	3.8×10^{21}
Reconnection flux from flare ribbon method (poloidal)	5.3×10^{21}
Reconnection flux from Post-Eruptive Arcades (poloidal)	6.8×10^{21}
Core dimming (toroidal)	1.8×10^{21}

In order to estimate the toroidal flux of the flux rope, we identified the core dimming region using the method given by Dissauer et al. (2018a). The left and middle panels of **Figure 8** show the minimum intensity maps obtained from AIA 211Å images for the logarithmic base ratio and base difference images, and the right panels co-spatial line-of-sight magnetogram with red contours showing the area of core dimming. Computing half of the total unsigned magnetic flux underlying the core dimming regions we obtained the toroidal flux as $\approx 2 \times 10^{21}$ Mx. We noticed that the identification of core dimming regions in our analysis may include projection effects due to the large erupting structure associated with the CME eruption and therefore, may not give the true estimation of the toroidal flux. The estimation of toroidal flux from core dimming method indicates that the magnitude of toroidal flux inside the flux rope is lower than the content of poloidal flux as estimated from the flare ribbon and PEA methods.

5.2. Magnetic Field Lineouts and Comparison to *in-situ* Observations

To obtain a prediction of the magnetic field time series at Earth from the simulation we define lineouts through the TMFM flux rope. The lineouts are made through the apex of the flux rope and through different distances from the apex along the flux rope axis. In **Figure 9** we show the flux rope axis as a black thick curve and the cut through the apex is denoted by a black vertical line. The selected distances from the apex are three steps to both directions with 30 Mm increments along the axis. These are indicated in the figure with blue (subtracted from the apex point) and red (added to the apex point) vertical lines.

The TMFM magnetic field time series are obtained through these lineouts and are then transformed to correspond to the GSE coordinates with a simple transformation. If we assume that the flux rope propagates directly from Sun to Earth the TMFM Z-direction corresponds to the GSE $-x$ direction, TMFM X-direction to the GSE $-y$ direction, and finally TMFM Y-direction to the GSE z direction.

In order to compare the temporal profiles of the magnetic field magnitude and field components from the TMFM to *in-situ* observations we need to scale the TMFM magnetic field time-series. There are two effects to consider. Firstly, the magnetic field magnitude in the simulation domain and within the flux rope decreases considerably from the bottom to the upper part of the domain. This is featured in **Figure 10** showing the magnetic field magnitude in the TMFM YZ-plane centered at $X = 14.2$ Mm and the negative twist contours for September 13, 07:36 UT. When the flux rope rises higher up in the corona and propagates in interplanetary space it is expected to relax to have a more uniform magnetic field magnitude within. In addition, we need to consider the general decrease of the magnetic field in the heliosphere from the Sun to the Earth. Since we are here just visually comparing the general trends in the magnetic field profiles between the TMFM flux rope and the *in-situ* magnetic cloud data, we simply use a constant scaling factor for all points that gives a rough match for this case between the magnetic field magnitudes. This means that we do not capture the possible front to rear asymmetries related to the expansion of the ICME flux ropes. To compensate for these two effects we apply a scaling of $(1/s)(Z_0/Z)^2$ in the TMFM flux rope magnetic field time-series, where $s = 100$ and where Z_0 is the height at the bottom part of the flux rope. The choice of $s = 100$ was based on obtaining the approximate match between the magnetic field magnitudes from TMFM simulation and *in-situ* observations to account for interplanetary field decrease. For more realistic forecasting the change in the magnetic field magnitude could be achieved e.g., by using TMFM results to constrain flux ropes in semi-empirical flux rope models or first principle simulations.

The results of the direct comparison are shown in **Figure 11** giving from top to bottom the magnetic field magnitude and GSE magnetic field x, y, and z components. The gray lines show the values measured at 1 AU, while the black, red and blue curves show different cuts through the TMFM flux rope transformed to GSE coordinates as described above. In the magnetic cloud observed by Wind B_x rotates quickly from ∼0 at the flux rope leading edge to its maximum value (∼ 20 nT) and then rotates slowly back to zero at the trailing edge. B_y rotates from its peak negative value (∼ − 20 nT) during the beginning of the cloud to around 0 nT for the trailing portion, while the B_z is positive and rotates from peak value of ∼ 20 nT close to zero.

Firstly, we note that the helicity sign of the magnetic cloud is negative as reported also in the Wind ICME list (https://wind.nasa.gov/ICMEindex.php, Nieves-Chinchilla et al., 2018) based on the circular-cylindrical flux rope analytical model (Nieves-Chinchilla et al., 2016). The helicity sign thus corresponds to the helicity sign of the simulated TMFM flux rope as well as that of the EUV sigmoids.

Figure 11 shows that the scaling in the lower corona $[(Z_0/Z)^2]$ yields sensible magnetic field profiles. For example, the magnetic field magnitude in the cut taken through the apex (the black line)

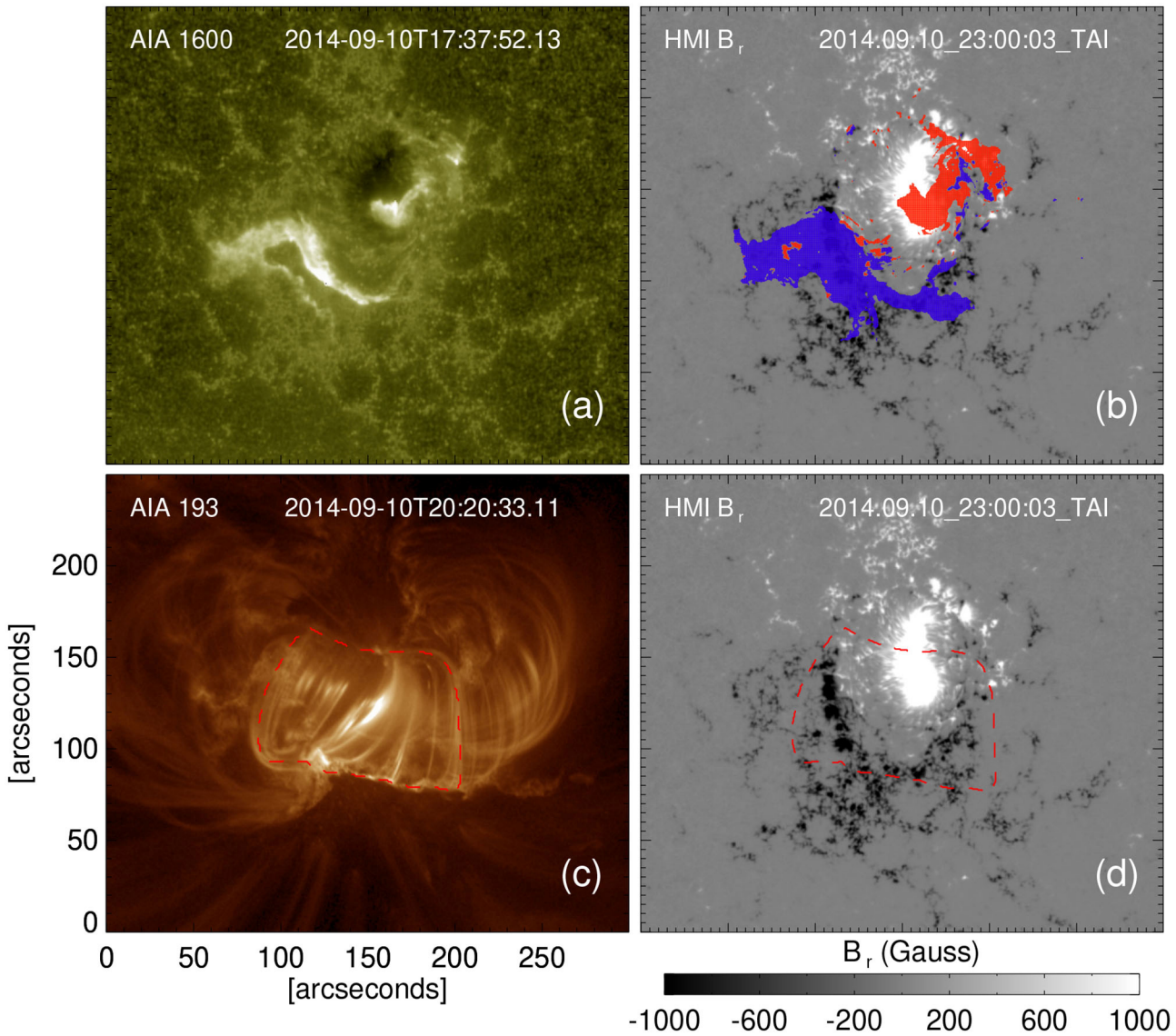

FIGURE 7 | (a) Depicts the flare ribbon in AIA 1,600 Å image. The red dashed boundary line in **(c)** marks the post-eruption arcades (PEAs) in AIA 193 Å image. **(b,d)** Illustrate the radial component of HMI vector magnetic field. The red and blue regions in **(b)** depict the cumulative flare ribbon area overlying the positive and negative magnetic field, respectively. The red dashed boundary in **(d)** is the over-plotted PEA region.

peaks approximately close to the axis of the flux rope (remember that we did not consider here expansion in interplanetary space). In addition, the figure shows that the simulation produces flux rope like rotations in all three components. The agreement with the *in-situ* observations is however not very good. None of the lineouts capture the positive GSE B_z in the flux rope. Only the red curves have positive B_z in the trailing part of the flux rope. The negative B_y in the beginning of the *in-situ* flux rope is also not captured, while the red curves show positive B_x similar to *in-situ* flux rope. We also tried several additional lineouts (data not shown) that were made at different distances in the y-direction from the axis at different distances along it. None of these showed a significantly improved match with the *in-situ* observations.

Differences between the TMFM estimates and *in-situ* observations can be due to evolution and deformation of the CME flux rope after it left the lower corona and/or due geometrical reasons, i.e., if the observing spacecraft crossed the flux rope loop significantly from below or above. The angle between the shock normal and the radial direction for this event is 29°, indicating the crossing from the intermediate distance from the apex of the flux rope (for the method see e.g., Janvier et al., 2015; Savani et al., 2015). The flux rope reconstruction in the Wind magnetic cloud list gives a very large impact factor of $y_0/R = -0.925$ (where y_0 is the closest approach distance of the spacecraft from the flux rope axis and R the flux rope radius) and the axis orientation with longitude $\phi = 350°$ and latitude $\phi = 9°$.

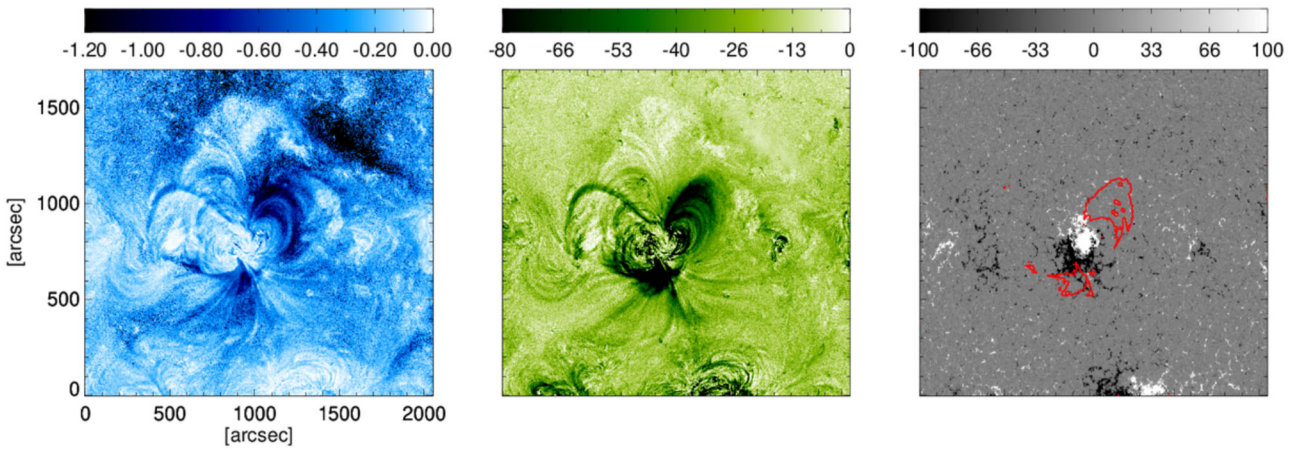

FIGURE 8 | Left panel shows the minimum intensity map of logarithmic base ratio images obtained from the sequence of AIA 211 Angstrom images. Middle panel shows the minimum intensity map of base difference images obtained from the sequence of AIA 211 Angstrom images. Right panel shows the co spatial line-of-sight magnetogram. The red contours denote the core dimming area.

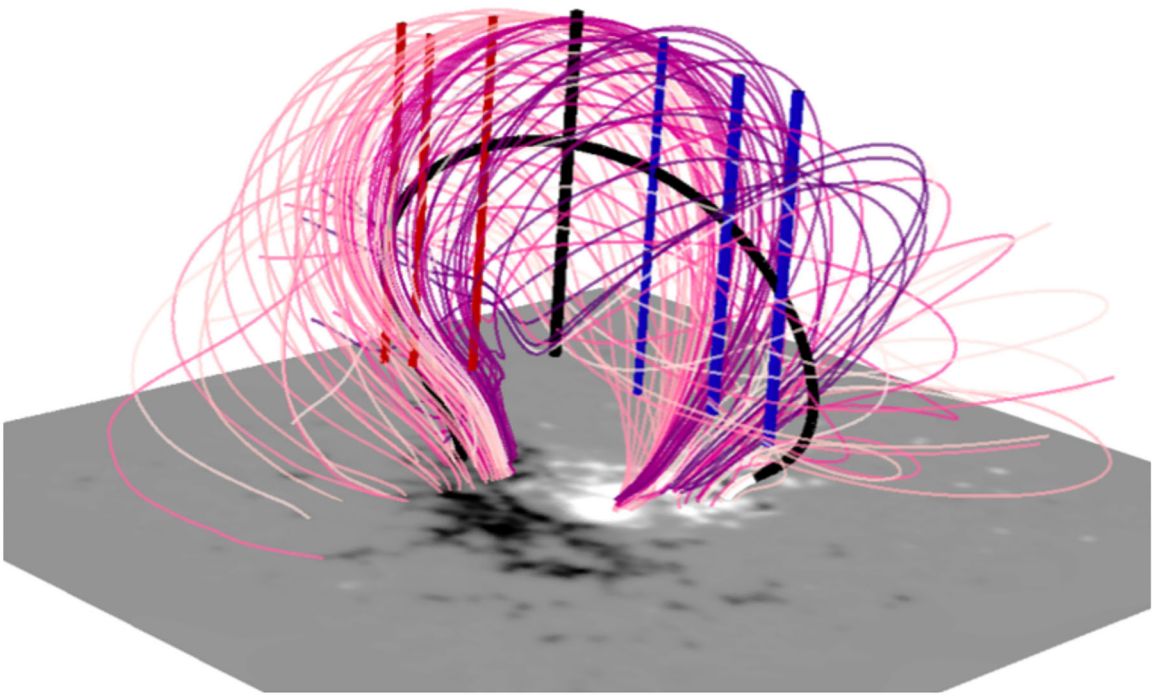

FIGURE 9 | Lineouts through the flux rope through the apex (black vertical line), and different distances from the apex along the axis (blue and red vertical lines) in steps of 30 Mm. The axis of the flux rope is shown with a thick black curve. Field lines are shown with different colors.

The quality of the reconstruction is not good for this case, but the above features clearly indicate that this magnetic cloud was not centrally encountered at Earth.

The TMFM B_Y maps (corresponding roughly the expected GSE B_Z in interplanetary space) in the XY plane for three different heights in the corona from close to the apex of the flux rope ($Z = 150$ Mm, left panel) to mid/bottom part of the flux rope ($Z = 70$ Mm, right panel) are shown in **Figure 12**. This figure shows that no matter how the lineouts are made through the flux rope, we do not get negative GSE B_Z in the front part of the flux rope. It could be that the Earth and the spacecraft at L1 intercepted only the lower part of the flux rope. This is consistent with coronagraph observations and DONKI ENLIL runs showing that the CME in question propagated northward of the ecliptic.

Another important point clearly visible from **Figure 11** is the sensitivity of the magnetic field profiles extracted from the

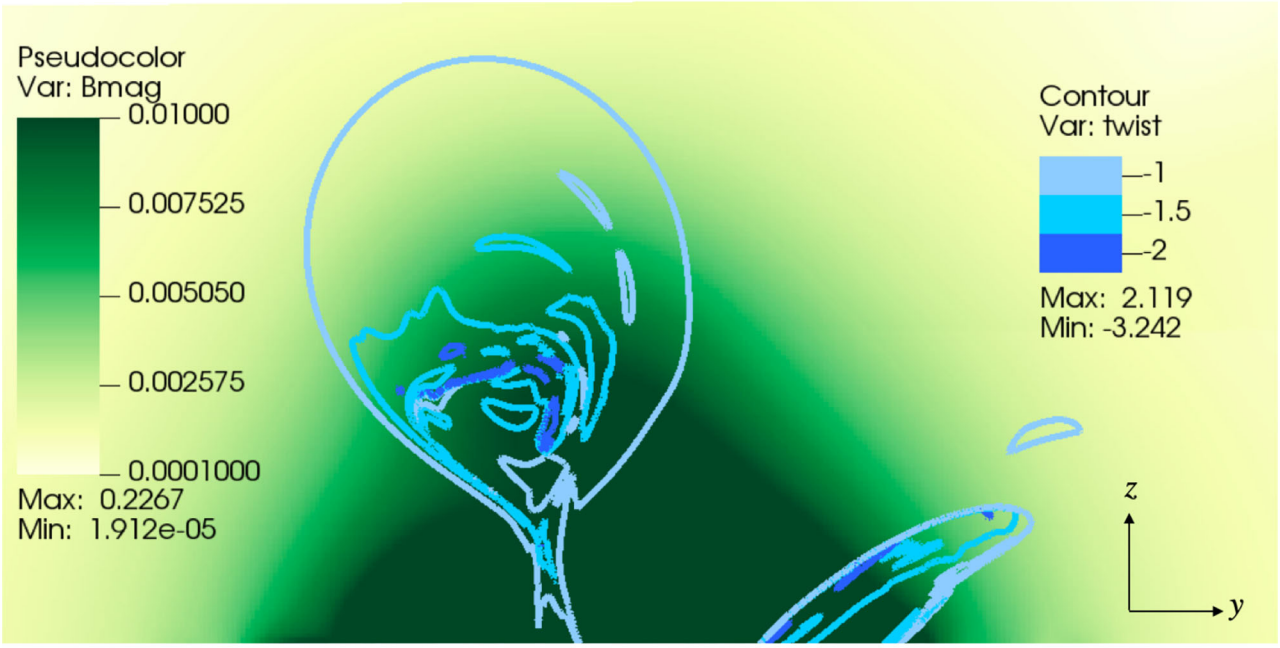

FIGURE 10 | TMFM magnetic field magnitude map of the YZ-plane centered at $X = 14.2$ Mm and the negative high twist contours on September 13, 07:36 UT in the simulation.

TMFM flux rope to the point where the cut is made. For this case this is particularly clear for the field magnitude and for the GSE B_x component. For the B_y and B_z the variations are less drastic, but still up to about $\sim$ 10 nT difference in the magnitude. For the cuts made away from the axis differences are even larger.

6. SUMMARY AND DISCUSSION

In this paper we have performed a fully data-driven simulation of the eruptive solar flux rope that formed into a CME observed on September 10, 2014 that originated from active region 12158. The data-driven simulation is based on the time-dependent magnetofrictional method (TMFM) that uses the electric field inverted from a time-series of photospheric vector magnetograms as its sole boundary condition. We described here the method to extract the flux rope from the simulation data based on the twist number (T_w) maps and extracting its key parameters.

Our simulation produced a very well-defined flux rope that rose through the simulation domain. The flux rope was identified as a coherent region of increased twist number ($|T_w| > 1$) according to the definition in Liu et al. (2016), in this case the twist was negative. Regions of higher $|T_w|$ formed during the early flux rope formation, but we did not find significant increase in $|T_w|$ as the flux rope rose.

The non-inductive electric field component of the photospheric boundary condition has been found critical for producing the flux rope and its eruption (section 2.2). We constrained it here using the *ad-hoc* assumption. It is an important and interesting question how the non-inductive electric field should be energy-optimized, in particular for the space weather purposes that requires a quick approach. Based on the studies conducted so far it seems that TMFM needs typically an overestimation of the helicity injection compared to the DAVE4VM reference value. The optimization is also done for the whole active region, while it is typically only a part of it that is involved in the eruption. Constraining of electric fields in TMFM can be done also using different approaches, e.g., using the PDFI (Poloidal-toroidal-decomposition-Doppler-Fourier-local-correlation-tracking-Ideal) electric field inversion method (Kazachenko et al., 2014). Using the preset range of *ad-hoc* U and Ω values in TMFM could however be a viable and quick solution for space weather forecasting purposes as they require only magnetograms as the input. Such approach however requires that the flux rope parameters (when it is produced in the simulation) do not change significantly depending on the U or Ω value. It is indeed hinted in our previous studies (Pomoell et al., 2019) that one cannot discriminate between the runs based only on energy injection.

The axis of the flux rope was determined using the state-of-the-art method in Liu et al. (2016) that is based on finding the local extremum in twist number T_w. For our case the extremum (minimum) could be located and the field lines visually wound about the common axis. We however note that the determination of the flux rope axis using this approach might not always be this straightforward (e.g., multiple local extremum due to complex twist distribution). Investigating the flux rope axis determination techniques and their robustness from the simulation data is needed.

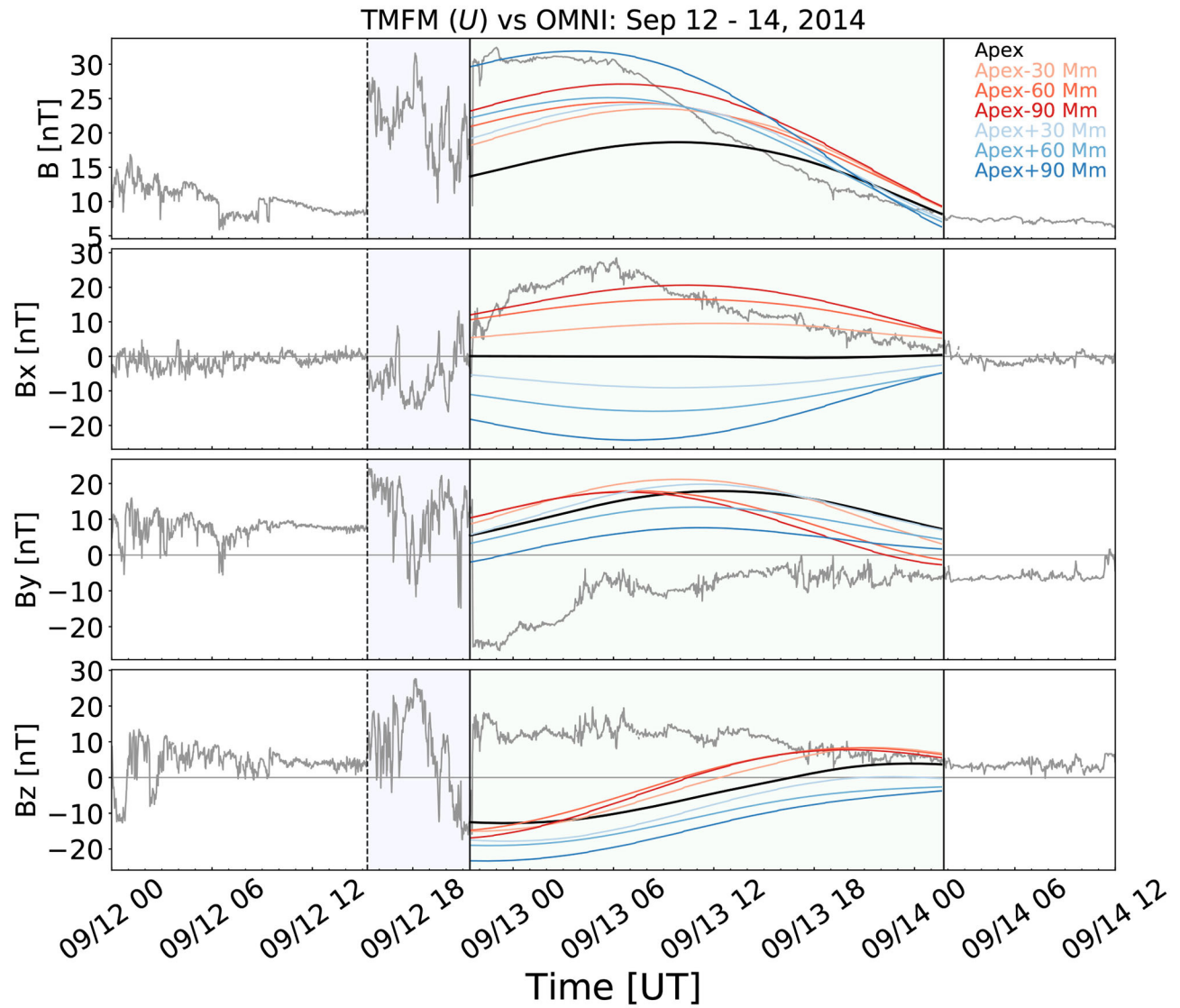

FIGURE 11 | Direct comparison of the TMFM results on September 12, 2014 at 12:36 UT to *in-situ* observations in the Near-Earth solar wind for seven different cuts along the axis of the flux rope. The black line is the cut through the apex of the flux rope ($x = 14$ Mm, $y = -42$ Mm). The blue (red) curves are when 30, 60, and 90 Mm distance along the axis are added to (subtracted from) the apex.

We found a very good visual agreement between the TMFM simulated flux rope field lines and the EUV observations of a sigmoidal structure at the time of the CME eruption. Both the simulation and observations also indicated that the flux rope had negative magnetic helicity. The obtained results are in addition in agreement with the previously reported NLFFF extrapolation results of the same event (Vemareddy et al., 2016; Zhao et al., 2016) that also yielded a good correspondence with observations.

Further support for the applicability of TMFM to model solar eruptions was given by the estimation of the axial magnetic flux enclosed by the TMFM flux rope. The obtained axial magnetic flux values remained consistent when calculated at different points along the axis and they matched with the factor of two with the axial flux estimated from the core dimming method. The poloidal fluxes estimated using PEA and flare ribbon techniques, both of which give the estimate of the flux added by magnetic reconnection during the eruption, were higher than the axial flux from the core dimming method and from the simulation, but still the same order of magnitude. The lower estimate for the toroidal flux from the dimming method than the estimate for the poloidal flux from the flare ribbon method found in this study is in agreement with the result obtained from the statistical study by Sindhuja and Gopalswamy (2020). Some studies have however also indicated a significant increase in toroidal flux due to flare reconnection during the CME eruption (e.g., Xing et al., 2020). The temporal evolution of axial/poloidal fluxes and twist in flux ropes, and determination of those from the simulation data,

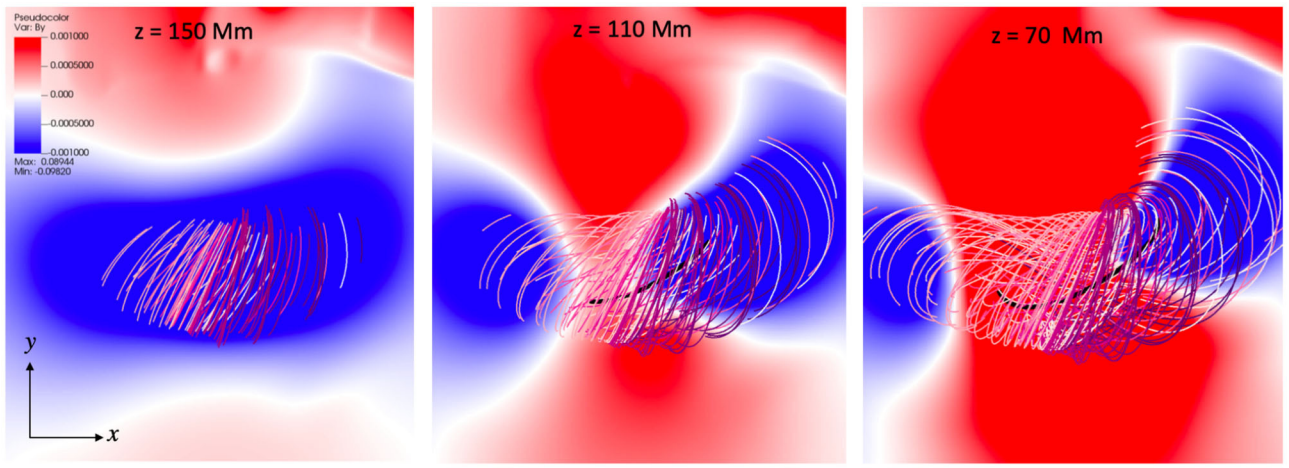

FIGURE 12 | TMFM flux rope field lines and the magnetic field B_y maps (corresponding roughly the GSE B_Z) in the *xy*-plane at three different heights in the corona.

are complicated research questions that require more extensive future investigations.

The extracted magnetic field lineouts through different parts of the TMFM flux rope are useful for giving the first estimate of the space weather response, although we emphasize that significant evolution and deformations can take place during the coronal and interplanetary propagation and interactions (e.g., Manchester et al., 2017). We also performed a scaling of the magnetic field to account for the magnetic field gradient in the lower corona in the simulation domain and the general decrease of the field in interplanetary space (see section 5.2).

For the investigated event the direct comparison of the TMFM derived time series of the magnetic field components (transferred straightforwardly to GSE coordinates) with *in-situ* observations did not produce a good visual agreement with any of the lineouts we made through the TMFM flux rope. The mismatch between the *in-situ* observations and TMFM predictions in this case is likely due to the Earth intercepting primarily the lower part of the CME, i.e., missing largely the southward fields in the top part of the flux rope. This is consistent with the CME propagating northward from the ecliptic as seen from the coronagraph imagery (section 3). As stated above, the discrepancy between the magnetic field time series estimated directly using the flux rope in the low corona and *in-situ* ones are also expected to arise due to deflections, rotation, expansion and deformations the CME flux rope may experience between the Sun and the Earth. The magnetic field time-series in the near-Earth solar wind associated with the September 10 CME were also estimated in a parametric study by An et al. (2019) using a 3D heliospheric MHD simulation Reproduce Plasma Universe (REPPU) with a spheromak CME model injected at 38 solar radii. The results showed that the magnetic field time series from the simulation varied significantly depending on the parameters of the injected CMEs, highlighting the importance of having the knowledge of realistic input values to magnetized CME models.

Our study also revealed that the resulting magnetic field magnitude and component profiles are very sensitive to how the lineout was made through the TMFM flux rope. This further emphasizes the importance to accurately forecast how the flux rope intercepts the Earth. In this effort the lower coronal evolution is critical. Several studies have indicated that the most dramatic changes in the propagation direction and tilt of CME flux ropes occurs soon after their eruption, i.e., within a first few solar radii from the Sun (e.g., Kay et al., 2013, 2017; Isavnin et al., 2014).

The simulation run produced the flux rope in the bottom of the simulation at the time corresponding closely to the actual eruption on September 10, 2014. The rise of the flux rope through the simulation domain is however significantly slower than in reality, taking ∼2 days. The slow rise is an intrinsic feature of the TMFM method where velocity does not include plasma dynamics terms, but is by the Lorentz force only, see also discussion in Pomoell et al. (2019). This is clearly an issue for long-lead time space weather forecasting. Price et al. (2020) performed relaxation runs to explore the eruption mechanism for the CME flux rope that erupted from the Sun on December 28, 2015 at about 11:30 UT. When the driving was stopped on December 28 at 12 UT, i.e., very shortly after the observed eruption, the rising continued but at a considerably slower rate. When the driving was stopped on December 29 at 12 UT the rise of the flux rope was largely unchanged compared to the case when driving was not stopped (see Figure 8 in Price et al., 2020). That is, the flux rope rise was not due to the photospheric evolution, but consistent with a torus-instability scenario. This means that the "freezing of magnetograms" in TMFM could be applied for space weather forecasting purposes. Another option is that if flux rope parameters do not generally change significantly during the rise, they could be extracted early in the simulation.

To summarize, data-driven and time-dependent modeling of eruptive coronal magnetic fields is a promising method

for operational space weather forecasting purposes as they can produce the magnetic structure of CME flux ropes using magnetograms as its sole boundary condition. Time-dependent magnetofrictional method (TMFM) presents a particularly viable option since it is comparatively computationally efficient. This study and previous works (see the Introduction) have clearly demonstrated that TMFM is capable of producing the formation and early evolution of solar flux ropes. We demonstrated here that the intrinsic flux rope parameters can be straightforwardly derived from the TMFM simulation data (such as a twist map, helicity sign, axial magnetic flux and magnetic field lineouts). They are important for giving the early estimate of the space weather response, but the strongest potential of data-driven flux rope modeling approaches in the low corona is expected to come from using them to constrain flux ropes in semi-empirical and first principle models. The success of the predictions from these models is crucially dependent on realistic input values. As discussed in the Introduction the lack of knowledge of the magnetic field properties in CMEs is in particular one of biggest current challenges in space weather predictions. There are however some challenges to be explored further whether the TMFM technique can be adapted as standard forecasting procedure.

DATA AVAILABILITY STATEMENT

The original contributions presented in the study are included in the article/**Supplementary Material**, further inquiries can be directed to the corresponding author/s. OMNI data was achieved through CDAWeb (https://cdaweb.gsfc.nasa.gov/; Last access: March 11, 2021).

AUTHOR CONTRIBUTIONS

EK has been the key responsible for writing this paper, compiled the simulation runs, flux rope analysis, and related the figures. JP was the author of the TMFM code and the programs to identify the flux rope and calculating its parameters from the simulation data and assisted in using them. DP has contributed to the writing of optimization programs and assisted in the simulation and analysis process. RS produced the magnetic flux calculations based on observational proxies and produced related figure. EA has made the event identification and assisted in related interpretations. All authors have contributed to the writing of the manuscript and the interpretation of the results.

FUNDING

This manuscript has received funding from the SolMAG project (ERC-COG 724391) funded by the European Research Council (ERC) in the framework of the Horizon 2020 Research and Innovation Programme, and the Academy of Finland project SMASH 1310445. The results presented in here have been achieved under the framework of the Finnish Centre of Excellence in Research of Sustainable Space (Academy of Finland grant number 312390), which we gratefully acknowledge. We acknowledge H2020 EUHFORIA 2.0 project (870405). EA acknowledges support from the Academy of Finland (Postdoctoral ResearcherGrant 322455).

ACKNOWLEDGMENTS

We acknowledge A. Szabo for the Wind/MFI data, and K. Ogilvie for the Wind/SWE data. The LASCO CME catalog was generated and maintained at the CDAW Data Center by NASA and The Catholic University of America in cooperation with the Naval Research Laboratory. SOHO was a project of international cooperation between ESA and NASA. SDO data were courtesy of NASA/SDO and the AIA and HMI science teams.

SUPPLEMENTARY MATERIAL

The Supplementary Material for this article can be found online at: https://www.frontiersin.org/articles/10.3389/fspas.2021.631582/full#supplementary-material

REFERENCES

An, J., Magara, T., Hayashi, K., and Moon, Y. J. (2019). Parametric study of ICME properties related to space weather disturbances via a series of three-dimensional MHD simulations. *Sol. Phys.* 294:143. doi: 10.1007/s11207-019-1531-6

Berger, M. A., and Prior, C. (2006). The writhe of open and closed curves. *J. Phys. A Math. Gen.* 39, 8321–8348. doi: 10.1088/0305-4470/39/26/005

Bothmer, V., and Schwenn, R. (1998). The structure and origin of magnetic clouds in the solar wind. *Ann. Geophys.* 16, 1–24. doi: 10.1007/s00585-997-0001-x

Bourdin, P. A. (2017). Plasma beta stratification in the solar atmosphere: a possible explanation for the penumbra formation. *Astrophys. J. Lett.* 850:L29. doi: 10.3847/2041-8213/aa9988

Brueckner, G. E., Howard, R. A., Koomen, M. J., Korendyke, C. M., Michels, D. J., Moses, J. D., et al. (1995). The large angle spectroscopic coronagraph (LASCO). *Sol. Phys.* 162, 357–402. doi: 10.1007/BF00733434

Burlaga, L., Sittler, E., Mariani, F., and Schwenn, R. (1981). Magnetic loop behind an interplanetary shock: Voyager, Helios, and IMP 8 observations. *J. Geophys. Res.* 86, 6673–6684. doi: 10.1029/JA086iA08p06673

Cane, H. V., Richardson, I. G., and Wibberenz, G. (1997). Helios 1 and 2 observations of particle decreases, ejecta, and magnetic clouds. *J. Geophys. Res.* 102, 7075–7086. doi: 10.1029/97JA00149

Chen, J. (2017). Physics of erupting solar flux ropes: coronal mass ejections (CMEs), recent advances in theory and observation. *Phys. Plasmas* 24:090501. doi: 10.1063/1.4993929

Cheung, M. C. M., De Pontieu, B., Tarbell, T. D., Fu, Y., Tian, H., Testa, P., et al. (2015). Homologous helical jets: observations by IRIS, SDO, and Hinode and magnetic modeling with data-driven simulations. *Astrophys. J.* 801:83. doi: 10.1088/0004-637X/801/2/83

Cheung, M. C. M., and DeRosa, M. L. (2012). A method for data-driven simulations of evolving solar active regions. *Astrophys. J.* 757:147. doi: 10.1088/0004-637X/757/2/147

Dissauer, K., Veronig, A. M., Temmer, M., Podladchikova, T., and Vanninathan, K. (2018a). On the detection of coronal dimmings and the extraction of their characteristic properties. *Astrophys. J.* 855:137. doi: 10.3847/1538-4357/aaadb5

Dissauer, K., Veronig, A. M., Temmer, M., Podladchikova, T., and Vanninathan, K. (2018b). Statistics of coronal dimmings associated with coronal mass

ejections. I. Characteristic dimming properties and flare association. *Astrophys. J.* 863:169. doi: 10.3847/1538-4357/aad3c6

Domingo, V., Fleck, B., and Poland, A. I. (1995). The SOHO mission: an overview. *Sol. Phys.* 162, 1–37. doi: 10.1007/BF00733425

Duan, A., Jiang, C., He, W., Feng, X., Zou, P., and Cui, J. (2019). A study of pre-flare solar coronal magnetic fields: magnetic flux ropes. *Astrophys. J.* 884:73. doi: 10.3847/1538-4357/ab3e33

Duan, A., Jiang, C., Hu, Q., Zhang, H., Gary, G. A., Wu, S. T., et al. (2017). Comparison of two coronal magnetic field models to reconstruct a sigmoidal solar active region with coronal loops. *Astrophys. J.* 842:119. doi: 10.3847/1538-4357/aa76e1

Dungey, J. W. (1961). Interplanetary magnetic field and the auroral zones. *Phys. Rev. Lett.* 6, 47–48. doi: 10.1103/PhysRevLett.6.47

Fisher, G. H., Abbett, W. P., Bercik, D. J., Kazachenko, M. D., Lynch, B. J., Welsch, B. T., et al. (2015). The coronal global evolutionary model: using HMI vector magnetogram and Doppler data to model the buildup of free magnetic energy in the solar corona. *Space Weather* 13, 369–373. doi: 10.1002/2015SW001191

Gary, G. A. (2001). Plasma beta above a solar active region: rethinking the paradigm. *Sol. Phys.* 203, 71–86. doi: 10.1023/A:1012722021820

Gloeckler, G., Cain, J., Ipavich, F. M., Tums, E. O., Bedini, P., Fisk, L. A., et al. (1998). Investigation of the composition of solar and interstellar matter using solar wind and pickup ion measurements with SWICS and SWIMS on the ACE spacecraft. *Space Sci. Rev.* 86, 497–539. doi: 10.1023/A:1005036131689

Gonzalez, W. D., Joselyn, J. A., Kamide, Y., Kroehl, H. W., Rostoker, G., Tsurutani, B. T., et al. (1994). What is a geomagnetic storm? *J. Geophys. Res.* 99, 5771–5792. doi: 10.1029/93JA02867

Gopalswamy, N., Akiyama, S., Yashiro, S., and Xie, H. (2018). "A new technique to provide realistic input to CME forecasting models," in *Space Weather of the Heliosphere: Processes and Forecasts, Volume 335 of IAU Symposium*, eds C. Foullon and O. E. Malandraki, 258–262. doi: 10.1017/S1743921317011048

Gopalswamy, N., Yashiro, S., Akiyama, S., and Xie, H. (2017). Estimation of reconnection flux using post-eruption arcades and its relevance to magnetic clouds at 1 AU. *Sol. Phys.* 292:65. doi: 10.1007/s11207-017-1080-9

Green, L. M., and Kliem, B. (2009). Flux rope formation preceding coronal mass ejection onset. *Astrophys. J. Lett.* 700, L83–L87. doi: 10.1088/0004-637X/700/2/L83

Green, L. M., Török, T., Vršnak, B., Manchester, W., and Veronig, A. (2018). The origin, early evolution and predictability of solar eruptions. *Space Sci. Rev.* 214:46. doi: 10.1007/s11214-017-0462-5

Howard, R. A., Moses, J. D., Vourlidas, A., Newmark, J. S., Socker, D. G., Plunkett, S. P., et al. (2008). Sun earth connection coronal and heliospheric investigation (SECCHI). *Space Sci. Rev.* 136, 67–115. doi: 10.1007/s11214-008-9341-4

Huttunen, K. E. J., Schwenn, R., Bothmer, V., and Koskinen, H. E. J. (2005). Properties and geoeffectiveness of magnetic clouds in the rising, maximum and early declining phases of solar cycle 23. *Ann. Geophys.* 23, 625–641. doi: 10.5194/angeo-23-625-2005

Isavnin, A., Vourlidas, A., and Kilpua, E. K. J. (2014). Three-dimensional evolution of flux-rope CMEs and its relation to the local orientation of the heliospheric current sheet. *Sol. Phys.* 289, 2141–2156. doi: 10.1007/s11207-013-0468-4

James, A. W., Valori, G., Green, L. M., Liu, Y., Cheung, M. C. M., Guo, Y., et al. (2018). An observationally constrained model of a flux rope that formed in the solar corona. *Astrophys. J. Lett.* 855:L16. doi: 10.3847/2041-8213/aab15d

Janvier, M., Dasso, S., Démoulin, P., Masías-Meza, J. J., and Lugaz, N. (2015). Comparing generic models for interplanetary shocks and magnetic clouds axis configurations at 1 AU. *J. Geophys. Res.* 120, 3328–3349. doi: 10.1002/2014JA020836

Jian, L., Russell, C. T., Luhmann, J. G., and Skoug, R. M. (2006). Properties of interplanetary coronal mass ejections at one AU during 1995–2004. *Sol. Phys.* 239, 393–436. doi: 10.1007/s11207-006-0133-2

Jiang, C., Wu, S. T., Feng, X., and Hu, Q. (2016). Data-driven magnetohydrodynamic modelling of a flux-emerging active region leading to solar eruption. *Nat. Commun.* 7:11522. doi: 10.1038/ncomms11522

Kaiser, M. L., Kucera, T. A., Davila, J. M., St. Cyr, O. C., Guhathakurta, M., and Christian, E. (2008). The STEREO mission: an introduction. *Space Sci. Rev.* 136, 5–16. doi: 10.1007/s11214-007-9277-0

Kay, C., Gopalswamy, N., Reinard, A., and Opher, M. (2017). Predicting the magnetic field of earth-impacting CMEs. *Astrophys. J.* 835:117. doi: 10.3847/1538-4357/835/2/117

Kay, C., Opher, M., and Evans, R. M. (2013). Forecasting a coronal mass ejection's altered trajectory: ForeCAT. *Astrophys. J.* 775:5. doi: 10.1088/0004-637X/775/1/5

Kazachenko, M. D., Fisher, G. H., and Welsch, B. T. (2014). A comprehensive method of estimating electric fields from vector magnetic field and Doppler measurements. *Astrophys. J.* 795:17. doi: 10.1088/0004-637X/795/1/17

Kazachenko, M. D., Lynch, B. J., Welsch, B. T., and Sun, X. (2017). A database of flare ribbon properties from the solar dynamics observatory. I. Reconnection flux. *Astrophys. J.* 845:49. doi: 10.3847/1538-4357/aa7ed6

Kilpua, E., Koskinen, H. E. J., and Pulkkinen, T. I. (2017a). Coronal mass ejections and their sheath regions in interplanetary space. *Liv. Rev. Sol. Phys.* 14:5. doi: 10.1007/s41116-017-0009-6

Kilpua, E. K. J., Balogh, A., von Steiger, R., and Liu, Y. D. (2017b). Geoeffective properties of solar transients and stream interaction regions. *Space Sci. Rev.* 212, 1271–1314. doi: 10.1007/s11214-017-0411-3

Kilpua, E. K. J., Jian, L. K., Li, Y., Luhmann, J. G., and Russell, C. T. (2011). Multipoint ICME encounters: pre-STEREO and STEREO observations. *J. Atmos. Sol. Terrest. Phys.* 73, 1228–1241. doi: 10.1016/j.jastp.2010.10.012

Kilpua, E. K. J., Lugaz, N., Mays, M. L., and Temmer, M. (2019). Forecasting the structure and orientation of earthbound coronal mass ejections. *Space Weather* 17, 498–526. doi: 10.1029/2018SW001944

Klein, L. W., and Burlaga, L. F. (1982). Interplanetary magnetic clouds at 1 AU. *J. Geophys. Res.* 87, 613–624. doi: 10.1029/JA087iA02p00613

Lemen, J. R., Title, A. M., Akin, D. J., Boerner, P. F., Chou, C., Drake, J. F., et al. (2012). The atmospheric imaging assembly (AIA) on the solar dynamics observatory (SDO). *Sol. Phys.* 275, 17–40. doi: 10.1007/s11207-011-9776-8

Lepping, R. P., Acũna, M. H., Burlaga, L. F., Farrell, W. M., Slavin, J. A., Schatten, K. H., et al. (1995). The wind magnetic field investigation. *Space Sci. Rev.* 71, 207–229. doi: 10.1007/BF00751330

Lin, R. P., Anderson, K. A., Ashford, S., Carlson, C., Curtis, D., Ergun, R., et al. (1995). A three-dimensional plasma and energetic particle investigation for the wind spacecraft. *Space Sci. Rev.* 71, 125–153. doi: 10.1007/BF00751328

Liu, R., Kliem, B., Titov, V. S., Chen, J., Wang, Y., Wang, H., et al. (2016). Structure, stability, and evolution of magnetic flux ropes from the perspective of magnetic twist. *Astrophys. J.* 818:148. doi: 10.3847/0004-637X/818/2/148

Lugaz, N., Farrugia, C. J., Manchester, IV, W. B., and Schwadron, N. (2013). The interaction of two coronal mass ejections: influence of relative orientation. *Astrophys. J.* 778:20. doi: 10.1088/0004-637X/778/1/20

Lumme, E., Pomoell, J., and Kilpua, E. K. J. (2017). Optimization of photospheric electric field estimates for accurate retrieval of total magnetic energy injection. *Sol. Phys.* 292:191. doi: 10.1007/s11207-017-1214-0

Manchester, W., Kilpua, E. K. J., Liu, Y. D., Lugaz, N., Riley, P., Török, T., et al. (2017). The physical processes of CME/ICME evolution. *Space Sci. Rev.* 212, 1159–1219. doi: 10.1007/s11214-017-0394-0

Möstl, C., Amerstorfer, T., Palmerio, E., Isavnin, A., Farrugia, C. J., Lowder, C., et al. (2018). Forward modeling of coronal mass ejection flux ropes in the inner heliosphere with 3DCORE. *Space Weather* 16, 216–229. doi: 10.1002/2017SW001735

Nieves-Chinchilla, T., Linton, M. G., Hidalgo, M. A., Vourlidas, A., Savani, N. P., Szabo, A., et al. (2016). A circular-cylindrical flux-rope analytical model for magnetic clouds. *Astrophys. J.* 823:27. doi: 10.3847/0004-637X/823/1/27

Nieves-Chinchilla, T., Vourlidas, A., Raymond, J. C., Linton, M. G., Al-haddad, N., Savani, N. P., et al. (2018). Understanding the internal magnetic field configurations of ICMEs using more than 20 years of wind observations. *Sol. Phys.* 293:25. doi: 10.1007/s11207-018-1247-z

Odstrcil, D., Riley, P., and Zhao, X. P. (2004). Numerical simulation of the 12 May 1997 interplanetary CME event. *J. Geophys. Res.* 109:A02116. doi: 10.1029/2003JA010135

Ogilvie, K. W., Chornay, D. J., Fritzenreiter, R. J., Hunsaker, F., Keller, J., Lobell, J., et al. (1995). SWE: a comprehensive plasma instrument for the wind spacecraft. *Space Sci. Rev.* 71, 55–77. doi: 10.1007/BF00751326

Ogilvie, K. W., and Desch, M. D. (1997). The wind spacecraft and its early scientific results. *Adv. Space Res.* 20, 559–568. doi: 10.1016/S0273-1177(97)00439-0

Palmerio, E., Kilpua, E. K. J., James, A. W., Green, L. M., Pomoell, J., Isavnin, A., et al. (2017). Determining the intrinsic CME flux rope type using remote-sensing solar disk observations. *Sol. Phys.* 292:39. doi: 10.1007/s11207-017-1063-x

Palmerio, E., Kilpua, E. K. J., Möstl, C., Bothmer, V., James, A. W., Green, L. M., et al. (2018). Coronal magnetic structure of earthbound CMEs and *in situ* comparison. *Space Weather* 16, 442–460. doi: 10.1002/2017SW001767

Pesnell, W. D., Thompson, B. J., and Chamberlin, P. C. (2012). The solar dynamics observatory (SDO). *Sol. Phys*. 275, 3–15. doi: 10.1007/s11207-011-9841-3

Pevtsov, A. A., and Balasubramaniam, K. S. (2003). Helicity patterns on the sun. *Adv. Space Res*. 32, 1867–1874. doi: 10.1016/S0273-1177(03)90620-X

Pomoell, J., Lumme, E., and Kilpua, E. (2019). Time-dependent data-driven modeling of active region evolution using energy-optimized photospheric electric fields. *Sol. Phys*. 294:41. doi: 10.1007/s11207-019-1430-x

Pomoell, J., and Poedts, S. (2018). EUHFORIA: European heliospheric forecasting information asset. *J. Space Weather Space Clim*. 8:A35. doi: 10.1051/swsc/2018020

Price, D. J., Pomoell, J., and Kilpua, E. K. J. (2020). Exploring the coronal evolution of AR 12473 using time-dependent, data-driven magnetofrictional modelling. *Astron. Astrophys*. 644:A28. doi: 10.1051/0004-6361/202038925

Price, D. J., Pomoell, J., Lumme, E., and Kilpua, E. K. J. (2019). Time-dependent data-driven coronal simulations of AR 12673 from emergence to eruption. *Astron. Astrophys*. 628:A114. doi: 10.1051/0004-6361/201935535

Pulkkinen, T. (2007). Space weather: terrestrial perspective. *Liv. Rev. Sol. Phys*. 4:1. doi: 10.12942/lrsp-2007-1

Richardson, I. G., and Cane, H. V. (2010). Near-earth interplanetary coronal mass ejections during solar cycle 23 (1996–2009): catalog and summary of properties. *Sol. Phys*. 264, 189–237. doi: 10.1007/s11207-010-9568-6

Richardson, I. G., and Cane, H. V. (2012). Solar wind drivers of geomagnetic storms during more than four solar cycles. *J. Space Weather Space Clim*. 2:A01. doi: 10.1051/swsc/2012001

Rust, D. M., and Kumar, A. (1996). Evidence for helically kinked magnetic flux ropes in solar eruptions. *Astrophys. J. Lett*. 464:L199. doi: 10.1086/310118

Sarkar, R., Gopalswamy, N., and Srivastava, N. (2020). An observationally constrained analytical model for predicting the magnetic field vectors of interplanetary coronal mass ejections at 1 au. *Astrophys. J*. 888:121. doi: 10.3847/1538-4357/ab5fd7

Savani, N. P., Vourlidas, A., Szabo, A., Mays, M. L., Richardson, I. G., Thompson, B. J., et al. (2015). Predicting the magnetic vectors within coronal mass ejections arriving at Earth: 1. Initial architecture. *Space Weather* 13, 374–385. doi: 10.1002/2015SW001171

Scherrer, P. H., Schou, J., Bush, R. I., Kosovichev, A. G., Bogart, R. S., Hoeksema, J. T., et al. (2012). The helioseismic and magnetic imager (HMI) investigation for the solar dynamics observatory (SDO). *Sol. Phys*. 275, 207–227. doi: 10.1007/s11207-011-9834-2

Schuck, P. W. (2008). Tracking vector magnetograms with the magnetic induction equation. *Astrophys. J*. 683, 1134–1152. doi: 10.1086/589434

Scolini, C., Chané, E., Temmer, M., Kilpua, E. K. J., Dissauer, K., Veronig, A. M., et al. (2020). CME-CME interactions as sources of CME geoeffectiveness: the formation of the complex ejecta and intense geomagnetic storm in 2017 early September. *Astrophys. J. Suppl*. 247:21. doi: 10.3847/1538-4365/ab6216

Scolini, C., Rodriguez, L., Mierla, M., Pomoell, J., and Poedts, S. (2019). Observation-based modelling of magnetised coronal mass ejections with EUHFORIA. *Astron. Astrophys*. 626:A122. doi: 10.1051/0004-6361/201935053

Shiota, D., and Kataoka, R. (2016). Magnetohydrodynamic simulation of interplanetary propagation of multiple coronal mass ejections with internal magnetic flux rope (SUSANOO-CME). *Space Weather* 14, 56–75. doi: 10.1002/2015SW001308

Sindhuja, G., and Gopalswamy, N. (2020). A study of the observational properties of coronal mass ejection flux ropes near the sun. *Astrophys. J*. 889:104. doi: 10.3847/1538-4357/ab620f

Stone, E. C., Frandsen, A. M., Mewaldt, R. A., Christian, E. R., Margolies, D., Ormes, J. F., et al. (1998). The advanced composition explorer. *Space Sci. Rev*. 86, 1–22. doi: 10.1023/A:1005082526237

Tsurutani, B. T., Lakhina, G. S., and Hajra, R. (2020). The physics of space weather/solar-terrestrial physics (STP): what we know now and what the current and future challenges are. *Nonlin. Process. Geophys*. 27, 75–119. doi: 10.5194/npg-27-75-2020

van Ballegooijen, A. A., Priest, E. R., and Mackay, D. H. (2000). Mean field model for the formation of filament channels on the sun. *Astrophys. J*. 539, 983–994. doi: 10.1086/309265

Vasyliunas, V. M. (1975). Theoretical models of magnetic field line merging. I. *Rev. Geophys*. 13, 303–336. doi: 10.1029/RG013i001p00303

Vemareddy, P., Cheng, X., and Ravindra, B. (2016). Sunspot rotation as a driver of major solar eruptions in the NOAA active region 12158. *Astrophys. J*. 829:24. doi: 10.3847/0004-637X/829/1/24

Verbeke, C., Pomoell, J., and Poedts, S. (2019). The evolution of coronal mass ejections in the inner heliosphere: implementing the spheromak model with EUHFORIA. *Astron. Astrophys*. 627:A111. doi: 10.1051/0004-6361/201834702

Vourlidas, A., Patsourakos, S., and Savani, N. P. (2019). Predicting the geoeffective properties of coronal mass ejections: current status, open issues and path forward. *Philos. Trans. A Math. Phys. Eng. Sci*. 377:20180096. doi: 10.1098/rsta.2018.0096

Webb, D. F., and Howard, T. A. (2012). Coronal mass ejections: observations. *Liv. Rev. Sol. Phys*. 9:3. doi: 10.12942/lrsp-2012-3

Webb, D. F., Lepping, R. P., Burlaga, L. F., DeForest, C. E., Larson, D. E., Martin, S. F., et al. (2000). The origin and development of the May 1997 magnetic cloud. *J. Geophys. Res*. 105, 27251–27260. doi: 10.1029/2000JA000021

Wiegelmann, T., and Sakurai, T. (2012). Solar force-free magnetic fields. *Liv. Rev. Sol. Phys*. 9:5. doi: 10.12942/lrsp-2012-5

Xing, C., Cheng, X., Qiu, J., Hu, Q., Priest, E. R., and Ding, M. D. (2020). Quantifying the toroidal flux of preexisting flux ropes of coronal mass ejections. *Astrophys. J*. 889:125. doi: 10.3847/1538-4357/ab6321

Yang, W. H., Sturrock, P. A., and Antiochos, S. K. (1986). Force-free magnetic fields: the magneto-frictional method. *Astrophys. J*. 309:383. doi: 10.1086/164610

Yardley, S. L., Mackay, D. H., and Green, L. M. (2018). Simulating the coronal evolution of AR 11437 using SDO/HMI magnetograms. *Astrophys. J*. 852:82. doi: 10.3847/1538-4357/aa9f20

Zhang, J., Liemohn, M. W., Kozyra, J. U., Lynch, B. J., and Zurbuchen, T. H. (2004). A statistical study of the geoeffectiveness of magnetic clouds during high solar activity years. *J. Geophys. Res*. 109:A09101. doi: 10.1029/2004JA010410

Zhang, J., Richardson, I. G., Webb, D. F., Gopalswamy, N., Huttunen, E., Kasper, J. C., et al. (2007). Solar and interplanetary sources of major geomagnetic storms (Dst $\leq$ −100 nT) during 1996–2005. *J. Geophys. Res*. 112:A10102. doi: 10.1029/2007JA012321

Zhao, J., Gilchrist, S. A., Aulanier, G., Schmieder, B., Pariat, E., and Li, H. (2016). Hooked flare ribbons and flux-rope-related QSL footprints. *Astrophys. J*. 823:62. doi: 10.3847/0004-637X/823/1/62

Zurbuchen, T. H., and Richardson, I. G. (2006). *In-situ* solar wind and magnetic field signatures of interplanetary coronal mass ejections. *Space Sci. Rev*. 123, 31–43. doi: 10.1007/s11214-006-9010-4

Conflict of Interest: The authors declare that the research was conducted in the absence of any commercial or financial relationships that could be construed as a potential conflict of interest.

frontiers in Astronomy and Space Sciences

REVIEW
published: 12 May 2021
doi: 10.3389/fspas.2021.651527

Improving the Medium-Term Forecasting of Space Weather: A Big Picture Review From a Solar Observer's Perspective

*Angelos Vourlidas**

Johns Hopkins University Applied Physics Laboratory, Laurel, MD, United States

We have improved considerably our scientific understanding of the key solar drivers of Space Weather, i.e., Coronal Mass Ejections, flares, in the last 20+ years thanks to a plethora of space missions and modeling advances. Yet, a major breakthrough in assessing the geo-effectiveness of a given CME and associated phenomena still escapes us, holding back actionable medium-term (up to 7 days) forecasting of Space Weather. Why is that? I adopt a two-pronged approach to search for answers. First, I assess the last 20+ years of research on solar drivers by identifying lessons-learned and paradigm shifts in our view of solar activity, always in relation to Space Weather concerns. Then, I review the state of key observation-based quantities used in forecasting to isolate the choke points and research gaps that limit medium-term forecasting performance. Finally, I outline a path forward along three vectors—breakthrough capabilities, geo-effective potential, and actionable forecast—with the strongest potential to improve space weather forecasting horizon and robustness.

Keywords: Sun, space weather, flares - Sun, coronal mass ejection, forecast

OPEN ACCESS

Edited by:
Nandita Srivastava, Physical Research Laboratory, India

Reviewed by:
Nat Gopalswamy, National Aeronautics and Space Administration, United States
Bojan Vrsnak, University of Zagreb, Croatia

***Correspondence:**
Angelos Vourlidas
angelos.vourlidas@jhuapl.edu

Specialty section:
This article was submitted to Stellar and Solar Physics, a section of the journal Frontiers in Astronomy and Space Sciences

Received: *10 January 2021*
Accepted: *09 April 2021*
Published: *12 May 2021*

Citation:
Vourlidas A (2021) Improving the Medium-Term Forecasting of Space Weather: A Big Picture Review From a Solar Observer's Perspective. Front. Astron. Space Sci. 8:651527. doi: 10.3389/fspas.2021.651527

1. INTRODUCTION

The Sun is a cauldron of activity. Its radiative, magnetic and plasma outputs vary at all timescales, from seconds to years to decades. The solar variability modulates the state of Earth's geospace (defined here as the region encompassing the mesosphere to the magnetosphere) and drives a range of phenomena that impact space and terrestrial infrastructure. In analogy to terrestrial weather, we denote as Space Weather (SWx) geospace phenomena that occur on relatively short timescales (of the order of a few days or less) and refer to longer timescale phenomena (months to years) as Space Climate.

Within the last 20 years or so, the increasing recognition of the impact that extreme SWx events have on critical systems, such as electric power, communications, and transportation (Baker and Lanzerotti, 2016, and references therein) has transformed SWx from a narrow research topic to a worldwide societal concern. recently, the term has outgrown its original Earth-centric definition to describe the solar influence on other planets and objects (natural or man-made) within the solar system and, under the term "exoplanet SWx," the influence of stars on their exoplanets.

Here, I focus on forecasting terrestrial SWx over medium timescales (from hours to days in advance) and review the role of solar drivers on improving the forecast accuracy. This is a practical

choice. SWx expresses the reaction or behavior of geospace, which is a highly complex and non-linear system. We are still a long way from understanding this system in sufficient detail to be able to predict its behavior. Understanding, however, the inputs to the system—the solar drivers—seems a more tractable problem. My objective is to provide a "big picture" overview of where do we stand now, how did we get here, and how could we move forward to improve the quality of the solar driver inputs (and hence the accuracy of SWx forecasting).

The paper begins with a short review of important lessons-learned from recent missions (section 2) and proceeds to identify three key paradigm shifts in our view of solar activity and in the interpretation of the observations (section 3). It then discusses the choke points in forecasting of several key observational parameters and the research gaps from which they arise (section 4). The paper concludes, in section 5, with a list of measurement strategies for moving forward. Hopefully, this information could assist in targeting research or hardware development efforts that can lead to robust improvements in SWx forecasting accuracy within the next decade or so.

2. LESSONS-LEARNED FROM THE RESEARCH ON SOLAR DRIVERS

The rise of SWx to societal prominence has been largely fueled by the great advances in our capabilities to observe the Sun-Earth system in the last 25 years, starting with the launch of the Solar and Heliospheric Observatory (SOHO; Domingo et al., 1995) mission in 1995, followed by the Advanced Composition Explorer (ACE; Stone et al., 1998) in 1997 and the arrival of the (Wind; Acuña et al., 1995) spacecraft at the Sun-Earth L1 Lagrange point and culminating with the launch of the Solar Terrestrial Relations Observatory (STEREO; Kaiser et al., 2008) and the Solar Dynamics Observatory (SDO; Pesnell et al., 2012) in 2007 and 2010, respectively. Although these missions were designed for research on fundamental solar and heliospheric science, they have evolved into indispensable assets for operational SWx forecasting. Their payload complements and concept of operations have influenced the strategic plans of space agencies worldwide and the designs of numerous mission proposals. SWx research is now a highly valued Heliophysics objective on par with the long-standing research objectives of coronal heating and the acceleration of the solar wind. But, *why is that?*

The answer is fundamental for devising a successful strategy to move forward in SWx[1] forecasting. I argue that the transformational shift in Heliophysics research priorities was brought about by a series of key measurement capabilities and discoveries from the aforementioned missions and in particular from coronal and heliospheric imaging. I consider these as lessons-learned since they form the foundation basis of any future plan of action. I should note some practical caveats driven by the limited available space for this review. First, the discussion and assessments concern solely SWx issues and leave out much of the exceptional research on many other Heliophysics topics. Second, the review focuses on the most important solar phenomena that drive short-term SWx; namely, Coronal Mass Ejections (CMEs) including their shocks, flares, and Solar Energetic Particles (SEPs). Third, I will provide limited background information on the physical properties or the SWx importance of the drivers. The discussion proceeds in, roughly, the order of importance or impact of each lesson-learned.

[1]for brevity, SWx will refer to the solar drivers, hereafter, unless explicitly mentioned otherwise.

2.1. "24x7"

Before SOHO, space-based observations were performed from low-Earth orbit with a nominal duty cycle of about 50 min per the 96-min orbit. While this concept of observations was sufficient to establish CMEs as a rather regular phenomenon, it was inadequate for capturing with clarity their life cycle and connections to other forms of solar activity. SOHO pioneered uninterrupted remote observations of solar and coronal activity owing to its placement around the Sun-Earth L1 Lagrange point. The continuity of *synoptic* observations, particularly from full-disk telescopes, such as the Extreme Ultraviolet Telescope (EIT; Delaboudiniere et al., 1995), the Michelson Doppler Imager (MDI; Scherrer et al., 1995), and Large Angle and Spectrometric Coronagraph (LASCO; Brueckner et al., 1995), began to clarify the connections between photospheric magnetic flux and coronal structure evolution and erupting events, led to the creation of extensive and detailed databases of CMEs (e.g., Gopalswamy et al., 2009) and subsequently to the realization of CMEs as the main SWx driver (Gopalswamy, 2009).

2.2. Observations in EUV and Visible Light

LASCO was the first "nested" coronagraph to fully cover the inner to outer corona. Up until the start of SOHO science operations, the concept of operations for EIT considered it as context imager in support of the higher priority spectroscopic experiments on board. LASCO and EIT were expected to acquire a handful of images per day but the reality turned out to be very different. With the first observations of propagating EUV waves (Moses et al., 1997) and the direct association of front-side EUV activity to an Earth-directed CME (Thompson et al., 1999), the combination of EUV full disk and coronagraphic observations became the indispensable tool for detecting the occurrence, source region, and approximate extend (roughly) of a CME. The end result is that both visible light coronagraphs and full disk imagers have become baseline instruments on NOAA's SWx operational infrastructure, replacing soft X-ray imagers whose operational utility was based on the previous "paradigm" of flares as the primary agents of SWx (more discussion under Paradigm 2 in section 3).

2.3. Multi-Viewpoint Imaging

The success of SOHO led to the development and launch of the Solar Terrestrial Relations Observatory (STEREO; Kaiser et al., 2008) mission devoted directly to the study of CMEs and their associated phenomena, such as shocks and SEPs. The mission objectives were built around the "EUV imager plus nested coronagraph" payload but extended it with two novel

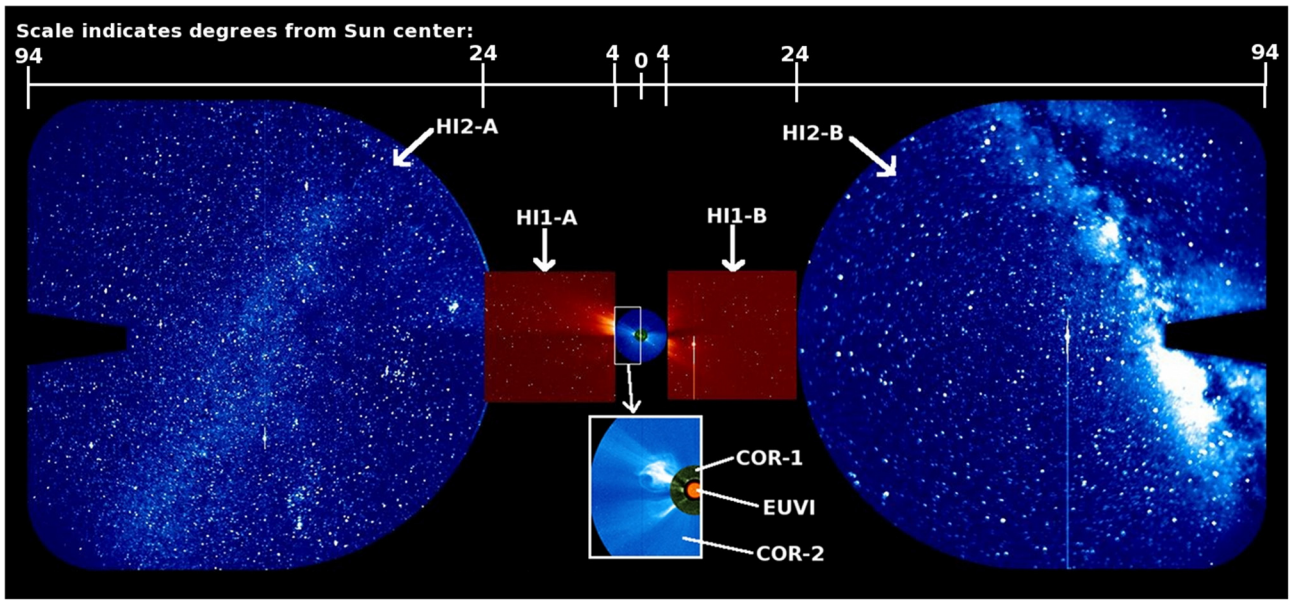

FIGURE 1 | Overview of the imaging capabilities available by the combined SECCHI payloads on the STEREO-A(head) and -B(ehind) spacecraft.

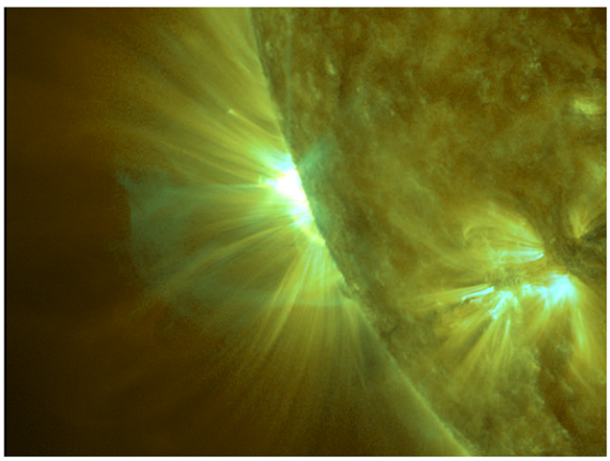

FIGURE 2 | SDO/AIA composite of 131 Å (silver) and 171 Å (gold) channels demonstrating the detection of a hot flux rope (HFR) during an eruptive flare on 29 November, 2020. The snapshots were taken at 12:48:30 UT (171 Å) and 12:48:57 UT (131 Å). The temperature of the elongated structure is likely 10 MK because it is detected only in 131 Å. See Nindos et al. (2020), for more examples.

"firsts." STEREO was the first mission to attempt 3D stereoscopy and reconstruction of astrophysical phenomena by deploying two spacecraft with nearly-identical payloads, on Earth-leading and trailing orbits, respectively, with gradually increasing inter-spacecraft angular separations of 22°/year. The other STEREO "first" was the deployment of visible light telescopes to image the inner heliosphere along the Sun-Earth line (SEL). The combined imaging payload, named the Sun-Earth Connection Coronal and Heliospheric Investigation (SECCHI; Howard et al., 2008), consists of an EUV Imager (EUVI), two nested coronagraphs (COR1, COR2), and two heliospheric imagers (HI1, HI2) and is capable of imaging, without interruptions, the full Sun-Earth space (**Figure 1**). STEREO has enabled routine 3D reconstructions of CMEs from the first moments of their eruption (e.g., Patsourakos et al., 2010), uncovering a hitherto unnoticed phase of lateral super-expansion (Patsourakos and Vourlidas, 2012), to the inner heliosphere (Poomvises et al., 2010) spurring a blooming of empirical and physics-based efforts to model the CME propagation and internal magnetic structure (e.g., Vourlidas et al., 2019, and references therein). The 3D information afforded by the multi-point imaging *and in-situ* measurements led to major insights in the origins and propagation of SEPs. STEREO revealed that SEPs undergo surprisingly wide longitudinal spread (e.g., Anastasiadis et al., 2019, and references, therein), which is likely due to the large extent of the CME shocks, even in the low corona (e.g., Lario et al., 2017). The latter finding was made possible thanks to our ability to 3D reconstruct both the shock and driver CME (Vourlidas et al., 2013, and references, therein) and even extract the physical properties at the shock remotely (e.g., Kwon and Vourlidas, 2018).

2.4. Imaging From Away the Sun-Earth Line (SEL)

The STEREO passage and observations from the L4 and L5 Lagrange points in 2009 crystallized the importance of off-SEL observations for tracking Earth-bound CMEs and CIRs (e.g., Harrison et al., 2017) and ignited strong advocacy for SWx monitoring and research from L5 (Webb et al., 2010; Vourlidas, 2015; Pevtsov et al., 2016), including concrete

mission designs (Gopalswamy et al., 2011) to the point where a mission to L5 is now considered the logical next step for improving SWx forecasting (Pulkkinen et al., 2019). Quadrature observations between the STEREO and SOHO imagers and coronagraphs, offer a straightforwad way to assess and correct projection effects in the kinematics of Earth-directed CMEs (e.g., Makela et al., 2016). The off-SEL viewpoint of STEREO-A was responsible for the discovery of the so-called "stealth" CMEs (Robbrecht et al., 2009). "Stealth" CMEs are generally slow events with low geoeffective potential in principle, but see Mishra and Srivastava (2019) and Zagainova et al. (2020) for counter examples. However, they still represent expulsions of large amounts of magnetized plasma in the heliosphere and their presence should be included in operational heliospheric models to properly assess the forecasting efficiency of these models, It should be noted that Earth-bound "stealth" CMEs are virtually impossible to detect from an Earth or L1 viewpoint. Given the observing challenges, it is unsurprising that a quantitative assessment of the geo-effectiveness of CMEs is currently lacking.

2.5. Hot Flux Ropes

Perhaps Solar Dynamics Observatory (SDO; Pesnell et al., 2012) mission's singular contribution in shaping SWx research was the detection of "hot flux ropes" (HFRs: **Figure 2**) in the Atmospheric Imaging Assembly (AIA; Lemen et al., 2012) 131 Å EUV channel (Cheng et al., 2011; Reeves and Golub, 2011). Deployed for the first time in the SDO mission, the 131 Å channel images primarily cool plasmas in Fe VIII (∼ 0.4 MK) but it is dominated by Fe XXI (∼ 11 MK) during flares (O'Dwyer et al., 2010). The fact that HFRs show only or most clearly in 131 Å (hence missed or rather went unnoticed e.g., Figure 6 in Vourlidas et al., 2012 by previous EUV experiments) along with the realization that they appear minutes (Zhang et al., 2012) or even *hours* (Patsourakos et al., 2013; Nindos et al., 2020) before the eruption opens a new perspective on how the coronal system evolves toward eruption. More crucially for medium-term forecasting, it offers the possibility to (1) isolate and better study the likely strongest magnetic structure of the erupting CME, and (2) develop a prediction capability if confined flares are indeed the tell-tale signs of HFRs formation ahead of an eventual eruption as suggested by Patsourakos et al. (2013) and Nindos et al. (2020). Deeper analyses of the phenomenon, including assessments on their appearance in other EUV wavelengths, are needed and should hopefully be forthcoming.

2.6. Sympathetic Eruptions

The long-standing question on whether eruptions (flares and CMEs) from different locations are causally linked has been finally put to test thanks to the wide longitudinal coverage afforded by SDO and STEREO. The observations showed (Schrijver and Title, 2011), and modeling supported (Török et al., 2011), that a CME over one polarity inversion line (PIL) can trigger eruptions (referred to as "sympathetic") over adjacent PILs. While the details remain to be worked out, numerical modeling indicates that the "seed" CME may trigger the subsequent eruptions via its effect on the global magnetic field, either by removing magnetic field or modifying its topology, (Jin et al., 2016). The implications for SWx forecasting are twofold: (1) the earlier CME(s) change the ambient density and magnetic field, altering the characteristic speeds of the medium and influencing the trailing event's kinematics and shock generation ability. The earlier events could also enhance the suprathermal particle background by accelerating particles out of the ambient medium thus increasing the SEP output from the trailing event(s) (e.g., Gopalswamy et al., 2002, 2015; Kahler and Vourlidas, 2014); (2) further out, "sympathetic" eruptions may interact with each other and/or change magnetic connectivity thus impacting the performance of operational forecasting models (Lugaz et al., 2017).

3. PARADIGM SHIFTS

The measurement capabilities and discoveries just described have transformed our view of solar eruptive activity over the last two cycles but I have not yet explained how. It is no easy task to crystallize the extraordinary amount of research on solar eruptions into a set of "paradigm shifts." I can discern three major "paradigms" (with SWx implications) that have undergone fundamental shifts due to the observations discussed in the previous section:

- Paradigm 1: *"Extreme Space Weather is expected during high sunspot number cycles."* The smoothed sunspot number (SSN) has been traditionally used as the indicator of solar activity levels. So much so that NOAA, NASA and the International Space Environmental Services (ISES) convened a Solar Cycle Prediction panel to forecast the next solar cycle SSN levels. Since higher SSN indicates more flares and CMEs, we have become accustomed to expect extreme SWx during strong (high SSN) cycles and to "lower our guard" during weak cycles. This is not, however, the lesson we should draw from the last cycle. Solar Cycle 24 (SC24) was the weakest cycle of the last 100 years and, more importantly for this discussion, the weakest cycle during the space era. While solar wind reached its lowest values ever measured (McComas et al., 2013), the cosmic ray background reached records values raising serious concerns on the viability of human deep space exploration during weak cycles (Schwadron et al., 2018). Although Earth experienced weaker geomagnetic storms than in SC23 (Manoharan et al., 2018) and only two Ground Level Enhancement (GLE) particle events, the CME rate was largely the same (Lamy et al., 2017). A likely reason for the absence of strong SWx events may be the lower rate of fast and/or wide CMEs in SC24 (Gopalswamy et al., 2020). However, STEREO's wide inner heliospheric coverage indicate that many more GLE-level events likely occurred, some even stronger than SC23 events (Cohen and Mewaldt, 2018) but Earth was not magnetically connected to them (Gopalswamy et al., 2014). Crucially, STEREO measured the strongest magnetic fields in an interplanetary CME (Russell et al., 2013; Liu et al., 2014) on July 23, 2012—an event that could have rivaled the *Carrington 1859 event*, the archetypal extreme SWx event,

if it was Earth-directed (Ngwira et al., 2013). In addition, a series of large eruptions from active regions 2673 and 2674 in September, 2017 (in the declining phase of a weak cycle) caused a host of SWx phenomena from Earth to Mars (e.g., Chertok et al., 2018; see other papers in the Space Weather Journal special issue). Although by no means complete (the passage of active region 1429 in March 2012 marked another period of intense activity, e.g., Patsourakos et al., 2016), these arguments should make the lessons learned clear; namely, (1) a Carrington-level event can occur at *any* cycle, even in the weakest cycle in 100 years, (2) weak cycles are as dangerous for human space exploration as stronger cycles, and hence (3) the sunspot number is an unreliable proxy—I would even call it a "red herring"—we should instead focus on individual regions and try to understand how regions like 1429, 1520, or 2674 (anti-Hale, δ-spot) form and evolve, if we want to address extreme SWx.

- Paradigm 2:*"Flares and CMEs evolve at different spatial and temporal scales."* Although CME and flares (eruptive flares, at least) are closely related, they are generally approached with different mentalities. Flares are characterized by a sharp brightness increase (rise time of $\sim$ 5 − 10 min) in heavy element emissions (e.g., Fe), implying heating to temperatures of 10s MK, in small-scale (order of arcseconds) loop systems, followed by a gradual increase in area and intensity before an hours-long return to pre-flare intensity levels (Benz, 2008). The brightness increase, small flare loop area, and (mostly) radiation effects contrast sharply with the usually hour-long acceleration, solar-radius spatial scales, and mass motions of CMEs. It is unsurprising that the two phenomena were studied in isolation, with different tools and models, and by different communities. The dichotomy extends to their SWx effects, particularly in the origin of SEPs (e.g., Reames, 2013) leading to a linear "flare-CME-SEP" paradigm of the solar SWx timeline.

  This turns out to be a rather simplistic, and potentially misleading, approach as the high quality and rapid cadence EUV imaging observations have demonstrated. The discovery of EUV waves (Thompson et al., 1999) and post-CME rays (Ciaravella et al., 2002) and their singular connection to eruptive flares (e.g., Long et al., 2017, and references therein) indicated a closer spatial and temporal relation between magnetic energy release and both flare and CME development that previously realized (Longcope and Beveridge, 2007; Qiu et al., 2007); see also Patsourakos et al. (2020), and references therein. In my opinion, a paradigm-shifting advance was the identification of the EUV wave driver with a *"super-expansion"* phase in the very first stages of CME formation (Patsourakos and Vourlidas, 2012). During this hitherto unknown phase, the injection of poloidal flux into the forming magnetic flux rope (MFR) leads to a fast lateral expansion of the nascent CME expands at speeds of about 1,000 km/s, reached within 5 min. These speeds are sufficient for driving shocks (manifested as EUV waves and metric type II bursts) and hence can accelerate SEPs to high energies. Importantly, the temporal profile of the "super-expansion" phase is similar to the impulsive phase of the flare, occurring in close proximity, though not always simultaneously (e.g., Patsourakos et al., 2010; Cheng et al., 2014). The "super-expansion" phase neatly integrates a host of disparate phenomena variously attributed to flares or CMEs, such as expanding flare ribbons, short-lived metric Type-II bursts, EUV waves, and even the somewhat puzzling detection of separate sites of γ-ray and Hard X-ray emission (Lin et al., 2003), implying separate ion and electron acceleration sites (Pomoell et al., 2008). I propose, in other words, that flares, CMEs and the highest energy and possibly even the "seed" populations of SEPs, should be viewed as co-located phenomena, of *initially* similar spatio-temporal scales, powered by the magnetic energy released via reconnection within extended current systems in the corona.
- Paradigm 3: *"All projections are created equal."* Any type of coronal imaging is subject to projection as the observed emission is optically thin, whether it arises from spectral line emission or scattering processes. Up until 2007, 30+ years of single viewpoint observations, all from the Sun-Earth line, had led to a certain degree of complacency regarding the effects of projection in our view of solar structures. Techniques to recover the unprojected quantities, and ensuing uncertainties, such as loop heights or CME speeds, were (and continue to be) commonplace, yet they had not been validated in any comprehensive manner. The underlying assumption that the observations capture a representative view of the actual 3D structure of the object of interest, went unchallenged. But what happens if it is not a valid assumption? What if, say, the halo-like feature in a coronagraph image is not the result of an Earth-directed CME but a chance co-temporal ejection of two oppositely-directed CMEs that pose no SWx threat? Or what if an Earth-directed CME happens to propagated behind the occulter until it leaves the field of view of a coronagraph?

  It was difficult to answer such questions and, in essence, to check the validity of much of previous studies without *observations from multiple vantage points*. The STEREO mission offered us that opportunity in 2007. The two STEREO viewpoints, often with a third one from LASCO, revealed a much more nuanced, and oftentimes surprising reality. For example, a single CME (Magdalenić et al., 2014) may be three CMEs (Colaninno and Vourlidas, 2015); halo CMEs are actually a manifestation of the shock and not the CME itself (Kwon et al., 2015); evidence for an entrained MFR or prominence material in a CME is a matter of viewpoint (e.g., Figures 6, 7 in Vourlidas et al., 2017); an MFR can have the textbook "slinky"-like helical morphology, or not, depending on its orientation before eruption (e.g., Figure 3 in Vourlidas, 2014). More importantly for our discussion here, the detection of an Earth-directed CME can only be guaranteed from off-SEL observations (e.g., **Figure 3** and Vourlidas et al., 2020a). In other words, "all projections are not created equal." The viewpoint matters and must be selected wisely. For SWx, the off-SEL viewpoints are more important the SEL ones, since the former can help decipher the CME structure.

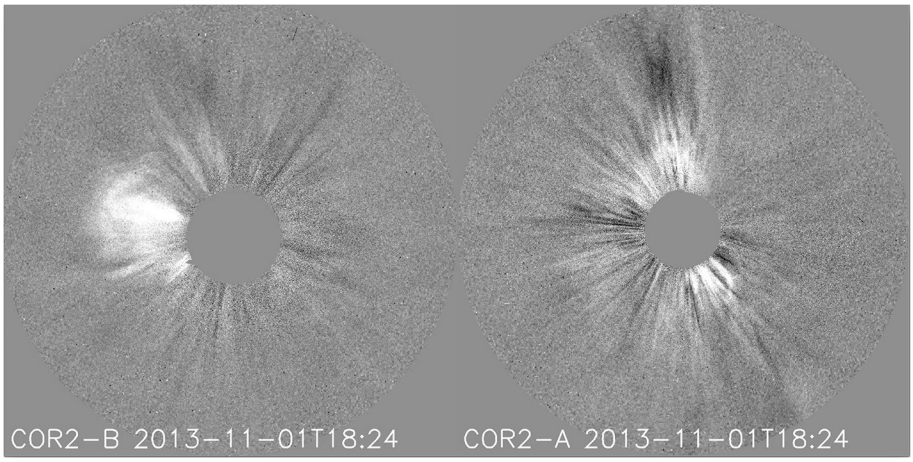

FIGURE 3 | An example of a projection effect with SWx implications. **Left**: Snapshot of a CME from COR2 on STEREO-B. **Right**: Simultaneous snapshot from COR2 on STEREO-A (69° away). The event, barely visible in COR2-A, lacks a clear halo appearance and may not have been classified as a COR2-A directed event without the COR2-B observations. The movie is available online from the COR2 catalog.

TABLE 1 | Forecasting status of key quantities used to assess the Geo-effectiveness of the main solar drivers of space weather.

Quantity	Observational inputs	Forecasting status	Choke points
CME/shock			
Direction (Hit/Miss)	Source region / flare location, 3D CME reconstruction	85%*	Deflection in low corona, IP evolution
Time-of-arrival	Speed in corona or inner heliosphere	9.8 ± 2 h[a]	IP propagation, CME/shock front shape at 1 AU
Speed-on-arrival	Speed in corona or inner heliosphere	±200 km/s*	Same as above
Density	CME mass	Unknown	IP propagation, small-scale structure of CME/shock sheath
Magnetic configuration	Radio emission, 3D CME reconstruction, coronal magn. field extrapolations	∼ 30 min (L1 *in-situ* meas.)	Coronal origin, evolution (< 3 Rs), IP propagation
Flares			
SXR class	Photosph. magn. field, flaring history	TSS ∼ 0.4[c]	Energy storage/release in corona
Intense radio bursts[b]	Ground-based radio antennas	No forecasting capability	Unknown physics
SEP			
Onset time	TypeII/III, flare (CME) occurrence & class (speed)	4 h > 10 MeV, 1 h > 100 MeV	High cadence imaging in the inner corona (< 3 Rs), "seed" particle observations, magnetic connectivity
Peak intensity	Same as above	Within ∼ 1 order of magnitude	Same as above
Intensity profile	Same as above	9 h (> 10 MeV), 33 h (> 100 Mev)	Same as above

[a] *Vourlidas et al. (2019).*
[b] *Next Step Space Weather Benchmarks Report (2019).*
[c] *TSS, True Skill Statistic (Leka et al., 2019).*

4. FORECAST "CHOKE POINTS" AND GRAND CHALLENGES

These research developments have advanced the sophistication and performance of forecasting models and have informed the strategy for the SWx operational infrastructure. But we still have some way to go. This is not solely driven by the solar driver observations. Accurate and actionable SWx forecasting is far more challenging than terrestrial weather. A key reason is that the geospace is a vast, complex, and sparsely sampled system compared to the troposphere. Another reason is the non-linear reaction of geospace to the solar inputs. The solar driver inputs, and the focus of this paper constitute only the third agent in the SWx problem.

In **Table 1**, I summarize the quantities most commonly used to assess the geo-effectiveness of the three solar drivers of

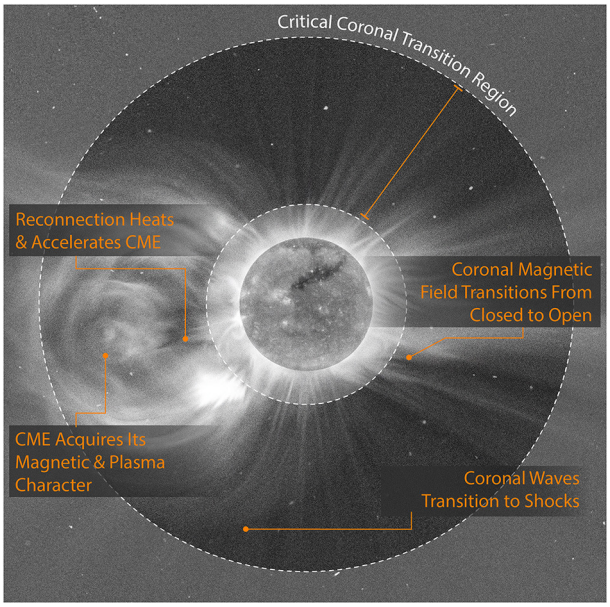

FIGURE 4 | Several important physical transitions during solar eruptions, directly relevant to SWx, occur within the inner corona—the region between 1.3 and 4 Rs, roughly. However, this critical coronal range remains poorly studied (more details in Vourlidas et al., 2020d).

concern; flares, CMEs, and SEPs. The parameter list is not meant to be exhaustive. For each quantity, **Table 1** provides a brief list of observational inputs used to forecast the quantity, the current forecasting accuracy, and the main issues that hinder the forecast. The selection of these "choke points" is based on my experience and understanding of the related literature, observational limitations and modeling requirements. I expect some disagreements on the details, but **Table 1** hopefully expresses the broad consensus on this area.

A key observation to draw from **Table 1** is that many "choke points" are common across all solar drivers. In fact, all "choke points" stem from incomplete physical understanding of the three lifetime phases of any transient; namely, the pre-eruptive phase, the formation phase, and the interplanetary (IP) propagation phase. Understanding these phases better would naturally lead to improved forecasting. To get started, we first need to consider the challenges (always in regards to SWx forecasting) that we are facing now. These *gland challenges* are as follows:

- *Pre-eruptive Phase:* The main challenge is to uncover the *coronal* magnetic configuration of the pre-eruptive structure and how it evolves toward eruption. This is a high-stakes challenge as the answer will enable prediction of both flares and CMEs (and consequently shocks and SEPs) from a few hours to possibly days before, Although we have learned a great deal on how flares and CMEs evolve over the last 20 years or so (Green et al., 2018), we are not yet close to addressing this challenge. The reason is rather simple; eruptions are (1) magnetically driven and (2) originate in the corona where we have few ways of measuring magnetic field. Thus, we cannot observe/measure many of the quantities important to coronal energy storage and release, such as magnetic free energy, helicity, or currents. Patsourakos et al. (2020) reviewed the subject in detail and put forth a range of ideas for moving forward.
- *Formation Phase:* As discussed earlier, most CMEs undergo their formation and acceleration phases in the inner corona (below 4 Rs). It is where shocks form and the highest energy particles are accelerated. Although the flare-related brightenings are smaller spatial scale phenomena restricted to the low corona, their eruptive manifestations, such as current sheets and the particles accelerated in them, can reach much higher. **Figure 4** summarizes the richness of the physical processes relevant to SWx in this coronal region (the specifics are not discussed here due to space constraints). Yet, this region remains poorly understood, mostly because it is visible in its entirety only during eclipses while it is only partially accessible at other times by disparate instruments, either coronagraphs (down to 1.5 Rs or so) or EUV imagers (up to 1.5 Rs). There are no comprehensive spectroscopic measurements of its physical state (density, temperature, composition) either. The importance of the inner corona is discussed in some detail in a white paper by Vourlidas et al. (2020d).
- *IP Propagation Phase:* It has been only 10 years since we started routine measurements of the IP propagation of transients (CMEs, shocks, SIRs) thanks to the operation of the heliospheric imagers on the STEREO mission. The discoveries and remaining challenges are reviewed by Manchester et al. (2017). The IP propagation affects most of the SWx-relevant properties of the solar drivers. Improvements in this area will benefit SWx forecasting across a wide range of users. There are essentially three challenges relevant to forecasting: (1) CME-solar wind interactions that are important for shocks, SIRs, and slower CMEs. They tend to affect the time and speed of transient at its 1 au arrival and possibly the direction of propagation; (2) CME-CME interactions that can lead to magnetic field compression and strengthening of the shocks, as they propagate through the slower CME (Lugaz et al., 2017) , which is an issue of SWx relevance closer to the Sun, as well (e.g., Liu et al., 2014); and (3) CME internal forces, namely the interplay between the magnetic forces of the entrained flux rope with the surrounding plasma and magnetic pressure (e.g., Yeh, 1995). The force balance of a CME is not well-understood. For example, *in-situ* measurements at 1 AU suggest the CME flux ropes are force-free, yet estimates from coronagraphic observations suggest the opposite (e.g., Subramanian et al., 2014). Large-scale studies indicate that only 65–70% of events within 15 Rs follow self-similar expansion (Balmaceda et al., 2020).

5. PATH FORWARD

The identification of the forecast "choke points" and the research challenges they originate from, allows us to define measurement strategies for addressing these challenges. In the following, I

organize these strategies according to the three phases: pre-eruptive, formation, and propagation. However, I list them according to their perceived SWx impact to emphasize the different value to SWx operations of each evolutionary phase:

- *Breakthrough Capabilities:* Predicting (reliably) the onset of a flare or a CME within a few hours of its occurrence will be a major breakthrough in SWx. To understand the pre-eruptive state, we must follow the flow of magnetic energy and helicity upwards from the photosphere and its storage in the corona, as well as, the reaction of the ambient field to this energy/helicity flow. **Multi-height vector magnetic field measurements**, from photosphere to (at least) the upper chromosphere, in active regions (because they host the most energetic eruptions), can provide the required information on energy and helicity flow and coronal currents. They will also provide strong constraints for coronal field extrapolations leading to robust 3D reconstructions of the magnetic morphology of the pre-eruptive structures thus removing the need for the much more difficult direct coronal field measurements (for more information and ideas see Patsourakos et al. 2020). The measurements could be achieved by a $>$ 1-m telescope with a visible-to-near infrared (NIR) magnetograph, perhaps launched as a balloon payload.

  The reaction of the ambient field and the slow rise of the system, which is typical before an eruption, can be captured via **off-limb spectroscopic measurements** in the UV and/or EUV, up to about 2.5 Rs or so. Doppler, temperature and density measurements will help constrain the force balance evolution of the system toward eruption and provide 3D information of the erupting structures and their interplay with the ambient magnetic systems. While ground-based off-limb spectroscopy in the visible and NIR could provide these measurements (e.g., McIntosh et al., 2019) and improve our understanding of the physics of eruption, they are of little direct use for SWx operation. SWx-relevant eruptions can only be measured and monitored from platforms away from the Sun-Earth line (SEL), such as around the Sun-Earth L4 and L5 Lagrangian points.
- *Geo-effective potential:* The majority of the energy release and the magnetic configuration of the erupting CME occur during the formation stage. The shocks (and accelerated particles) and magnetic content of the CME are established in that phase. In other words, understanding the formation phase will improve forecasting of the geo-effective potential of a solar transient. A straightforward improvement will come from emulating solar eclipses to provide **uninterrupted coronal coverage** from the solar surface to 10-15 Rs. A long boom visible coronagraph or an expanded version of a formation-flying coronagraph (Galano et al., 2018) can provide such an eclipse-like field of view. The addition of a wide-field EUV imager/coronagraph could fill in the gap from the disk to the inner corona and provide additional density and temperature information, depending on the channel selection. Detailed physical properties, however, can only be obtained via **off-limb spectroscopy** in the UV/EUV to 2–5 Rs (e.g., Ko et al., 2016), heights inaccessible for ground-based visible-NIR spectroscopy. Again, the best viewing locations for SWx operations are off-SEL, which would necessitate the development of small volume/simple spectrograph and coronagraph concepts. Radio spectroscopy can play an important role in this area by tracking interplanetary shocks in the kHz-MHz range or probing CME magnetic fields via Faraday rotation measurements (e.g., Vourlidas et al., 2020b). Carley et al. (2020) reviews extensively the SWx-related radio infrastructure upgrades under way. Finally, **stereoscopic EUV imaging with vector magnetic field measurements** of Earth-facing active regions can provide strong (and possibly early) constrains of the erupted field strength and configuration by comparing before after magnetic field extrapolations and stereoscopy, as discussed in Schrijver et al. (2015).
- *Actionable Forecast:* Resolving the issues surrounding the propagation of solar transients in the inner heliosphere is the most direct way to obtain actionable forecasts in the near-term. IP propagation is a concern for almost all solar drivers of interest; CMEs, shocks, SIRs, and SEPs. To understand it, we need to overcome a major barrier—the sparse coverage of the vast Sun-Earth space. I can see three ways to overcome this: (1) Obtain **off-SEL high signal-to-noise ratio (SNR) heliospheric imaging** to enable tracing of the magnetic flux rope entrained in the CME and cleaner separation of the sheath and CME structures. Better observations of the kinematic and dynamic evolution of these features will increase understanding of CME-solar wind and CME-CME interactions, as we discussed in section 4 (see also the "path forward" discussion in Vourlidas et al., 2019); (2) design missions for **distributed particles and fields measurements from 0.7 to 1 AU** to provide $\sim$ 24-h forecasting horizon of magnetic and kinematic parameters of incoming transients; and (3) obtain **multi-point particles and fields measurements with a $<$ 8° angular separation** to investigate the medium-scale structure of these transients, preferably upstream of L1 (Lugaz et al., 2018).

  All three measurement types are achievable with current spacecraft technologies and sufficient investment. A more comprehensive solution that is scientifically rewarding but technically challenging will come from **off-SEL**, and particularly **off-ecliptic heliospheric imaging** (Gibson et al., 2018) to image directly deflections and interactions in the ecliptic without the ambiguities that plague imaging from within the ecliptic.The proper combination of ecliptic and off-ecliptic imaging of the solar surface to the extended corona offers a particularly ground-braking capability—**the 4π coverage** of the solar atmosphere. (Vourlidas et al., 2018; Berger et al., 2019). The resulting measurements will impact research and forecasting across the whole SWx enterprise (e.g., Vourlidas et al., 2020c).

In closing, I reiterate that I did not intent to provide an exhaustive review of all possible obstacles and remedies for improving the medium-term forecasting of SWx. Such gap analyses require careful consideration and community-wide input. Thankfully, both NOAA and NASA are in the midst of such efforts as of this writing. The aim of the paper is twofold: (1) capture the status of our physical understanding of

solar drivers and their SWx effects from a research perspective and (2) demonstrate that there is a clear and executable path forward. All that is left is to put this plan in motion as resources and opportunities arise across the world. Space Weather is a concern for all humans as we try to expand our footprint in space.

AUTHOR CONTRIBUTIONS

AV was the sole contributor to this paper.

FUNDING

AV was supported by the NASA STEREO (80NSSC19K1261) and LWS (80NSSC19K0069) programs.

ACKNOWLEDGMENTS

The authors is thankful to Dr. R. Howard for pointing errors in the final manuscript. The STEREO/SECCHI/COR2 CME catalog was generated and maintained at JHUAPL, in collaboration with the NRL and GSFC, and was supported by NASA.

REFERENCES

Acuña, M. H., Ogilvie, K. W., Baker, D. N., Curtis, S. A., Fairfield, D. H., and Mish, W. H. (1995). The global geospace science program and its investigations. *Space Sci. Rev*. 71, 5–21. doi: 10.1007/BF00751323

Anastasiadis, A., Lario, D., Papaioannou, A., Kouloumvakos, A., and Vourlidas, A. (2019). Solar energetic particles in the inner heliosphere: status and open questions. *Philos. Trans. R. Soc. A Math. Phys. Eng. Sci*. 377:20180100. doi: 10.1098/rsta.2018.0100

Baker, D. N., and Lanzerotti, L. J. (2016). Resource letter SW1: space weather. *Am. J. Phys*. 84, 166–180. doi: 10.1119/1.4938403

Balmaceda, L. A., Vourlidas, A., Stenborg, G., and St. Cyr, O. C. (2020). On the expansion speed of coronal mass ejections: implications for self-similar evolution. *Solar Phys*. 295:107. doi: 10.1007/s11207-020-01672-6

Benz, A. O. (2008). Flare observations. *Living Rev. Solar Phys*. 5:1. doi: 10.12942/lrsp-2008-1

Berger, T. E., Bosanac, N., Smith, T. R., Duncan, N. A., Wu, G., Turner, E., et al. (2019). "The Solar Polar Observing Constellation (SPOC) Mission: research and operational monitoring of space weather from polar heliocentric orbits," in *AGU Fall Meeting Abstracts* (Washington, DC).

Brueckner, G. E., Howard, R. A., Koomen, M. J., Korendyke, C. M., Michels, D. J., Moses, J. D., et al. (1995). The large angle spectroscopic coronagraph (LASCO). *Solar Phys*. 162, 357–402. doi: 10.1007/BF00733434

Carley, E. P., Baldovin, C., Benthem, P., Bisi, M. M., Fallows, R. A., Gallagher, P. T., et al. (2020). Radio observatories and instrumentation used in space weather science and operations. *J. Space Weather Space Clim*. 10:7. doi: 10.1051/swsc/2020007

Cheng, X., Ding, M. D., Guo, Y., Zhang, J., Vourlidas, A., Liu, Y. D., et al. (2014). Tracking the evolution of a coherent magnetic flux rope continuously from the inner to the outer corona. *Astrophys. J*. 780:28. doi: 10.1088/0004-637X/780/1/28

Cheng, X., Zhang, J., Liu, Y., and Ding, M. D. (2011). Observing flux rope formation during the impulsive phase of a solar eruption. *Astrophys. J*. 732:L25. doi: 10.1088/2041-8205/732/2/L25

Chertok, I. M., Belov, A. V., and Abunin, A. A. (2018). Solar eruptions, forbush decreases, and geomagnetic disturbances from outstanding active region 12673. *Space Weather* 16, 1549–1560. doi: 10.1029/2018SW001899

Ciaravella, A., Raymond, J. C., Li, J., Reiser, P., Gardner, L. D., Ko, Y.-K., et al. (2002). Elemental abundances and post-coronal mass ejection current sheet in a very hot active region. *Astrophys. J*. 575:1116. doi: 10.1086/341473

Cohen, C. M. S., and Mewaldt, R. A. (2018). The ground-level enhancement event of september 2017 and other large solar energetic particle events of cycle 24. *Space Weather* 16, 1616–1623. doi: 10.1029/2018SW002006

Colaninno, R. C., and Vourlidas, A. (2015). Using multiple-viewpoint observations to determine the interaction of three coronal mass ejections observed on 2012 march 5. *Astrophys. J*. 815:70. doi: 10.1088/0004-637X/815/1/70

Delaboudiniere, J. P., Artzner, G. E., Brunaud, J., Gabriel, A. H., Hochedez, J. F., Millier, F., et al. (1995). EIT: extreme-ultraviolet imaging telescope for the SOHO mission. *Solar Phys*. 162, 291–312. doi: 10.21236/ADA530511

Domingo, V., Fleck, B., and Poland, A. I. (1995). The SOHO mission: an overview. *Solar Phys*. 162, 1–37. doi: 10.1007/BF00733425

Galano, D., Bemporad, A., Buckley, S., Cernica, I., Daniel, V., Denis, F., et al. (2018). "Development of aspiics: a coronagraph based on proba-3 formation flying mission," in *Space Telescopes and Instrumentation 2018: Optical, Infrared, and Millimeter Wave* (Austin, TX: International Society for Optics and Photonics). doi: 10.1117/12.2312493

Gibson, S. E., Vourlidas, A., Hassler, D. M., Rachmeler, L. A., Thompson, M. J., Newmark, J., et al. (2018). Solar physics from unconventional viewpoints. *Front. Astron. Space Sci*. 5:32. doi: 10.3389/fspas.2018.00032

Gopalswamy, N. (2009). "Coronal mass ejections and space weather," in *Climate and Weather of the Sun-Earth System (CAWSES) Selected Papers from the 2007 Kyoto Symposium* (Kyoto), 77–120.

Gopalswamy, N., Akiyama, S., Yashiro, S., Michalek, G., Xie, H., and Mäkelä, P. (2020). "Effect of the weakened heliosphere in solar cycle 24 on the properties of coronal mass ejections," in *Journal of Physics Conference Series* (Santa Fe). doi: 10.1088/1742-6596/1620/1/012005

Gopalswamy, N., Davila, J., St. Cyr, O., Sittler, E., Auchére, F., Duvall, T. Jr., et al. (2011). Earth-affecting solar causes observatory (EASCO): a potential international living with a star mission from Sun-Earth L5. *J. Atmos. Solar Terrest. Phys*. 73, 658–663. doi: 10.1016/j.jastp.2011.01.013

Gopalswamy, N., Tsurutani, B., and Yan, Y. (2015). Short-term variability of the Sun-Earth system: an overview of progress made during the CAWSES-II period. *Prog. Earth Planet. Sci*. 2:13. doi: 10.1186/s40645-015-0043-8

Gopalswamy, N., Xie, H., Akiyama, S., Mäkelä, P. A., and Yashiro, S. (2014). Major solar eruptions and high-energy particle events during solar cycle 24. *Earth Planets Space* 66:104. doi: 10.1186/1880-5981-66-104

Gopalswamy, N., Yashiro, S., Michałek, G., Kaiser, M. L., Howard, R. A., Reames, D. V., et al. (2002). Interacting coronal mass ejections and solar energetic particles. *Astrophys. J. Lett*. 572, L103–L107. doi: 10.1086/341601

Gopalswamy, N., Yashiro, S., Michalek, G., Stenborg, G., Vourlidas, A., Freeland, S., et al. (2009). The SOHO/LASCO CME catalog. *Earth Moon Planets* 104, 295–313. doi: 10.1007/s11038-008-9282-7

Green, L. M., Torok, T., Vrsnak, B., Manchester, W., and Veronig, A. (2018). The origin, early evolution and predictability of solar eruptions. *Space Sci. Rev*. 214:46. doi: 10.1007/s11214-017-0462-5

Harrison, R. A., Davies, J. A., Biesecker, D., and Gibbs, M. (2017). The application of heliospheric imaging to space weather operations: lessons learned from published studies. *Space Weather* 15:2017SW001633. doi: 10.1002/2017SW001633

Howard, R. A., Moses, J. D., Vourlidas, A., Newmark, J. S., Socker, D. G., Plunkett, S. P., et al. (2008). Sun earth connection coronal and heliospheric investigation (SECCHI). *Space Sci. Rev*. 136, 67–115. doi: 10.1007/s11214-008-9341-4

Jin, M., Schrijver, C. J., Cheung, M. C. M., DeRosa, M. L., Nitta, N. V., and Title, A. M. (2016). A numerical study of long-range magnetic impacts during coronal mass ejections. *Astrophys. J*. 820:16. doi: 10.3847/0004-637X/820/1/16

Kahler, S. W., and Vourlidas, A. (2014). Do interacting coronal mass ejections play a role in solar energetic particle events? *Astrophys. J*. 784:47. doi: 10.1088/0004-637X/784/1/47

Kaiser, M. L., Kucera, T. A., Davila, J. M., St. Cyr, O. C., Guhathakurta, M., and Christian, E. (2008). The stereo mission: an introduction. *Space Sci. Rev*. 136, 5–16. doi: 10.1007/978-0-387-09649-0_2

Ko, Y.-K., Moses, J. D., Laming, J. M., Strachan, L., Tun Beltran, S., Tomczyk, S., et al. (2016). Waves and magnetism in the solar atmosphere (WAMIS). *Front. Astron. Space Sci*. 3:1. doi: 10.3389/fspas.2016.00001

Kwon, R.-Y., and Vourlidas, A. (2018). The density compression ratio of shock fronts associated with coronal mass ejections. *J. Space Weather Space Clim*. 8:A08. doi: 10.1051/swsc/2017045

Kwon, R.-Y., Zhang, J., and Vourlidas, A. (2015). Are halo-like solar coronal mass ejections merely a matter of geometric projection effects? *Astrophys. J. Lett*. 799:L29. doi: 10.1088/2041-8205/799/2/L29

Lamy, P., Floyd, O., Quémerais, E., Boclet, B., and Ferron, S. (2017). Coronal mass ejections and solar wind mass fluxes over the heliosphere during solar cycles 23 and 24 (1996-2014): CMEs and solar wind mass fluxes. *J. Geophys. Res. Space Phys*. 122, 50–62. doi: 10.1002/2016JA022970

Lario, D., Kwon, R.-Y., Riley, P., and Raouafi, N. E. (2017). On the link between the release of solar energetic particles measured at widespread heliolongitudes and the properties of the associated coronal shocks. *Astrophys. J*. 847:103. doi: 10.3847/1538-4357/aa89e3

Leka, K. D., Park, S.-H., Kusano, K., Andries, J., Barnes, G., Bingham, S., et al. (2019). A comparison of flare forecasting methods. III. Systematic behaviors of operational solar flare forecasting systems. *Astrophys. J*. 881:101. doi: 10.3847/1538-4357/ab2e11

Lemen, J. R., Title, A. M., Akin, D. J., Boerner, P. F., Chou, C., Drake, J. F., et al. (2012). The Atmospheric Imaging Assembly (AIA) on the Solar Dynamics Observatory (SDO). *Solar Physics* 275, 17–40. doi: 10.1007/s11207-011-9776-8

Lin, R. P., Krucker, S., Hurford, G. J., Smith, D. M., Hudson, H. S., Holman, G. D., et al. (2003). Rhessi observations of particle acceleration and energy release in an intense solar gamma-ray line flare. *Astrophys. J. Lett*. 595:L69. doi: 10.1086/378932

Liu, Y. D., Luhmann, J. G., Kajdič, P., Kilpua, E. K. J., Lugaz, N., Nitta, N. V., et al. (2014). Observations of an extreme storm in interplanetary space caused by successive coronal mass ejections. *Nat. Commun*. 5:3481. doi: 10.1038/ncomms4481

Long, D. M., Bloomfield, D. S., Chen, P. F., Downs, C., Gallagher, P. T., Kwon, R.-Y., et al. (2017). Understanding the physical nature of coronal "EIT waves". *Solar Phys*. 292:7. doi: 10.1007/s11207-016-1030-y

Longcope, D. W., and Beveridge, C. (2007). A quantitative, topological model of reconnection and flux rope formation in a two-ribbon flare. *Astrophys. J*. 669, 621–635. doi: 10.1086/521521

Lugaz, N., Farrugia, C. J., Winslow, R. M., Al-Haddad, N., Galvin, A. B., Nieves-Chinchilla, T., et al. (2018). On the spatial coherence of magnetic ejecta: measurements of coronal mass ejections by multiple spacecraft longitudinally separated by 0.01 au. *Astrophys. J. Lett*. 864:L7. doi: 10.3847/2041-8213/aad9f4

Lugaz, N., Temmer, M., Wang, Y., and Farrugia, C. J. (2017). The interaction of successive coronal mass ejections: a review. *Solar Phys*. 292:64. doi: 10.1007/s11207-017-1091-6

Magdalenić, J., Marqué, C., Krupar, V., Mierla, M., Zhukov, A. N., Rodriguez, L., et al. (2014). Tracking the CME-driven shock wave on 2012 march 5 and radio triangulation of associated radio emission. *Astrophys. J*. 791:115. doi: 10.1088/0004-637X/791/2/115

Makela, P., Gopalswamy, N., and Yashiro, S. (2016). The radial speed-expansion speed relation for earth-directed CMEs. *Space Weather* 14:2015SW001335. doi: 10.1002/2015SW001335

Manchester, W., Kilpua, E. K. J., Liu, Y. D., Lugaz, N., Riley, P., Torok, T., et al. (2017). The physical processes of CME/ICME evolution. *Space Sci. Rev*. 212, 1159–1219. doi: 10.1007/s11214-017-0394-0

Manoharan, P. K., Mahalakshmi, K., Johri, A., Jackson, B. V., Ravikumar, D., Kalyanasundaram, K., et al. (2018). Current state of reduced solar activity: intense geomagnetic storms. *Sun Geosphere* 13, 135–143. doi: 10.31401/SunGeo.2018.02.03

McComas, D. J., Angold, N., Elliott, H. A., Livadiotis, G., Schwadron, N. A., Skoug, R. M., et al. (2013). Weakest solar wind of the space age and the current "mini" solar maximum. *Astrophys. J*. 779:2. doi: 10.1088/0004-637X/779/1/2

McIntosh, S., Tomczyk, S., Gibson, S. E., Burkepile, J., Wijn, A. D., Fan, Y., et al. (2019). *Investigating Coronal Magnetism with COSMO: Science on the Critical Path To Understanding The "Weather" of Stars and Stellarspheres*. Bulletin of the AAS, 51.

Mishra, S. K., and Srivastava, A. K. (2019). Linkage of geoeffective stealth CMEs associated with the eruption of coronal plasma channel and jet-like structure. *Solar Phys*. 294:169. doi: 10.1007/s11207-019-1560-1

Moses, D., Clette, F., Delaboudiniere, J.-P., Artzner, G. E., Bougnet, M., Brunaud, J., et al. (1997). EIT observations of the extreme ultraviolet sun. *Solar Phys*. 175, 571–599. doi: 10.1007/978-94-011-5236-5_32

Next Step Space Weather Benchmarks Report (2019). *Number NS GR-10982 in IDA Group Report*.

Ngwira, C. M., Pulkkinen, A., Leila Mays, M., Kuznetsova, M. M., Galvin, A. B., Simunac, K., et al. (2013). Simulation of the 23 July 2012 extreme space weather event: what if this extremely rare cme was earth directed? *Space Weather* 11, 671–679. doi: 10.1002/2013SW000990

Nindos, A., Patsourakos, S., Vourlidas, A., Cheng, X., and Zhang, J. (2020). When do solar erupting hot magnetic flux ropes form? *Astron. Astrophys*. 642:A109. doi: 10.1051/0004-6361/202038832

O'Dwyer, B., Del Zanna, G., Mason, H. E., Weber, M. A., and Tripathi, D. (2010). SDO/AIA response to coronal hole, quiet sun, active region, and flare plasma. *Astron. Astrophys*. 521:21. doi: 10.1051/0004-6361/201014872

Patsourakos, S., Georgoulis, M. K., Vourlidas, A., Nindos, A., Sarris, T., Anagnostopoulos, G., et al. (2016). The major geoeffective solar eruptions of 2012 march 7: comprehensive sun-to-earth analysis. *Astrophys. J*. 817:14. doi: 10.3847/0004-637X/817/1/14

Patsourakos, S., and Vourlidas, A. (2012). On the nature and genesis of EUV waves: a synthesis of observations from SOHO, STEREO, SDO, and hinode (invited review). *Solar Phys*. 281, 187–222. doi: 10.1007/s11207-012-9988-6

Patsourakos, S., Vourlidas, A., and Kliem, B. (2010). Toward understanding the early stages of an impulsively accelerated coronal mass ejection. SECCHI observations. *Astron. Astrophys*. 522:100. doi: 10.1051/0004-6361/200913599

Patsourakos, S., Vourlidas, A., and Stenborg, G. (2013). Direct evidence for a fast coronal mass ejection driven by the prior formation and subsequent destabilization of a magnetic flux rope. *Astrophys. J*. 764:125. doi: 10.1088/0004-637X/764/2/125

Patsourakos, S., Vourlidas, A., Torok, T., Kliem, B., Antiochos, S. K., Archontis, V., et al. (2020). Decoding the pre-eruptive magnetic field configurations of coronal mass ejections. *Space Sci. Rev*. 216:131. doi: 10.1007/s11214-020-00757-9

Pesnell, W. D., Thompson, B. J., and Chamberlin, P. C. (2012). The solar dynamics observatory (SDO). *Solar Phys*. 275, 3–15. doi: 10.1007/s11207-011-9841-3

Pevtsov, A. A., Bertello, L., MacNeice, P., and Petrie, G. (2016). What if we had a magnetograph at Lagrangian L5? *Space Weather* 14:2016SW001471. doi: 10.1002/2016SW001471

Pomoell, J., Vainio, R., and Kissmann, R. (2008). MHD modeling of coronal large-amplitude waves related to CME lift-off. *Solar Phys*. 253, 249–261. doi: 10.1007/s11207-008-9186-8

Poomvises, W., Zhang, J., and Olmedo, O. (2010). Coronal mass ejection propagation and expansion in three-dimensional space in the heliosphere based on STEREO/SECCHI observations. *Astrophys. J*. 717, L159–L163. doi: 10.1088/2041-8205/717/2/L159

Pulkkinen, A. A., Bisi, M. M., Luntama, J. P., Kraft, S., Glover, A., and Heil, M. (2019). "ESA Lagrange space weather monitoring mission to L5 point," in *AGU Fall Meeting Abstracts* (Washington, DC).

Qiu, J., Hu, Q., Howard, T. A., and Yurchyshyn, V. B. (2007). On the magnetic flux budget in low-corona magnetic reconnection and interplanetary coronal mass ejections. *Astrophys. J*. 659, 758–772. doi: 10.1086/512060

Reames, D. V. (2013). The two sources of solar energetic particles. *Space Sci. Rev*. 175, 53–92. doi: 10.1007/s11214-013-9958-9

Reeves, K. K., and Golub, L. (2011). Atmospheric imaging assembly observations of hot flare plasma. *Astrophys. J*. 727:L52. doi: 10.1088/2041-8205/727/2/L52

Robbrecht, E., Patsourakos, S., and Vourlidas, A. (2009). No trace left behind: STEREO observation of a coronal mass ejection without low coronal signatures. *Astrophys. J*. 701, 283–291. doi: 10.1088/0004-637X/701/1/283

Russell, C. T., Mewaldt, R. A., Luhmann, J. G., Mason, G. M., von Rosenvinge, T. T., Cohen, C. M. S., et al. (2013). The very unusual interplanetary coronal mass ejection of 2012 July 23: a blast wave mediated by solar energetic particles. *Astrophys. J*. 770:38. doi: 10.1088/0004-637X/770/1/38

Scherrer, P. H., Bogart, R. S., Bush, R. I., Hoeksema, J. T., Kosovichev, A. G., Schou, J., et al. (1995). The solar oscillations investigation - michelson doppler imager. *Solar Phys*. 162, 129–188. doi: 10.1007/BF00733429

Schrijver, C. J., Kauristie, K., Aylward, A. D., Denardini, C. M., Gibson, S. E., Glover, A., et al. (2015). Understanding space weather to shield society: a global road map for 2015–2025 commissioned by COSPAR and ILWS. *Adv. Space Res*. 55, 2745–2807. doi: 10.1016/j.asr.2015.03.023

Schrijver, C. J., and Title, A. M. (2011). Long-range magnetic couplings between solar flares and coronal mass ejections observed by SDO and STEREO. *J. Geophys. Res.* 116:04108. doi: 10.1029/2010JA016224

Schwadron, N. A., Rahmanifard, F., Wilson, J., Jordan, A. P., Spence, H. E., Joyce, C. J., et al. (2018). Update on the worsening particle radiation environment observed by CRaTER and implications for future human deep-space exploration. *Space Weather* 16, 289–303. doi: 10.1002/2017SW001803

Stone, E., Frandsen, A., Mewaldt, R., Christian, E., Margolies, D., Ormes, J., et al. (1998). The advanced composition explorer. *Space Sci. Rev.* 86, 1–22. doi: 10.1023/A:1005082526237

Subramanian, P., Arunbabu, K. P., Vourlidas, A., and Mauriya, A. (2014). Self-similar expansion of solar coronal mass ejections: implications for Lorentz self-force driving. *Astrophys. J.* 790, 125. doi: 10.1088/0004-637X/790/2/125

Thompson, B. J., Gurman, J. B., Neupert, W. M., Newmark, J. S., Delaboudiniere, J.-P., Cyr, O. C. S., et al. (1999). SOHO/EIT observations of the 1997 April 7 coronal transient: Possible evidence of coronal moreton waves. *Astrophys. J. Lett.* 517:L151. doi: 10.1086/312030

Török, T., Panasenco, O., Titov, V. S., Mikia, Z., Reeves, K. K., Velli, M., et al. (2011). A model for magnetically coupled sympathetic eruptions. *Astrophys. J.* 739:L63. doi: 10.1088/2041-8205/739/2/L63

Vourlidas, A. (2014). The flux rope nature of coronal mass ejections. *Plasma Phys. Control. Fusion* 56:064001. doi: 10.1088/0741-3335/56/6/064001

Vourlidas, A. (2015). Mission to the Sun-Earth L5 Lagrangian point: an optimal platform for space weather research. *Space Weather* 13, 197–201. doi: 10.1002/2015SW001173

Vourlidas, A., Balmaceda, L. A., Stenborg, G., and Lago, A. D. (2017). Multi-viewpoint coronal mass ejection catalog based on STEREO COR2 observations. *Astrophys. J.* 838:141. doi: 10.3847/1538-4357/aa67f0

Vourlidas, A., Balmaceda, L. A., Xie, H., and Cyr, O. C. S. (2020a). The coronal mass ejection visibility function of modern coronagraphs. *Astrophys. J.* 900:161. doi: 10.3847/1538-4357/abada5

Vourlidas, A., Carley, E. P., and Vilmer, N. (2020b). Radio observations of coronal mass ejections: space weather aspects. *Front. Astron. Space Sci.* 7:43. doi: 10.3389/fspas.2020.00043

Vourlidas, A., Gibson, S., Hassler, D., Hoeksema, T., Linton, M., Lugaz, N., et al. (2020c). The science case for the 4 perspective: a polar/global view for studying the evolution propagation of the solar wind and solar transients. *arXiv preprint arXiv:2009.04880*.

Vourlidas, A., Liewer, P. C., Velli, M., and Webb, D. (2018). Solar polar diamond explorer (SPDEX): Understanding the origins of solar activity using a new perspective. *arXiv preprint arXiv: 1805.04172*.

Vourlidas, A., Lynch, B. J., Howard, R. A., and Li, Y. (2013). How many CMEs have flux ropes? Deciphering the signatures of shocks, flux ropes, and prominences in coronagraph observations of CMEs. *Solar Phys.* 284, 179–201. doi: 10.1007/s11207-012-0084-8

Vourlidas, A., Patsourakos, S., and Savani, N. P. (2019). Predicting the geoeffective properties of coronal mass ejections: current status, open issues and path forward. *Philos. Trans. R. Soc. A Math. Phys. Eng. Sci.* 377:20180096. doi: 10.1098/rsta.2018.0096

Vourlidas, A., Syntelis, P., and Tsinganos, K. (2012). Uncovering the birth of a coronal mass ejection from two-viewpoint SECCHI observations. *Solar Phys.* 280, 509–523. doi: 10.1007/s11207-012-9933-8

Vourlidas, A., Viall, N., Laming, M., Cranmer, S., Arge, C., DeForest, C., et al. (2020d). Exploring the critical coronal transition region: the key to uncovering the genesis of the solar wind and solar eruptions. *Earth Space Sci. Open Arch.* doi: 10.1002/essoar.10504451.1

Webb, D. F., Biesecker, D. A., Gopalswamy, N., Cyr, O. C. S., Davila, J. M., Eyles, C. J., et al. (2010). Using STEREO-B as an L5 space weather pathfinder mission. *Space Res. Tdy.* 178, 10–16. doi: 10.1016/j.srt.2010.07.004

Yeh, T. (1995). A dynamical model of magnetic clouds. *Astrophys. J.* 438:975. doi: 10.1086/175139

Zagainova, I. S., Fainshtein, V. G., Gromova, L. I., and Gromov, S. V. (2020). Source region identification and geophysical effects of stealth coronal mass ejections. *J. Atmos. Solar Terrest. Phys.* 208:105391. doi: 10.1016/j.jastp.2020.105391

Zhang, J., Cheng, X., and Ding, M.-D. (2012). Observation of an evolving magnetic flux rope before and during a solar eruption. *Nat. Commun.* 3:747. doi: 10.1038/ncomms1753

Conflict of Interest: The author declares that the research was conducted in the absence of any commercial or financial relationships that could be construed as a potential conflict of interest.

frontiers in Astronomy and Space Sciences

ORIGINAL RESEARCH
published: 13 May 2021
doi: 10.3389/fspas.2021.634358

Investigating Width Distribution of Slow and Fast CMEs in Solar Cycles 23 and 24

V. Pant[1,2,3]*, *S. Majumdar*[4], *R. Patel*[1,4], *A. Chauhan*[5], *D. Banerjee*[1,4,6] *and N. Gopalswamy*[7]

[1]Aryabhatta Research Institute of Observational Sciences, Nainital, India, [2]Instituto de Astrofisíca de Canarias, Tenerife, Spain, [3]Departamento de Astrofisíca, Universidad de La Laguna, Tenerife, Spain, [4]Indian Institute of Astrophysics, Bangalore, India, [5]Harish-Chandra Research Institute, Allahabad, India, [6]Center of Excellence in Space Sciences, IISER, Kolkata, India, [7]NASA Goddard Space Flight Center, Greenbelt, MD, United States

Coronal Mass Ejections (CMEs) are highly dynamic events originating in the solar atmosphere, that show a wide range of kinematic properties and are the major drivers of the space weather. The angular width of the CMEs is a crucial parameter in the study of their kinematics. The fact that whether slow and fast CMEs (as based on their relative speed to the average solar wind speed) are associated with different processes at the location of their ejection is still debatable. Thus, in this study, we investigate their angular width to understand the differences between the slow and fast CMEs. We study the width distribution of slow and fast CMEs and find that they follow different power law distributions, with a power law indices (α) of –1.1 and –3.7 for fast and slow CMEs respectively. To reduce the projection effects, we further restrict our analysis to only limb events as derived from manual catalog and we find similar results. We then associate the slow and fast CMEs to their source regions, and classified the sources as Active Regions (ARs) and Prominence Eruptions. We find that slow and fast CMEs coming from ARs and PEs, also follow different power laws in their width distributions. This clearly hints toward a possibility that different mechanisms might be involved in the width expansion of slow and fast CMEs coming from different sources.These results are also crucial from the space weather perspective since the width of the CME is an important factor in that aspect.

Keywords: coronal mass ejections, corona, kinematics, space weather, solar cycle

OPEN ACCESS

Edited by:
Nandita Srivastava,
Physical Research Laboratory, India

Reviewed by:
Jiajia Liu,
Queen's University Belfast, United Kingdom
Abhishek Kumar Srivastava,
Indian Institute of Technology (BHU), India

***Correspondence:**
V. Pant
vaibhav.pant@aries.res.in

Specialty section:
This article was submitted to Stellar and Solar Physics, a section of the journal Frontiers in Astronomy and Space Sciences

Received: *27 November 2020*
Accepted: *26 April 2021*
Published: *13 May 2021*

Citation:
Pant V, Majumdar S, Patel R, Chauhan A, Banerjee D and Gopalswamy N (2021) Investigating Width Distribution of Slow and Fast CMEs in Solar Cycles 23 and 24. Front. Astron. Space Sci. 8:634358. doi: 10.3389/fspas.2021.634358

1 INTRODUCTION

Coronal mass ejections (CMEs) consist of plasma and magnetic field that are expelled from the solar atmosphere into the heliosphere at speeds which can range from 100 to 3,000 km s^{-1} (Gopalswamy, 2004; Gopalswamy, 2010; Manoharan and Mujiber Rahman, 2011; Yashiro et al., 2004; Manoharan and Mujiber Rahman, 2011; Webb and Howard, 2012). They appear as bright, white-light features moving outward in the coronagraph field of view (FOV) (Hundhausen et al., 1984; Schwenn, 1996). Though, early observations of CMEs date back to 1970s (Hansen et al., 1971), it is Tousey (1973) who first observed CMEs in the coronagraph images (see recent review by Gopalswamy (2016), on the history of CMEs). Since the launch of the Large Angle and Spectrometric Coronagraph (LASCO) (Brueckner et al., 1995) on the *Solar and Heliospheric Observatory (SOHO)* and Sun Earth Connection Coronal and Heliospheric Investigation (SECCHI) (Howard et al., 2008) on the *Solar Terrestrial Relation Observatory (STEREO)*, CMEs are being routinely monitored.

CMEs are the major drivers of space weather, as they are capable of producing shock waves and interplanetary disturbances (Gosling et al., 1991; Gosling, 1993), where the height of formation of the shock wave can often be estimated from the radio observations (Gopalswamy et al., 2013). Recently, Vourlidas et al. (2020) have outlined the role of radio observations of CMEs during different stages of the CME eruption and its subsequent propagation in the heliosphere. Thus it is important to understand the kinematics of CMEs. CMEs during their radial propagation, have been known to follow a three phase kinematic profile (Zhang et al., 2001; Zhang and Dere, 2006; Webb and Howard, 2012). During their propagation, they interact with the ambient solar wind and experience a drag, which leads to a decreasing or constant speed in the later stages of their propagation (Webb and Howard, 2012). This average solar wind speed reportedly divides the CMEs into slow and fast (Gopalswamy et al., 2000). CMEs are also known to be associated with active regions and eruptive prominences (Subramanian and Dere, 2001; Webb and Howard, 2012). These two classes of source regions of CMEs tend to associate CMEs to two distinct classes (MacQueen and Fisher, 1983). Sheeley et al. (1999) used the data from LASCO and confirmed this classification by suggesting that there are two dynamical classes of CMEs, which are gradual and impulsive CMEs. The former are slower and are preferentially associated with eruptive prominences, whereas, the latter CMEs are faster and are mostly associated with flares and active regions. So, it seems that these two classes of source regions of CMEs also tend to segregate CMEs into being gradual or impulsive events. The most intriguing question in this context is whether there are two physically different processes that are involved in the launch of these slow and fast CMEs or whether they belong to a dynamical continuum with a single unified process, the answer to which is still not clear (also see Webb and Howard, 2012).

Apart from their radial propagation, CMEs are also known to exhibit lateral expansion that leads to an increase in their angular width as they propagate outwards (Kay et al., 2015; Cremades et al., 2020; Majumdar et al., 2020) and that it is the Lorentz force at their source region that is closely responsible for translating and expanding them (Subramanian et al., 2014). In this regard, Zhao et al. (2017) reported on the importance of the angular width of a CME, in determining whether the corresponding interplanetary CME and the preceding shock will reach Earth. Lugaz et al. (2017a) reported on the importance of studying the expansion in slow CMEs on their ability to drive shocks. The width of the CME also sheds light on the source region of the CME it is coming from. Moore et al. (2007) showed that the strength of the magnetic field of the source region flare arcade producing a CME can be estimated from the final angular width of the CME and the angular width of the flare arcade. Recently Majumdar et al. (2020) connected 3D profiles of width evolution to the 3D acceleration profiles of slow and fast CMEs and found that the vanishing of the initial impulsive acceleration phase and the ceasing of width expansion phase both tend to occur in a height range of 2.5–3 $R_{\odot}$, thus showing the observational evidence of the height of impact of Lorentz force on CME kinematics. So, it is evident that the width of a CME is an essential ingredient in the understanding of their kinematics, and is also an important parameter for the consideration of their space weather impact. Furthermore, since the width largely influences the kinematics of CMEs, it is still not known whether we observe any differences in the angular width distribution of slow and fast CMEs originating from different source regions.

It has also been reported that the width distribution of CMEs follow a power law (Yashiro et al., 2006; Robbrecht et al., 2009; D'Huys et al., 2014). A study of the statistical distribution of a physical parameter sheds light on the underlying physics of it, and a presence of power law in the distribution of a quantity indicates the presence of Self-Organized Criticality (Bak et al., 1987). The presence of power laws, and hence Self-Organized Criticality (SOC) in nature have become evident in the last few years in many different areas and astrophysical phenomena (Aschwanden et al., 2018, and references therein). The presence of power laws in solar astrophysics, in the global energetics of solar flares, has also been reported by Aschwanden (2016). Thus, a study of the distribution of the angular width of CMEs should provide important clues in understanding the physical mechanisms responsible for expanding the CMEs. Recently, Bidhu et al. (2017) studied the distribution of width of CMEs during the maximum phase of solar cycle 23 and 24. Meng et al. (2014) studied the distribution of CME width and its comparison with the phase of sunspot number in solar cycle 23. Inspite of these studies, whether the slow and fast CMEs follow different width distributions or whether there is any imprint of the source regions on the width distribution of these slow and fast CMEs, is still not properly understood. Thus it is worth looking at the width distribution of slow and fast CMEs and also if there is any imprint of the source region of these two dynamical classes on their width distribution.

Motivated by the above findings and the deficit in our understanding of these slow and fast CMEs, we in this work study the width distribution of slow and fast CMEs that occurred during different phases of cycle 23 and 24. We outline the data sources and the working method in **Section 2**, followed by our results in **Section 3**. Finally, we outline our main conclusions from this work in **Section 4**.

2 DATA AND METHOD

2.1 Data Source

We use the data from CDAW catalog for the analysis presented in this paper. The CDAW catalog lists the properties of CMEs detected manually (Yashiro et al., 2004; Gopalswamy et al., 2009) in SOHO/LASCO images. The work on source region identification and segregation is done with the images taken by *Atmospheric Imaging Assembly* (AIA) on-board *Solar Dynamics Observatory* (SDO) (Lemen et al., 2011) and the Extreme Ultraviolet Imager (EUVI) on-board STEREO (for details, refer to **Section 2.4**).

2.2 Event Selection

We have selected the CMEs from the CDAW catalog that have occurred during different phases of solar cycle 23 and 24. For the

TABLE 1 | Power–law indices of width distribution of fast and slow CMEs obtained using two different methods.

Catalog	Total CMEs	Fast CMEs							Slow CMEs						
		Total	GF		MLE				Total	GF		MLE			
			W_m	α	W_m	α_m	W_d	α_d		W_m	α	W_m	α_m	W_d	α_d
CDAW[a]	19,046	3,031	30	−1.3	30	−1.13	66	−1.48	4,925	70	−3.8	30	−1.8	89	−4.36
CDAW[b]	11,329	2,680	30	−1.1	30	−1.01	66	−1.37	2,357	70	−3.7	30	−1.53	80	−3.74
Limb CMEs	531	266	30	−0.4	30	−1	68	−1	169	70	−3.8	30	−1.8	68	−4.16

[a]*CMEs excluding "very poor" CMEs.*

[b]*CMEs excluding "poor" and "very poor" CMEs.*

W_m is the minimum width threshold used to fit datasets. α is the power index estimated using graphical fitting (GF) method.

α_m is the derived power index using the Maximum likelihood Estimate (MLE) by giving a minimum width threshold, specified by W_m.

W_d is the derived minimum width by minimizing the Kolmogorov-Smirnov (KS) distance.

α_d is the derived power index by applying MLE using minimum width threshold as W_d.

Limb CMEs are extracted from the CDAW catalog according to the criteria in Gopalswamy et al. (2014).

analysis presented in this work, we first remove the "very poor" CMEs from the CDAW catalog. Wang and Colaninno (2014) reported that the detection of "very poor" CMEs are based on the discretion of manual operators, we discard such CMEs in order to remove any bias from our analysis. It should be noted that some of the "very poor" CMEs may be the real CMEs but we remove them from the analysis because there are large errors in the measurement of the properties of such CMEs. Furthermore, we impose a lower threshold of 30° on CME width to remove narrow CMEs. Yashiro et al. (2008) and Gopalswamy et al. (2010) have reported that there exists a discrepancy in the detection of the number of CMEs with width $<<30°$ when both CACTus and CDAW catalogs were compared. Also Yashiro et al. (2003) studied the statistical properties of narrow CMEs, and reported that they do not form a subset of normal CMEs and have different acceleration mechanism. In addition to a lower threshold, we also apply an upper threshold of 180° on the width because such CMEs mostly suffer from projection effects and thus the width estimation will be affected. It is worth noting that CMEs with width between 30° and 180° also suffer from projection effects. In order to reduce projection effects, we also use limb CMEs (whose source regions were found within 30° of the limb) for the analysis. The selection criteria for the limb CMEs is reported in Gopalswamy et al. (2014).

2.3 Segregation of CMEs Into Slow and Fast

After shortlisting the CMEs based on the above selection criteria, we segregate the CMEs as slow and fast based on their speeds. CMEs are usually classified as slow and fast relative to the speed of the solar wind. The slow solar wind typically has speeds less than 400 km s^{-1} while the fast solar wind has speeds greater 400 km s^{-1} (see, Schwenn, 2006). Therefore, 400 km s^{-1} can be taken as the average solar wind speed for a long term statistical study. We classify CMEs with speeds less than 300 km s^{-1} as slow CMEs and those with speeds greater than 500 km s^{-1} as fast CMEs. We consider CMEs with speeds between 300 km s^{-1} and 500 km s^{-1} as intermediate CMEs, as they cannot be strictly categorized as either slow or fast CMEs because of uncertainties in speed measurements. It is worth noting at this point that the speeds of CMEs listed in the CDAW catalog are the speeds with which the leading edge of a CME propagates. **Table 1** lists the number of fast and slow CMEs in the CDAW catalog.

2.4 Segregation of the Slow and Fast CMEs on the Basis of Their Source Region

After segregating the CMEs as slow and fast, we search their source regions on the solar disk. For this we included a total of 1,064 events that occurred during 2000–2002, 2008, 2009, and also from 2012 to 2014, which covers the maxima of cycle 23, the minima of cycle 24 and the maxima of cycle 24. Here, we have followed a similar method as reported in Majumdar et al. (2020) and using the JHelioviewer software (Muller et al., 2009; Müller et al., 2017) to back-project the CMEs onto the solar disk. We further segregated the identified source regions of the CMEs into two broad categories, namely 1) Active Regions(ARs) and 2) Prominence Eruptions(PEs). We define them as follows:

Active Regions(ARs) (refer **Figure 1**) are prime features making up only a small fraction of the total surface area of the Sun, but harboring most of the solar activity (Webb and Howard, 2012). These being areas of strong magnetic field, are predominantly hotter and denser than the background coronal plasma, producing bright emission in the soft X-ray and extreme ultraviolet regions. In order to identify ARs, we look into the images taken by 1) the Extreme Ultraviolet Imaging Telescope (EIT; Delaboudinière et al., 1995) (195 Å) onboard SOHO, 2) Atmospheric Imaging Assembly (AIA; Lemen et al., 2011) (171 Å, 193 Å) onboard SDO, and also 3) the Extreme Ultraviolet Imager (EUVI; Wuelser et al., 2004) (171 Å, 195 Å) onboard STEREO SECCHI. We also detect the ARs by the Active Region numbers provided by the National Oceanic and Atmospheric Administration (NOAA) as supplied by Space Weather Event Knowledgebase (SWEK) using Jhelioviewer[1] (Müller et al., 2017).

Prominences (refer **Figure 1**) are cool dense material (8000 K) embedded in the hotter corona, observed as an emission feature when seen at the solar limb, and an absorption feature when seen

[1]https://www.jhelioviewer.org/

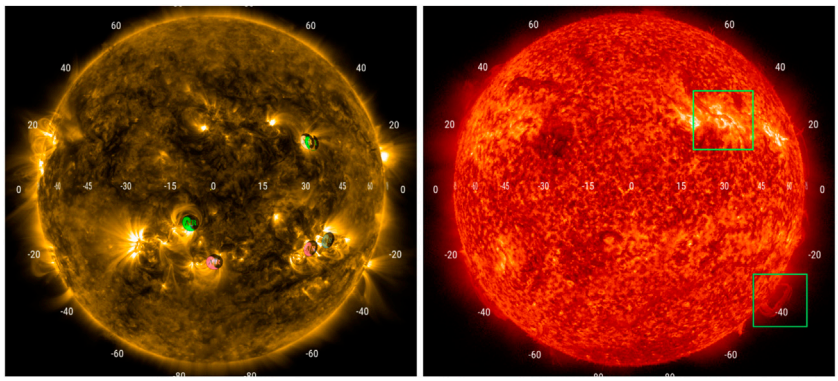

FIGURE 1 | (Left) Active regions (ARs) as observed in the corona on May 03, 2012. The image is taken by AIA 171 Å. The ARs (pointed out in the figure by circular marks with AR written on them), are identified as bright regions, being hotter and denser than the background coronal plasma, showing strong magnetic activity **(Right)** Prominence Eruptions (PEs, enclosed in green box) as observed in the corona on April 04, 2012. This image is taken by AIA 304 Å. The dark strands of plasma as seen projected against the disk of the sun are filaments (at a position angle of 40° and 300° in this image), whereas the same object is termed as a prominence when observed at the solar limb (at a position angle of 235° in this image).

projected against the background hotter corona (termed as filament) (Gilbert et al., 2000). We classify an eruption as a prominence eruption if we see a strong radial component of motion away from the solar surface where all or some of the prominence material is seen to escape the gravitational field of the Sun. For a filament eruption (we include these in the same category with prominence eruption) we either looked for tangential motion across the solar surface with a subsequent eruption, or simply by observing any disappearance of the filament in the subsequent images with a transient coronal manifestation following it (also refer Webb and Hundhausen (1987)). It is also important to note that, there can be possibilities of failed eruptions (Joshi et al., 2013a), CME-jet interactions (Duan et al., 2019; Solanki et al., 2020), and CME-CME interactions (Joshi et al., 2013b; Lugaz et al., 2017b) which can influence the kinematic properties. Furthermore, CMEs are also observed to be associated with coronal jets, minifilaments, etc (Liu et al., 2015; Duan et al., 2019; Solanki et al., 2019). It is also not properly understood whether such CMEs can be categorized as the active region eruptions and prominence eruptions or classified as a different category. Thus, in the present work, we exclude such events. Furthermore, CMEs are also related to the active region filaments, however, due to the lack of comparable statistics with the other two classes (ARs and PEs), we have excluded such events from our analysis. To detect PEs, we look into the images taken by, 1) EIT 195 Å, 304 Å, 2) AIA 304 Å, and 3) EUVI 304 Å. Finally, it should be borne in mind that kinematic properties of CMEs largely depend on the overlying field strength and decay index (Xu et al., 2012; Joshi et al., 2013a). In this work we do not consider these effects into account.

For a spatial association (see Gilbert et al., 2000; Majumdar et al., 2020) between a source region and a subsequent CME, we require that the latitude of the source region to be around ± 30° to that of the PA of the center of the CME as reported in the CDAW catalog. In the case of a filament eruption, due to larger uncertainty of its spatial location, we look for an erupting filament around ± 40° around the PA of the CME converted to equivalent apparent latitude (lat_{PA}) by the following relation:

$$lat_{PA} = 90 - PA \quad [0 \le PA \le 180] \qquad lat_{PA} = PA - 270 \quad [180 < PA \le 360] \tag{1}$$

For a temporal association we consider source region to erupt or show radially outward movement in the above latitude window in a time interval of at least 30 min before the first appearance of the leading front in the LASCO C2 field of view.

3 DATA ANALYSIS AND RESULTS

3.1 Width Distribution of CMEs

Recently, it has been reported that the CMEs evolve non self-similarly in the inner corona (see Cremades et al., 2020; Majumdar et al., 2020). In the CDAW catalog, the width of a CME is defined as the maximum angle subtended by a CME on the center of the Sun when the CME enters the LASCO C3 field of view (FOV) where the width appears to approach a constant value (Gopalswamy, 2004). To investigate the width distribution of CMEs during solar cycle 23 and 24, we fit a power law to it as follows:

$$N(W) = CW^{\alpha} \tag{2}$$

where N is the number of CMEs with width W, α is the power-law exponent, and C a constant. In **Figure 2** we plot the histogram (left panel) of the width distribution and the width distribution in log scale (right panel) with the power law fit for all CMEs excluding the "very poor" events as mentioned in the CDAW catalog. It is worth noting that after removing "very poor" CMEs from our analysis, we believe that we have reduced the bias introduced by manual operators, respectively. We find a power law index of −1.9. In order to understand the goodness of fit we perform the Kolmogorov Smirnov (KS) test where the KS

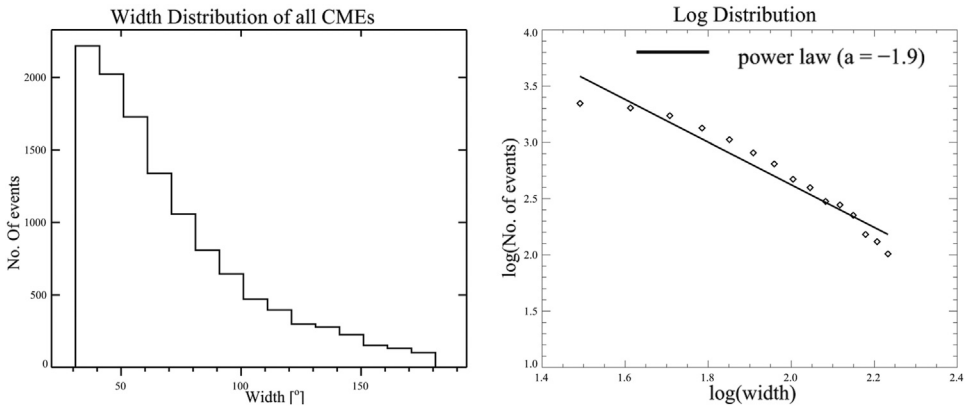

FIGURE 2 | Width distribution of all CMEs (excluding "very poor" events) during solar cycle 23 and 24 using the CDAW catalog. The black line corresponds to a power law fit to the width distribution where α is the power law index.

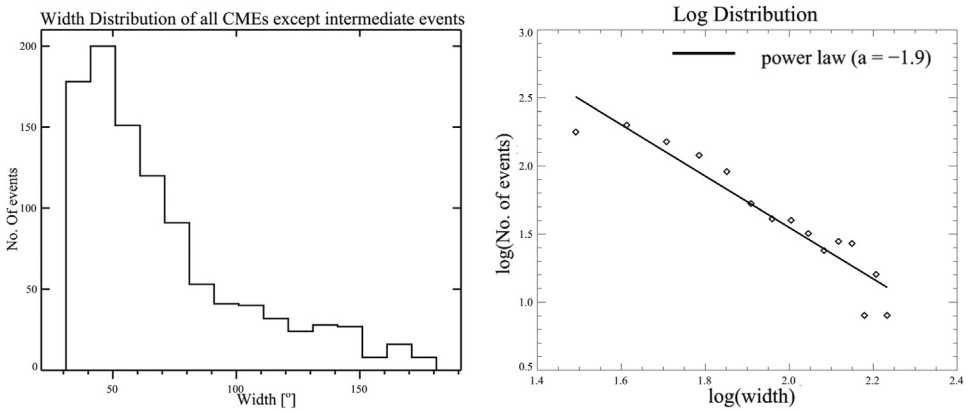

FIGURE 3 | Width distribution of CMEs (excluding the intermediate and "very poor" events) during solar cycle 23 and 24 using the CDAW catalog. The black line corresponds to a power law fit to the width distribution where α is the power law index.

distance (see Clauset et al., 2007) which is defined as the maximum distance between the empirical distribution function of the sample and cumulative distribution function of the assumed expression, is minimum for the distribution which fits the data best with a corresponding high p-value that gives the probability confidence. Here we find the KS distance and p-value as 0.13 and 0.99. It is worth noting from **Figure 2**, that the width distribution is not fitted well by a single power law. This serves as a motivation for us to investigate power laws segregating fast and slow CMEs. Since we aim to understand the width distribution of slow and fast CMEs, we next remove the intermediate events from our study sample, as such events are neither fast nor slow (refer **section 3.2**). We again study the width distribution of all events except the "very poor" and the intermediate events (**Figure 3**). We find that after removing the intermediate events, we still get the same power law index of −1.9 with the KS distance and p-value to be the almost same. Thus we ensure that there is no bias introduced in the estimation of the power law index of widths distribution by rejecting the intermediate events from our sample. The graphical fitting (GF) of the data points used above is not the best method to estimate the power-law, especially when number of data points is small (D'Huys et al., 2016). Therefore, we also use maximum likelihood estimate (MLE) fitting method to derive the power-law index, α. Using MLE, we get the power law index to be −1.6 which again remains the same for CMEs with or without the intermediate events.

Now that we have ensured that the exclusion of the intermediate events does not affect our study, we try to understand now if the slow and fast CMEs follow different power laws in their width distribution.

3.2 Width Distribution of Slow and Fast CMEs

In this section we study the width distribution of slow and fast CMEs separately. We use the same power law distribution as mentioned in **Eq. 2**. **Figure 4A** shows the histograms of the width

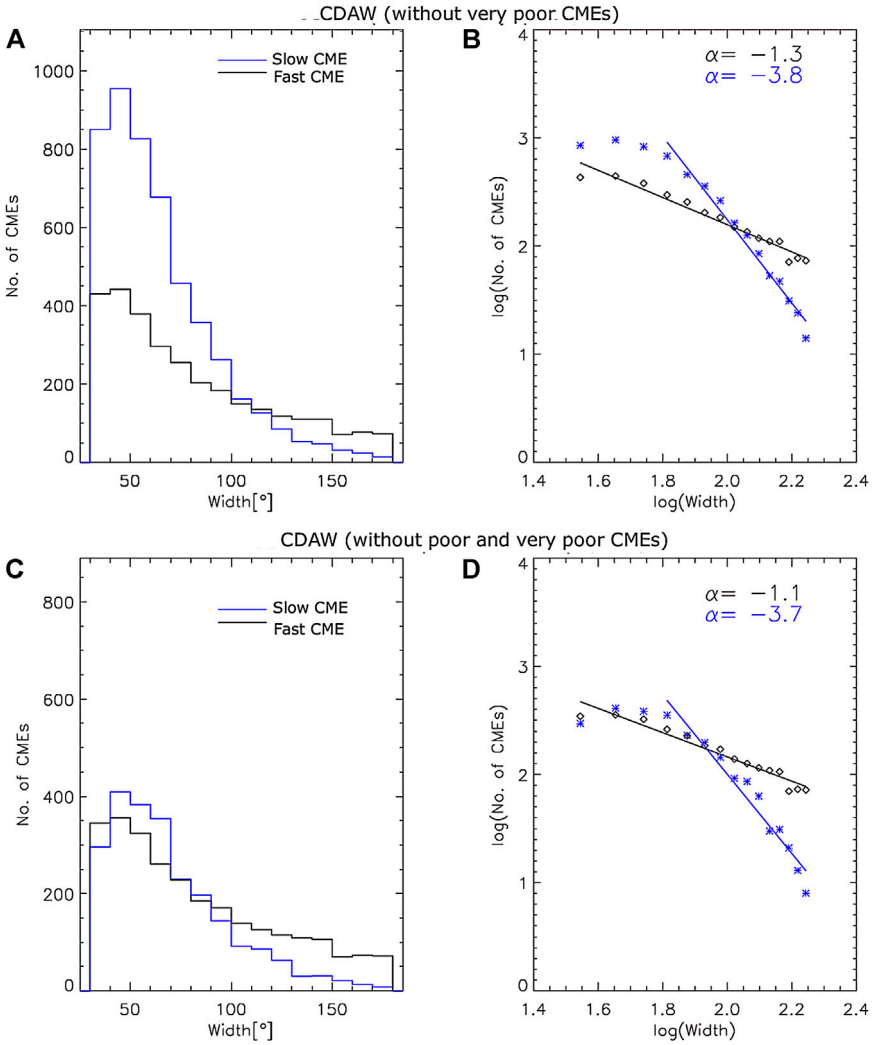

FIGURE 4 | (A): Width distribution and, **(B)**: log distribution of width for slow and fast CMEs using CDAW catalog after excluding "very poor" CMEs. The best fit straight line to the data points of fast CMEs is overplotted in black. The best fit straight line to the data points (except first three points) of slow CMEs is overplotted in blue. **(C)** and **(D)** are the same as **(A)** and **(B)** but excluding "poor" and "very poor" CMEs from the CDAW catalog.

distribution of fast (black line) and slow (blue line) CMEs using CDAW catalog after excluding the "very poor" CMEs and the intermediate CMEs. **Figure 4B**, shows the width distributions in log scale. Black and blue lines represent the best fit power-laws obtained for the fast and slow CMEs, respectively using least square fitting method. We estimate α as −1.3 and −3.8 for fast and slow CMEs respectively. Thus we find that the slow and fast CMEs follow different power laws in their width distribution, but to get a better confidence on our result, we again perform power law fitting by MLE.

It should be noted that the number of slow CMEs in CDAW catalog with widths less than 70° flattens. This could partially be due to the observational limitations of C2 coronagraph or human subjectivity or both. The minimum width for the graphical fitting is decided by visually inspecting the distribution and choosing the width beyond which the distribution is supposedly following a power-law. Thus, we fit the tail of the width distribution of slow CMEs with a power-law. Later, we used MLE to derive the minimum width beyond which the distribution is best represented by the power law.

We performed MLE fitting in two different ways. First we set the minimum width value, W_m as 30° for both fast CMEs and slow CMEs and estimate the power-law index. Second, we derive the minimum width value, W_d for both fast and slow CMEs by minimizing the KS distance and estimate the power-law index. The second method tells us that beyond W_d, the data points best follow the power-law. **Table 1** lists the power indices estimated using two methods described above for fast and slow CMEs. We see that indeed the slow and fast CMEs follow distinctly different power laws in their width distribution.

We also remove the CMEs labeled as "poor" in the CDAW catalog to study their effects on the width distribution. We find that removal of both "poor" and "very poor" CMEs has little effect

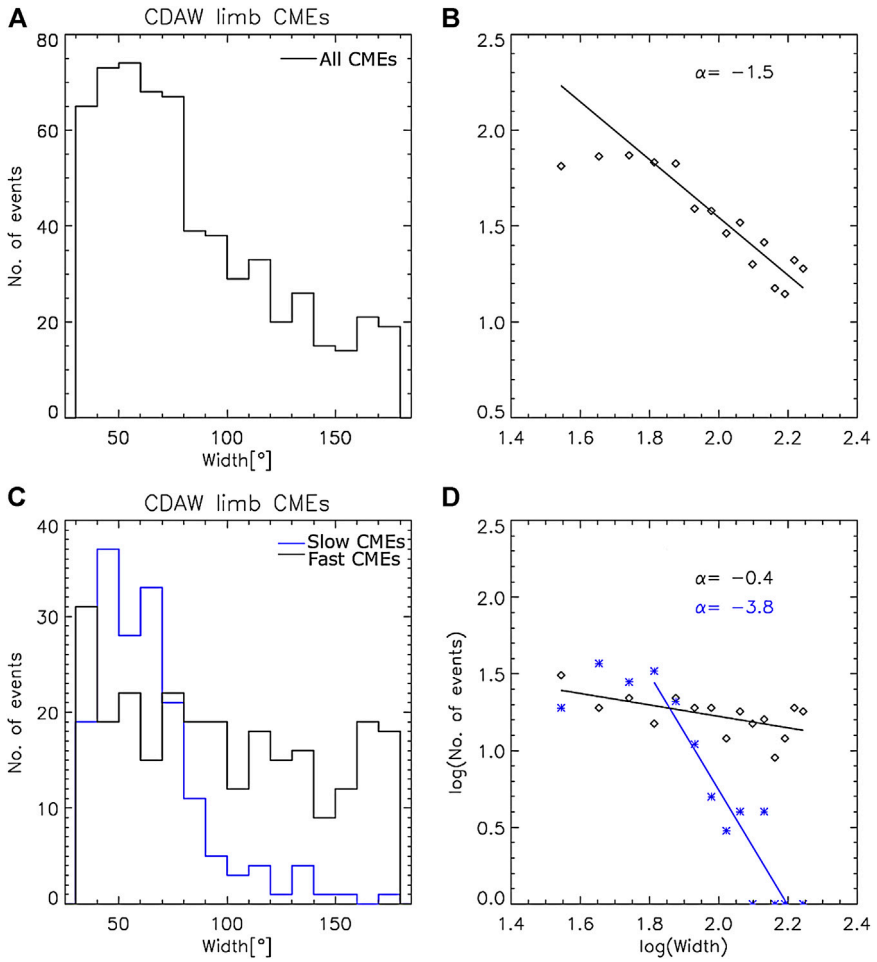

FIGURE 5 | (A): Width distribution for all limb CMEs extracted from CDAW catalog without velocity thresholding. **(B)** is the log-distribution of limb CMEs. **(C)** and **(D)**: Width distribution of slow and fast limb CMEs extracted from CDAW catalog.

on the width distribution and power-law indices (see, **Figures 4C,D** and **Table 1**) of slow and fast CMEs. The speeds listed in the CDAW catalog are the projected speeds in the plane of sky measured at a fixed position angle. Therefore, applying a speed threshold uniformly to all CMEs introduces projection effects. In order to reduce projection effects, we also estimate the power-law for fast and slow limb CMEs in solar cycles 23 and 24. First we plot CMEs with all velocities whose widths fall between 30 and 180° (top panel of **Figure 5**). We estimate the power index of −1.5 and −1.19 using the GF and MLE methods for the minimum width threshold of 30°. Then, we segregate fast and slow CMEs and estimate the power indices using the GF (bottom panel of **Figure 5**) and MLE methods (see **Table 1**). We find that the power indices for fast and slow limb CMEs are different from each other; they are different from the power index of non–limb fast and slow CMEs. One of the reasons for this discrepancy is the small number of slow and fast limb CMEs. From **Table 1**, we note that the fast and slow limb CMEs are 10–20 times less than fast and slow CMEs when non-limb events are also considered. To evaluate the goodness of fit we again estimate the KS distance. The KS distances for fast limb CMEs and all fast CMEs are 0.09 and 0.01, respectively. The critical values of KS distances with 99% of confidence limit for fast limb CMEs and all fast CMEs are 0.1 and 0.03, respectively. Smaller the KS distance, better is the fit. Similarly, KS distances for slow limb CMES and all slow CMEs are 0.04 and 0.02, respectively. Further, critical KS distance at 99% of confidence limit for slow limb CMEs and all slow CMEs are 0.13 and 0.03, respectively.Thus the power indices corresponding to the limb CMEs differ from that of non-limb cases. We want to emphasize that the slow CME power-law is steeper than that of the fast CMEs in both cases, although the values may differ. However, the limb CME values may be closer to reality because of minimal projection effects. It should be noted that the results are consistent with the speed–width relation as reported in Gopalswamy et al. (2014); where authors have reported wider CMEs tend to propagate faster than narrow CMEs. Also, we note that the KS distance of fast CMEs without "very poor" and intermediate events is of an order of magnitude better than KS distance estimated by fitting a single power law to all CMEs. This demonstrates that fast and slow

TABLE 2 | Power-law indices of width distribution of fast and slow CMEs from different source regions obtained using two different methods.

Regions	Total	Fast CMEs							Slow CMEs						
Source	CMEs	Total	GF		MLE				Total	GF		MLE			
			W_m	α	W_m	α	W_d	α_d		W_m	α	W_m	α	W_d	α_d
ARs	694	291	30	−1.29	30	−1.23	–	–	403	60	−3.20	30	−1.91	60	−3.11
PEs	281	89	60	−3.43	30	−2.00	60	−3.74	192	60	−3.53	30	−2.08	60	−3.75

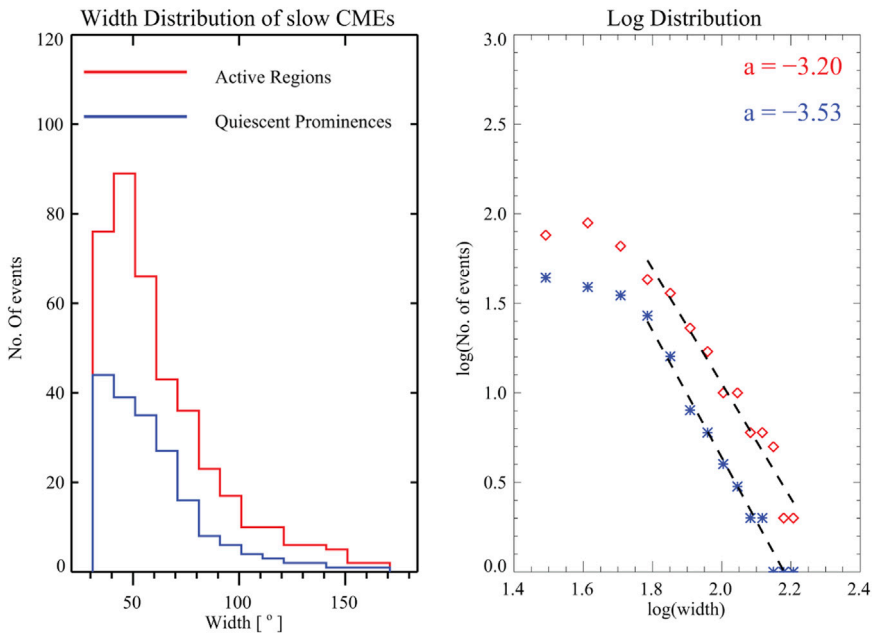

FIGURE 6 | (Left) Width distribution of slow CMEs from different source regions, with their widths taken from the CDAW catalog. **(Right)** power-law fitting of the width distribution. The black line is the power-law fit to the data.

CMEs are better represented by different power-laws than fast and slow CMEs combined.

3.3 Width Distribution of Slow and Fast CMEs Coming from ARs and PEs

In previous sections, we note that the slow and fast CMEs follow different power laws. This lights on the fact that may be the slow and fast CMEs have different physics involved in the mechanism that leads to their expansion and hence their widths. Since Lorentz force is responsible for propelling and expanding a CME (refer **Section 1**), we expect to see its imprint in the width distribution of slow and fast CMEs originating from different source regions.

The entries in **Table 2** have been computed by taking events from different phases of cycle 23 and 24 as mentioned in **Section 2.4**. After segregating the source regions, their width distribution is studied separately. Here we use a similar power-law fitting to the width distribution of CMEs coming from the two source regions. We do power-law fitting by graphical fitting and also by MLE to estimate power-law indices.

Figures 6, **7** show the width distribution of slow and fast CMEs originating from ARs and PEs, and plotted alongside it are the power-law fit (in black). We get α as −1.29 and −3.43 for fast CMEs coming from ARs and PEs with a KS distance of 0.13 (p-value 0.99) and 0.22 (p-value 0.86) respectively. Thus we see that indeed the width distribution of fast CMEs have different power indices for CMEs originating from ARs and PEs. In the case of slow CMEs we get α as −3.20 and −3.53 for CMEs from ARs and PEs with a KS distance of 0.14 (p-value 0.99) and 0.21 (p-value 0.86) respectively. Thus for slow CMEs too the power indices are slightly different for CMEs from ARS and PEs. Again, GF is not the best method to estimate the power-law since the number of data points is small here, by using MLE fitting, we get α as −1.23 and −2.00 for fast CMEs coming from ARs and PEs respectively, whereas for slow CMEs we get α as −1.91 and −2.08 for CMEs from ARs and PEs keeping $W_m = 30^\circ$ (refer, **Table 2**). The 1-sigma error involved for power-law fitting of width of fast CMEs from ARs and PEs are 0.22 and 0.24 respectively, and that for slow CMEs from ARs and PEs are 0.14 and 0.03 respectively. **Table 2** clearly depicts that the power-laws followed by slow and fast CMEs coming from ARs and PEs are distinctly different and

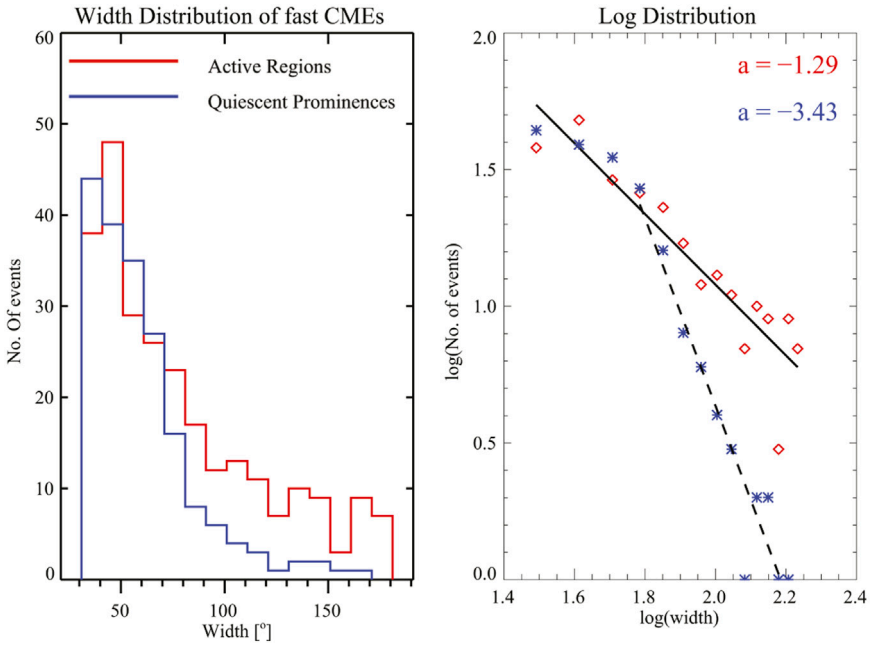

FIGURE 7 | (Left) Width distribution of fast CMEs from different source regions, with their widths taken from the CDAW catalog. **(Right)** power-law fitting of the width distribution. The black line is the power-law fit to the data.

thus supports our earlier conjecture. We note that although the slow CMEs are seen to follow a steeper power-law than the fast ones (as we have found earlier), the difference in power law indices is more pronounced for the case of CMEs associated with the ARs. Furthermore, CMEs associated with prominence eruptions and slow CMEs have steeper power index than fast CMEs coming from the active regions. The power index of fast CMEs matches with those estimated for flares. Thus it is evident that possibly the mechanism involved in the width expansion of slow and fast CMEs are different for the CMEs originating from ARs and PEs. We also note that the p-value for the power law fit to the width distribution for CMEs from different sources is lower, and this is due to the lower statistics that we have in each cases.

Thus the fact that slow and fast CMEs from ARs and PEs following different power laws in their width distribution vividly points toward a possibly different mechanism that leads to the width expansion of these CMEs and hence demands a more deeper understanding of the same. It should be noted that a few studies Zuccarello et al. (2014); Seaton et al. (2011); O'Kane et al. (2019) have tried to explore the possible mechanims of the CMEs but these studies are confined to isolated cases of CMEs. Also, a few statistical studies on large number of CMEs suggested that there may be different classes of CMEs with different driving mechanisms (Cyr et al., 1999; Subramanian and Dere, 2001; Moon et al., 2002).

From **Figures 6**, **7** we also note that in case of the fast CMEs, effect of change in source region is more pronounced unlike the case for slow events. The limit of the field strength in the source region could be the physical reason for the strength of field in ARs, which in turn determines the available energy to power the eruptions, whereas in case of the CMEs from PEs, the magnetic structure in the periphery of the ejection site controls the chances of ejection and eventually the observed kinematic properties of the ejected material (Gopalswamy, 2017). So, possibly a different mechanism governs the width expansion of CMEs coming from ARs and PEs, irrespective of them being slow or fast.

4 SUMMARY AND CONCLUSION

In this work, we study the width distribution of CMEs that occurred during different phases of solar cycle 23 and 24. The CMEs were then segregated into slow ($\leq \leq 300$ km s^{-1}) and fast CMEs ($\geq \geq 500$ km s^{-1}) based on the average solar wind speed, and then their width distribution was studied. We further associate the slow and fast CMEs to the source regions they originated from, and classified the identified source regions into two broad categories, ARs and PEs. We investigate if the source regions have any imprint on the width distribution of these slow and fast CMEs. The data from the CDAW catalog has been used throughout this study. In the following, we conclude our main results from this work.

1. CMEs excluding 'very poor' events from the CDAW catalog tend to follow a power law in their width distribution with a power law index of −1.9 (**Figure 2**). Using MLE, we find the power law index to be −1.6. This power law index remains unchanged on the exclusion of the intermediate events from our sample set (**Figure 3**). Thus the intermediate events do not affect our results and thus we removed them from our sample set, as they cannot

be strictly considered either slow or fast. Using GF method, we note that a single power law is unable to explain the observed distribution.

2. We find different power indices for the width distribution of fast and slow CMEs (see **Table 1**). To reduce the projection effects from our results, we study the width distribution of slow and fast limb CMEs, and we found that they follow different power laws and the results remain unchanged. However, the absolute value of power indices are not the same as compared to limb and non limb CMEs which may be due to poor statistics, as demonstrated by KS test. Since both fast and slow limb and non-limb CMEs follow different power-laws in width distribution, we believe that slow and fast CMEs may have different energy sources and generation mechanisms.
3. We study the width distribution of slow and fast CMEs coming from different source regions (ARs and PEs), and find that the power law indices are different for CMEs coming from ARs and PEs (refer **Table 2**). Furthermore, CMEs coming from PEs tend to follow a steeper power law irrespective of their speeds. Also, we find that slow CMEs tend to follow a steeper power law than fast CMEs, irrespective of the source region they are coming from. This clearly hints toward a possibly different mechanism for width expansion of these CMEs.

Thus we find from this study that apart from their speeds, slow and fast CMEs are also distinctly different in terms of the distribution of their angular width in each case. We believe that this study will help in a better understanding of the mechanism of width expansion of slow and fast CMEs coming from different source regions, and in establishing the width of a CME as a crucial parameter in the study of kinematics of CMEs and their ejection mechanisms. Extending this work on a larger sample of CMEs using de-projection methods will further help in better confirmation of our conclusions.

DATA AVAILABILITY STATEMENT

The datasets presented in this study can be found in online repositories. The names of the repository/repositories and accession number(s) can be found below: CDAW Catalogue.

AUTHOR CONTRIBUTIONS

VP planned the study and performed initial analysis. SM, RP generated source region catalog. VP and SM wrote manuscript. AC performed analysis on the limb events. VP, SM, DB, and NG interpreted the results. All authors took part in the discussion.

FUNDING

VP was further supported by the GOA-2015-014 (KU Leuven) and the European Research Council (ERC) under the European Union's Horizon 2020 research and innovation program (grant agreement No. 724326). VP is supported by the Spanish Ministerio de Ciencia, Innovación y Universidades through project PGC2018-102108-B-I00 and FEDER funds.

ACKNOWLEDGMENTS

We thank referees for their comments which has improved the presentation. The authors thank IAC and IIA for providing the required computational facilities for doing this work. We also thank Mr. Bibhuti Kumar Jha for his useful comments during the work.

REFERENCES

Aschwanden, M. J. (2016). Global Energetics of Solar Flares. IV. Coronal Mass Ejection Energetics. *Astrophys. J.* 831, 105. doi:10.3847/0004-637X/831/1/105

Aschwanden, M. J., Scholkmann, F., Béthune, W., Schmutz, W., Abramenko, V., Cheung, M. C. M., et al. (2018). Order Out of Randomness: Self-Organization Processes in Astrophysics. *Space Sci. Rev.* 214, 55. doi:10.1007/s11214-018-0489-2

Bak, P., Tang, C., and Wiesenfeld, K. (1987). Self-organized Criticality: An Explanation of the 1/f Noise. *Phys. Rev. Lett.* 59, 381–384. doi:10.1103/PhysRevLett.59.381

Bidhu, S., Iren, S., and Benjamin, D. (2017). Cme Speed and Angular Width Distributions during 23 and 24 Solar Cycle Maximum. *J. Space Explor.* 6, 122. doi:10.1007/s11214-019-0605-y

Brueckner, G. E., Howard, R. A., Koomen, M. J., Korendyke, C. M., Michels, D. J., Moses, J. D., et al. (1995). The Large Angle Spectroscopic Coronagraph (LASCO). *Solar Phys.* 162, 357–402. doi:10.1007/BF00733434

Clauset, A., Rohilla Shalizi, C., and Newman, M. E. J. (2007). Power-Law Distributions in Empirical Data. *SIAM Rev.* 51, 661–703. 10.1137/070710111

Cremades, H., Iglesias, F. A., and Merenda, L. A. (2020). Asymmetric Expansion of Coronal Mass Ejections in the Low Corona. *Astron. Astrophys.* 635, A100. doi:10.1051/0004-6361/201936664

Cyr, St. O. C., Burkepile, J. T., Hundhausen, A. J., and Lecinski, A. R. (1999). A Comparison of Ground-Based and Spacecraft Observations of Coronal Mass Ejections from 1980–1989. *J. Geophys. Res.* 104, 12493–12506. doi:10.1029/1999JA900045

Delaboudinière, J.-P., Artzner, G. E., Brunaud, J., Gabriel, A. H., Hochedez, J. F., Millier, F., et al. (1995). EIT: Extreme-Ultraviolet Imaging Telescope for the SOHO Mission. *Solar Phys.* 162, 291–312. doi:10.1007/BF00733432

D'Huys, E., Berghmans, D., Seaton, D. B., and Poedts, S. (2016). The Effect of Limited Sample Sizes on the Accuracy of the Estimated Scaling Parameter for Power-Law-Distributed Solar Data. *Solar Phys.* 291, 1561–1576. doi:10.1007/s11207-016-0910-5

D'Huys, E., Seaton, D. B., Poedts, S., and Berghmans, D. (2014). Observational Characteristics of Coronal Mass Ejections without Low-Coronal Signatures. *Astrophys. J.* 795, 49. doi:10.1088/0004-637X/795/1/49

Duan, Y., Shen, Y., Chen, H., and Liang, H. (2019). The Birth of a Jet-Driven Twin CME and its Deflection from Remote Magnetic Fields. *Astrophys. J.* 881, 132. doi:10.3847/1538-4357/ab32e9

Gilbert, H. R., Holzer, T. E., Burkepile, J. T., and Hundhausen, A. J. (2000). Active and Eruptive Prominences and Their Relationship to Coronal Mass Ejections. *Astrophysical J.* 537, 503–515. doi:10.1086/309030

Gopalswamy, N. (2004). "A Global Picture of CMEs in the Inner Heliosphere," in *The Sun and the Heliosphere as an Integrated System*. Editors G. Poletto and S. T. Suess (Dordrecht, The Netherlands: Astrophysics and Space Science Library), vol. 317, 201. doi:10.1007/978-1-4020-2666-9_8

Gopalswamy, N. (2010). "Corona Mass Ejections: A Summary of Recent Results," in 20th National Solar Physics Meeting. Editor I. Dorotovic (Papradno, Slovakia: Proceedings of the 20th National Solar Physics Meeting), 108–130.

Gopalswamy, N. (2017). Extreme Solar Eruptions and Their Space Weather Consequences. *arXiv:1709.03165*.

Gopalswamy, N. (2016). History and Development of Coronal Mass Ejections as a Key Player in Solar Terrestrial Relationship. *Geosci. Lett.* 3, 8. doi:10.1186/s40562-016-0039-2

Gopalswamy, N., Akiyama, S., Yashiro, S., and Mäkelä, P. (2010). Coronal Mass Ejections from Sunspot and Non-Sunspot Regions. *Astrophys. Space Sci. Proc.* 19, 289–307. doi:10.1007/978-3-642-02859-524

Gopalswamy, N., Akiyama, S., Yashiro, S., Xie, H., Mäkelä, P., and Michalek, G. (2014). Anomalous Expansion of Coronal Mass Ejections during Solar Cycle 24 and its Space Weather Implications. *Geophys. Res. Lett.* 41, 2673–2680. doi:10.1002/2014GL059858

Gopalswamy, N., Lara, A., Lepping, R. P., Kaiser, M. L., Berdichevsky, D., and Cyr, St. O. C. (2000). Interplanetary Acceleration of Coronal Mass Ejections. *Geophys. Res. Lett.* 27, 145–148. doi:10.1029/1999GL003639

Gopalswamy, N., Xie, H., Mäkelä, P., Yashiro, S., Akiyama, S., Uddin, W., et al. (2013). Height of Shock Formation in the Solar Corona Inferred from Observations of Type II Radio Bursts and Coronal Mass Ejections. *Adv. Space Res.* 51, 1981–1989. doi:10.1016/j.asr.2013.01.006

Gopalswamy, N., Yashiro, S., Michalek, G., Stenborg, G., Vourlidas, A., Freeland, S., et al. (2009). The SOHO/LASCO CME Catalog. *Earth Moon Planets* 104, 295–313. doi:10.1007/s11038-008-9282-7

Gosling, J. T. (1993). The Solar Flare Myth. *J. Geophys. Res.* 98, 18937–18950. doi:10.1029/93JA01896

Gosling, J. T., McComas, D. J., Phillips, J. L., and Bame, S. J. (1991). Geomagnetic Activity Associated with Earth Passage of Interplanetary Shock Disturbances and Coronal Mass Ejections. *J. Geophys. Res.* 96, 7831–7839. doi:10.1029/91JA00316

Hansen, R. T., Garcia, C. J., Grognard, R. J.-M., and Sheridan, K. V. (1971). A Coronal Disturbance Observed Simultaneously with a White-Light Corona-Meter and the 80 MHz Culgoora Radioheliograph. *Proc. Astron. Soc. Aust.* 2, 57.

Howard, R. A., Moses, J. D., Vourlidas, A., Newmark, J. S., Socker, D. G., Plunkett, S. P., et al. (2008). Sun Earth Connection Coronal and Heliospheric Investigation (SECCHI). *Space Sci. Rev.* 136, 67–115. doi:10.1007/s11214-008-9341-4

Hundhausen, A. J., Sawyer, C. B., House, L., Illing, R. M. E., and Wagner, W. J. (1984). Coronal Mass Ejections Observed during the Solar Maximum Mission - Latitude Distribution and Rate of Occurrence. *J. Geophys. Res.* 89, 2639–2646. doi:10.1029/JA089iA05p02639

Joshi, N. C., Srivastava, A. K., Filippov, B., Uddin, W., Kayshap, P., and Chandra, R. (2013a). A Study of a Failed Coronal Mass Ejection Core Associated with an Asymmetric Filament Eruption. *Astrophys. J.* 771, 65. doi:10.1088/0004-637X/771/1/65

Joshi, N. C., Uddin, W., Srivastava, A. K., Chandra, R., Gopalswamy, N., Manoharan, P. K., et al. (2013b). A Multiwavelength Study of Eruptive Events on January 23, 2012 Associated with a Major Solar Energetic Particle Event. *Adv. Space Res.* 52, 1–14. doi:10.1016/j.asr.2013.03.009

Kay, C., Opher, M., and Evans, R. M. (2015). Global Trends of CME Deflections Based on CME and Solar Parameters. *Astrophys. J.* 805, 168. doi:10.1088/0004-637x/805/2/168

Lemen, J., Title, A., Boerner, P., Chou, C., Drake, J., Duncan, D., et al. (2011). The Atmospheric Imaging Assembly (Aia) on the Solar Dynamics Observatory (Sdo). *Solar Phys.* 275, 17–40. doi:10.1007/s11207-011-9776-8

Liu, J., Wang, Y., Shen, C., Liu, K., Pan, Z., and Wang, S. (2015). A Solar Coronal Jet Event Triggers a Coronal Mass Ejection. *Astrophys. J.* 813, 115. doi:10.1088/0004-637X/813/2/115

Lugaz, N., Farrugia, C. J., Winslow, R. M., Small, C. R., Manion, T., and Savani, N. P. (2017a). Importance of CME Radial Expansion on the Ability of Slow CMEs to Drive Shocks. *Astrophys. J.* 848, 75. doi:10.3847/1538-4357/aa8ef9

Lugaz, N., Temmer, M., Wang, Y., and Farrugia, C. J. (2017b). The Interaction of Successive Coronal Mass Ejections: A Review. *Solar Phys.* 292, 64. doi:10.1007/s11207-017-1091-6

MacQueen, R. M., and Fisher, R. R. (1983). The Kinematics of Solar Inner Coronal Transients. *Solar Phys.* 89, 89–102. doi:10.1007/BF00211955

Majumdar, S., Pant, V., Patel, R., and Banerjee, D. (2020). Connecting 3D Evolution of Coronal Mass Ejections to Their Source Regions. *Astrophys. J.* 899, 6. doi:10.3847/1538-4357/aba1f2

Manoharan, P. K., and Mujiber Rahman, A. (2011). Coronal Mass Ejections–Propagation Time and Associated Internal Energy. *J. Atmos. Solar-Terr. Phys.* 73, 671–677. doi:10.1016/j.jastp.2011.01.017

Meng, W.-J., Le, G.-M., Lin, Z.-X., Zhang, Y., and Yang, X.-X. (2014). Distribution of CMEs with Different Angular Widths and Comparison with the Phase of Sunspot Number in the 23rd Solar Cycle. *Chin. Astron. Astrophys.* 38, 85–91. doi:10.1016/j.chinastron.2014.01.008

Moon, Y. J., Choe, G. S., Wang, H., Park, Y. D., Gopalswamy, N., Yang, G., et al. (2002). A Statistical Study of Two Classes of Coronal Mass Ejections. *Astrophys. J.* 581, 694–702. doi:10.1086/344088

Moore, R. L., Sterling, A. C., and Suess, S. T. (2007). The Width of a Solar Coronal Mass Ejection and the Source of the Driving Magnetic Explosion: A Test of the Standard Scenario for CME Production. *Astrophys. J.* 668, 1221–1231. doi:10.1086/521215

Muller, D., Fleck, B., Dimitoglou, G., Caplins, B. W., Amadigwe, D. E., García Ortiz, J. P., et al. (2009). JHelioviewer: Visualizing Large Sets of Solar Images Using JPEG 2000. *Comput. Sci. Eng.* 11, 38–47. doi:10.1109/MCSE.2009.142

Müller, D., Nicula, B., Felix, S., Verstringe, F., Bourgoignie, B., Csillaghy, A., et al. (2017). JHelioviewer. Time-dependent 3D Visualisation of Solar and Heliospheric Data. *Astron. Astrophys.* 606, A10. doi:10.1051/0004-6361/201730893

O'Kane, J., Green, L., Long, D. M., and Reid, H. (2019). Stealth Coronal Mass Ejections from Active Regions. *Astrophys. J.* 882, 85. doi:10.3847/1538-4357/ab371b

Robbrecht, E., Berghmans, D., and Van der Linden, R. A. M. (2009). Automated LASCO CME Catalog for Solar Cycle 23: Are CMEs Scale Invariant?. *Astrophys. J.* 691, 1222–1234. doi:10.1088/0004-637X/691/2/1222

Schwenn, R. (1996). An Essay on Terminology, Myths and Known Facts: Solar Transient - Flare - CME - Driver Gas - Piston - BDE - Magnetic Cloud - Shock Wave - Geomagnetic Storm. *Astrophys. Space Sci.* 243, 187–193. doi:10.1007/BF00644053

Schwenn, R. (2006). Space Weather: The Solar Perspective. *Living Rev. Solar Phys.* 3, 2. doi:10.12942/lrsp-2006-2

Seaton, D. B., Mierla, M., Berghmans, D., Zhukov, A. N., and Dolla, L. (2011). SWAP-SECCHI Observations of a Mass-Loading Type Solar Eruption. *Astrophys. J. Lett.* 727, L10. doi:10.1088/2041-8205/727/1/L10

Sheeley, N. R., Walters, J. H., Wang, Y. M., and Howard, R. A. (1999). Continuous Tracking of Coronal Outflows: Two Kinds of Coronal Mass Ejections. *J. Geophys. Res.* 104, 24739–24768. doi:10.1029/1999JA900308

Solanki, R., Srivastava, A. K., and Dwivedi, B. N. (2020). CME Productive and Non-productive Recurring Jets Near an Active Region AR11176. *Solar Phys.* 295, 27. doi:10.1007/s11207-020-1594-4

Solanki, R., Srivastava, A. K., Rao, Y. K., and Dwivedi, B. N. (2019). Twin CME Launched by a Blowout Jet Originated from the Eruption of a Quiet-Sun Mini-Filament. *Solar Phys.* 294, 68. doi:10.1007/s11207-019-1453-3

Subramanian, P., Arunbabu, K. P., Vourlidas, A., and Mauriya, A. (2014). Self-Similar Expansion of Solar Coronal Mass Ejections: Implications for Lorentz Self-Force Driving. *Astrophys. J.* 790, 125. doi:10.1088/0004-637x/790/2/125

Subramanian, P., and Dere, K. P. (2001). Source Regions of Coronal Mass Ejections. *Astrophys. J.* 561, 372–395. doi:10.1086/323213

Tousey, R. (1973). "The Solar Corona," in Space Research Conference. Editors M. J. Rycroft and S. K. Runcorn, vol. 2, 713–730.

Vourlidas, A., Carley, E. P., and Vilmer, N. (2020). Radio Observations of Coronal Mass Ejections: Space Weather Aspects. *Front. Astron. Space Sci.* 7, 43. doi:10.3389/fspas.2020.00043

Wang, Y.-M., and Colaninno, R. (2014). Is Solar Cycle 24 Producing More Coronal Mass Ejections Than Cycle 23? *Astrophys. J. Lett.* 784, L27. doi:10.1088/2041-8205/784/2/L27

Webb, D. F., and Howard, T. A. (2012). Coronal Mass Ejections: Observations. *Living Rev. Solar Phys.* 9, 3. doi:10.12942/lrsp-2012-3

Webb, D. F., and Hundhausen, A. J. (1987). Activity Associated with the Solar Origin of Coronal Mass Ejections. *Solar Phys.* 108, 383–401. doi:10.1007/BF00214170

Wuelser, J.-P., Lemen, J. R., Tarbell, T. D., Wolfson, C. J., Cannon, J. C., Carpenter, B. A., et al. (2004). "EUVI: the STEREO-SECCHI Extreme Ultraviolet Imager," in *Telescopes and Instrumentation for Solar Astrophysics*. Editors S. Fineschi and M. A. Gummin (Society of Photo-Optical Instrumentation Engineers (SPIE) Conference Series), vol. 5171, 111–122. doi:10.1117/12.506877

Xu, Y., Liu, C., Jing, J., and Wang, H. (2012). On the Relationship between the Coronal Magnetic Decay Index and Coronal Mass Ejection Speed. *Astrophys. J.* 761, 52. doi:10.1088/0004-637X/761/1/52

Yashiro, S., Akiyama, S., Gopalswamy, N., and Howard, R. A. (2006). Different Power-Law Indices in the Frequency Distributions of Flares with and without Coronal Mass Ejections. *Astrophys. J. Lett.* 650, L143–L146. doi:10.1086/508876

Yashiro, S., Gopalswamy, N., Michalek, G., Cyr, St. O. C., Plunkett, S. P., Rich, N. B., et al. (2004). A Catalog of White Light Coronal Mass Ejections Observed by the SOHO Spacecraft. *J. Geophys. Res. (Space Phys.)* 109, A07105. doi:10.1029/2003JA010282

Yashiro, S., Gopalswamy, N., Michalek, G., and Howard, R. A. (2003). Properties of Narrow Coronal Mass Ejections Observed with LASCO. *Adv. Space Res.* 32, 2631–2635. doi:10.1016/j.asr.2003.03.018

Yashiro, S., Michalek, G., and Gopalswamy, N. (2008). A Comparison of Coronal Mass Ejections Identified by Manual and Automatic Methods. *Ann. Geophys.* 26, 3103–3112. doi:10.5194/angeo-26-3103-2008

Zhang, J., and Dere, K. P. (2006). A Statistical Study of Main and Residual Accelerations of Coronal Mass Ejections. *Astrophys. J.* 649, 1100–1109. doi:10.1086/506903

Zhang, J., Dere, K. P., Howard, R. A., Kundu, M. R., and White, S. M. (2001). On the Temporal Relationship between Coronal Mass Ejections and Flares. *Astrophys. J.* 559, 452–462. doi:10.1086/322405

Zhao, X. H., Feng, X. S., Feng, H. Q., and Li, Z. (2017). Correlation between Angular Widths of CMEs and Characteristics of Their Source Regions. *Astrophys. J.* 849, 79. doi:10.3847/1538-4357/aa8e49

Zuccarello, F. P., Seaton, D. B., Mierla, M., Poedts, S., Rachmeler, L. A., Romano, P., et al. (2014). Observational Evidence of Torus Instability as Trigger Mechanism for Coronal Mass Ejections: The 2011 August 4 Filament Eruption. *Astrophys. J.* 785, 88. doi:10.1088/0004-637X/785/2/88

Conflict of Interest: The authors declare that the research was conducted in the absence of any commercial or financial relationships that could be construed as a potential conflict of interest.

frontiers in Astronomy and Space Sciences

ORIGINAL RESEARCH
published: 13 May 2021
doi: 10.3389/fspas.2021.639986

Drag-Based Model (DBM) Tools for Forecast of Coronal Mass Ejection Arrival Time and Speed

Mateja Dumbović[1], Jaša Čalogović[1], Karmen Martinić[1], Bojan Vršnak[1], Davor Sudar[1], Manuela Temmer[2] and Astrid Veronig[2,3]*

[1] Hvar Observatory, Faculty of Geodesy, University of Zagreb, Zagreb, Croatia, [2] Institute of Physics, University of Graz, Graz, Austria, [3] Kanzelhöhe Observatory for Solar and Environmental Research, University of Graz, Graz, Austria

OPEN ACCESS

Edited by:
Nandita Srivastava, Physical Research Laboratory, India

Reviewed by:
Phillip Hess, United States Naval Research Laboratory, United States
Ramesh Chandra, Kumaun University, India

***Correspondence:**
Mateja Dumbović
mdumbovic@geof.hr

Specialty section:
This article was submitted to Stellar and Solar Physics, a section of the journal Frontiers in Astronomy and Space Sciences

Received: *10 December 2020*
Accepted: *23 March 2021*
Published: *13 May 2021*

Citation:
Dumbović M, Čalogović J, Martinić K, Vršnak B, Sudar D, Temmer M and Veronig A (2021) Drag-Based Model (DBM) Tools for Forecast of Coronal Mass Ejection Arrival Time and Speed. Front. Astron. Space Sci. 8:639986. doi: 10.3389/fspas.2021.639986

Forecasting the arrival time of coronal mass ejections (CMEs) and their associated shocks is one of the key aspects of space weather research. One of the commonly used models is the analytical drag-based model (DBM) for heliospheric propagation of CMEs due to its simplicity and calculation speed. The DBM relies on the observational fact that slow CMEs accelerate whereas fast CMEs decelerate and is based on the concept of magnetohydrodynamic (MHD) drag, which acts to adjust the CME speed to the ambient solar wind. Although physically DBM is applicable only to the CME magnetic structure, it is often used as a proxy for shock arrival. In recent years, the DBM equation has been used in many studies to describe the propagation of CMEs and shocks with different geometries and assumptions. In this study, we provide an overview of the five DBM versions currently available and their respective tools, developed at Hvar Observatory and frequently used by researchers and forecasters (1) basic 1D DBM, a 1D model describing the propagation of a single point (i.e., the apex of the CME) or a concentric arc (where all points propagate identically); (2) advanced 2D self-similar cone DBM, a 2D model which combines basic DBM and cone geometry describing the propagation of the CME leading edge which evolves in a self-similar manner; (3) 2D flattening cone DBM, a 2D model which combines basic DBM and cone geometry describing the propagation of the CME leading edge which does not evolve in a self-similar manner; (4) DBEM, an ensemble version of the 2D flattening cone DBM which uses CME ensembles as an input; and (5) DBEMv3, an ensemble version of the 2D flattening cone DBM which creates CME ensembles based on the input uncertainties. All five versions have been tested and published in recent years and are available online or upon request. We provide an overview of these five tools, as well as of their similarities and differences, and discuss and demonstrate their application.

Keywords: coronal mass ejections, solar wind, interplanetary shocks, magnetohydrodynamical drag, space weather forecast

1. INTRODUCTION

Coronal mass ejections (CMEs) are one of most prominent drivers of space weather in the heliosphere. They are the causes of largest geomagnetic storms (e.g., Zhang et al., 2003) as they may carry enhanced and specifically oriented magnetic fields (see e.g., Bothmer and Schwenn, 1998; Démoulin et al., 2008). Forecasting the arrival time of CMEs and their associated shocks is therefore one of the key aspects of space weather research. Therefore, there is a variety of CME models available in recent times, some focusing only on the arrival time forecast and other, more complex models focusing on the forecast of other CME properties (see e.g., Siscoe and Schwenn, 2006; Zhao and Dryer, 2014; Vourlidas et al., 2019; Zhang, 2021, and references therein).

Propagation of CMEs in the heliosphere with the purpose of obtaining the time of arrival (ToA) and speed of arrival (SoA) of CMEs can be modeled by empirical models (e.g., Gopalswamy et al., 2001; Paouris and Mavromichalaki, 2017), kinematic shock propagation models (e.g., Dryer et al., 2001; Zhao et al., 2016; Takahashi and Shibata, 2017), machine-learning models (e.g., Sudar et al., 2016; Liu et al., 2018), numerical 3D magnetohydrodynamical (MHD) models [e.g., H3DMHD model by Wu et al. (2011), WSA-ENLIL+Cone model by Odstrcil et al. (2004), EUHFORIA model by Pomoell and Poedts (2018), CORHEL model by Mikić et al. (1999), or AWSoM model by van der Holst et al. (2014)], and drag-based models (see below). All CME propagation models need CME input as well as input of the background solar wind characteristics, where both may have large uncertainties. Therefore, it is not surprising that, despite their differences, ToA errors of different propagation models revolve at around 10 h (Riley et al., 2018; Vourlidas et al., 2019).

One of the most popular CME propagation setups used in forecast models in recent times is the drag-based propagation. In this concept, the CME, which is initially under the influence of Lorentz force, gravity, and drag force due to interaction with the ambient medium, at a certain distance from the Sun is influenced dominantly by the drag force (see e.g., Zhang et al., 2006; Temmer, 2016, and references therein). This concept is supported by the observational fact that slow CMEs accelerate whereas fast CMEs decelerate (Sheeley et al., 1999; Gopalswamy et al., 2000; Sachdeva et al., 2015). The drag force can be represented by the aerodynamic drag equation describing the kinetic drag effect in a fluid (Cargill, 2004; Vršnak and Žic, 2007); however, it should be noted that, in the interplanetary (IP) space, i.e., collisionless solar wind environment, the drag is caused primarily by the emission of MHD waves and not particle collisions (Cargill et al., 1996).

Drag-based models (DBMs) typically use the same form of the basic drag equation applied to various geometries representing the CME structure of different dimensionality, e.g., 1D Drag-Based Model (DBM, Vršnak et al., 2013, 2014) and Enhanced DBM (Hess and Zhang, 2014, 2015), 2D Drag-Based Model (Žic et al., 2015), the 2D Ellipse Evolution Model (ElEvo, Möstl et al., 2015) and a version of ElEvo using data from Heliospheric Imagers (ElEvoHi, Rollett et al., 2016), and 3D flux rope models such as ANother Type of Ensemble Arrival Time Results (ANTEATR, Kay and Gopalswamy, 2018) or 3-Dimensional Coronal ROpe Ejection (3DCORE, Möstl et al., 2018). Since DBMs use an analytical equation to describe the time-dependent evolution of the CME, they are computationally efficient and thus widely used in probabilistic/ensemble modeling approaches (e.g., Amerstorfer et al., 2018, 2021; Dumbović et al., 2018; Kay and Gopalswamy, 2018; Napoletano et al., 2018; Kay et al., 2020). The advantage of ensemble modeling is that it gives the probability of arrival, as well as the range of possible arrival times and speeds.

Starting with a basic 1D DBM (Vršnak et al., 2013), five versions of the drag-based model versions have been developed by the Hvar Observatory solar and heliospheric group in close collaboration with the solar and heliospheric group at the University of Graz. These five versions include three different geometries, as discussed in section 2.2, and two different ensemble versions, as discussed in section 2.3. We provide an overview of these five DBM versions and their respective tools in section 2 and demonstrate their application on a real event in section 3.

2. OVERVIEW OF DBM TOOLS

2.1. The Basic Description of the Model

The DBM tools are all based on the equation of motion analogous to the aerodynamic drag:

$$a(t) = -\gamma(v(t) - w)|v(t) - w|\,, \tag{1}$$

where $a(t) = \mathrm{d}^2R(t)/\mathrm{d}t^2$ is the CME acceleration, $v(t) = \mathrm{d}R(t)/\mathrm{d}t$ is the CME speed, $R(t)$ is the heliospheric distance, γ is the drag parameter, which describes the rate of change of CME speed and is assumed to be constant, and w is the solar wind speed, also assumed to be constant. Along with the initial properties of the CME, which can be obtained from the coronagraphic observation, γ and w have to be specified to obtain analytical solutions of Equation (1) for a specific CME, $R(t)$ and $v(t)$, given by Vršnak et al. (2013):

$$\begin{aligned} R(t) &= \frac{S}{\gamma} ln[1 + S\gamma(v_0 - w)t] + wt + R_0 \\ v(t) &= \frac{v_0 - w}{1 + S\gamma(v_0 - w)t} + w\,, \end{aligned} \tag{2}$$

where $v_0 = v(t = 0)$ is the initial CME speed, $R_0 = R(t = 0)$ is the corresponding starting radial distance, and S is a sign function ($S = 1$ for $v_0 > w$, $S = -1$ for $v_0 < w$). These solutions describe the time-dependent part of the drag-based CME propagation and are thus the same in all tools, regardless of their different geometries.

We note that, generally speaking, γ and w are not constant in time. However, it can be shown that, at a sufficient distance from the Sun, γ and w become approximetely constant and may be represented by their asymptotic values, which are approximately equal to the values at 1 AU (see Vršnak and Žic, 2007; Vršnak et al., 2013; Žic et al., 2015; Manchester et al., 2017, for details). Theoretically, the distance at which $\gamma = const.$ and $w = const.$ assumptions should hold is beyond $\approx 15R_\odot$ (Žic et al., 2015). On the other hand, the distance at which the drag force becomes

dominant varies from case to case and is farther away for slower CMEs (Vršnak, 2001; Vršnak et al., 2004; Sachdeva et al., 2015). Therefore, $R_0 \leq 15R_\odot$ might not be an optimal choice for the model. The Lorentz force was found to generally peak between 1.65 and 2.45 $R_\odot$ and becomes negligible for faster CMEs at $3.5 - 4R_\odot$ as well as for slower CMEs at $12 - 50R_\odot$ (Sachdeva et al., 2017). As the optimal value for the starting radial distance, the DBM tools recommendation is $\geq 20R_\odot$, as this assumption was shown to be valid for a number of cases (Vršnak et al., 2010, 2013) and should hold unless the CME is very slow and/or has a prolonged acceleration phase (Vršnak, 2001; Vršnak et al., 2004; Sachdeva et al., 2015, 2017). Nevertheless, it is recommended to always check whether the early CME kinematics indicates that the starting radial distance $\geq 20R_\odot$ is suitable for the observed CME.

2.1.1. Using Empirical *w* and γ Values in DBM

An important DBM issue is how to determine the input for w and γ. There are several options to determine the input for w: (1) using an empirical value determined from statistical analysis; (2) using a solar wind model (e.g., the numerical heliospheric model, an empirical model based on CH observation or persistence model); (3) using the solar-wind speed based on the *in-situ* measurements at 1 AU at the time of the ICME take-off. Using w based on the *in-situ* measurements at the time of the ICME take-off was shown to be the same or even worse than using the empirically obtained values (Vršnak et al., 2013). Statistical analysis has shown that the most appropriate values for w should be in the range $300 - 600\,\mathrm{km\,s^{-1}}$, with $w = 500\,\mathrm{km\,s^{-1}}$ as the optimal value (i.e., applicable to the broadest subset of CMEs Vršnak et al., 2013). However, the optimal empirically derived value is sample-dependent and was found to be lower for a different sample (Vršnak et al., 2014). Therefore, as an optimal empiricallybased value, w is set at$-450\,\mathrm{km\,s^{-1}}$ for all tools. Recent analysis has shown that this value seems optimal even during the conditions of low solar activity (Čalogović et al., submitted to Solar Physics). It should be noted that this value might not be valid if there is an equatorial coronal hole in the vicinity of the CME source region, where one should apply a higher value to take into account CME propagation through the high speed stream. For that purpose, one can use a model of the solar wind speed where empirical solar wind models are especially suitable due to their simplicity and speed. DBM tools available at the European Space Agency (ESA) Space Situational Awareness (SSA) portal can be coupled with the Empirical Solar Wind Forecast tool, which is based on empirical modeling of the high-speed stream (HSS) arrival derived from coronal hole area observations (see Temmer et al., 2007; Vršnak et al., 2007; Rotter et al., 2012; Reiss et al., 2016).

The γ parameter is given by the expression (e.g., Vršnak et al., 2013):

$$\gamma = \frac{c_\mathrm{d} A \rho_\mathrm{w}}{M + M_\mathrm{v}} = \frac{c_\mathrm{d}}{L(\frac{\rho}{\rho_\mathrm{w}} + \frac{1}{2})}, \tag{3}$$

where A is the CME cross-sectional area, ρ_w is the solar-wind density and M is the CME mass, M_v is the so-called virtual mass (i.e., the mass of the material piled-up in front of the CME, L is the CME thickness in the radial direction, ρ is the CME density, and c_d is the dimensionless drag coefficient, which in the DBM tools is taken to be 1 according to Cargill, 2004). Theoretically, it is possible to estimate relative CME mass density and radial size to determine γ based on coronagraphic measurements. However, the errors corresponding to these estimations ($\approx$ 15% for the mass Bein et al., 2013) can yield γ with a very large uncertainty. For a CME that is several times denser than the surrounding corona (e.g., $\rho/\rho_\mathrm{w} \approx 5$) and of the radial size $1 - 10R_\odot$, one finds an approximate range of $\gamma = 0.2 - 2 \cdot 10^{-7}\ \mathrm{km^{-1}}$, which roughly corresponds to the range obtained from statistical analysis (Vršnak et al., 2013). The distribution of the γ obtained from statistical analysis is highly asymmetrical and weighted toward the lower values (Vršnak et al., 2013), where $\gamma = 0.2 \cdot 10^{-7}\ \mathrm{km^{-1}}$ was found as an optimal value in combination with $w = 450\,\mathrm{km\,s^{-1}}$ (Vršnak et al., 2013, 2014). Therefore, this value has been chosen as optimal empirically-based value for DBM tools (customized values are allowed).

In addition, some of the DBM tools offer γ options for slower and faster CMEs. Observationally, the CME peak speed is related to the peak soft X-ray flux (Vršnak et al., 2005; Maričić et al., 2007), and the flare fluence is related to the CME mass (Yashiro and Gopalswamy, 2009; Dissauer et al., 2019). This is interpreted in the context of a feedback relationship between the CME dynamics and the reconnection process in the wake of the CME (Vršnak, 2016). Consequently, we would expect faster CMEs to be more massive and thus expect lower γ for faster CMEs and higher γ for slower CMEs. Additional empirical-based fine-tuning of the γ parameter may be performed by the user according to the relative CME brightness in the coronagraphic images, which is generally related to the CME mass (see e.g., Colaninno and Vourlidas, 2009, and references therein). Massive CMEs are generally observed as brighter objects in the coronagraphic images; therefore, one may use a lower value of γ in the case of very bright CMEs or increase it for very faint CMEs. However, one needs to keep in mind that the observed intensity of a CME (and thus mass calculation) depends on the angle between the line-of-sight of the observer and the plane-of-sight, i.e., the CME direction with respect to the Thomson surface (for details see Colaninno and Vourlidas, 2009; Howard and Tappin, 2009). Finally, fine-tuning of the γ parameter may be performed to account for the pre-conditioning of the interplanetary space due to preceding CME(s). Namely, preceding CME(s) may "deplete" the heliospheric sector before the CME in question, resulting in lower density and thus lower drag forces (Temmer and Nitta, 2015; Temmer et al., 2017; Desai et al., 2020). This effect can be taken into account by using a lower value for the γ parameter (see e.g., Temmer and Nitta, 2015; Dumbović et al., 2019). However, when "customizing" γ, one needs to be careful not to underestimate or overestimate it as this can lead to underestimation or overestimation of the transit time, respectively. It was recently shown by Paouris et al. (2021) that underestimated γ can lead to significant underestimation of the transit time, even if w is underestimated, especially for the fast CMEs.

2.1.2. Running DBM for Shock Propagation

While propagating in the interplanetary space, CMEs may or may not drive shocks; however, if they do, the arrival of the CME magnetic structure (i.e., ejected twisted magnetic structure) is preceded by the shock arrival (for ICME overview see e.g., Zurbuchen and Richardson, 2006; Kilpua et al., 2017). Physically, the DBM equation of motion describes the propagation of the CME magnetic structure and not of the associated shock. However, the comparison of the DBM with the heliospheric model, ENLIL (Odstrcil et al., 2004), in which the CME is initiated as a pressure pulse and thus more suitable to track the shock front, has shown that there is, in general, a good agreement between the two when a lower value of the γ parameter is applied (Vršnak et al., 2014). Moreover, Hess and Zhang (2015) have found that, both the shock front and the CME leading edge, can be modeled in the heliosphere with a drag model, where the CME ejecta front undergoes a more rapid deceleration than the shock front and the propagation of the two fronts is not completely coupled in the heliosphere. Indeed, some drag-based models such as the ElEvo (Möstl et al., 2015) and ElEvoHi (Rollett et al., 2016) standardly follow the shock front. Dumbović et al. (2018) also used a lower γ value ($\gamma = 0.1 \cdot 10^{-7}\ km^{-1}$) to apply the DBM ensemble version to simulate CME shock propagation, whereas Temmer and Nitta (2015) and Guo et al. (2018) have used DBM to model both shock and CME propagation, separately, both using a different input and a lower γ value for the shock propagation. Therefore, we note that the DBM tools can be used to simulate both CME and shock propagation; however, it is important to keep in mind that:(1) the shock propagation is not necessarily coupled to CME propagation; (2) proper CME/shock input is used; and (3) lower γ values should be applied to shock as compared to the CME propagation.

2.2. DBM Tools With Different Geometries

The basic form of the DBM was formulated by Vršnak and Žic (2007) and Vršnak et al. (2010) and analyzed in detail by Vršnak et al. (2013), where the basic 1D DBM tool was first presented. The basic 1D version of DBM is available as an online tool at the Hvar Observatory webpage[1] and relies on solutions given in Equation (2). Since it is a 1D equation, it considers propagation of a single point, i.e., CME apex. The tool is also applicable to determine the propagation of an arbitrary, non-apex point of the CME leading edge, assuming that the CME leading edge evolves self-similarly as a circular arc concentric with the solar surface (i.e., all elements of the ICME front have the same heliocentric distance). As can be seen in **Figures 1**, **2**, this concentric geometry results in a self-similarly evolving CME leading edge. However, since the tool does not consider CME angular extent or its direction, it does not provide information on whether or not this point hits a specific target. The basic assumptions, input, output, and tool specifications are given in the second column of **Table 1**.

The advanced form of the DBM was formulated by Žic et al. (2015), who applied a 2D cone geometry to the basic 1D DBM solutions given in Equation (2). The cone geometry was selected as it is a standard geometry used in heliospheric models, such as ENLIL (Odstrcil et al., 2004) or EUHFORIA (Pomoell and Poedts, 2018), and therefore, their input would be suitable for use in DBM as well. The cone angular dependence is introduced in DBM in the following form:

$$\begin{aligned} R(\alpha) &= R_0 \frac{\cos\alpha + \sqrt{\tan^2\omega - \sin^2\alpha}}{1+\tan\omega} \\ v(\alpha) &= v_0 \frac{\cos\alpha + \sqrt{\tan^2\omega - \sin^2\alpha}}{1+\tan\omega}, \end{aligned} \tag{4}$$

where R_0 and v_0 are distance and speed of the plasma element at the CME apex, ω is the half-width of the cone (i.e., of the CME opening angle), and α is the opening angle corresponding to the plasma element in question. Depending on the applications of the cone-geometry given by Equation (4) to the basic 1D DBM solutions given in Equation (2), two different evolutions of the CME leading edge are possible, namely self-similar cone evolution and the flattening cone evolution.

The self-similar evolution of the cone leading edge is obtained assuming that the CME front does not change its shape, i.e., when the DBM solutions for a plasma element after time t at the angular distance α from the apex at the leading edge is given by:

$$\begin{aligned} R(\alpha,t) &= R_0(t) \frac{\cos\alpha + \sqrt{\tan^2\omega - \sin^2\alpha}}{1+\tan\omega} \\ v(\alpha,t) &= v_0(t) \frac{\cos\alpha + \sqrt{\tan^2\omega - \sin^2\alpha}}{1+\tan\omega}, \end{aligned} \tag{5}$$

where $R_0(t)$ and $v_0(t)$ are given by Equation (2). The self-similar cone leading edge is compared to the concentric geometry as well as the flattening cone leading edge in **Figures 1**, **2**. This has been adopted by the online DBM tool that runs on the Hvar Observatory webpage[2], as well as the Community Coordinated Modeling Centre (CCMC)[3]. Since the tool does implement information on the CME angular extent and its direction, it also provides information of whether or not the CME hits the target.The basic assumptions, input, output, and tool specifications are given in the third column of **Table 1**.

The flattening cone leading edge evolution is obtained by propagating each plasma element of the CME leading edge independently, using the CME 2D cone geometry given by Equation (4) as the initial leading edge. The DBM solutions for a plasma element after time t at the angular distance α from the apex at the leading edge is given by:

$$\begin{aligned} R(\alpha,t) &= \frac{S}{\gamma} ln[1 + S\gamma(v_0(\alpha) - w)t] + wt + R_0(\alpha) \\ v(\alpha,t) &= \frac{v_0(\alpha) - w}{1 + S\gamma(v_0(\alpha) - w)t} + w, \end{aligned} \tag{6}$$

where $R_0(\alpha)$ and $v_0(\alpha)$ are given by Equation (4). The flattening cone leading edge is also shown in **Figures 1**, **2** and similarly as 2D self-similar DBM provides information whether or

[1]http://oh.geof.unizg.hr/DBM/dbm.php.

[2]http://oh.geof.unizg.hr/DBM/dbm.php.

[3]https://ccmc.gsfc.nasa.gov.

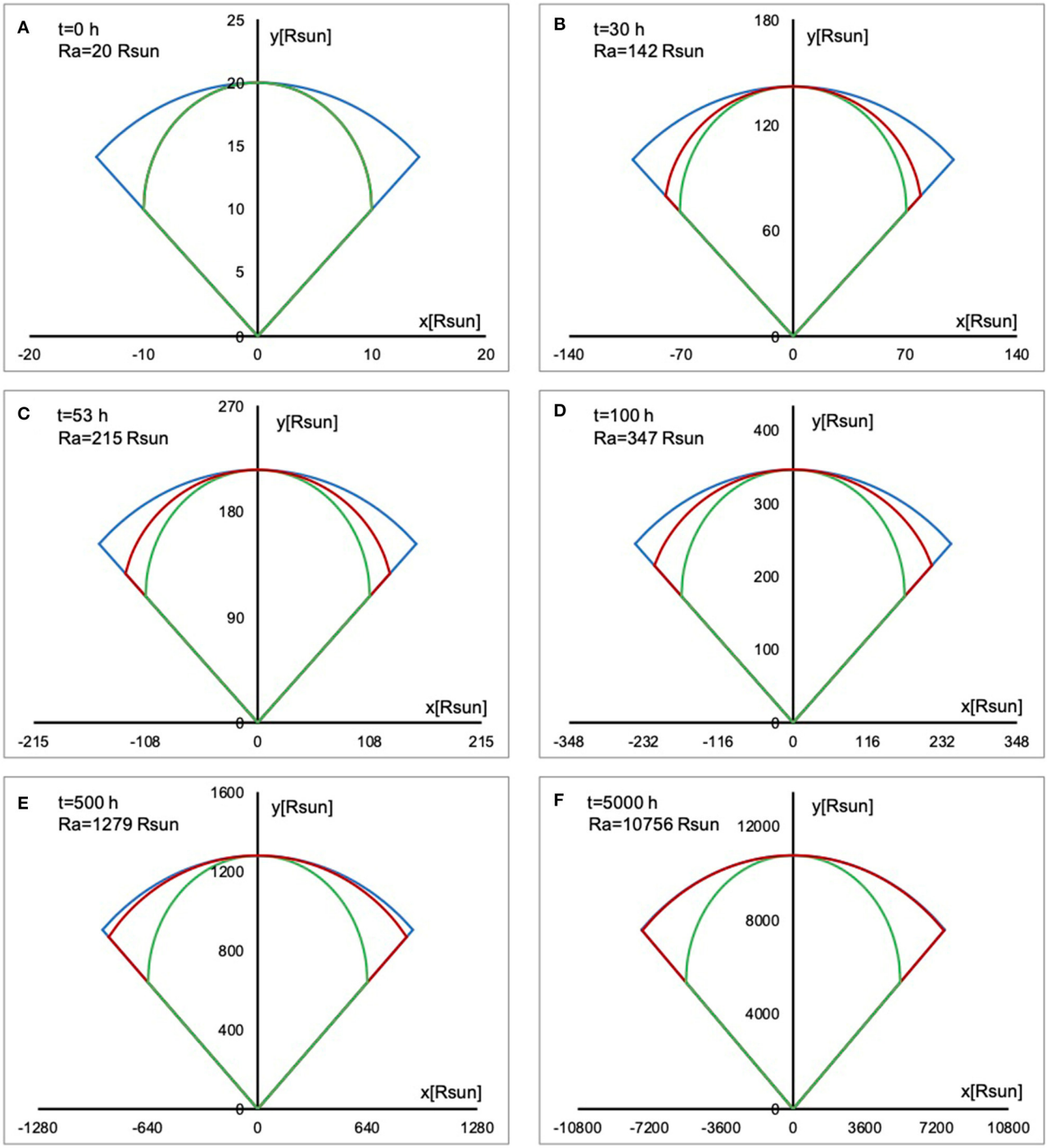

FIGURE 1 | The differences between the fronts at six arbitrarily chosen time-steps for the three DBM tools: basic 1D DBM (the concentric leading edge, blue), advanced 2D DBM with self-similar cone geometry (green), and the advanced 2D DBM with flattening cone geometry (red). The subplots show the position of the leading edge in the XY coordinate system (i.e., the solar equatorial plane). The heliospheric distance of the apex, R_a, is highlighted in each time-step. The following DBM parameters were used to create the plots: initial CME speed of 1,000 $km\,s^{-1}$, initial distance of $20R_{\odot}$, γ of $0.2 \cdot 10^{-7}\,km^{-1}$, and solar wind speed w of $450\,km\,s^{-1}$.

not the CME hits the target. The basic assumptions, input, output, and tool specifications are given in the fourth column of **Table 1**.

To summarize, three different geometries of the CME leading edge (CME front) are considered in DBM tools: concentric arc, self-similarly evolving cone, and flattening cone. The differences

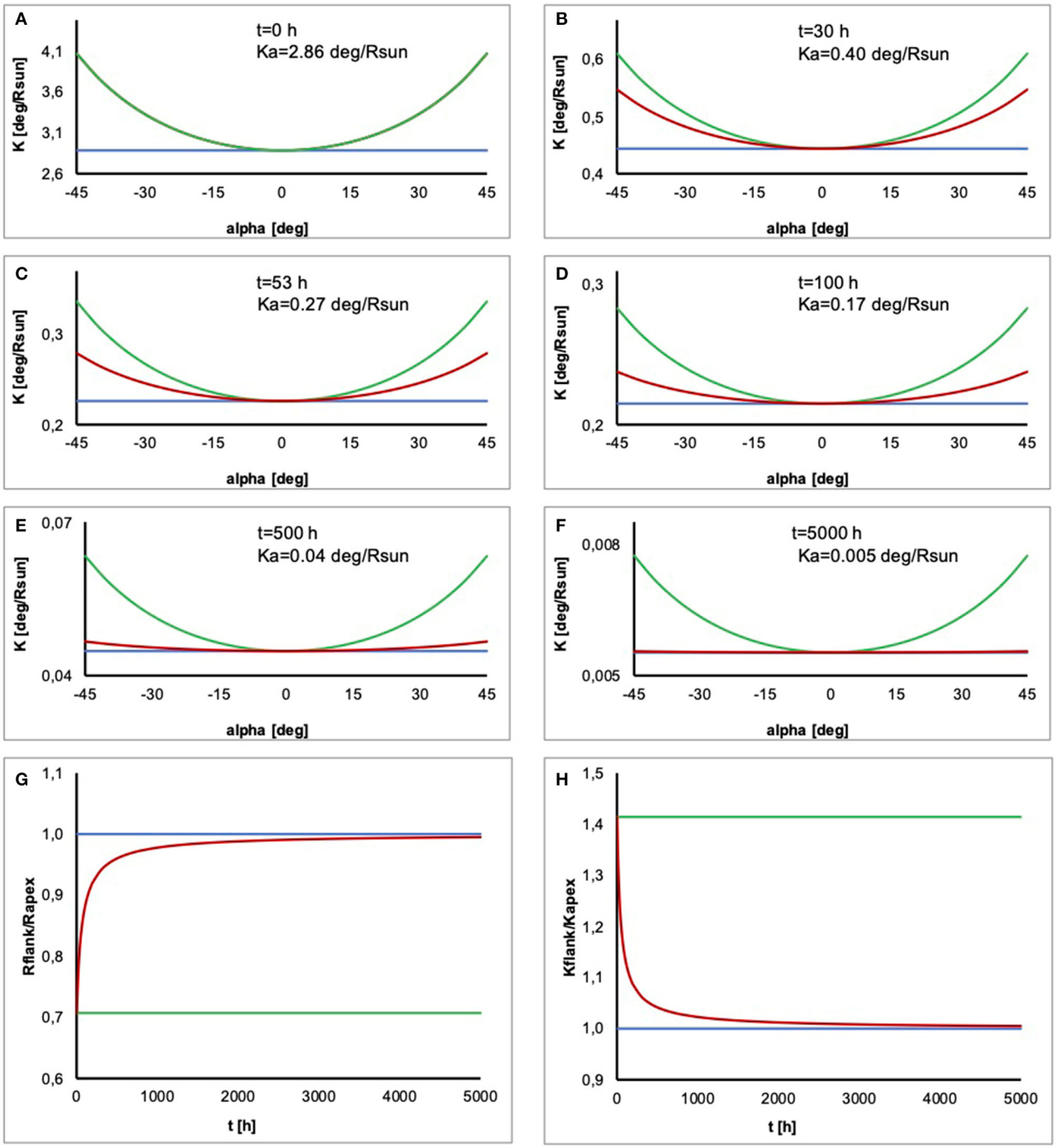

FIGURE 2 | The differences between the curvatures of the fronts at different time-steps for the three DBM tools: basic 1D DBM (the concentric leading edge, blue), advanced 2D DBM with self-similar cone geometry (green), and the advanced 2D DBM with flattening cone geometry (red). The time-steps and DBM parameters correspond to those used in **Figure 1**. The subplots **(A–F)** show how the curvature K along the leading edge behaves in time. The curvature at the apex, K_a, is highlighted in each time-step. The subplot **(G)** shows how the ratio of the flank heliospheric distance and the apex heliospheric distance (R_f/R_a) evolves in time, whereas subplot **(H)** shows how the ratio of the curvature at the flank and at the apex (K_f/K_a) evolves in time.

between the fronts and their evolution for the three tools described above are shown in **Figure 1** for halfwidth $< 90°$ at several arbitrarily chosen time-steps. The x subplots (a–f) show the position of the leading edge in the XY coordinate system for six different time-steps. It can be seen that initially (at $t = 0$) we differentiate only 2 geometries, the concentric arc and the

TABLE 1 | Comparison of DBM tools.

		1D DBM	2D DBM		DBEM	DBEMv3
			self-similar cone	flattening cone		
BASIC ASSUMPTIONS	drag parameter	$\gamma = const$	$\gamma = const$	$\gamma = const$	$\gamma = const$	$\gamma = const$
	solar wind speed	$w = const$	$w = const$	$w = const$	$w = const$	$w = const$
	self-similarity	Y	Y	N	N	N
	2D geometry	concentric circular arc	ice cream cone	ice cream cone	ice cream cone	ice cream cone
INPUT[a]	optimal R_0[$R_\odot$]	$R_0 = 20$	$R_0 = 20$	$R_0 = 20$	$R_0 = 20$	$R_0 = 20$
	CME width input	N	Y	Y	Y	Y
	source position input	N	Y	Y	Y	Y
	GCS input	N	N	N	N	Y
	optimal w[km s^{-1}]	$w = 450$	$w = 450$	$w = 450$	$w = 450$	$w = 450$
	modeled w option[b]	N	N	Y	N	Y
	optimal γ[10^{-7} km^{-1}]	0.2	0.2	0.1 (fast CME)	0.1 (fast CME)	0.1 (fast CME)
				0.2 (normal CME)	0.2 (normal CME)	0.2 (normal CME)
				0.5 (slow CME)	0.5 (slow CME)	0.5 (slow CME)
OUTPUT	CME arrival time	Y	Y	Y	Y	Y
	CME arrival speed	Y	Y	Y	Y	Y
	CME arrival probability	N	N	N	Y	Y
TOOL SPECS	typical runtime	0.5 sec	2 sec	2 sec	$<$ 2 min (average PC)	6 sec
	source	OH[c]	OH, CCMC[d]	ESA SSA[e]	run-on-request[f]	ESA SSA
	reference	(Vršnak et al., 2013)	(Žic et al., 2015)	(Žic et al., 2015)	(Dumbović et al., 2018)	(Čalogović et al., submitted to Solar Physics)

[a] *not including basic CME input which is the same for all tools: CME take-off date & time, CME initial speed.*
[b] *using the ESWF tool, see section2.1.1.*
[c] *http://oh.geof.unizg.hr/DBM/dbm.php.*
[d] *https://ccmc.gsfc.nasa.gov.*
[e] *http://swe.ssa.esa.int.*
[f] *runs are available upon request to mdumbovic@geof.hr.*

cone geometry leading edge. Although the initial shape of the flattening cone leading edge is that of a 2D cone, at $t > 0$, the shape of the leading edge starts to increasingly deviate from the initial cone shape. This is because each plasma element of the leading edge is propagated independently using different initial parameters. A plasma element at the flank will have a lower value of the initial speed than, e.g., a plasma element at the apex and will therefore experience less drag if the CME is faster than the solar wind and more drag if the CME is slower than the solar wind. Since the drag will not act equally on each plasma element across the leading edge, the evolution of the leading edge will not be self-similar. Instead, as can be seen in **Figure 1**, during the evolution, the leading edge will gradually change from the initial cone shape toward a flatter shape.

This can be seen more prominently in **Figure 2**, which shows the time-evolution of the curvature of the CME leading edge with respect to the center of the Sun, calculated as $K = \Delta\Theta/\Delta L$, where $\Delta\Theta = |\Theta_1 - \Theta_2|$ is the angular distance and $\Delta L = \int_{\Theta_1}^{\Theta_2} \sqrt{r^2 + (\mathrm{d}r/\mathrm{d}\Theta)^2}\,\mathrm{d}\Theta$ is the corresponding arc length of the curve in polar coordinates. Note that thus defined K does not correspond to the standard mathematical term curvature, which is defined with respect to the center of the circle and thus remains always constant across the circular arc. Instead, we define quantity K to differ between the concentric arc and self-similar cone in the polar coordinates with the origin at the center of the Sun. We can see that K of the concentric arc is constant across the leading edge, whereas K of the 2D cone at the apex is identical to that of the concentric arc but increases toward the flanks. However, the difference in K between the flank and the apex remains constant in time for a self-similarly evolving cone front, whereas it reduces for the flattening cone front.

The last two subplots of **Figure 2** show the ratio of the flank distance to the apex distance, R_f/R_a, and the ratio of the curvature at the flank and at the apex, K_f/K_a. For self-similarly evolving fronts, R_f/R_a and K_f/K_a are constant and, in the specific case of a concentric leading edge, both equal to 1 (values at the flank are equal to the values at the apex). We see that the apex evolves identically in all three cases. For a self-similarly evolving cone, R_f/R_a and K_f/K_a remain constant. For the flattening cone, R_f/R_a and K_f/K_a are not constant, as the R_f/R_a increases and K_f/K_a decreases in time, both approaching the values for the concentric leading edge. It should be noted, however, that they never actually reach the values for the concentric leading edge. This is because, although the flank experiences different drag than the apex, it is slower than the apex. The difference between R_f and R_a is increasing, converging to a certain value, as the drag eventually adjusts the speed of both the apex and the flank to the ambient solar wind speed. As the distance from the Sun increases, the difference between R_f and R_a becomes very small compared to values of R_f and R_a; therefore, R_f/R_a seems to converge to 1,

although mathematically it will never reach it and the flattening cone will never truly become a concentric arc. It is also important to note that, for a halfwidth of 90°, all three fronts are semi-circles with the origin at the center of the Sun and thus evolve identically, as the concentric arc.

2.3. The Ensemble Versions of the DBM

As noted in section 1, DBMs are computationally efficient and thus widely used in probabilistic/ensemble modeling approaches. Ensemble forecasting takes into account the errors and uncertainties of the input to quantify the resulting uncertainties in the model predictions. The variability of an observational input is introduced by making an ensemble, i.e., sets of CME observations to calculate a distribution of predictions and forecast the confidence in the likelihood of the prediction. This can be achieved in two ways: (1) by taking independently built sets of CME observations (e.g., as provided by different observers) or (2) by creating sets of CME observations (by, e.g., using measurements and error estimations provided by a single observer). These two ensemble options were adopted in the Drag-based ensemble model (DBEM) (Dumbović et al., 2018) and DBEMv3 web tool (Čalogović et al., submitted to Solar Physics), respectively, which both use 2D DBM with flattening cone as a background physical model. The output of both tools is the probability of arrival, which is calculated as the ratio of the number of runs that predict a hit and total number of runs. Based on the runs that predict a hit, distributions of arrival time and speed are generated, where the calculated medians represent the likeliest arrival time and speed, and the uncertainty range is given by 95% confidence interval. Note that initially there was a DBEMv2, which was replaced by a more advanced DBEMv3.

For a single CME, DBEM uses an ensemble of n measurements of the same CME, which may not be mutually related in any way (e.g., it might be obtained by different observers, different methods, or even measurements from different instruments). Each ensemble member has the same weight. Moreover, there is no assumption that the CME measurements of a particular CME, i.e., ensemble member, are independent of each other or that their spread in values follow a certain distribution. The variability of solar wind speed, w, and drag parameter, γ, are taken into account by producing m of their synthetic values. These synthetic values are combined with an ensemble of n CME measurements to give a final ensemble of $n \cdot m^2$ members as an input, which, after $n \cdot m^2$ runs, produces a distribution of $n \cdot m^2$ calculated CME transit times and arrival speeds. The synthetic values for w and γ are produced by assuming that their real measurements follow a normal distribution with a mean value and SD serving as the model input. A cumulative standard normal distribution is then generated, defined on an interval $[0, m-1]$, where m is the number of synthetic measurements, also used as the model input. The m values which correspond to the integer values of the cumulative standard normal distribution are selected as synthetic measurements. This way, for identical distribution and m, the selection always results in an identical set of synthetic values, which include the tips of the distribution tail. Therefore, for small m the distribution of chosen synthetic measurements is too heavily weighed to the tail compared to the normal distribution, and larger m is needed for synthetic measurements to be weighted properly, $m > 15$ (Dumbović et al., 2018). The basic assumptions, input, output, and tool specifications of DBEM are given in the fifth column of **Table 1**.

In DBEMv3, the CME ensemble is not produced by the observer, but the tool. Observational input values and uncertainties are provided for the CME input as well as for w and γ, from which the tool generates m ensemble members. Each ensemble member is produced by randomly picking one value for each input parameter, assuming that it follows a normal distribution with the observational input value as mean and SD derived from uncertainty (uncertainty$= 3\sigma$). Due to this randomness (which cannot be controlled), the ensemble is not likely to be identical each time an identical input is used, which produces small differences in the output of the model for different runs using identical input. However, for large ensembles, $m > 10,000$, the differences of the output are negligible (see documentation of the DBEMv3 at ESA/SSA[4] as well as Čalogović et al., submitted to Solar Physics). The basic assumptions, input, output, and tool specifications of DBEMv3 are given in the last column of **Table 1**.

We note that, in the DBEMv3, the CME input parameters are considered to be independent of each other and therefore, the procedure is somewhat similar to error propagation. In DBEM, the CME parameters within one measurement set are not necessarily independent of each other, CME sets are independent of each other. This is important due to the nature of the model input used, i.e., obtaining CME input from coronagraphic measurements. Coronagraphs only display a projection of a 3D structure. Therefore, in order to derive parameters of a 3D CME, some assumptions need to be made on the CME geometry. These assumptions, as well as their applications can vary from observer-to-observer and result in CME measurement sets where the distribution of single parameter variability may differ substantially from the normal distribution. A single observer, on the other hand, is more likely to provide CME measurements with errors that follow a normal distribution. While a single observer is more likely to bias the mean of the normal distribution of an input parameter and thus introduce errors, we note that, in the near-real-time forecasting, where a quick estimation of the CME input is needed, DBEMv3 is more applicable, since it uses input provided by only one observer/method.

3. RUNNING THE DBM TOOLS: EXAMPLE EVENT

We demonstrate the performance of DBM tools described in section 2 by running all the tools using the same example event. As the example event, we chose a previously studied CME that erupted on April 3, 2010 and hit Earth on April 5, 2010 (e.g., Möstl et al., 2010; Wood et al., 2011; Rodari et al., 2018). This event can be found in the SOHO/LASCO CME catalog [5], where it is listed as a halo with the first appearance in LASCO-C2 on

[4]https://swe.ssa.esa.int.

[5]https://cdaw.gsfc.nasa.gov/CME_list/.

TABLE 2 | CME measurements and the corresponding DBM input and output for the April 3rd 2010 CME for 5 different observers using 3 different methods.

			observer 1 (GCS)	(Rodari et al., 2018) (GCS)	Wood+2017	AFFECTS-GCS	AFFECTS-CAT
INPUT	CME measurements	obs time	04/03 10:54	04/03 11:24	04/03 10:00	04/03 12:08	04/03 12:08
		height [$R_\odot$]	8.1	15.6	7.3	13.6	21.5
		lon [deg]	5	3	3	4	0
		lat [deg]	-26	-28.5	-16	-26	24.6
		tilt [deg]	11	1.7	-80	-1	–
		kappa	0.35	0.3	0.21	0.42	–
		halfangle [deg]	37	24.3	60	16	–
	DBM input	liftoff time	04/03 13:24	04/03 12:19	04/03 12:30	04/03 13:29	04/03 11:47
		v0 [$km\,s^{-1}$]	920	920	960	920	812
		lon [deg]	5	3	3	4	0
		half width [deg]	53	41	19	41	30
ICME		ToA*	04/05 12:00	04/05 12:00	04/05 12:00	04/05 12:00	04/05 12:00
OBSERVATION		SoA** [$km\,s^{-1}$]	640 (790)	640 (790)	640 (790)	640 (790)	640 (790)
		ToA	04/05 17:39	04/05 16:34	04/05 16:45	04/05 17:44	04/05 19:43
OUTPUT	basic	ToA $O-C$ [h]***	5.7	4.6	4.7	5.7	7.7
	1D DBM	SoA [$km\,s^{-1}$]	620	620	620	620	597
		SoA $O-C$ [$km\,s^{-1}$]	20 (170)	20 (170)	20 (170)	20 (170)	43 (193)
		ToA	04/05 17:51	04/05 16:41	04/05 17:01	04/05 17:56	04/05 19:43
	2D self-similar	ToA $O-C$ [h]	5.9	4.7	5.0	5.9	7.7
	cone DBM	SoA [$km\,s^{-1}$]	618	619	617	618	597
		SoA $O-C$ [$km\,s^{-1}$]	22 (172)	21 (171)	23 (173)	22 (172)	43 (193)
		ToA	04/05 17:47	04/05 16:36	04/05 15:37	04/05 17:46	04/05 19:37
	2D flattening	ToA $O-C$ [h]	5.8	4.6	3.6	5.8	7.6
	cone DBM	SoA [$km\,s^{-1}$]	619	620	627	620	598
		SoA $O-C$ [$km\,s^{-1}$]	21 (171)	20 (170)	13 (163)	20 (170)	42 (192)
		arrival probability [%]	100%	100%	91.5%	100%	99.2%
		ToA	04/05 18:06	04/05 17:14	04/05 18:04	04/05 18:28	04/05 20:51
		ToA CI [h]****	+5.6/-5.1	+5.1/-5.8	+5.6/-6.9	+5.3/-5.8	+5.9/-7.7
	DBEMv3	ToA $O-C$ [h]	6.1	5.2	6.1	6.5	8.9
		SoA [$km\,s^{-1}$]	618	616	612	615	591
		SoA CI [$km\,s^{-1}$]	+64/-52	+70/-63	+54/-65	+51/-68	+51/-59
		SoA $O-C$ [$km\,s^{-1}$]	22 (172)	24 (174)	28 (178)	25 (175)	49 (199)
		arrival probability [%]			100%		
		ToA			04/05 16:44		
	DBEM	ToA CI [h]			+5.8/-5.4		
		ToA $O-C$ [h]			4.7		
		SoA [$km\,s^{-1}$]			617		
		SoA CI [$km\,s^{-1}$]			+97/-65		
		SoA $O-C$ [$km\,s^{-1}$]			23 (173)		

ToA=time of arrival.

***SoA=speed of arrival; observed mean ICME speed (peak speed is given in brackets).*

****O-C=absolute value of the difference between observed and calculated values.*

*****CI=confidence interval (95%).*

April 3, 2010 at 10:33 UT. In order to reconstruct the flux rope structure of the CME, we used the graduated cylindrical shell (GCS) model (Thernisien et al., 2006, 2009; Thernisien, 2011).

Graduated cylindrical shell is a geometrical model used to describe the flux rope structure of the CME to study its three-dimensional morphology, position, and kinematics. The flux rope is approximated with a self-similarly expanding hollow croissant originating from the center of the Sun, where the legs are conical and cross-section circular and the front is pseudo-circular. The croissant is fully defined by six GCS parameters: (1) longitude, (2) latitude, (3) height corresponding to the apex of the croissant, (4) the tilt of the croissant axis to the solar equatorial plane, (5) the croissant half-angle measured between the apex and the central axis of its leg, and (6) the "aspect ratio" (i.e., the sine of the angle defining the "thickness" of the croissant leg). The GCS parameters were obtained by fitting its 2D projections to

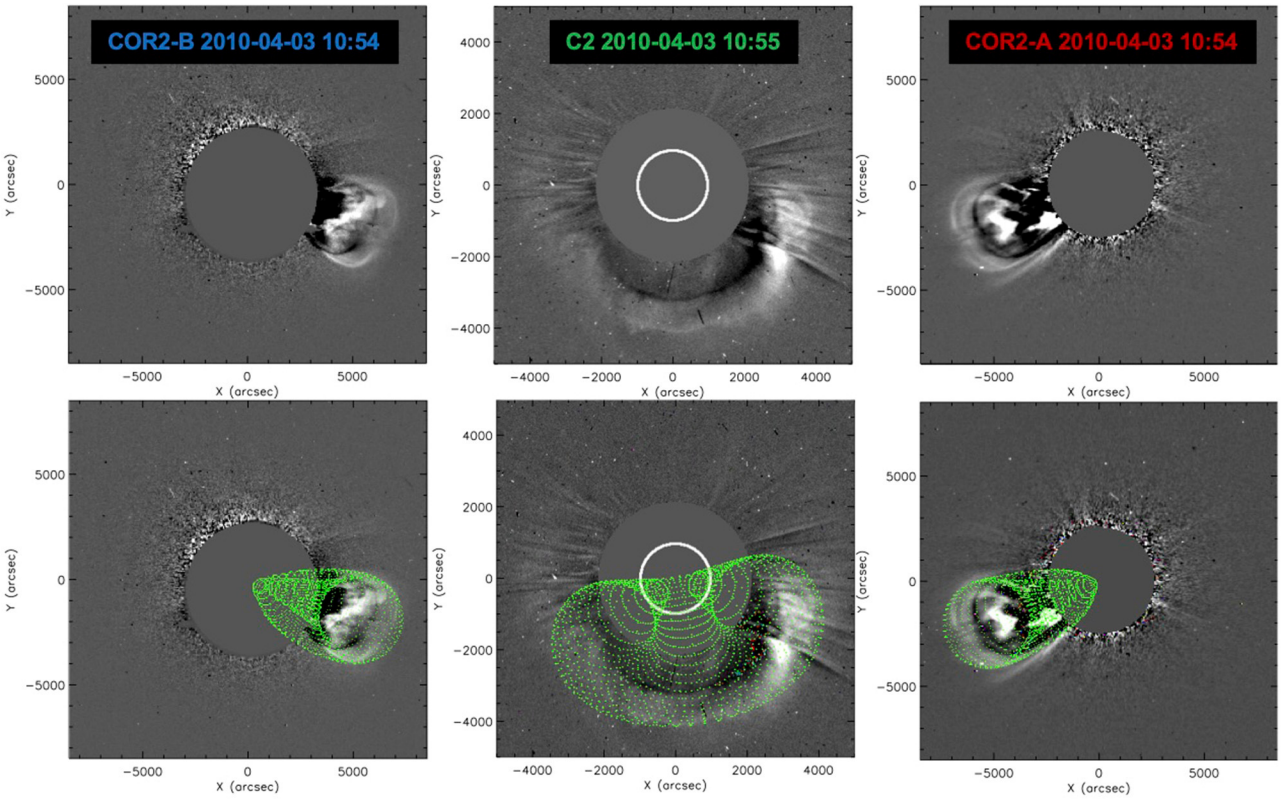

FIGURE 3 | The CME of April 3, 2010, observed in running difference images in STEREO/COR2 and SOHO/LASCO coronagraphs and the GCS reconstruction of the CME (green mesh).

the respective coronagraphic images, where at least two different vantage points are needed to constrain the geometry (for further details on GCS, see Thernisien et al., 2006, 2009; Thernisien, 2011).

To perform the reconstruction, we used coronagraph images taken by SECCHI/COR2 (Howard et al., 2008) onboard STEREO-A and B, as well as LASCO-C3 (Brueckner et al., 1995) onboard SOHO spacecraft on April 3, 2010 at 10:54 UT. Furthermore, the GCS reconstruction was done in four consecutive time-steps, following the CME leading edge while changing only the height parameter, i.e., assuming self-similar expansion. Based on these four measurements, a CME linear speed of 920 km s^{-1} was estimated. The GCS best fit parameters and linear speed are given in the second column of **Table 2** and the reconstruction is shown in **Figure 3**.

Based on the results of the GCS reconstruction, we derived the input for the DBM tools (see column 4 in **Table 2**). Using the CME linear speed, we extrapolated the CME apex to $R_0 = 20R_\odot$ assuming constant speed, which is taken as the initial CME speed, v_0. The CME angular extent (i.e., CME angular half width, λ) in the solar equatorial plane was estimated based on the GCS-derived tilt, as well as the GCS face-on and edge-on widths, as described by Dumbović et al. (2019) and adopted in DBEMv3. The projection of the GCS reconstructed CME in the solar equatorial plane is shown in **Figure 4**, as well as the calculated CME angular extent and the positions of the spacecraft. We can see that, due to relatively small tilt and large half-angle, the angular extent of the CME is quite large. In addition, we can see that the direction of the apex (given by the longitude of the CME source region, ϕ_{CME}) is very close to the Sun-Earth line. We next ran DBM tools for the input obtained from the GCS reconstruction (bottom rows of **Table 2**). In order to run DBEM, for which different sets of CME measurements are needed as input, we utilized measurements from previous studies on this event (Wood et al., 2017; Rodari et al., 2018) and from online catalogs provided by the Advanced Forecast For Ensuring Communications Through Space (AFFECTS)[6] catalogs. We used CME input provided by the AFFECTS-GCS database and the AFFECTS-CAT database, where the latter is obtained with the CME Analysis Tool (CAT) modeling technique developed by Millward et al. (2013). We also ran all other DBM tools for these various CME inputs [as given in columns (5-8)]. The DBM input for these CME measurements was derived the same way as for the GCS reconstruction performed here. The CME speed for AFFECTS-GCS catalog was assumed to be the same as that in other two GCS reconstructions. CME measurements provided by five different observers using three different measurement

[6]http://www.affects-fp7.eu/home/.

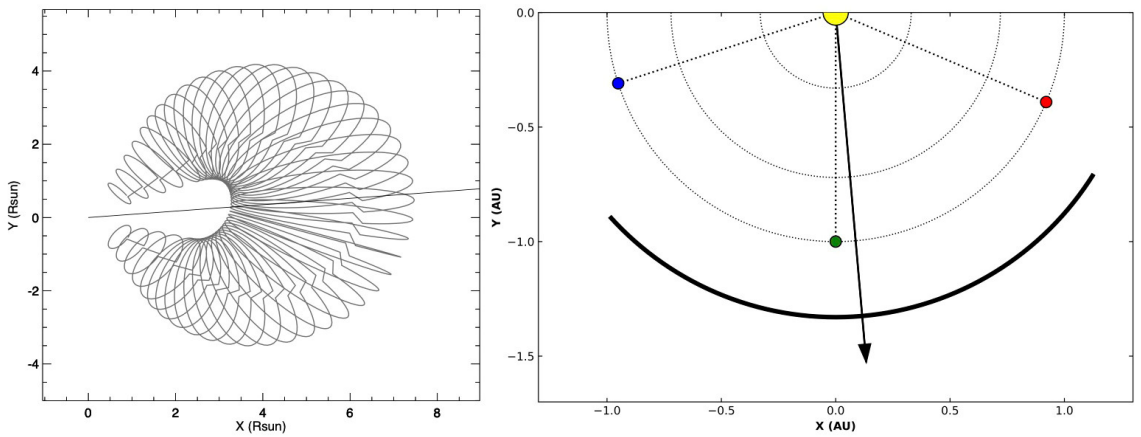

FIGURE 4 | (Left) The projection of the GCS croissant of the on April 3, 2010, CME in the XY plane of the Heliocentric Earth Equatorial (HEEQ) coordinate system (i.e., plane of the solar equator). The direction of the apex is marked by a solid black line. **(Right)** The direction and angular extent of the April 3rd 2010 CME (black arrow and black arc, respectively) and the positions of the three spacecrafts in the HEEQ coordinate system at the CME liftoff time: STEREO-B (blue), SOHO (green), and STEREO-A (red).

methods, as well as the corresponding five DBM inputs the are given in **Table 2**.

The inner boundary, the drag parameter, the solar wind speed, and target distance are the same for each of the five DBM inputs and are $R_0 = 20\,R_\odot$, $\gamma = 0.2 \cdot 10^{-7}$ km^{-1}, $w = 450$ km s^{-1}, and $R_{\rm target} = 1$ au, respectively. In DBEM, 15 synthetic values of γ and w were used within the uncertainty ranges $\pm 0.1 \cdot 10^{-7}$ km^{-1} and ± 50 km s^{-1}, respectively. In DBEMv3, default uncertainty ranges of the tool were used: ± 30 min, $\pm 0.1 \cdot 10^{-7}$ km^{-1}, ± 50 km s^{-1}, ± 200 km s^{-1}, $\pm 15^\circ$, and $\pm 30\circ$ for lift-off time, γ, w, v_0, λ, and $\phi_{\rm CME}$, respectively, and 10,000 runs were performed to obtain the results. It can be seen in **Table 2** that the difference in the output of different DBM tools is very similar for all DBM tools that use a single input set (basic 1D DBM, 2D self-similar DBM, 2D flattening cone DBM, and DBEMv3). This is because the direction of the apex is very close to the direction of the target, i.e., the CME is likely to hit the target close to the apex, where all geometries evolve similarly. This is also the reason for very high arrival probability, given that the most of the input sets consider a relatively wide CME. The input set derived based on measurements given by Wood et al. (2017) in their study is the only one yielding a DBEMv3 arrival probability < 100%, because the estimated CME half width is low compared to the uncertainty. The difference of the output is more prominent between different input sets than between different tools, with the exception of DBEM, which shows slightly different results compared to other tools. This is because, unlike other DBM tools, DBEM does not use a single input but takes into account the variability of different input sets.

The last two rows of **Table 2** show the observational results for the CME arrival, which are based on the CME-ICME association made by Möstl et al. (2010) and the arrival time and speed values provided by the ICME catalog of Richardson and Cane (2010)[7], where the mean ICME speed is taken as the arrival speed and the ICME start (not the start of the disturbance) is taken as the arrival time. Measured ICME peak speed is also given for reference. We can see that, all DBM outputs in **Table 2** overestimate arrival time by a couple of hours and underestimate arrival speed by couple of tens of km s^{-1}, which indicated that the drag was overestimated. Indeed, as this is a fast event, 2D flattening cone DBM, DBEM, and DBEMv3 would suggest the $\gamma = 0.1 \cdot 10^{-7}$ km^{-1} option. Running DBEMv3 and DBEM with $\gamma = 0.1 \cdot 10^{-7}$ km^{-1} and keeping other input identical, as given in **Table 2** yield arrival times 2010-04-05 13:20 and 2010-04-05 11:50 UT, respectively, i.e., very close to the observed arrival time. The DBEMv3 and DBEM outputs, for arrival speed are 705 km s^{-1} for both, which is closer to the observed ICME peak speed instead of the ICME mean speed.

4. DISCUSSION AND CONCLUSION

The basic DBM equations (Equations 1, 2) describe CME propagation in a simple, physics-based and analytical way. Therefore, even when CME geometry is included (2D DBM) and in the ensemble mode, the model runs very quickly (**Table 1**). With the development of different tools and their performance analysis, optimized DBM parameters (e.g., initial distance, solar wind speed, and drag parameter) have been established, which are offered as default parameters in the DBM tools (**Table 1**). This makes the tools very easy to use, even for the unexperienced users. On the other hand, the tools allow customized input for more experienced users (as described in section 2.1.1). Therefore, DBM tools are simple to use and computationally efficient, which is their main advantage, compared to numerical MHD models.

DBM tools offer three different geometries, which identically describe the propagation of the CME apex, but differ in the description of the CME flanks, and might therefore differ in the applicability. For instance, both 2D DBM tools assume initial

[7]http://www.srl.caltech.edu/ACE/ASC/DATA/level3/icmetable2.htm.

cone geometry; however, one propagates it in a self-similar manner, whereas the other does not. Therefore, it is reasonable to assume that 2D self-similar DBM might be more suitable for CMEs with (near) the self-similar expansion. This might be the case with slower CMEs, which show more symmetric *in situ* profiles (Masías-Meza et al., 2016). Since they propagate with speeds closer to the solar wind speed, they experience less drag. On the other hand, 2D flattening cone DBM might be more suitable for very fast CMEs, which show quite asymmetric *in situ* profiles (Masías-Meza et al., 2016), indicating non-self similar expansion. They propagate with speeds much larger than the solar wind speed and thus experience more drag. The non-self similar vs. self-similar evolution might become even more important for considerations of 3D geometries. It is important to note that 2D flattening cone DBM does not consider change of the front in a manner that the flanks catch-up or overtake the apex. It is a purely geometrical effect, a change from a highly-curved cone geometry toward a less-curved concentric-arc-like geometry, and is not related to, e.g., non-homogeneous drag or internal forces that might cause the "pancaking effect" (e.g., Cargill et al., 1994). The cone geometry is also suitable to describe the propagation of a CME driven shock, which is typically faster and stronger at the nose compared to flanks (e.g., Neugebauer, 2013); thus, the flanks are "delayed" with respect to the nose. On the other hand, for a freely propagating shock, assuming it propagates in a homogeneous medium, a concentric arc geometry might be more suitable. As demonstrated on an example event, for CME propagation near the apex, all geometries and, therefore, all DBM tools show similar results (provided that the CME input is the same, see **Table 2**).

The ensemble options of the DBM provide a more comprehensive prediction compared to the other three tools, as they additionally calculate arrival probability and confidence interval of the arrival time and speed. In addition, although they rely on a large number of DBM runs ($> 1,000$), they are still computationally inexpensive (**Table 1**). Therefore, they are quite useful from the aspect of space weather forecast and its evaluation. Since there is a difference in the implementation of the CME input in DBEM and DBEMv3, their applicability may also differ. The DBEMv3 tool is much faster and only needs input from one observer; thus, it is easy to use in near-real time forecasts. On the other hand, DBEM may use various CME input sets, provided by different observers, different methods, or even different instruments, and may thus be more suitable for evaluation purposes.

To summarize, this study provides an overview of the assumptions, applications, and performance of the five DBM tools developed at Hvar Observatory. It is important to note that, although these tools were developed sequentially and therefore each more recent tool contains improvements compared to the older version, the older versions still have their applicability.

DATA AVAILABILITY STATEMENT

The original contributions presented in the study are included in the article/supplementary material, further inquiries can be directed to the corresponding author/s.

AUTHOR CONTRIBUTIONS

MD, MT and JC contributed to the initial conception of the paper. MD, with the help of KM, wrote the main draft and prepared figures, having discussion on analysis with other co-authors. All of the authors have read the paper and approved its final version.

ACKNOWLEDGMENTS

MD acknowledges support by the Croatian Science Foundation under the project IP-2020-02-9893 (ICOHOSS) and International Space Science Institute (ISSI) team Understanding Our Capabilities in Observing and Modeling Coronal Mass Ejections, led by C. Verbeke and M. Mierla. JC, BV, and DS acknowledge support by the Croatian Science Foundation under the project 7549 (MSOC). KM acknowledges support by the Croatian Science Foundation in the scope of the Young Researchers Career Development Project Training New Doctoral Students. This research has received financial support from the European Union's Horizon 2020 research and innovation program under grant agreement no. 824135 (SOLARNET).

REFERENCES

Amerstorfer, T., Hinterreiter, J., Reiss, M. A., Möstl, C., Davies, J. A., Bailey, R. L., et al. (2021). Evaluation of CME arrival prediction using ensemble modeling based on heliospheric imaging observations. *Space Weather*. 19:e02553. doi: 10.1029/2020SW002553

Amerstorfer, T., Möstl, C., Hess, P., Temmer, M., Mays, M. L., Reiss, M. A., et al. (2018). Ensemble prediction of a Halo coronal mass ejection using heliospheric imagers. *Space Weather* 16, 784–801. doi: 10.1029/2017SW001786

Bein, B. M., Temmer, M., Vourlidas, A., Veronig, A. M., and Utz, D. (2013). The height evolution of the "True" coronal mass ejection mass derived from STEREO COR1 and COR2 observations. *Astrophys. J.* 768:31. doi: 10.1088/0004-637X/768/1/31

Bothmer, V., and Schwenn, R. (1998). The structure and origin of magnetic clouds in the solar wind. *Ann. Geophys.* 16, 1–24. doi: 10.1007/s00585-997-0001-x

Brueckner, G. E., Howard, R. A., Koomen, M. J., Korendyke, C. M., Michels, D. J., Moses, J. D., et al. (1995). The large angle spectroscopic coronagraph (LASCO). *Solar Phys.* 162, 357–402.

Cargill, P. J. (2004). On the aerodynamic drag force acting on interplanetary coronal mass ejections. *Solar Phys.* 221, 135–149. doi: 10.1023/B:SOLA.0000033366.10725.a2

Cargill, P. J., Chen, J., Spicer, D. S., and Zalesak, S. T. (1994). "The deformation of flux tubes in the solar wind with applications to the structure of magnetic clouds and CMEs," in *Solar Dynamic Phenomena and Solar Wind Consequences, the Third SOHO Workshop*, Vol. 373, ed J. J. Hunt (Estes Park, CO: ESA Special Publication), 291.

Cargill, P. J., Chen, J., Spicer, D. S., and Zalesak, S. T. (1996). Magnetohydrodynamic simulations of the motion of magnetic flux tubes through a magnetized plasma. *J. Geophys. Res.* 101, 4855–4870. doi: 10.1029/95JA03769

Colaninno, R. C., and Vourlidas, A. (2009). First determination of the true mass of coronal mass ejections: a novel approach to using the Two STEREO viewpoints. *Astrophys. J.* 698, 852–858. doi: 10.1088/0004-637X/698/1/852

Démoulin, P., Nakwacki, M. S., Dasso, S., and Mandrini, C. H. (2008). Expected *in situ* velocities from a hierarchical model for expanding interplanetary coronal mass ejections. *Solar Phys.* 250, 347–374. doi: 10.1007/s11207-008-9221-9

Desai, R. T., Zhang, H., Davies, E. E., Stawarz, J. E., Mico-Gomez, J., and Iváñez-Ballesteros, P. (2020). Three-dimensional simulations of solar wind preconditioning and the 23 July 2012 interplanetary coronal mass ejection. *Solar Phys.* 295:130. doi: 10.1007/s11207-020-01700-5

Dissauer, K., Veronig, A. M., Temmer, M., and Podladchikova, T. (2019). Statistics of coronal dimmings associated with coronal mass ejections. II. Relationship between coronal dimmings and their associated CMEs. *Astrophys. J.* 874:123. doi: 10.3847/1538-4357/ab0962

Dryer, M., Fry, C. D., Sun, W., Deehr, C., Smith, Z., Akasofu, S.-I., et al. (2001). Prediction in real time of the 2000 july 14 heliospheric shock wave and its companions during the 'Bastille' Epoch*. *Solar Phys.* 204, 265–284. doi: 10.1023/A:1014200719867

Dumbović, M., Čalogović, J., Vršnak, B., Temmer, M., Mays, M. L., Veronig, A., et al. (2018). The drag-based ensemble model (DBEM) for coronal mass ejection propagation. *Astrophys. J.* 854:180. doi: 10.3847/1538-4357/aaaa66

Dumbović, M., Guo, J., Temmer, M., Mays, M. L., Veronig, A., Heinemann, S. G., et al. (2019). Unusual plasma and particle signatures at mars and STEREO-A related to CME–CME interaction. *Astrophys. J.* 880:18. doi: 10.3847/1538-4357/ab27ca

Gopalswamy, N., Lara, A., Lepping, R. P., Kaiser, M. L., Berdichevsky, D., and St. Cyr, O. C. (2000). Interplanetary acceleration of coronal mass ejections. *Geophys. Res. Lett.* 27, 145–148. doi: 10.1029/1999GL003639

Gopalswamy, N., Lara, A., Yashiro, S., Kaiser, M. L., and Howard, R. A. (2001). Predicting the 1-AU arrival times of coronal mass ejections. *J. Geophys. Res.* 106, 29207–29218. doi: 10.1029/2001JA000177

Guo, J., Dumbović, M., Wimmer-Schweingruber, R. F., Temmer, M., Lohf, H., Wang, Y., et al. (2018). Modeling the evolution and propagation of 10 september 2017 CMEs and SEPs arriving at mars constrained by remote sensing and *in situ* measurement. *Space Weather* 16, 1156–1169. doi: 10.1029/2018SW001973

Hess, P., and Zhang, J. (2014). Stereoscopic study of the kinematic evolution of a coronal mass ejection and its driven shock from the sun to the earth and the prediction of their arrival times. *Astrophys. J.* 792:49. doi: 10.1088/0004-637X/792/1/49

Hess, P., and Zhang, J. (2015). Predicting CME ejecta and sheath front arrival at L1 with a data-constrained physical model. *Astrophys. J.* 812:144. doi: 10.1088/0004-637X/812/2/144

Howard, R. A., Moses, J. D., Vourlidas, A., Newmark, J. S., Socker, D. G., Plunkett, S. P., et al. (2008). Sun earth connection coronal and heliospheric investigation (SECCHI). *Space Sci. Rev.* 136, 67–115. doi: 10.1007/s11214-008-9341-4

Howard, T. A., and Tappin, S. J. (2009). Interplanetary coronal mass ejections observed in the heliosphere: 1. Review of theory. *Space Sci. Rev.* 147, 31–54. doi: 10.1007/s11214-009-9542-5

Kay, C., and Gopalswamy, N. (2018). The effects of uncertainty in initial CME input parameters on deflection, rotation, B_z, and arrival time predictions. *J. Geophys. Res.* 123, 7220–7240. doi: 10.1029/2018JA025780

Kay, C., Mays, M. L., and Verbeke, C. (2020). Identifying critical input parameters for improving drag-based CME arrival time predictions. *Space Weather* 18:e02382. doi: 10.1029/2019SW002382

Kilpua, E., Koskinen, H. E. J., and Pulkkinen, T. I. (2017). Coronal mass ejections and their sheath regions in interplanetary space. *Liv. Rev. Solar Phys.* 14:5. doi: 10.1007/s41116-017-0009-6

Liu, J., Ye, Y., Shen, C., Wang, Y., and Erdélyi, R. (2018). A new tool for CME arrival time prediction using machine learning algorithms: CAT-PUMA. *Astrophys. J.* 855:109. doi: 10.3847/1538-4357/aaae69

Manchester, W., Kilpua, E. K. J., Liu, Y. D., Lugaz, N., Riley, P., Török, T., et al. (2017). The physical processes of CME/ICME evolution. *Space Sci. Rev.* 212, 1159–1219. doi: 10.1007/s11214-017-0394-0

Maričić, D., Vršnak, B., Stanger, A. L., Veronig, A. M., Temmer, M., and Roša, D. (2007). Acceleration phase of coronal mass ejections: II. Synchronization of the energy release in the associated flare. *Solar Phys.* 241, 99–112. doi: 10.1007/s11207-007-0291-x

Masías-Meza, J. J., Dasso, S., Démoulin, P., Rodriguez, L., and Janvier, M. (2016). Superposed epoch study of ICME sub-structures near Earth and their effects on Galactic cosmic rays. *Astron. Astrophys.* 592:A118. doi: 10.1051/0004-6361/201628571

Mikić, Z., Linker, J. A., Schnack, D. D., Lionello, R., and Tarditi, A. (1999). Magnetohydrodynamic modeling of the global solar corona. *Phys. Plasmas* 6, 2217–2224. doi: 10.1063/1.873474

Millward, G., Biesecker, D., Pizzo, V., and de Koning, C. A. (2013). An operational software tool for the analysis of coronagraph images: determining CME parameters for input into the WSA-Enlil heliospheric model. *Space Weather* 11, 57–68. doi: 10.1002/swe.20024

Möstl, C., Amerstorfer, T., Palmerio, E., Isavnin, A., Farrugia, C. J., Lowder, C., et al. (2018). Forward modeling of coronal mass ejection flux ropes in the inner heliosphere with 3DCORE. *Space Weather* 16, 216–229. doi: 10.1002/2017SW001735

Möstl, C., Rollett, T., Frahm, R. A., Liu, Y. D., Long, D. M., Colaninno, R. C., et al. (2015). Strong coronal channelling and interplanetary evolution of a solar storm up to Earth and Mars. *Nat. Commun.* 6:7135. doi: 10.1038/ncomms8135

Möstl, C., Temmer, M., Rollett, T., Farrugia, C. J., Liu, Y., Veronig, A. M., et al. (2010). STEREO and Wind observations of a fast ICME flank triggering a prolonged geomagnetic storm on 5-7 April 2010. *Geophys. Res. Lett.* 37:L24103. doi: 10.1029/2010GL045175

Napoletano, G., Forte, R., Moro, D. D., Pietropaolo, E., Giovannelli, L., and Berrilli, F. (2018). A probabilistic approach to the drag-based model. *J. Space Weather Space Clim.* 8:A11. doi: 10.1051/swsc/2018003

Neugebauer, M. (2013). Propagating shocks. *Space Sci. Rev.* 176, 125–132. doi: 10.1007/s11214-010-9707-2

Odstrcil, D., Riley, P., and Zhao, X. P. (2004). Numerical simulation of the 12 May 1997 interplanetary CME event. *J. Geophys. Res.* 109:A02116. doi: 10.1029/2003JA010135

Paouris, E., Čalogović, J., Dumbović, M., Mays, M. L., Vourlidas, A., Papaioannou, A., et al. (2021). Propagating conditions and the time of ICME arrival: a comparison of the effective acceleration model with ENLIL and DBEM models. *Solar Phys.* 296:12. doi: 10.1007/s11207-020-01747-4

Paouris, E., and Mavromichalaki, H. (2017). Effective acceleration model for the arrival time of interplanetary shocks driven by coronal mass ejections. *Solar Phys.* 292:180. doi: 10.1007/s11207-017-1212-2

Pomoell, J., and Poedts, S. (2018). EUHFORIA: European heliospheric forecasting information asset. *J. Space Weather Space Clim.* 8:A35. doi: 10.1051/swsc/2018020

Reiss, M. A., Temmer, M., Veronig, A. M., Nikolic, L., Vennerstrom, S., Schöngassner, F., et al. (2016). Verification of high-speed solar wind stream forecasts using operational solar wind models. *Space Weather* 14, 495–510. doi: 10.1002/2016SW001390

Richardson, I. G., and Cane, H. V. (2010). Near-earth interplanetary coronal mass ejections during solar cycle 23 (1996 - 2009): catalog and summary of properties. *Solar Phys.* 264, 189–237. doi: 10.1007/s11207-010-9568-6

Riley, P., Mays, M. L., Andries, J., Amerstorfer, T., Biesecker, D., Delouille, V., et al. (2018). Forecasting the arrival time of coronal mass ejections: analysis of the CCMC CME scoreboard. *Space Weather* 16, 1245–1260. doi: 10.1029/2018SW001962

Rodari, M., Dumbović, M., Temmer, M., Holzknecht, L., and Veronig, A. (2018). 3D reconstruction and interplanetary expansion of the 2010 April 3rd CME. *Central Eur. Astrophys. Bull.* 42:11.

Rollett, T., Möstl, C., Isavnin, A., Davies, J. A., Kubicka, M., Amerstorfer, U. V., et al. (2016). ElEvoHI: a novel CME prediction tool for heliospheric imaging combining an elliptical front with drag-based model fitting. *Astrophys. J.* 824:131. doi: 10.3847/0004-637X/824/2/131

Rotter, T., Veronig, A. M., Temmer, M., and Vršnak, B. (2012). Relation between coronal hole areas on the sun and the solar wind parameters at 1 AU. *Solar Phys.* 281, 793–813. doi: 10.1007/s11207-012-0101-y

Sachdeva, N., Subramanian, P., Colaninno, R., and Vourlidas, A. (2015). CME propagation: where does aerodynamic drag 'Take Over'? *Astrophys. J.* 809:158. doi: 10.1088/0004-637X/809/2/158

Sachdeva, N., Subramanian, P., Vourlidas, A., and Bothmer, V. (2017). CME dynamics using STEREO and LASCO observations: the relative importance of lorentz forces and solar wind drag. *Solar Phys.* 292:118. doi: 10.1007/s11207-017-1137-9

Sheeley, N. R., Walters, J. H., Wang, Y.-M., and Howard, R. A. (1999). Continuous tracking of coronal outflows: two kinds of coronal mass ejections. *J. Geophys. Res.* 104, 24739–24768. doi: 10.1029/1999JA900308

Siscoe, G., and Schwenn, R. (2006). CME disturbance forecasting. *Space Sci. Rev.* 123, 453–470. doi: 10.1007/978-0-387-45088-9_17

Sudar, D., Vršnak, B., and Dumbović, M. (2016). Predicting coronal mass ejections transit times to Earth with neural network. *Mon. Not. R. Astron. Soc.* 456, 1542–1548. doi: 10.1093/mnras/stv2782

Takahashi, T., and Shibata, K. (2017). Sheath-accumulating propagation of interplanetary coronal mass ejection. *Astrophys. J. Lett.* 837:L17. doi: 10.3847/2041-8213/aa624c

Temmer, M. (2016). Kinematical properties of coronal mass ejections. *Astron. Nachr.* 337:1010. doi: 10.1002/asna.201612425

Temmer, M., and Nitta, N. V. (2015). Interplanetary propagation behavior of the fast coronal mass ejection on 23 July 2012. *Solar Phys.* 290, 919–932. doi: 10.1007/s11207-014-0642-3

Temmer, M., Reiss, M. A., Nikolic, L., Hofmeister, S. J., and Veronig, A. M. (2017). Preconditioning of interplanetary space due to transient CME disturbances. *Astrophys. J.* 835:141. doi: 10.3847/1538-4357/835/2/141

Temmer, M., Vršnak, B., and Veronig, A. M. (2007). Periodic appearance of coronal holes and the related variation of solar wind parameters. *Solar Phys.* 241, 371–383. doi: 10.1007/s11207-007-0336-1

Thernisien, A. (2011). Implementation of the graduated cylindrical shell model for the three-dimensional reconstruction of coronal mass ejections. *Astrophys. J. Suppl.* 194:33. doi: 10.1088/0067-0049/194/2/33

Thernisien, A., Vourlidas, A., and Howard, R. A. (2009). Forward modeling of coronal mass ejections using STEREO/SECCHI data. *Solar Phys.* 256, 111–130. doi: 10.1007/s11207-009-9346-5

Thernisien, A. F. R., Howard, R. A., and Vourlidas, A. (2006). Modeling of flux rope coronal mass ejections. *Astrophys. J.* 652, 763–773. doi: 10.1086/508254

van der Holst, B., Sokolov, I. V., Meng, X., Jin, M., Manchester, W. B., I., Tóth, G., et al. (2014). Alfvén Wave Solar Model (AWSoM): coronal heating. *Astrophys. J.* 782:81. doi: 10.1088/0004-637X/782/2/81

Vourlidas, A., Patsourakos, S., and Savani, N. P. (2019). Predicting the geoeffective properties of coronal mass ejections: current status, open issues and path forward. *Philos. Trans. R. Soc. Lond. Ser. A* 377:20180096. doi: 10.1098/rsta.2018.0096

Vršnak, B. (2001). Dynamics of solar coronal eruptions. *J. Geophys. Res.* 106, 25249–25260. doi: 10.1029/2000JA004007

Vršnak, B. (2016). Solar eruptions: the CME-flare relationship. *Astron. Nachr.* 337:1002. doi: 10.1002/asna.201612424

Vršnak, B., Ruždjak, D., Sudar, D., and Gopalswamy, N. (2004). Kinematics of coronal mass ejections between 2 and 30 solar radii. What can be learned about forces governing the eruption? *Astron. Astrophys.* 423, 717–728. doi: 10.1051/0004-6361:20047169

Vršnak, B., Sudar, D., and Ruždjak, D. (2005). The CME-flare relationship: are there really two types of CMEs? *Astron. Astrophys.* 435, 1149–1157. doi: 10.1051/0004-6361:20042166

Vršnak, B., Temmer, M., and Veronig, A. M. (2007). Coronal holes and solar wind high-speed streams: I. Forecasting the solar wind parameters. *Solar Phys.* 240, 315–330. doi: 10.1007/s11207-007-0285-8

Vršnak, B., Temmer, M., Žic, T., Taktakishvili, A., Dumbović, M., Möstl, C., et al. (2014). Heliospheric propagation of coronal mass ejections: comparison of numerical WSA-ENLIL+Cone model and analytical drag-based model. *Astrophys. J. Suppl.* 213:21. doi: 10.1088/0067-0049/213/2/21

Vršnak, B., and Žic, T. (2007). Transit times of interplanetary coronal mass ejections and the solar wind speed. *Astron. Astrophys.* 472, 937–943. doi: 10.1051/0004-6361:20077499

Vršnak, B., Žic, T., Falkenberg, T. V., Möstl, C., Vennerstrom, S., and Vrbanec, D. (2010). The role of aerodynamic drag in propagation of interplanetary coronal mass ejections. *Astron. Astrophys.* 512:A43. doi: 10.1051/0004-6361/200913482

Vršnak, B., Žic, T., Vrbanec, D., Temmer, M., Rollett, T., Möstl, C., et al. (2013). Propagation of interplanetary coronal mass ejections: The drag-based model. *Solar Phys.* 285, 295–315. doi: 10.1007/s11207-012-0035-4

Wood, B. E., Wu, C.-C., Lepping, R. P., Nieves-Chinchilla, T., Howard, R. A., Linton, M. G., et al. (2017). A STEREO survey of magnetic cloud coronal mass ejections observed at earth in 2008-2012. *Astrophys. J. Suppl.* 229:29. doi: 10.3847/1538-4365/229/2/29

Wood, B. E., Wu, C. C., Howard, R. A., Socker, D. G., and Rouillard, A. P. (2011). Empirical reconstruction and numerical modeling of the first geoeffective coronal mass ejection of solar cycle 24. *Astrophys. J.* 729:70. doi: 10.1088/0004-637X/729/1/70

Wu, C.-C., Dryer, M., Wu, S. T., Wood, B. E., Fry, C. D., Liou, K., et al. (2011). Global three-dimensional simulation of the interplanetary evolution of the observed geoeffective coronal mass ejection during the epoch 1-4 August 2010. *J. Geophys. Res.* 116:A12103. doi: 10.1029/2011JA016947

Yashiro, S., and Gopalswamy, N. (2009). "Statistical relationship between solar flares and coronal mass ejections," in *Universal Heliophysical Processes*, Vol. 257, eds N. Gopalswamy and D. F. Webb (Ioannina), 233–243.

Zhang, J., Dere, K. P., Howard, R. A., and Bothmer, V. (2003). Identification of solar sources of major geomagnetic storms between 1996 and 2000. *Astrophys. J.* 582, 520–533. doi: 10.1086/344611

Zhang, J., Temmer, M., Gopalswamy, N., Malandraki, O., Nitta, N. V., Patsourakos, S., et al. (2021). Earth-affecting solar transients: a review of progresses in solar cycle 24. *Progr. Earth Planet. Sci.* (In press).

Zhang, T. L., Baumjohann, W., Delva, M., Auster, H. U., Balogh, A., Russell, C. T., et al. (2006). Magnetic field investigation of the Venus plasma environment: Expected new results from Venus Express. *Planet. Space Sci.* 54, 1336–1343. doi: 10.1016/j.pss.2006.04.018

Zhao, X., and Dryer, M. (2014). Current status of cme/shock arrival time prediction. *Space Weather* 12, 448–469. doi: 10.1002/2014SW001060

Zhao, X., Liu, Y. D., Inhester, B., Feng, X., Wiegelmann, T., and Lu, L. (2016). Comparison of CME/shock propagation models with heliospheric imaging and *in situ* observations. *Astrophys. J.* 830:48. doi: 10.3847/0004-637X/830/1/48

Žic, T., Vršnak, B., and Temmer, M. (2015). Heliospheric propagation of coronal mass ejections: drag-based model fitting. *Astrophys. J. Suppl.* 218:32. doi: 10.1088/0067-0049/218/2/32

Zurbuchen, T. H., and Richardson, I. G. (2006). *In-situ* solar wind and magnetic field signatures of interplanetary coronal mass ejections. *Space Sci. Rev.* 123, 31–43. doi: 10.1007/978-0-387-45088-9_3

Conflict of Interest: The authors declare that the research was conducted in the absence of any commercial or financial relationships that could be construed as a potential conflict of interest.

frontiers in Astronomy and Space Sciences

ORIGINAL RESEARCH
published: 20 May 2021
doi: 10.3389/fspas.2021.672203

Geoeffectiveness Prediction of CMEs

Diana Besliu-Ionescu[1,2]* *and Marilena Mierla*[3,2]

[1]Astronomical Institute of the Romanian Academy, Bucharest, Romania, [2]Institute of Geodynamics of the Romanian Academy, Bucharest, Romania, [3]Royal Observatory of Belgium, Brussels, Belgium

Coronal mass ejections (CMEs), the most important pieces of the puzzle that drive space weather, are continuously studied for their geomagnetic impact. We present here an update of a logistic regression method model, that attempts to forecast if a CME will arrive at the Earth and it will be associated with a geomagnetic storm defined by a minimum Dst value smaller than −30 nT. The model is run for a selection of CMEs listed in the LASCO catalogue during the solar cycle 24. It is trained on three fourths of these events and validated for the remaining one fourth. Based on five CME properties (the speed at 20 solar radii, the angular width, the acceleration, the measured position angle and the source position – binary variable) the model successfully predicted 98% of the events from the training set, and 98% of the events from the validation one.

Keywords: CMEs, ICMEs, geomagnetic storm, logistic regression, geoeffectiveness

OPEN ACCESS

Edited by:
Xueshang Feng,
National Space Science Center (CAS), China

Reviewed by:
Abhishek Kumar Srivastava,
Indian Institute of Technology (BHU), India
Chenglong Shen,
University of Science and Technology of China, China

***Correspondence:**
Diana Besliu-Ionescu
diana.ionescu@astro.ro

Specialty section:
This article was submitted to Stellar and Solar Physics, a section of the journal Frontiers in Astronomy and Space Sciences

Received: *25 February 2021*
Accepted: *30 April 2021*
Published: *20 May 2021*

Citation:
Besliu-Ionescu D and Mierla M (2021) Geoeffectiveness Prediction of CMEs. Front. Astron. Space Sci. 8:672203. doi: 10.3389/fspas.2021.672203

1 INTRODUCTION

Forecasting if a coronal mass ejection (CME) is geoeffective (i.e., capable of causing a geomagnetic disturbance) is a subject of increasing interest during the last decade, because of the high impact these eruptive events may have on the technological system in orbit or on Earth. Each model must take into consideration some approximation and, thus, no model can currently predict with a 100% accuracy the impact of a CME.

1.1 Geoeffectiveness of CMEs

It is known that the CMEs reaching Earth's magnetosphere can produce large perturbations in the geomagnetic field known as geomagnetic storms. The first indication of a geomagnetic storm is shown by a decrease of the Dst index, with storms being classified as small if $-50\ \text{nT} < \text{Dst} \leqslant -30\ \text{nT}$, moderate ($-50\ \text{nT} \geqslant \text{Dst} > -100\ \text{nT}$), and intense ($\text{Dst} \leqslant -100\ \text{nT}$) (Gonzalez et al., 1994).

The geoeffective CMEs predominantly originate from sources near the central meridian, mostly from the western hemisphere (Srivastava and Venkatakrishnan, 2004; Zhang et al., 2007). The most geoeffective tend to be the energetic frontside halo CMEs, which are associated with strong soft X-ray flares (Gopalswamy et al., 2007).

The geoeffectiveness of the CME will also depend on its particular evolution, which is related to both internal CME properties (kinematic, geometric and magnetic), and (external) solar wind plasma properties (see e.g., the review by Manchester et al., 2017).

It was shown that interacting CMEs in the heliosphere amplify the geomagnetic response (Scolini et al., 2020). This amplification could be due to shock compression inside interplanetary CMEs (ICMEs) (see e.g., Shen et al., 2018; Xu et al., 2019), due to the generation of high energy protons (see e.g., Joshi et al., 2013) or due to the heights above the photosphere at which the shocks are formed (see e.g., Gopalswamy et al., 2013).

1.2 Solar Cycle Dependence

Correlations between CMEs, ICMEs and the sunspot number have been intensively studied (Gopalswamy et al., 2010; Webb and Howard, 2012; Lamy et al., 2019) to conclude that the CME rate usually follows the solar activity indices (Möstl et al., 2020). Chi et al. (2016) confirmed that the yearly ICME rate follows the sunspot number. This implies that during maximum of solar activity more CMEs arrive at Earth compared with the minimum solar activity period.

Comparing the last two solar cycles, the 23rd one has been more geoeffective than the 24th one (Bhatt and Chandra, 2020). Solar cycle 24 was characterized by low flare activity and the main contribution to geoeffective events was made by CMEs (Bruevich and Yakunina, 2020).

The present study covers the solar cycle 24 and it takes into consideration the possibility that there is a model simple enough, based only on CME parameters derived close to the Sun, which could predict that a CME will reach the Earth and it will produce a geomagnetic storm.

The model is based on an updated logistic regression method (Srivastava, 2005; Besliu-Ionescu et al., 2019), that attempts to forecast if a CME will arrive at the Earth and if it will trigger a geomagnetic storm. The model is run for a selection of CMEs listed in the LASCO catalogue (Yashiro et al., 2004) from January 2008 to May 2020.

The model takes into consideration the full-chain of events CMEs-ICMEs-Geomagnetic Storms and outputs the probability of a CME being geoeffective or not.

The paper is structured as follows: **Section 2** presents the method used in this study, **Section 3** describes the results of the non-linear logistic regression model, **Section 4** discusses the main findings of this study and proposes future research.

2 NONLINEAR LOGISTIC REGRESSION

2.1 Data Selection

In order to select our events we looked in the LASCO CME catalogue (https://cdaw.gsfc.nasa.gov/CME_list/) in the period between January 2008 and May 2020.

In this period there were approximately 17,000 CMEs detected. We excluded CMEs catalogued with "poor events" and "very poor events," which amounted to more than 12,500 CMEs, i.e., about 73% of the total CMEs observed by LASCO in the studied period. The classification of events is linked to the quality index (0–5) for the tracking feature (leading edge) of each CME: very poor, poor, fair, typical, good, and excellent. Very poor event (quality index 0) means a CME with an ill-defined leading edge and poor event (quality index 1) is a CME where the leading edge is not clear and sharp enough to be accurately tracked in different frames (see e.g., Yashiro et al., 2004). The poor events were excluded in order to have a consistent list where one can measure with accuracy different characteristics of the CMEs (speed, angular width, etc.). This selection criteria left us with a database of 4,576 CMEs.

We further excluded the CMEs that have an angular width smaller than 60°, leaving us with 2,794 CMEs to study. This second selection criteria is justified since, in order for a CME to arrive at the Earth and to produce a geomagnetic storm it should have a large angular extent (e.g., Schwenn, 2006; Zhang et al., 2007).

In general, full halo (apparent angular width of 360°) and partial halo (apparent angular width larger than 120°) CMEs in LASCO images are considered as potential candidates to impact the Earth (if their source region is on the Earth-facing solar disk). A normal CME, seen above the limb with an angular width of around 60°, will appear as a halo CME or partial halo CME when oriented along the Sun-Earth-line (both: towards to or away from Earth) or some 40° off that line, respectively (e.g., Schwenn, 2006).

However, it was also demonstrated that narrow CMEs (AW $\leqslant$ 20°) can arrive at Earth and exhibit clear *in-situ* signatures (e.g., Kilpua et al., 2014). Still, none of these narrow CMEs that arrived at Earth were detected by LASCO. Many studies consider eruptions below 10° angular width as being jets and not CMEs (e.g., Paraschiv et al., 2010) (review of Raouafi et al., 2016, etc.). The averaged angular width of the CMEs wider than 30° is around 60° (e.g., the review of Webb and Howard, 2012) which also contributed to our selection criteria. We decided to re-include two CMEs that were poor events, but have reached the interplanetary space, such as listed by the ICME catalogue (Richardson and Cane, 2010). Thus, the database for the current study has 2,796 events.

The association of our events with the interplanetary disturbances was extracted from the ICME Catalogue (Richardson and Cane, 2010) which is available online at http://www.srl.caltech.edu/ACE/ASC/DATA/level3/icmetable2.htm. There where 49 CMEs that have reached the Earth during the selected period. CME-ICME association method, described by Cane and Richardson (2003), is based on studying the proton temperature from the solar wind for periods of abnormally low values. Then the ratio of the observed *vs.* the expected proton temperature is evaluated and the magnetic observations are added. An ICME interval could be inferred from reduced fluctuations and some degree of organization in the magnetic field and will be bounded by distinct magnetic field discontinuities which may be accompanied by abrupt changes in plasma parameters (Cane and Richardson, 2003).

Out of these 49 ICMEs, 16 did not produce any geomagnetic disturbances (i.e., Dst_{min} was larger than −30 nT), four were associated with minor geomagnetic storms (Dst_{min} between −30 and −50 nT) and 29 were followed by moderate or intense geomagnetic storms ($Dst_{min} \leqslant -50$ nT).

The Dst_{min} is the minimum value of the Dst index recorded during the geomagnetic storm marking the end of its main phase, value which is used when cataloging the intensity of the storm.

The location of the CME on the solar disk was derived by checking each event individually. We looked for signatures like dimmings, waves, eruptive prominences. We looked at the combined EUV (SOHO/EIT or SDO/AIA) and white-light (LASCO) movies as given in the catalogue. If nothing was seen in running difference images, we checked EUV normal movies (for e.g., sdoa193_c2rdf.html in Java Movie) to better see the dimmings and the waves. For dimmings we also checked the Solar Demon catalogue (Kraaikamp and Verbeeck, 2015): http://solardemon.oma.be/science/dimmings.php?days=0&dimming_threshold=0&dimming_location=1&science=1.

For erupting prominences we checked the AIA prominence catalogue (Yashiro et al., 2020): https://cdaw.gsfc.nasa.gov/CME_list/autope/.

2.2 Method

Predictive models are used in almost every scientific field. Given a set of independent variables, the output of such a model will compute the probability that the dependant variable will have a certain behavior when the combination of the independent variables is the "right-one."

The logistic regression is a class of regression that needs an independent variable or a set of independent variables to predict a dependent one. Therefore, besides the five independent variables (CME speed at 20 solar radii, its angular width, measured position angle, the acceleration and a binary variable for position), the model needs a dependent one. For this we have chosen a binary variable defined by 0 if the Dst_{min} value was > -30 nT (i.e., no geomagnetic storm detected), and 1 for $\mathrm{Dst}_{min} \leqslant -30$ nT (i.e., a storm was identified), identical to the binary one used by Besliu-Ionescu et al. (2019).

The solar wind sometimes completes accelerating before 20 solar radii (Nakagawa et al., 2006). Thus, the speed at 20 solar radii better represents the state of the CME after escaping the solar corona.

The model used in this study is a modified version of Srivastava (2005) and has been applied in Besliu-Ionescu et al. (2019) in a modified version.

The equation used in the model is:

$$\Pi_i = \frac{1}{1 + e^{(-Z_i)}} \tag{1}$$

where Z_i is

$$Z_i = b_0 + \sum_{j=1}^{5} b_j \times x_j \tag{2}$$

Π represents the probability of the occurrence of a geomagnetic storm given the ith observation of the CME. Z_i is a linear function of the observations estimated as a natural logarithm of the odds of the occurrence of the geomagnetic storm (Srivastava, 2005). x_i represents the CME observations (CME speed at 20 solar radii, CME angular width, measured position angle, acceleration and a binary variable for its position).

The initial Srivastava (2005) model used a database of 55 geoeffective events that were defined as full chains CME–ICME–geomagnetic storms (intense and super intense). They used a set of seven independent variables describing the CME: its width, speed, its association with flare and its location; and the interplanetary conditions: the magnetic field intensity, the southern component of the interplanetary magnetic field and the ram pressure. The goal of the model was to predict the occurrence of a geomagnetic storm according to the properties of the selected events, used as independent variables, by defining a binary dependant variable with 0, for intense geomagnetic storms, and 1, for super-intense ones. The dataset was divided in training (46 events) and validation (9) sets and the obtained success rates for that model were 85 and 77.7% for the training, respectively, validation sets.

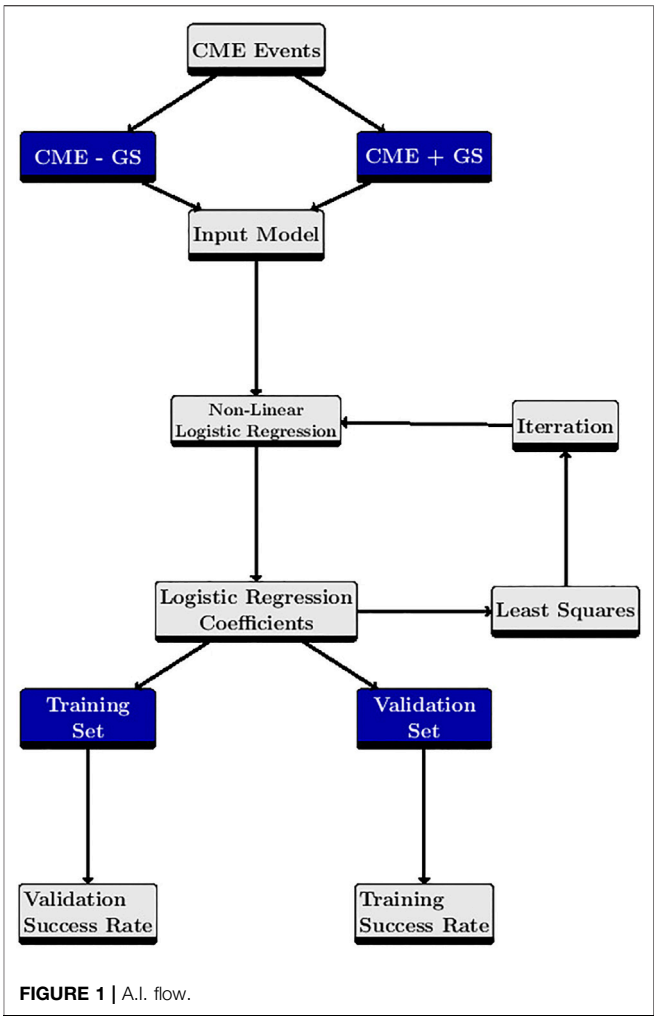

FIGURE 1 | A.I. flow.

Besliu-Ionescu et al. (2019) had a slightly different approach than Srivastava (2005) as they used only CME solar parameters and excluded any ICMEs measurements. The parameters (independent variables in the model) used by Besliu-Ionescu et al. (2019) were the measured position angle of the CME, its angular width, linear speed, the acceleration, the latitude and longitude of its source, the association with a flare (binary variable to be 1 for the events where there was a flare associated with the CME, and 0 otherwise), the flare importance index (Maris et al., 2002), the magnetic active region type (a scaled value between 0 and 1 as a function of the magnetic classification of the active region) and the orientation of the neutral line (a number describing the direction of the neutral line – NS, EW, NW-SW and NE-SW). The computed proportions of correctness (PC), the ratio of total number of correct forecasts and the total number of forecasts, were over 0.95.

In this study we use a similar approach to Besliu-Ionescu et al. (2019), that we applied to a different set of independent variables.

The software used was selected from the IMSL package of the Interactive Data Language (IDL). IMSL_nonlinregress is a function that fits a nonlinear regression model using least squares. All the details about its programming notes, usage

TABLE 1 | The resulting logistic regression coefficients following the non-linear logistic regression model for normalized values (first row) and for standardized values (second row).

Indenpendent variable/coefficient	V_{20R}	AW_{CME}	MPA_{CME}	Acc_{CME}	Pos_{CME}	b_0
Regression coefficient	−1.8616	34.4414	−0.3007	21.4110	9.1932	−44.7622
Regression coefficient *ST	−0.1706	8.3054	−0.0862	0.8432	9.2338	−31.9990

and output can be found at https://www.l3harrisgeospatial.com/docs/IMSL_NONLINREGRESS.html.

Figure 1 represents a schematic chart for the method flow as described above.

2.3 Selection of Independent Variables

We studied all the properties listed in the LASCO catalogue linear speed, second order speed at final height, second order speed at 20 solar radii, the central and measured position angle, the angular width, the acceleration, the mass and energy of the CME.

We eliminated variables that correlated amongst them. The full correlation tables of all CME parameters can be found in Besliu-Ionescu et al. (2019). We selected parameters with small correlation coefficients such that the non-linear logistic regression is correctly applied. We decided to exclude the linear speed as there is supporting evidence (Verma et al., 2013) that the correlation between the linear speed of the CME and the Dst index is weak. There were two classes of variables that were correlated: the three types of CME velocities (V_{lin}, V_{20R} and V_{2f}) and the two angles–measured and central position angles (MPA and CPA). We chose one per each class. The speed at 20 solar radii better represents the state of the CME after escaping the solar corona. Then, we eliminated the mass and energy of the CME because of the large uncertainties due to poor measurements.

Hence, in this study the new set of independent variables consisted of: the speed of the CME at 20 solar radii, its angular width, measured position angle, acceleration and the location of the source region. The location bin variable was set to be 0 if the source was on the backside of the Sun, and 1 if the source was on the frontside, disregarding its exact latitude and longitude. Thus our dataset of 2,796 CMES consists of 1,647 frontside CMEs and 1,149 backside ones.

The measurements that were not binary variables defined (speed at 20 solar radii, measured position angle and angular width) were normalized to unity in order to minimize the possible numerical errors or discrepancies due to the variable ranges.

We also used a set of standardized data computed by removing the mean and dividing by the standard deviation (e.g., Gelman, 2008) (denoted by *ST in **Table 1**).

3 RESULTS

The output after running the non-linear logistic regression model are the six coefficients, $b_0 \ldots b_5$ (see **Eqs 2–4**) which are also displayed in **Table1**.

$$Z_i = -44.7622 - 1.8616 \times V_{20R} + 34.4414 \times AW_{CME} - 0.3007 \times MPA_{CME} + 9.1932 \times POS_{CME} \quad (3)$$

$$Z_i(*ST) = 31.9990 - 0.1706 \times V_{20R} + 8.3054 \times AW_{CME} - 0.0862 \times MPA_{CME} + 9.2338 \times POS_{CME} \quad (4)$$

Choosing standardized input data puts all predictors on a common scale (Gelman, 2008) allowing us to compare the resulting logistic regression coefficients. The classification of coefficients as response given by predictors between the two methods of preparing the data is very similar. The difference between them consists in the order of the first three predictors–the source position, the acceleration and the angular width.

Choosing the normalization method of data preparation suggest that the CME angular width is the most important predictor, while choosing the standardization method, the most important one is the CME source position.

The other predictors have the same importance in both methods. The residual sum of squares for both methods has the same value.

The presented set of independent variables was selected because it had the smallest residual sum of squares value. The residual sum of squares was calculated by IDL and stored into the SSE variable.

Other sets that we have tried were: [$Vlin_{CME}$, CPA_{CME}, AW_{CME}, Acc_{CME}, $RSSn$], [$V2f_{CME}$, CPA_{CME}, AW_{CME}, AW_{CME}, $RSSn$], [$V20R_{CME}$, CPA_{CME}, AW_{CME}, Acc_{CME}, $RSSn$], [$V2f_{CME}$, MPA_{CME}, AW_{CME}, AW_{CME}, $RSSn$] [$V2f_{CME}$, MPA_{CME}, AW_{CME}, AW_{CME}, $RSSn$], [$V2f_{CME}$, MPA_{CME}, AW_{CME}, AW_{CME}, $RSSn$]. In this notations, V_{lin} is the linear speed of the CME, $V2f_{CME}$ second order speed at final height, $RSSn$ the smoothed sunspot number.

3.1 Training Set

As already mentioned, we divided the events into the two categories needed for running the model, training and validation, three fourths for the training one, and the remaining one fourth for the validation one.

Thus, the training set contained 2,097 events, with 33 positive events included. By positive event we define a CME that reached the Earth and that was associated with a geomagnetic storm (i.e., a minimum Dst value $\leqslant -30$ nT). The vast majority of the events (2,763) were negative events, meaning that CMEs never reached the Earth, or they were not associated with a geomagnetic storm.

Using the coefficients displayed in **Table 1** we have computed the probability that a geomagnetic storm is produced (**Formula 1**) for each considered event using the regression model.

Π is the probability of the occurrence of a geomagnetic storm (Dst $\leqslant -30$ nT). If Π is bigger than 50% then we considered that

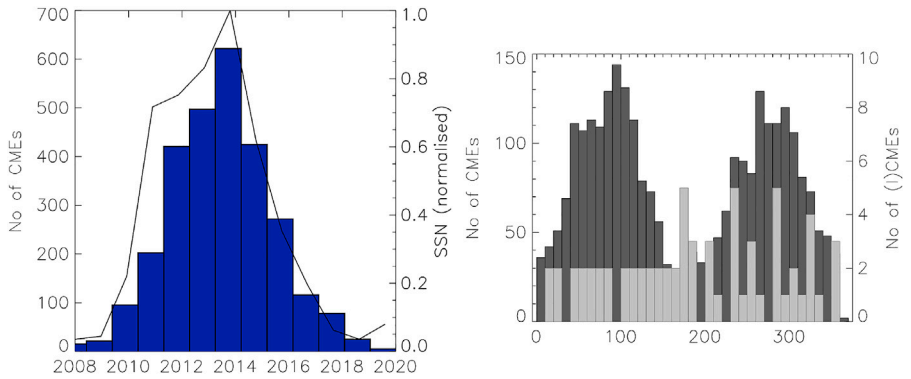

FIGURE 2 | (A): Total number of CMEs per year (blue histograms) and yearly smoothed sunspot number (black line). **(B)**: The measured position angle for all CMEs studied here during 2008–2020 (black histograms) and for CMEs that have reached the interplanetary space (gray histograms).

a geomagnetic storm was forecasted by the model and if Π is smaller than 50% then there was no geomagnetic storm. A correct forecast will mean a probability bigger than 50% for a positive event and a probability less than 50% for a negative event. Hence, the success rate was computed as the number of correct forecasts divided by the total number of events. The general success rate (considering both positive and negative events) was 0.986, and 0.987, respectively for the normalized and standardized set. During training, the model did not successfully predict any of the 27 positive events.

3.2 Validation Set

The validation set contained 699 events with six positive events included. For this set the success rate was 0.989 and 0.989, respectively for the normalized and standardized set. The validation set din not correctly forecasted any of the six CMEs that were associated with geomagnetic storms.

4 DISCUSSION

4.1 CME Activity During SC24

In order to study the geoeffectiveness of our 2,796 CMEs during SC24, we have attempted a statistical analysis of the CME evolution with the solar cycle. **Figure 2** shows in the left panel the annual number of detected CMEs in blue bars and the yearly smoothed sunspot number in a black line.

Every aspect of the solar activity varies during the 11-years solar cycle. Taking the sunspot number as the most significant indicator of the cycle's activity, this would mean that coronal mass ejections will also vary with the sunspot number, either in correlation or anticorrelation. **Figure 2** shows a good correlation between the number of detected CMEs and the sunspot number.

Solar cycle 24 began on January 1, 2007 with its ascending phase lasting fifteen months until April 1, 2010. Solar cycle's maximum phase started on July 1, 2011 and ended on March 31, 2015. It had two maxima on October 2013 and February 2014. The descending phase ended on July 31, 2017. The maximum number of detected CMEs coincides with the year of the maximum monthly smoothed sunspot number. In another study, no significant correlation between the phases of solar cycle and yearly occurrence of intense and great storms has been found (Rathore and Parashar, 2011).

Generally, the yearly number of detected CMEs follows the yearly smoothed sunspot number as seen in **Figure 2**. It is clearly observable that there are less CMEs detected during the descending phase of SC24 by comparison with its ascending phase.

We have observed that 68% of the CMEs were detected during the maximum phase of the solar cycle and that the descending phase had the least events–only 10%. Similarly, high speed CMEs (the speed at 20 solar radii exceeding 1,000 km/s) were significantly more during the maximum phase of the cycle (129), while the descending phase had the smallest number (20).

Considering CMEs from the point of view of the MPA, there are more CMEs measured in the northern hemisphere–with ~ 8% more than the sourthern one. The explicit division as a function of the MPA is 28% in the NE quadrant, 26% NW quadrant, 24 and 22%, respectively for the southern ones (SE/SW). This difference is considered to be too small to be motivated by a certain preference.

The right panel of **Figure 2** shows a histogram that represents in dark gray the total number of CMEs and in light gray the CMEs which arrived at the Earth (ICMEs) as a function of their measured position angle. This histogram is constructed in bins of 10 degrees for all CMEs studied here and shows a preference for 80–120° and 260–300° latitudinal bands.

The slight preference for the northern hemisphere is not reproduced for the CMEs that were detected near Earth. There were 15 CMEs coming from regions near the poles (± 30°) that reached the Earth, and only nine have produced geomagnetic storms.

Nine out of these 15 ICMEs were detected during the maximum phase of SC24, which is contrary to the fact that most of the ICMEs were detected during the descending phase (29 ICMEs out of the 49 included in our set). 21 were followed by geomagnetic storms. Halo CMEs are most geoeffective between the maximum and descending phases of SC23 (Shrivastava,

2011). Zhang et al. (2008) found similar results for CIRs during the descending phase of SC23.

Gopalswamy et al. (2020) analyzed 44 and 38 limb halo CMEs in cycles 23 and 24, respectively, in order to quantify the effect of the heliospheric influence on CME properties. Their study reveals the effect of the reduced total pressure in the heliosphere that allows cycle 24 CMEs to expand more and become halos sooner than those from cycle 23. They also found similar results regarding the CME activity during the solar cycle, more specifically, that the maximum number of detected CMEs coincides with the maximum value of the relative sunspot number, which can easily be confirmed from **Figure 2**.

A better understanding of the linkage between CMEs and solar activity cycle should improve our understanding about their geoeffectiveness. Some studies (e.g., Wang et al., 2002; Echer et al., 2008; Rathore and Parashar, 2011; Verma et al., 2013) show that there are more geomagnetic storms related to eruptive phenomena during the descending phase of a solar cycle.

A classification of CMEs by their linear speed into three categories ($v < 250$, $250 \leqslant v < 1{,}000$, $v \leqslant 1{,}000$ km/s, respectively) led Miteva et al. (2017) to see the same coincidence between the number of CMEs and the sunspot number. They also confirm that SC24 was low in 25–50 MeV proton events, X-to-C class solar flares and faster than 1,000 km/s CMEs, all these phenomena being reduced by 30–45% with respect to SC23.

Our study has 1,352 CMEs coming from the western hemisphere and 1,444 from the eastern one. Out of these, there were 23 ICMEs and 26, respectively. Cycle 24 lacks in events driving extreme geomagnetic storms compared to past solar cycles. Out of the 49 ICMEs included in our study, 33 have been followed by geomagnetic storms.

For solar cycle 24 Hess and Zhang (2017) have identified 70 Earth-affecting interplanetary coronal mass ejections (ICMEs). They found that Earth-affecting CMEs in the first half of Cycle 24 are more likely to come from the northern hemisphere, but after April 2012, it reverses. They also found that in past solar cycles, CMEs from the western hemisphere were more likely to reach Earth.

Only around 50% of the ICMEs were generating GSs during the years 1996–2017. Out of these, around 23% generated intense GSs (with $Dst \leqslant -100$ nT) and the probability for severe storms ($Dst \leqslant -200$ nT) was 4% (Alexakis and Mavromichalaki, 2019). Similar results were found also by Richardson and Cane (2011) for the time period 1995–2009. For our selected events the percentage of ICMEs followed by geomagnetic storms, including minor ones, is $\sim 67\%$.

In our dataset containing 49 ICMEs there are nine intense geomagnetic storms associated with them, and only one severe storm ($Dst_{min} = -223$ nT). This means that $\sim$ 59% of ICMEs were followed by geomagnetic storms.

Using a Spearman rank correlation coefficient between Dst index and CME speed for 33 halo CMEs from the beginning of the past solar cycle (2009–2013). Bisht et al. (2017) showed that high speed CMEs and big flares are not the effective and significant parameters for the geoeffectiveness of these selected halo events. This supported our decision for eliminating the parameter related to the flare-CME association.

In our study, out of the 2,796 CMEs, there were 276 halo ones, out of which 24 were associated with geomagnetic storms, having velocities ranging from 143 to 3,163 km/s. This resulted in a 0.08 Spearman coefficient between the linear speed and the Dst index.

In a propagation through the interplanetary space analysis of 53 fast Earth-directed halo CMEs observed by the LASCO instrument during the period January 2009–September 2015 Scolini et al. (2018) found that 82% of the CMEs arrived at Earth in the next 4 days. The events were propagated to 1AU by means of the WSA-ENLIL +Cone model and almost all of them triggered geomagnetic storms. The average time delay in the case of our geoeffective CMEs was ~ 3 days.

No other statistics of the measured CME properties have shown a noticeable dependence of the solar cycle evolution.

4.2 Concluding Remarks

We have applied a non-linear logistic regression model to a selected set of CMEs detected by LASCO in order to evaluate their geoeffectiveness such as defined by their association to a geomagnetic storm. The selected CMEs excluded "poor" and "very poor" events and CMEs with angular width less than 60°, thus obtaining a database of 2,796 events. These CMEs were divided into training (three quarters) and validation (one quarter) sets. Using a set of five independent variables (V_{20R}, AW_{CME}, MPA_{CME}, Acc_{CME}, Pos_{CME}), the correlation to ICMEs and geomagnetic storms according to the ICME catalogue (Richardson and Cane, 2011), we have computed the probability that a CME will be associated with a geomagnetic storm. We normalized and standardized the input data such that we minimize the numerical errors. We have obtained greater than 0.98 success rates for all categories. However, there were no positive events correctly forecasted.

Besides CME-CME interaction there is now an increasing concern that stealth CMEs are also important from the space weather perspective (e.g., Nitta and Mulligan, 2017; Mishra and Srivastava, 2019). The stealth CMEs lack any low coronal signatures (see e.g., Robbrecht et al., 2009; D'Huys et al., 2014) which is why they are more difficult to forecast if they erupt from the visible part of the Sun and if they arrive at Earth. Such CMEs have an important physical concern for other planetary magnetospheres as well (see e.g., Thampi et al., 2021). Our model forecasted that stealth CMEs will not have any impact on the Earth, as their location was originating from the backside.

As the stealth CMEs are lacking low-coronal signatures, their source regions could not be identified. In consequence, these CMEs were considered as originating from the backside of the Sun (location variable was set to 0). This implies that our model will not forecast that stealth CMEs will have any impact on the Earth.

During their journey from the Sun to the Earth, CMEs can accelerate/decelerate, deflect, rotate and deform (see e.g., Manchester et al., 2014; Manchester et al., 2017). Syed Ibrahim et al. (2019) found that the ICME transit-time decreases with the increase in the CME initial speed, although a broad range of transit times were observed for a given CME speed. For slow CMEs (< 400 km/s), the energy is transferred from the solar wind to the CMEs, while faster events ($\geqslant$400 km/s) tend to lose their energy to the ambient medium (e.g., Soni et al., 2019).

The paragraphs above reveal the limitation of our model by using only the CME parameters as input for the model. A possible

improvement might be the addition of some weighting coefficients to increase the significance of the positive events in the training process. For a more robust analysis one also needs to take into consideration the interaction between the CMEs and the ambient solar wind during their journey to the Earth. Throughout their propagation, the CME parameters like speed, shape, etc. change considerably and this has a big impact on their geoeffective response.

However, we consider this model to be a sustainable one for the purpose of predicting the association of a geomagnetic storm to a CME which arrived at Earth, based solely on the measurements of the CME's properties.

Another improvement of this model could be the addition of the tilt angle of the CME to the dataset, in order to better estimate the direction of the CME propagation, even though it will not take into consideration the interplanetary interactions.

DATA AVAILABILITY STATEMENT

The raw data supporting the conclusions of this article will be made available by the authors, without undue reservation.

AUTHOR CONTRIBUTIONS

DB-I contributed to construction of database, running the model, main writer of the text. MM contributed to construction of database, writing and reviewing text and software.

FUNDING

Part of DB-I's work was supported by a grant of the Romanian Ministery of Research and Innovation, CCCDI - UEFISCDI, project number PN-III-P1-1.2-PCCDI-2017-0226/16PCCDI/2018, within PNCDI III.

ACKNOWLEDGMENTS

The CME LASCO catalog is generated and maintained at the CDAW Data Center by NASA and The Catholic University of America in cooperation with the Naval Research Laboratory. SOHO is a project of international cooperation between ESA and NASA.

REFERENCES

Alexakis, P., and Mavromichalaki, H. (2019). Statistical Analysis of Interplanetary Coronal Mass Ejections and Their Geoeffectiveness During the Solar Cycles 23 and 24. *Astrophys. Space Sci.* 364, 187. doi:10.1007/s10509-019-3677-y

Besliu-Ionescu, D., Talpeanu, D.-C., Mierla, M., and Muntean, G. M. (2019). On the Prediction of Geoeffectiveness of CMEs During the Ascending Phase of SC24 Using a Logistic Regression Method. *J. Atmos. Solar-Terrestrial Phys.* 193, 105036. doi:10.1016/j.jastp.2019.04.017

Bhatt, B., and Chandra, H. (2020). Relationship Between Rising Phase of Solar Cycle 23rd and 24th With Respect to Geoeffectiveness. *Adv. Sci. Engng Med.* 12, 70–74. doi:10.1166/asem.2020.2518

Bisht, H., Pande, B., Chandra, R., and Pande, S. (2017). Geoeffectiveness of Solar Eruptions During the Rising Phase of Solar Cycle 24. *New Astron.* 51, 74–85. doi:10.1016/j.newast.2016.08.014

Bruevich, E. A., and Yakunina, G. V. (2020). 24th Cycle of Solar Activity: Geoefficiency of Flares. *Geomagn. Aeron.* 60, 876–880. doi:10.1134/S0016793220070087

Cane, H. V., and Richardson, I. G. (2003). Interplanetary Coronal Mass Ejections in the Near-Earth Solar Wind During 1996–2002. *J. Geophys. Res.* 108, 1156. doi:10.1029/2002JA009817

Chi, Y., Shen, C., Wang, Y., Xu, M., Ye, P., and Wang, S. (2016). Statistical Study of the Interplanetary Coronal Mass Ejections from 1995 to 2015. *Sol. Phys.* 291, 2419–2439. doi:10.1007/s11207-016-0971-5

D'Huys, E., Seaton, D. B., Poedts, S., and Berghmans, D. (2014). Observational Characteristics of Coronal Mass Ejections Without Low-Coronal Signatures. *Astrophysical J.* 795, 49. doi:10.1088/0004-637X/795/1/49

Echer, E., Gonzalez, W. D., Tsurutani, B. T., and Gonzalez, A. L. C. (2008). Interplanetary Conditions Causing Intense Geomagnetic Storms (Dst ≤ −100 nT) During Solar Cycle 23 (1996–2006). *J. Geophys. Res.* 113, A05221. doi:10.1029/2007JA012744

Gelman, A. (2008). Scaling Regression Inputs by Dividing by Two Standard Deviations. *Statist. Med.* 27, 2865–2873. doi:10.1002/sim.3107

Gonzalez, W. D., Joselyn, J. A., Kamide, Y., Kroehl, H. W., Rostoker, G., Tsurutani, B. T., et al. (1994). What is a Geomagnetic Storm? *J. Geophys. Res.* 99, 5771–5792. doi:10.1029/93JA02867

Gopalswamy, N., Akiyama, S., Yashiro, S., and Makela, P. (2010). Coronal Mass Ejections from Sunspot and Non-Sunspot Regions. *Astrophy. Space Sci. Proc.* 19, 289–307. doi:10.1007/978-3-642-02859-5_24

Gopalswamy, N., Yashiro, S., and Akiyama, S. (2007). Geoeffectiveness of Halo Coronal Mass Ejections. *J. Geophys. Res.* 112, A06112. doi:10.1029/2006JA012149

Gopalswamy, N., Mäkelä, P., Xie, H., and Yashiro, S. (2013). Testing the Empirical Shock Arrival Model Using Quadrature Observations. *Space Weather* 11, 661–669. doi:10.1002/2013SW000945

Gopalswamy, N., Akiyama, S., and Yashiro, S. (2020). The State of the Heliosphere Revealed by Limb-Halo Coronal Mass Ejections in Solar Cycles 23 and 24. *Astrophys. J., Lett.* 897, L1. doi:10.3847/2041-8213/ab9b7b

Hess, P., and Zhang, J. (2017). A Study of the Earth-Affecting CMEs of Solar Cycle 24. *Sol. Phys.* 292, 80. doi:10.1007/s11207-017-1099-y

Joshi, N. C., Uddin, W., Srivastava, A. K., Chandra, R., Gopalswamy, N., Manoharan, P. K., et al. (2013). A Multiwavelength Study of Eruptive Events on January 23, 2012 Associated With a Major Solar Energetic Particle Event. *Adv. Space Res.* 52, 1–14. doi:10.1016/j.asr.2013.03.009

Kilpua, E. K. J., Mierla, M., Zhukov, A. N., Rodriguez, L., Vourlidas, A., and Wood, B. (2014). Solar Sources of Interplanetary Coronal Mass Ejections During the Solar Cycle 23/24 Minimum. *Sol. Phys.* 289, 3773–3797. doi:10.1007/s11207-014-0552-4

Kraaikamp, E., and Verbeeck, C. (2015). Solar Demon - an Approach to Detecting Flares, Dimmings, and euv Waves on sdo/aia Images. *J. Space Weather Space Clim.* 5, A18. doi:10.1051/swsc/2015019

Lamy, P. L., Floyd, O., Boclet, B., Wojak, J., Gilardy, H., and Barlyaeva, T. (2019). Coronal Mass Ejections over Solar Cycles 23 and 24. *Space Sci. Rev.* 215, 39. doi:10.1007/s11214-019-0605-y

Manchester, W., Kilpua, E. K. J., Liu, Y. D., Lugaz, N., Riley, P., Török, T., et al. (2017). The Physical Processes of CME/ICME Evolution. *Space Sci. Rev.* 212, 1159–1219. doi:10.1007/s11214-017-0394-0

Manchester, W. B., van der Holst, B., and Lavraud, B. (2014). Flux Rope Evolution in Interplanetary Coronal Mass Ejections: the 13 May 2005 Event. *Plasma Phys. Control Fusion* 56, 064006. doi:10.1088/0741-3335/56/6/064006

Maris, G., Popescu, M.-D., and Mierla, M. (2002). "Geomagnetic Consequences of the Solar Flares During the Last Hale Solar Cycle (II),". in Solspa 2001, Proceedings of the Second Solar Cycle and Space Weather Euroconference, Vico Equense, Italy, September 24–29, 2001. Editor H. Sawaya-Lacoste (Noordwijk, Netherlands: ESA Special Publication), 477, 451–454.

Mishra, S. K., and Srivastava, A. K. (2019). Linkage of Geoeffective Stealth CMEs Associated With the Eruption of Coronal Plasma Channel and Jet-Like Structure. *Sol. Phys.* 294, 169. doi:10.1007/s11207-019-1560-1

Miteva, R., Samwel, S. W., Costa-Duarte, M. V., and Malandraki, O. E. (2017). Solar Cycle Dependence of Wind/EPACT Protons, Solar Flares and Coronal Mass Ejections. *Sun Geosphere* 12, 11–19.

Möstl, C., Weiss, A. J., Bailey, R. L., Reiss, M. A., Amerstorfer, T., Hinterreiter, J., et al. (2020). Prediction of the *In Situ* Coronal Mass Ejection Rate for Solar Cycle 25: Implications for Parker Solar Probe *In Situ* Observations. *Astrophys. J.* 903, 92. doi:10.3847/1538-4357/abb9a1

Nakagawa, T., Gopalswamy, N., and Yashiro, S. (2006). Solar Wind Speed Within 20RSof the Sun Estimated from Limb Coronal Mass Ejections. *J. Geophys. Res.* 111, A01108. doi:10.1029/2005JA011249

Nitta, N. V., and Mulligan, T. (2017). Earth-Affecting Coronal Mass Ejections Without Obvious Low Coronal Signatures. *Sol. Phys.* 292, 125. doi:10.1007/s11207-017-1147-7

Paraschiv, A. R., Lacatus, D. A., Badescu, T., Lupu, M. G., Simon, S., Sandu, S. G., et al. (2010). Study of Coronal Jets During Solar Minimum Based on STEREO/SECCHI Observations. *Sol. Phys.* 264, 365–375. doi:10.1007/s11207-010-9584-6

Raouafi, N. E., Patsourakos, S., Pariat, E., Young, P. R., Sterling, A. C., Savcheva, A., et al. (2016). Solar Coronal Jets: Observations, Theory, and Modeling. *Space Sci. Rev.* 201, 1–53. doi:10.1007/s11214-016-0260-5

Rathore, B. S., Kaushik, S. C., Parashar, K., Bhadoria, R. S., and Kapil, P. (2011). Statistical Study of Geomagnetic Storms and Their Classification During Solar Cycle-23. *Int. J. Phys. Appl.* 3, 91–96.

Richardson, I. G., and Cane, H. V. (2010). Near-Earth Interplanetary Coronal Mass Ejections During Solar Cycle 23 (1996–2009): Catalog and Summary of Properties. *Sol. Phys.* 264, 189–237. doi:10.1007/s11207-010-9568-6

Richardson, I. G., and Cane, H. V. (2011). Geoeffectiveness (Dst and Kp) of Interplanetary Coronal Mass Ejections During 1995–2009 and Implications for Storm Forecasting. *Space Weather* 9, S07005. doi:10.1029/2011SW000670

Robbrecht, E., Patsourakos, S., and Vourlidas, A. (2009). No Trace Left Behind: Stereo Observation of a Coronal Mass Ejection Without Low Coronal Signatures. *Astrophys. J.* 701, 283–291. doi:10.1088/0004-637X/701/1/283

Schwenn, R. (2006). Space Weather: The Solar Perspective. *Living Rev. Solar Phys.* 3, 2. doi:10.12942/lrsp-2006-2

Scolini, C., Chané, E., Temmer, M., Kilpua, E. K. J., Dissauer, K., Veronig, A. M., et al. (2020). CME-CME Interactions as Sources of CME Geoeffectiveness: The Formation of the Complex Ejecta and Intense Geomagnetic Storm in 2017 Early September. *Astrophys. J. Supple. Ser.* 247, 21. doi:10.3847/1538-4365/ab6216

Scolini, C., Messerotti, M., Poedts, S., and Rodriguez, L. (2018). Halo Coronal Mass Ejections during Solar Cycle 24: Reconstruction of the Global Scenario and Geoeffectiveness. *J. Space Weather Space Clim.* 8, A09. doi:10.1051/swsc/2017046

Shen, C., Xu, M., Wang, Y., Chi, Y., and Luo, B. (2018). Why the Shock-ICME Complex Structure is Important: Learning From the Early 2017 September CMEs. *Astrophys. J.* 861, 28. doi:10.3847/1538-4357/aac204

Shrivastava, P. K., and Mishra, B. K. (2011). Geoeffectiveness of Halo CMEs During Different Phases of Solar Activity Cycle 23. *Int. Cosmic Ray Conf.* 11, 280. doi:10.7529/ICRC2011/V11/0070

Soni, S. L., Singh, P. R., Nigam, B., Gupta, R. S., and Shrivastava, P. K. (2019). The Analysis of Interplanetary Shocks Associated with Six Major Geo-Effective Coronal Mass Ejections during Solar Cycle 24. *Int. J. Astron. Astrophys.* 09, 191–199. doi:10.4236/ijaa.2019.93014

Srivastava, N. (2005). A Logistic Regression Model for Predicting the Occurrence of Intense Geomagnetic Storms. *Ann. Geophys.* 23, 2969–2974. doi:10.5194/angeo-23-2969-2005

Srivastava, N., and Venkatakrishnan, P. (2004). Solar and Interplanetary Sources of Major Geomagnetic Storms during 1996–2002. *J. Geophys. Res.* 109, A10103. doi:10.1029/2003JA010175

Syed Ibrahim, M., Joshi, B., Cho, K.-S., Kim, R.-S., and Moon, Y.-J. (2019). Interplanetary Coronal Mass Ejections During Solar Cycles 23 and 24: Sun-Earth Propagation Characteristics and Consequences at the Near-Earth Region. *Sol. Phys.* 294, 54. doi:10.1007/s11207-019-1443-5

Thampi, S. V., Krishnaprasad, C., Nampoothiri, G. G., and Pant, T. K. (2021). The Impact of a Stealth CME on the Martian Topside Ionosphere. *Monthly Notices R. Astronom. Soc.* 503, 625–632. doi:10.1093/mnras/stab494

Verma, R., Kumar, S., and Dubey, S. (2013). Coronal Mass Ejection, Magnetic Cloud and Their Geoeffectiveness During 1996–2009. *Int. J. Sci. Res.* 5, 1832–1836.

Wang, Y. M., Ye, P. Z., Wang, S., Zhou, G. P., and Wang, J. X. (2002). A Statistical Study on the Geoeffectiveness of Earth-Directed Coronal Mass Ejections from March 1997 to December 2000. *J. Geophys. Res.* 107, 1340. doi:10.1029/2002JA009244

Webb, D. F., and Howard, T. A. (2012). Coronal Mass Ejections: Observations. *Living Rev. Solar Phys.* 9, 3. doi:10.12942/lrsp-2012-3

Xu, M., Shen, C., Wang, Y., Luo, B., and Chi, Y. (2019). Importance of Shock Compression in Enhancing ICME's Geoeffectiveness. *Astrophys. J. Lett.* 884, L30. doi:10.3847/2041-8213/ab4717

Yashiro, S., Gopalswamy, N., Akiyama, S., and Mäkelä, P. A. (2020). A Catalog of Prominence Eruptions Detected Automatically in the SDO/AIA 304 Å Images. *J. Atmos. Solar-Terrestrial Phys.* 205, 105324. doi:10.1016/j.jastp.2020.105324

Yashiro, S., Gopalswamy, N., Michalek, G., Cyr, St. O. C., Plunkett, S. P., Rich, N. B., et al. (2004). A Catalog of White Light Coronal Mass Ejections Observed by the SOHO Spacecraft. *J. Geophys. Res.* 109, A07105. doi:10.1029/2003JA010282

Zhang, J., Richardson, I. G., Webb, D. F., Gopalswamy, N., Huttunen, E., Kasper, J. C., et al. (2007). Solar and Interplanetary Sources of Major Geomagnetic Storms (Dst≤ −100 nT) During 1996–2005. *J. Geophys. Res.* 112, A10102. doi:10.1029/2007JA012321

Zhang, Y., Sun, W., Feng, X. S., Deehr, C. S., Fry, C. D., and Dryer, M. (2008). Statistical Analysis of Corotating Interaction Regions and Their Geoeffectiveness during Solar Cycle 23. *J. Geophys. Res.* 113, A08106. doi:10.1029/2008JA013095

Conflict of Interest: The authors declare that the research was conducted in the absence of any commercial or financial relationships that could be construed as a potential conflict of interest.

frontiers in Astronomy and Space Sciences

ORIGINAL RESEARCH
published: 05 July 2021
doi: 10.3389/fspas.2021.695966

Investigating Remote-Sensing Techniques to Reveal Stealth Coronal Mass Ejections

Erika Palmerio[1,2], Nariaki V. Nitta[3], Tamitha Mulligan[4], Marilena Mierla[5,6], Jennifer O'Kane[7], Ian G. Richardson[8,9], Suvadip Sinha[10], Nandita Srivastava[11], Stephanie L. Yardley[7] and Andrei N. Zhukov[5,12]*

[1]Space Sciences Laboratory, University of California, Berkeley, CA, United States, [2]CPAESS, University Corporation for Atmospheric Research, Boulder, CO, United States, [3]Lockheed Martin Solar and Astrophysics Laboratory, Palo Alto, CA, United States, [4]Space Sciences Department, The Aerospace Corporation, Los Angeles, CA, United States, [5]Solar–Terrestrial Centre of Excellence, Royal Observatory of Belgium, Brussels, Belgium, [6]Institute of Geodynamics of the Romanian Academy, Bucharest, Romania, [7]Mullard Space Science Laboratory, University College London, Dorking, United Kingdom, [8]Department of Astronomy, University of Maryland, College Park, MD, United States, [9]Heliospheric Physics Division, NASA Goddard Space Flight Center, Greenbelt, MD, United States, [10]CESSI, Indian Institute of Science Education and Research Kolkata, Mohanpur, India, [11]Udaipur Solar Observatory, Physical Research Laboratory, Udaipur, India, [12]Skobeltsyn Institute of Nuclear Physics, Moscow State University, Moscow, Russia

OPEN ACCESS

Edited by:
Xueshang Feng, State Key Laboratory of Space Weather, National Space Science Center (CAS), China

Reviewed by:
Huw Morgan, Aberystwyth University, United Kingdom
Ming Xiong, National Space Science Center (CAS), China

***Correspondence:**
Erika Palmerio
epalmerio@berkeley.edu

Specialty section:
This article was submitted to Stellar and Solar Physics, a section of the journal Frontiers in Astronomy and Space Sciences

Received: *15 April 2021*
Accepted: *14 June 2021*
Published: *05 July 2021*

Citation:
Palmerio E, Nitta NV, Mulligan T, Mierla M, O'Kane J, Richardson IG, Sinha S, Srivastava N, Yardley SL and Zhukov AN (2021) Investigating Remote-Sensing Techniques to Reveal Stealth Coronal Mass Ejections. Front. Astron. Space Sci. 8:695966. doi: 10.3389/fspas.2021.695966

Eruptions of coronal mass ejections (CMEs) from the Sun are usually associated with a number of signatures that can be identified in solar disc imagery. However, there are cases in which a CME that is well observed in coronagraph data is missing a clear low-coronal counterpart. These events have received attention during recent years, mainly as a result of the increased availability of multi-point observations, and are now known as "stealth CMEs." In this work, we analyze examples of stealth CMEs featuring various levels of ambiguity. All the selected case studies produced a large-scale CME detected by coronagraphs and were observed from at least one secondary viewpoint, enabling a priori knowledge of their approximate source region. To each event, we apply several image processing and geometric techniques with the aim to evaluate whether such methods can provide additional information compared to the study of "normal" intensity images. We are able to identify at least weak eruptive signatures for all events upon careful investigation of remote-sensing data, noting that differently processed images may be needed to properly interpret and analyze elusive observations. We also find that the effectiveness of geometric techniques strongly depends on the CME propagation direction with respect to the observers and the relative spacecraft separation. Being able to observe and therefore forecast stealth CMEs is of great importance in the context of space weather, since such events are occasionally the solar counterparts of so-called "problem geomagnetic storms."

Keywords: sun, coronal mass ejection, stealth coronal mass ejection, solar corona, space weather, remote-sensing analysis

1 INTRODUCTION

Coronal mass ejections (CMEs) are powerful solar eruptions containing large amounts of plasma and magnetic field that are regularly expelled from the Sun into the heliosphere. They were first identified in white light in the early 1970s (Tousey, 1973; Gosling et al., 1974) in images from the 7th Orbiting Solar Observatory (OSO-7) coronagraph (Koomen et al., 1975) and the coronagraph onboard the Skylab space station that formed part of the Apollo Telescope Mount (ATM; Tousey, 1977) suite of solar instruments. Around the same time, the low-coronal counterparts of white-light CMEs were being observed through multi-wavelength solar disc imagery, e.g., in extreme ultra-violet (EUV), soft X-rays, and Hα, using data from OSO-7, Skylab, and ground-based observatories (e.g., Demastus et al., 1973; Munro et al., 1979). The typical low-coronal signatures of CMEs were reviewed by Hudson and Cliver. (2001). These include the appearance of coronal dimmings (e.g., Thompson et al., 2000; Kahler and Hudson, 2001), flare ribbons (e.g., Rust and Bar, 1973; Martin, 1979), post-eruption arcades (e.g., Rust and Webb, 1977; Tripathi et al., 2004), and EUV waves (e.g., Thompson et al., 1998; Zhukov and Auchère, 2004), as well as the disappearance of filament material (e.g., Rust et al., 1975; Sheeley et al., 1975) and X-ray sigmoids (e.g., Rust and Kumar, 1996; Green et al., 2007). A major step forward in CME research was achieved in the early 1980s, when Howard et al. (1982) reported observations of the first Earth-directed CME (in that case, a halo CME[1]) in white-light images from the Solwind coronagraph (Michels et al., 1980) and linked this "coronal transient"[2] with a disappearing filament on the solar disc and with a shock wave detected near Earth about 3 days later. The following decade saw the launch of two missions that have made a major impact on the field of solar physics, namely Yohkoh (also known as Solar-A; Ogawara et al., 1991) and the Solar and Heliospheric Observatory (SOHO; Domingo et al., 1995). Yohkoh carried several solar imagers, including the Soft X-ray Telescope (SXT; Tsuneta et al., 1991), while the SOHO payload includes remote-sensing and *in-situ* instruments, several of which are still operational, including the venerable Large Angle Spectroscopic Coronagraph (LASCO; Brueckner et al., 1995). By then, the whole Sun-to-Earth picture of CMEs was seemingly quite clear: The presence of low-coronal signatures preceding a halo CME observed by LASCO would signify that the CME is Earth-directed, whereas the lack of visible activity on the solar disc would indicate that the CME was associated with a far-sided eruption.

However, it was not long before this picture was shown to not always hold true. Studies of CMEs detected *in situ* near Earth noted that a large number of such events lacked clear solar associations (e.g., Cane and Richardson, 2003; Richardson and Cane, 2010). Specifically, Schwenn et al. (2005), reported that 20% of interplanetary CMEs could not be linked to a front-sided (partial or full) halo CME source, and Zhang et al. (2007) reported that 11% of CME-driven storms with minimum $Dst \leq -100$ nT could not be linked to eruptive signatures in the low corona. A turning point came with the launch of the Solar Terrestrial Relations Observatory (STEREO; Kaiser et al., 2008) mission in 2006. The STEREO mission consisted of twin spacecraft, one advancing ahead of Earth in its orbit (STEREO-A) and one trailing behind (STEREO-B), thus enabling observations of the Sun from multiple viewpoints. Using data from the Sun Earth Connection Coronal and Heliospheric Investigation (SECCHI; Howard et al., 2008) suite onboard both STEREO spacecraft when they were separated by 53°, Robbrecht et al. (2009) reported that a CME erupted "leaving no trace behind on the solar disc." Although the authors were able to identify a slow, streamer-blowout CME erupting off the limb in STEREO-A imagery, there were no corresponding on-disc signatures in STEREO-B data. The Robbrecht et al. (2009) event represents the first direct observation of what is now known in the solar physics community as a "stealth CME." In the following years, numerous additional stealth events have been reported (Ma et al., 2010; D'Huys et al., 2014; Kilpua et al., 2014). According to these studies, CMEs that lack distinct low-coronal signatures tend to occur close to solar minimum, are generally slow and narrow, and often form at higher altitudes in the solar atmosphere. One major question that started to be raised is whether the eruption mechanism for stealth CMEs is fundamentally different from that of "ordinary" CMEs, or if stealth CMEs simply represent the lowest end of the full energy spectrum of solar eruptions (Howard and Harrison, 2013; Lynch et al., 2016). Additionally, it was soon clear that stealth CMEs can be detected *in situ*, starting with the Robbrecht et al. (2009) event that was observed at STEREO-B featuring a classic flux-rope structure (Möstl et al., 2009; Lynch et al., 2010; Nieves-Chinchilla et al., 2011). It also became evident that the interplanetary counterparts of stealth CMEs are able to cause significant space weather disturbances if they encounter Earth (Nitta and Mulligan, 2017). CME-driven storms that cannot be linked to a clear source on the Sun or to appreciable solar activity are particularly challenging to forecast and are known as "problem geomagnetic storms" (e.g., McAllister et al., 1996).

During the last decade, routine observations of the solar disc have advanced considerably due to the high temporal and spatial resolution of data from the Solar Dynamics Observatory (SDO; Pesnell et al., 2012), launched in 2010. Nevertheless, despite the improvement of EUV observations with respect to previous instrumentation, stealth CMEs continue to be reported (e.g., Nitta and Mulligan, 2017). It has been suggested that apparently stealth CMEs result from observational limitations such as instrument sensitivity and bandwidth issues, even in the SDO era (Howard and Harrison, 2013), and that advanced image processing techniques may reveal hard-to-observe signatures in both solar disc and coronagraph imagery (Alzate and Morgan, 2017; O'Kane et al., 2019). Additionally, some studies have applied geometric triangulation and reconstruction techniques

[1]Note that a halo CME is not necessarily Earth-directed, and a CME does not need to be a halo in order to impact Earth.

[2]CMEs have been called by various names since their discovery, ranging from "coronal transient phenomena" (MacQueen et al., 1974) to "mass ejections from the Sun" (Gosling et al., 1974). The term "coronal mass ejection" was first introduced by Gosling. (1975), but came into common usage only in the early 1980s.

to data from complementary viewpoints in order to trace stealth CMEs back to an approximate source region on the disc (Pevtsov et al., 2012; O'Kane et al., 2019; Talpeanu et al., 2020). These methods, however, have not been tested on a large number of events and hence it is not known whether they are suitable to all circumstances or whether they can be applied only to a limited number of cases. To complicate things further, there is currently no formal definition describing what a stealth CME is or defining the "observational limit" below which a CME can be considered to be stealthy.

In this paper, we contemplate the following question: Since stealth CMEs can present diverse characteristics, is it possible that there exists a class of "extremely stealth" CMEs that cannot be revealed even with the aid of state-of-the-art techniques? In order to address this issue, this work aims to investigate the efficacy of various techniques applied to remote-sensing data in revealing the signatures of CMEs that are elusive on the solar disc. We test such techniques on four well-studied stealth CMEs for which the "true" source is more or less known because of the availability of remote-sensing imagery from additional viewpoints. This will ensure that any solar activity that is observed away from the expected source region will not be mistakenly interpreted as a signature of the stealth CME under analysis. This manuscript is organized as follows. In **Section 2**, we present and describe the imaging and geometric techniques that we employ in this study to analyze stealth CMEs. In **Section 3**, we apply these techniques to four case studies and compare them with information that can be retrieved from plain inspection of intensity images only. Finally, in **Section 4** we discuss our results and present our conclusions.

2 TECHNIQUES EMPLOYED

This section summarizes the remote-sensing techniques that are used throughout this work to analyze the four elusive CMEs under study. Imaging techniques are described in **Section 2.1**, while geometric techniques are presented in **Section 2.2**.

2.1 Imaging Techniques

2.1.1 Image Differencing

The image differencing technique simply consists of subtracting from an image a preceding one, so that changes in total intensity over time appear as patches that are either dark (denoting an intensity decrease) or bright (denoting an intensity increase). This method has been long used in solar physics applications for both on-disc and coronagraph observations (e.g., Burlaga et al., 1982; Hudson et al., 1992). The commonly used nomenclature for the technique is that subtracting a pre-event image yields a "base difference" image, while subtracting successive images yields a "running difference" image. Base-difference images are often used to highlight transient phenomena that develop over larger time scales, such as coronal dimmings (e.g., Attrill and Wills-Davey, 2010), while running-difference images are often used to highlight short-term transient features such as EUV waves (e.g., Attrill et al., 2007). Since stealth CMEs tend to be slow, i.e. they erupt and accelerate over the course of several hours, their evolution is not expected to be captured in running-difference images, hence we focus in this work on using image differencing over longer time scales. In particular, Nitta and Mulligan. (2017) noted that in the case of stealth CMEs, difference images with "long enough" temporal separations (of the order of ~ 10 h) should often be used in order to reveal weak low-coronal signatures, including dimmings and post-eruption arcades. In this work, in order to minimize the appearance of artifacts at the solar limb due to rotation (which are still present even after accounting for differential rotation), we calculate the percentage variation between each couple of images and use a fixed temporal separation of $\Delta t = 12$ h.

2.1.2 Wavelet Packets Equalization

The Wavelet Packets Equalization (WPE; Stenborg and Cobelli, 2003; Stenborg et al., 2008) technique is a multi-resolution image processing method that can be applied to enhance features based on their multi-scale nature. In the WPE technique, an image is first decomposed over both dimensions using spatially localized functions known as wavelets. We have implemented the Stenborg and Cobelli (2003) procedure using a 2D à trous wavelet transform (e.g., Shensa, 1992), where the scaling function is a B_3-spline corresponding to a 5×5 smoothing kernel. This produces a set of wavelet planes at different spatial scales (called wavelet scales) derived from the initial image, together with the remaining "continuum" background image representing the lowest frequencies and largest scales. A wavelet-processed image is constructed by summing over all the wavelet planes and the continuum background with user-defined weights to emphasize the desired scale sizes. In general, the weighting strategy must be fine-tuned to both the particular image (e.g., different EUV wavelengths or different coronagraphs) and to the spatial scales of interest. In the case of stealth CMEs, the WPE technique has been used to enhance off-limb structures from secondary viewpoints (e.g., Vourlidas et al., 2011; Nieves-Chinchilla et al., 2013; Liewer et al., 2021), and had been explored to search for elusive on-disc signatures by Robbrecht et al. (2009).

2.1.3 Multi-Scale Gaussian Normalization

The Multi-scale Gaussian Normalization (MGN; Morgan and Druckmüller, 2014) technique, similarly to the WPE method described in **Section 2.1.2**, is based on a multi-scale normalization algorithm. In the MGN technique, a set of 2D Gaussian kernels of different scale lengths are used to locally normalize an image using a set of local mean and standard deviation values. A weighted combination of the normalized components is then used to obtain a weighted mean locally normalized image, which is finally superposed to the corresponding global gamma-transformed image. This results in an enhancement of the local intensity fluctuations within the images. The MGN image processing tool has been applied to EUV images to identify the low-coronal signatures associated with stealth events in both on-disc and off-limb observations (Alzate and Morgan, 2017; O'Kane et al., 2019, 2021b).

2.2 Geometric Techniques

2.2.1 Latitude Projection

Since all CMEs investigated in this study have been observed off limb from at least one additional perspective, a simple approach to adopt when triangulation is not possible (i.e., when only one "non-stealthy" viewpoint is available) is to project the approximate latitude from which the CME originated onto the "stealthy" field of view. Considering a "classic" three-part CME structure in coronagraph imagery (Illing and Hundhausen, 1985), we trace back to the solar disc the approximate latitude of the central, bright core that is observed off limb. We note that not all CMEs feature a three-part structure (e.g., Vourlidas et al., 2013), but stealth CMEs often belong to the streamer blowout category, in which flux rope signatures tend to occur at a higher rate than in the general CME population (Vourlidas and Webb, 2018). The projected latitude of the source region from the off-limb viewpoint naturally focuses the search for any possible faint or ambiguous on-disc signature to a more localized area. This enhances the potential to find any low-coronal signatures or dynamics that, by themselves, would not have necessarily been interpreted as being eruption-related.

2.2.2 Tie-Point Technique

The Tie-point (TP) triangulation technique was formulated by Inhester. (2006) and first employed by Thompson. (2009) to study a Sun-grazing comet. The principle on which the TP technique is based is that two separate observers and the point of interest in space (to be triangulated) form a plane called "epipolar plane," which is reduced to a line ("epipolar line") in image projections. A point identified in an image from the first observer must lie on the same epipolar line in the corresponding image from the second observer. Larger-scale features can be tracked by finding correspondences between different pixels along epipolar line pairs in images from both spacecraft. The 3D reconstruction or triangulation is then achieved by finding the intersection of the two lines of sight (for each pixel of interest) along the corresponding epipolar plane, which is unambiguously defined. In solar physics applications, the TP method has been used to evaluate the 3D morphology of erupting filaments (e.g., Bemporad et al., 2011; Thompson et al., 2012; Panasenco et al., 2013; Palmerio et al., 2021) and the evolution of CME fronts or cores in coronagraph data (e.g., Mierla et al., 2008, 2009; Srivastava et al., 2009; Liewer et al., 2011).

2.2.3 Graduated Cylindrical Shell

The Graduated Cylindrical Shell (GCS; Thernisien et al., 2006, Thernisien et al., 2009; Thernisien, 2011) model is a reconstruction technique usually applied to white-light coronagraph images. In the GCS model, a wireframe describing the geometry of flux ropes is used to fit CMEs from one or more simultaneous viewpoints. Within a single reconstruction, six free parameters (latitude, longitude, axis tilt, apex height, half-angle, and aspect ratio) can be adjusted until they best match the CME morphology observed in one or more images. The geometry of the model itself is often referred to as a "hollow croissant" and consists of a half-torus frontal part with two conical legs connected to the Sun. The resulting shape, reminiscent of a croissant, is "hollow" in the sense that the electron density is placed uniquely on the shell of the model. Thus, fits performed with the GCS model can provide information on the morphology of CMEs, but not on their magnetic field structure. The GCS technique is widely used in solar physics and space weather applications to determine geometric and kinematic parameters of CMEs and their shocks through the corona (e.g., Mierla et al., 2010; Shi et al., 2015; Schmidt et al., 2016), also in the case of stealth CMEs (e.g., Lynch et al., 2010; He et al., 2018). More recently, O'Kane et al. (2019), and Freiherr von Forstner et al. (2021) used the inferred propagation latitude and longitude from GCS reconstructions to obtain an approximate location for the source region of the stealth CMEs they analyzed. The full list of GCS-reconstructed parameters for all CMEs studied in this work can be found in **Supplementary Table S1**.

3 ANALYSIS OF SAMPLE STEALTH EVENTS

We present in this section the remote-sensing analysis of four CMEs with elusive on-disc signatures: 2008 June 1, 2011 March 3, 2012 February 4, and 2016 October 8. These events were selected based on two main factors. First of all, they were all observed as classic three-part CMEs including a flux rope by at least one spacecraft, i.e., they do not belong to the so-called "jet" and/or "blob" categories. Furthermore, each event was observed from at least one additional viewpoint, enabling estimation of its approximate source region on the solar disc. Such observations are provided for each case study as supplementary videos in which EUV data have been enhanced with a radial filter, in order to bring out off-limb emission. The reader is invited to initially rapidly move the video player slider back and forth, so that the motion catches the eye. As stealth CMEs are usually slower than average, it may be difficult to identify erupting structures that evolve over extremely long time scales when played at the speeds shown in the videos (i.e., 2–4 h per second). Additionally, kinematic (height–time) plots for each event based on observations from these additional viewpoints are provided in **Supplementary Figure S1**.

3.1 Event 1: 2008 June 1

The first CME that we focus on in this study (Event 1) erupted on 2008 June 1 and was a stealth event as seen from STEREO-B. This CME was first reported by Robbrecht et al. (2009) and its eruption was later modeled by Lynch et al. (2016). As mentioned in the Introduction, this event marked the first direct observation of a CME that left "no trace behind" in EUV imagery from one viewpoint, hence we treat it here as a "stealth CME prototype." At the time of this event, STEREO-A was located 28° west of Earth and STEREO-B was positioned 25° east of Earth. The pre-eruptive configuration and eruption process were well observed by STEREO-A, as shown in Extreme UltraViolet Imager (EUVI) and COR1 coronagraph data shown in **Supplementary Video S1**. From the STEREO-A perspective, a flux rope structure (observed as a characteristic cavity in off-limb imagery; Gibson et al., 2006) can be seen to lie at relatively high

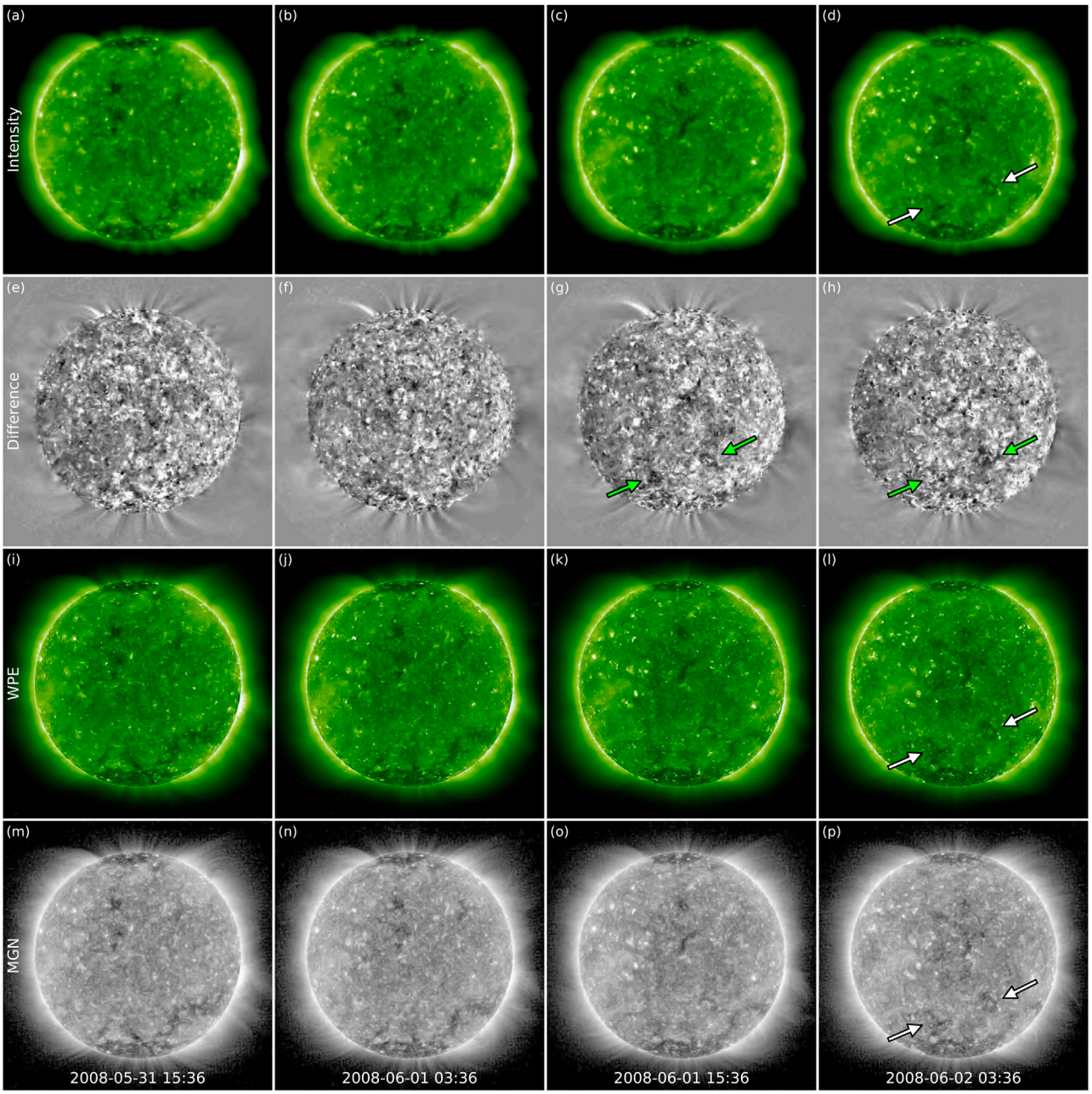

FIGURE 1 | Imaging techniques applied to the 2008 June 1 CME (Event 1). STEREO/SECCHI/EUVI-B 195Å images are shown at four different times and processed with four different methods. **(A–D)** Intensity images. **(E–H)** Difference images with fixed Δt = 12 h. **(I–L)** WPE-processed images. **(M–P)** MGN-processed images. Two faint dimmings are indicated with arrows (see text for details).

altitudes below a coronal streamer above the southeastern limb. The eruption itself took place over large time scales (~ 1.5 days), during which the flux rope slowly lifted off (starting around 15:00 UT on May 31), causing the streamer to swell and resulting in a classic streamer-blowout CME that reached the COR2-A coronagraph field of view around 22:00 UT on June 1. We remark that corresponding images from the Extreme-ultraviolet Imaging Telescope (EIT; Delaboudinière et al., 1995) onboard SOHO are not available because of a data gap.

EUVI images from STEREO-B for the eruption period processed with different techniques are shown in **Figure 1** and **Supplementary Video S2**. It is clear that the succession of images in **Figure 1** does not show any strong indication that an eruption has occurred. Nevertheless, it is possible to note two extremely faint dimmings (indicated with arrows) developing in the southern hemisphere starting around 15:00 UT on June 1 (see also **Supplementary Video S2**). These dimmings are not straightforward to identify even in

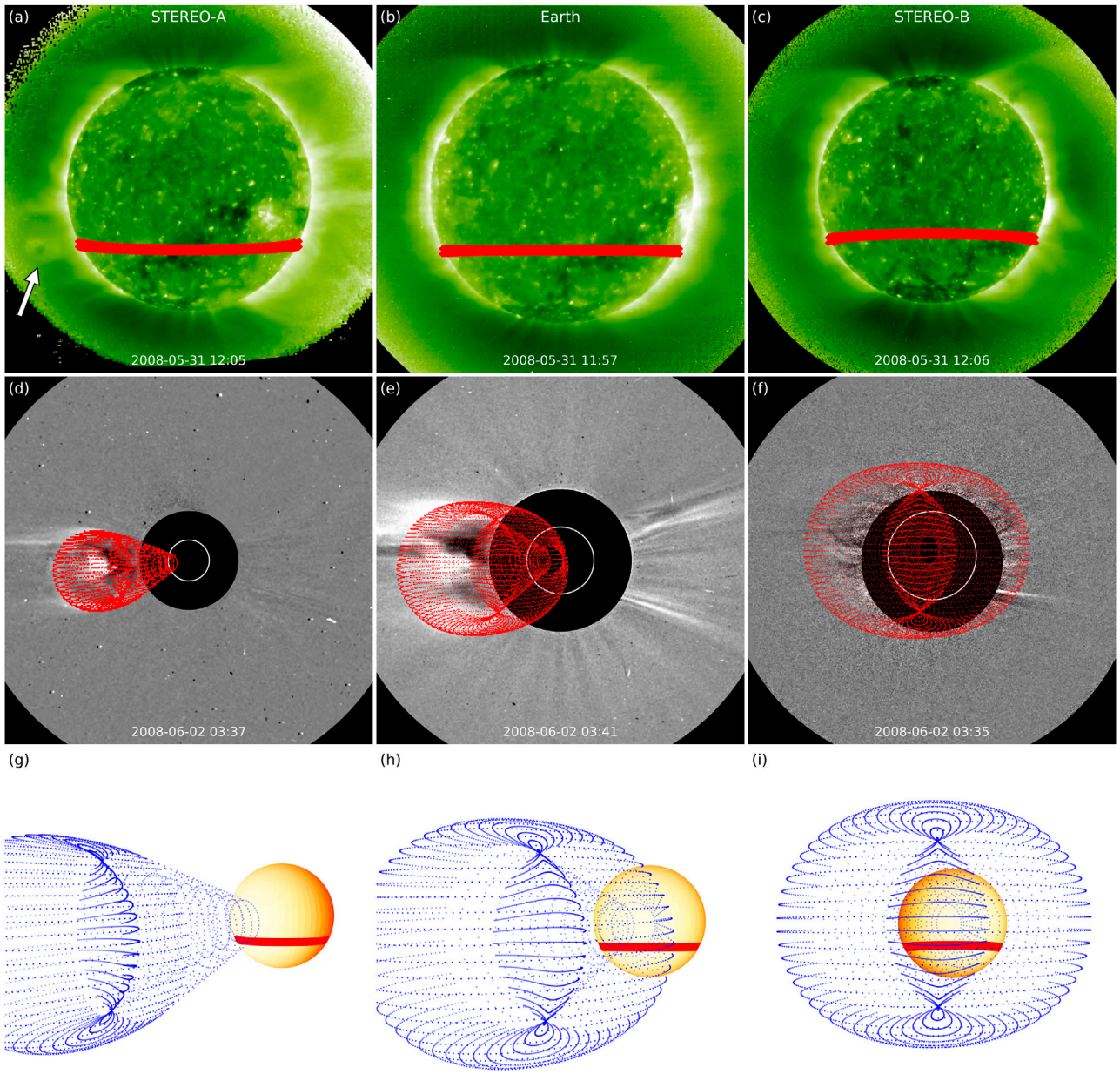

FIGURE 2 | Geometric techniques applied to the 2008 June 1 CME (Event 1). **(A–C)** Latitude (thick red line) of the CME core (indicated with an arrow) projected onto the solar disc as seen by STEREO-A, SOHO, and STEREO-B. **(D–F)** GCS reconstruction applied to the white-light structure seen in STEREO-A, SOHO, and STEREO-B imagery. **(G–I)** The GCS-reconstructed CME displayed together with the "source latitude" in a 3D representation and shown from the three viewpoints of STEREO-A, Earth, and STEREO-B.

difference data, possibly because they are rather weak and hence appear "camouflaged" by other intensity fluctuations on the solar disc. We also note that these signatures appear equally visible in images produced using the other three methods (i.e., intensity, WPE, and MGN). The dimmings seem to be spatially consistent with the approximate CME source region deduced from STEREO-A imagery (see **Supplementary Video S1**), but because they are so faint it is not possible to draw strong conclusions as to their association with the 2008 June 1 CME.

Results from the application of geometric techniques to Event 1 are shown in **Figure 2**. In the top row, the approximate latitude of the footpoints of the flux rope structure seen in off-limb imagery from STEREO-A (marked with an arrow in **Figure 2A**, see also **Supplementary Video S1**) is projected onto the solar disc from all three available viewpoints. The flux rope lifted off from ~ S27°, roughly consistently with the location of the faint dimmings shown in **Figure 1**, which extend between ~S20° and ~S50°. We also perform a GCS reconstruction of the large-scale CME in the corona, shown in the middle row of

Figure 2. We remark that, given that the eruption is a halo from STEREO-B and rather close to the central meridian as seen from Earth, the first available time for a meaningful fitting is ~3.5 h after the first appearance of the CME in the COR2-A field of view. According to GCS results, the CME apex is located at S04°E29° as seen from Earth, which converts into a longitude of E04° as seen from STEREO-B. While the value for latitude is significantly different, the longitude is quite consistent with that of the faint dimmings indicated in the last column of **Figure 1**, which cover a longitudinal span of E25°–W25° in the STEREO-B reference frame (note that the images in the middle row of **Figure 2** and those in the last column of **Figure 1** are taken at the same time). The "source latitude" and the reconstructed GCS wireframe are shown together in a 3D representation in the bottom row of **Figure 2**. It is clear that the CME deflected significantly toward the solar equatorial plane during its early evolution, which is also visible from **Supplementary Video S1** and is consistent with the tendency of CMEs to align themselves with the heliospheric current sheet during solar minimum (e.g., Yurchyshyn et al., 2009; Isavnin et al., 2014). Hence, we conclude that searching for the source of the eruption based on coronagraph images and GCS reconstructions alone would have likely resulted in a somewhat misleading region.

3.2 Event 2: 2011 March 3

The second CME that we analyze in this work (Event 2) erupted on 2011 March 3 and was a stealth event as seen from Earth. This case study was previously analyzed by Pevtsov et al. (2012), Nitta and Mulligan. (2017), O'Kane et al. (2019), and O'Kane et al. (2021b), who all placed the CME source region in the vicinity of active region AR 11165, located close to the central meridian from Earth's perspective. Hence, we investigate this event as a possible case of a more localized, active region stealth CME. At the time of this eruption, STEREO-A was located 87° west of Earth and STEREO-B was positioned 95° east of Earth, meaning that the two spacecraft had a nearly quadrature view of the event from opposite sides. Such observations are shown in **Supplementary Video S3**, which presents simultaneous EUVI and COR1 data from the twin STEREOs. In the video, a large bubble-shaped set of loops can be initially seen to lie off the limb above AR 11165, before slowly inflating (starting around 18:00 UT on March 2) and erupting as a flux rope CME that reached the COR2 field of view around 04:00 UT on March 3. From the STEREO-A perspective, high-altitude post-eruption arcades could be observed after the CME lifted off as AR 11165 rotated into view, forming just above the longer-lived active region loops. It is clear from these observations alone that this CME indeed originated from AR 11165, albeit from higher altitudes than usual and thus away from stronger active region fields. This may be a contributing factor to the stealthiness of the event in on-disc imagery, as suggested by O'Kane et al. (2019).

Images from the Atmospheric Imaging Assembly (AIA; Lemen et al., 2012) instrument onboard SDO corresponding to the eruption period are shown in **Figure 3** and **Supplementary Video S4**. While the intensity, MGN, and WPE images do not show strong eruptive signatures, the difference images in the second row display clearer signs of activity on the solar disc. First of all, an extended pair of dimmings and flare loops at the southern periphery of a large coronal hole in the western hemisphere can be observed in **Figure 3E** (indicated with arrows). These are found to be associated with a filament eruption that occurred on March 1, which possibly destabilized the nearby active region fields and thus triggered the later stealth CME. The successive panels are characterized by a series of dimmings (starting around 22:00 UT on March 2 and marked in panels (F) and (G)) and a strong brightening (starting around 01:00 UT on March 3 and marked in panel (H)) around AR 11165 (indicated with a circle in the first column of **Figure 3**). It can be seen that initially, a pair of dimmings develops north–south of the active region and later a third, more diffuse dimming appears to the east of the fading southern one. Corresponding images obtained with other techniques, on the other hand, show more elusive signatures. A faint pair of dimmings north and south of AR 11165 can be seen in **Supplementary Video S4** (the northern dimming is marked in panels (C), (K), and (O) of **Figure 3**), together with the appearance of a set of loops that seem to correspond to the post-eruption arcade seen by STEREO-A (marked in panels (D), (L), and (P) of **Figure 3**). We emphasize that these signatures are rather weak, and thus without prior knowledge of an eruption having occurred they would have been easily overlooked. Furthermore, we note that although the arcade is well observed in all non-differenced data (i.e., intensity, WPE, and MGN), its fine structure is more easily revealed in images processed with advanced techniques.

Results from the application of geometric techniques to Event 2 are shown in **Figure 4**. Since the pre-eruptive structure was well observed by both STEREO spacecraft, we analyze it using the TP technique. The triangulated balloon-shaped feature is overlaid onto EUVI images in panels (A) and (C). However, despite the favourable viewing perspective of nearly quadrature with Earth from both observers, it is not possible to obtain a meaningful triangulation of the loop onto the solar disc imaged by SDO. This is because the uncertainty associated with the TP technique depends on the angle between the observing spacecraft, and specifically is proportional to the inverse of the sine of the separation angle (Inhester, 2006). In the case of this event, the separation of ~ 180° between the two STEREOs results in a large uncertainty in the east–west direction. Hence, the only information that can be retrieved from the TP technique applied to Event 2 is the latitudinal position of each point part of the triangulated loop, resulting in a vertical bar in **Figure 4B** that is arbitrarily placed at central meridian relative to Earth since its exact longitude is not known. The extent of the loop in the north–south direction is consistent with the location of AR 11165, as expected. Results of the GCS reconstruction are shown in the middle panels of **Figure 4**. Since the CME was well observed as a limb event from both STEREO spacecraft, we perform our reconstruction while the transient is still visible in SECCHI/COR1 and before it reaches the LASCO/C2 field of view, in order to capture the eruption as close as possible to its initial state. This results in a propagation direction of S27°W07° as seen from Earth, rather close to location of AR 11165 at the reconstruction time (S17°W12°), but still suggesting a slight

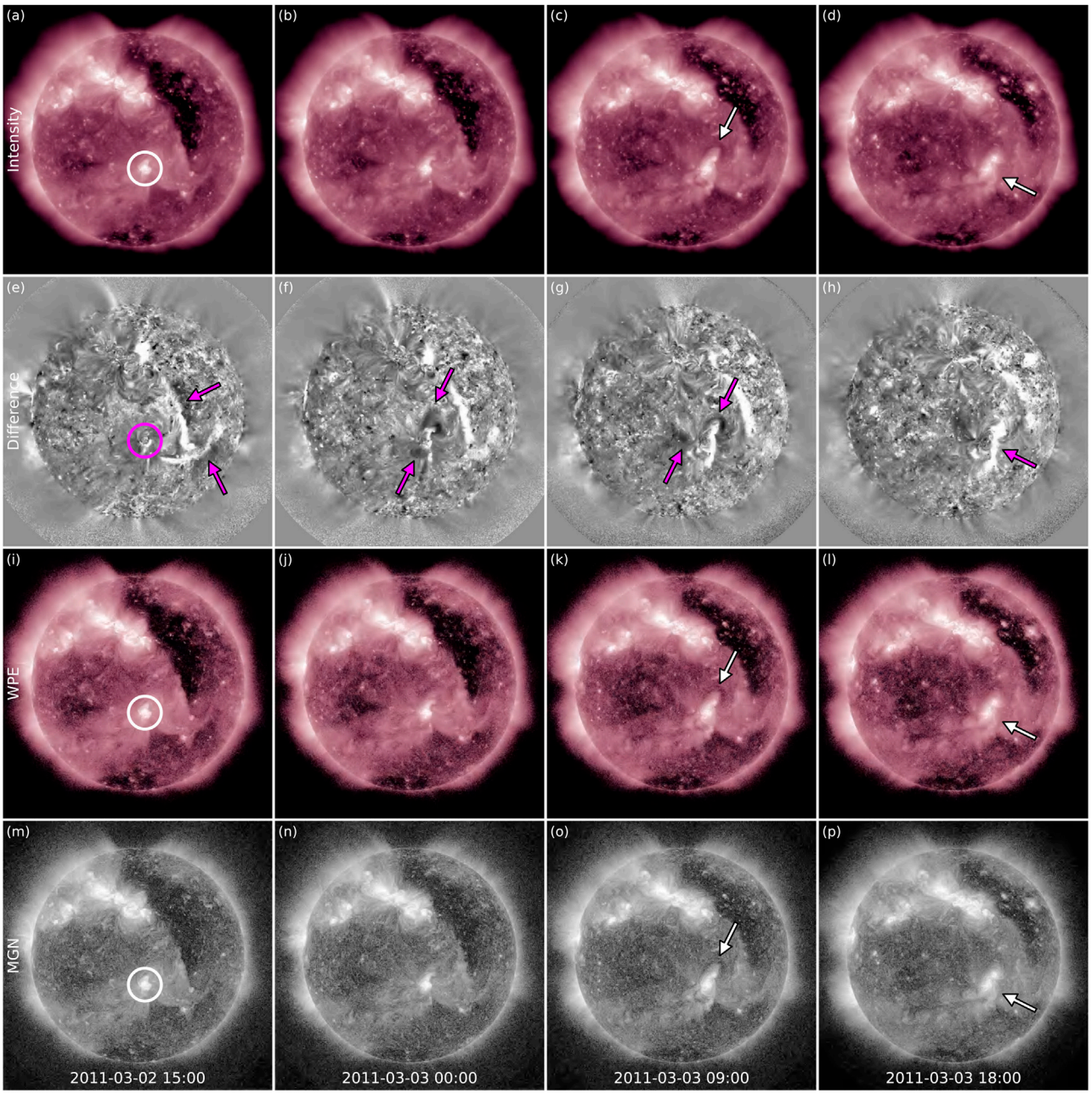

FIGURE 3 | Imaging techniques applied to the 2011 March 3 CME (Event 2). SDO/AIA 211Å images are shown at four different times and processed with four different methods. **(A–D)** Intensity images. **(E–H)** Difference images with fixed Δt = 12 h. **(I–L)** WPE-processed images. **(M–P)** MGN-processed images. AR 11165 is circled in the first column. Dimming and brightening regions are indicated with arrows (see text for details).

southward deflection. Results from the two geometric techniques are shown together in a 3D representation in the bottom panels of **Figure 4**. Despite the issues with the application of the TP technique for this particular event discussed above, the two structures obtained match fairly well. Even if an exact longitude of the source region cannot be retrieved from TP, it may be argued that the viewing geometry of the two STEREO spacecraft implies that the triangulated structure was located close to central meridian. An alternative would be to perform a GCS reconstruction based on the EUV images, as made e.g., by O'Kane et al. (2021a).

3.3 Event 3: 2012 February 4

The third CME that we analyze in this work (Event 3) erupted on 2012 February 4 and was a stealth event as seen from Earth. This CME was first reported by D'Huys et al. (2014) and was further analyzed by Alzate and Morgan. (2017). This event was also well observed off limb by both STEREO spacecraft, with STEREO-A

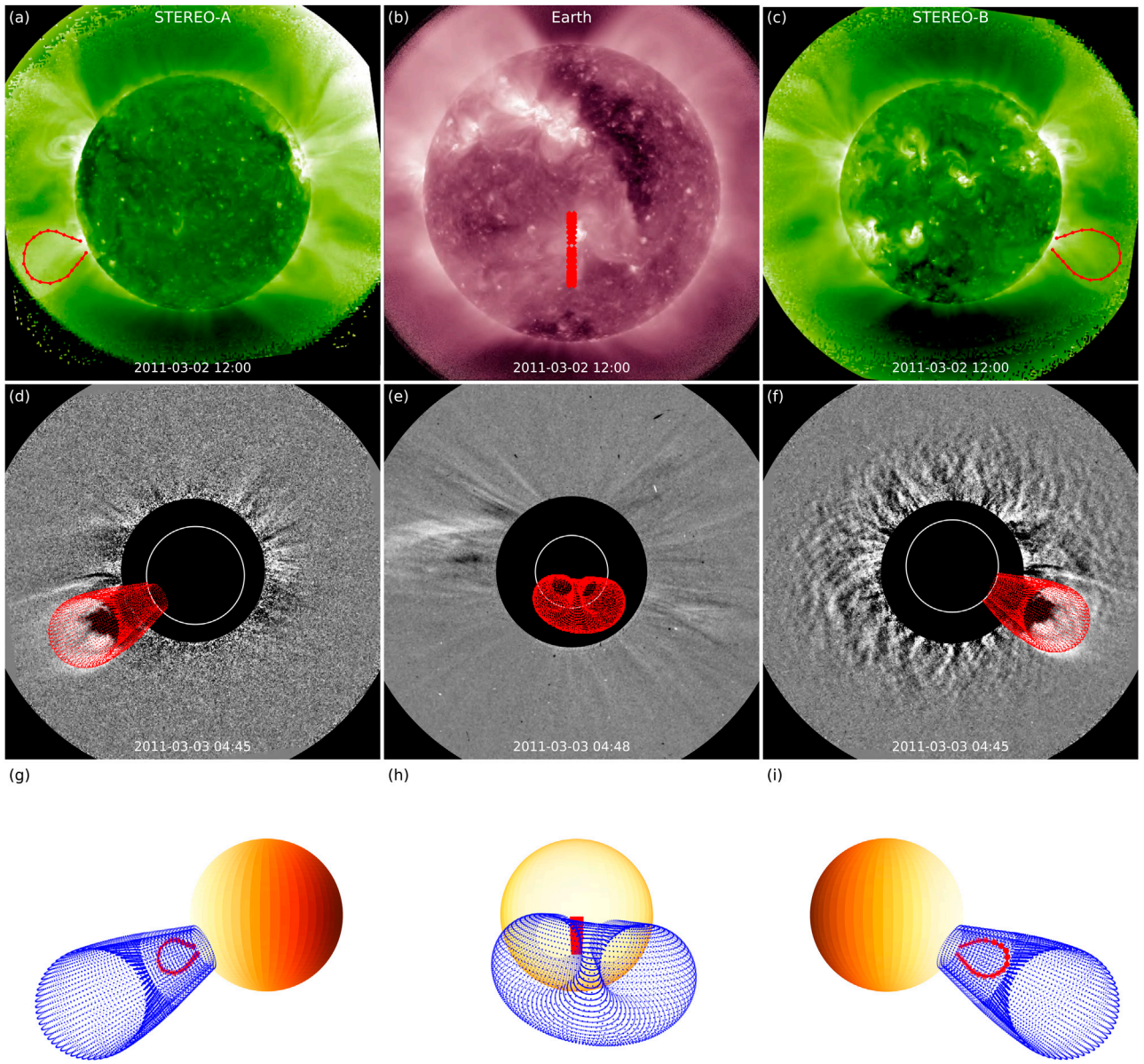

FIGURE 4 | Geometric techniques applied to the 2011 March 3 CME (Event 2). **(A–C)** Application of the TP technique to the pre-eruptive structure. The technique is applied to STEREO-A and STEREO-B images and the latitudinal extent of the triangulated loop is projected onto the SDO/AIA field of view (and displayed over the central meridian). **(D–F)** GCS reconstruction applied to the white-light structure seen in STEREO-A, SOHO, and STEREO-B imagery. **(G–I)** Results of the TP and GCS reconstruction techniques displayed together in a 3D representation and shown from three viewpoints: STEREO-A, Earth, and STEREO-B.

being located 108° west of Earth and STEREO-B being placed 115° east of Earth. Observations from both EUVI and COR1 telescopes are provided in **Supplementary Video S5** and show the CME of interest being ejected off the northeastern limb from STEREO-A's viewpoint and off the northwestern limb from STEREO-B's perspective, indicating that the eruption originated from the Earth-facing Sun. The pre-eruptive structure could be observed for several hours above the limb from both spacecraft before its slow lift-off (starting around 04:00 UT on February 4), indicating that the CME flux rope erupted from unusually high altitudes. The CME reached the COR2 field of view around 10:00 UT on February 4.

SDO/AIA images corresponding to the eruption period are shown in **Figure 5** and **Supplementary Video S6**. As is often the case for stealth CMEs, these data do not show "explosive" eruption signatures that are more typical of active-region CMEs. Nevertheless, it is possible to distinguish rather clear indications that an eruption occurred, as marked with arrows in the difference image in **Figure 5H**. Specifically, we observe an elongated pair of brightenings attributable to flare ribbons, the

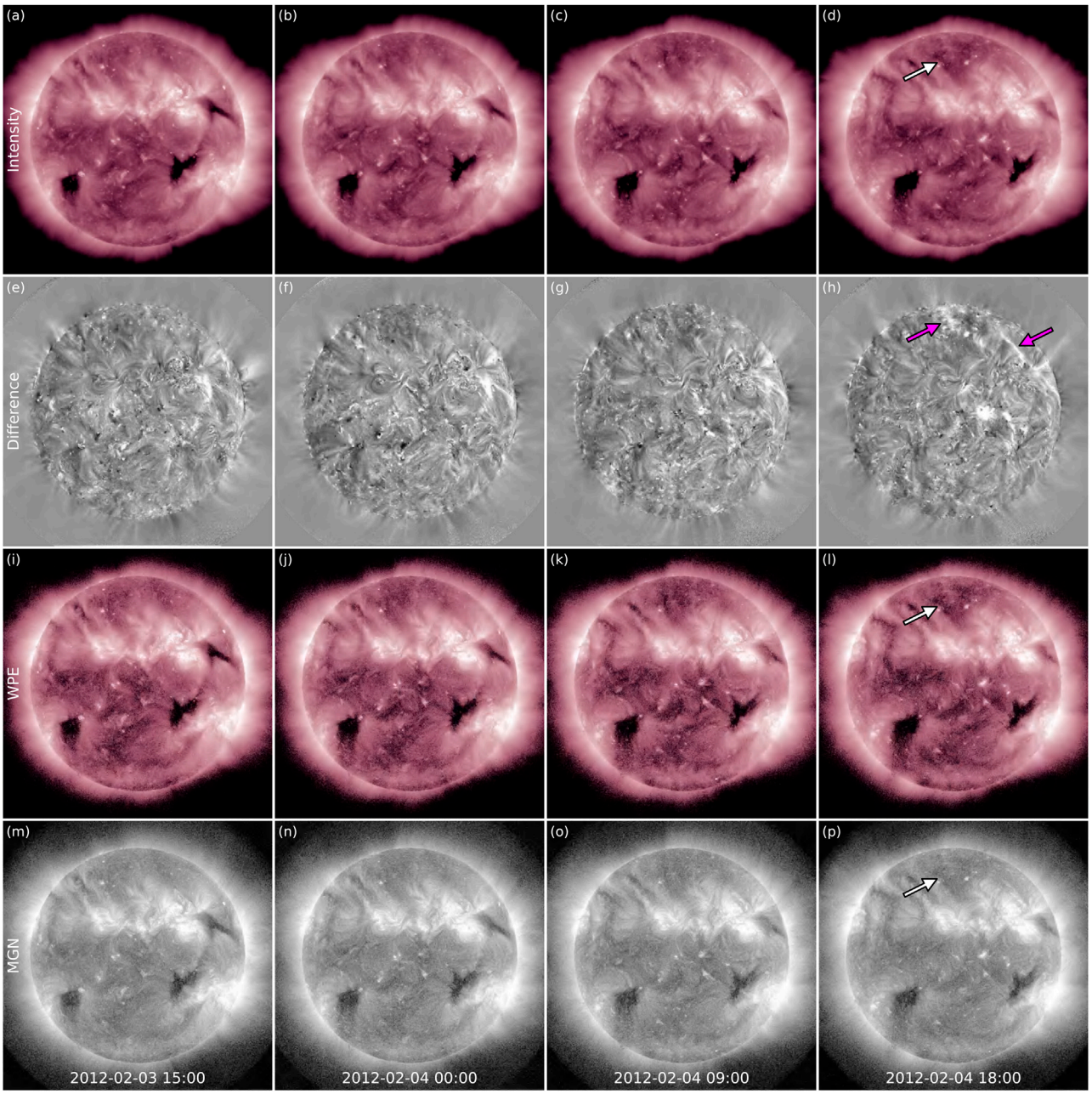

FIGURE 5 | Imaging techniques applied to the 2012 February 4 CME (Event 3). SDO/AIA 211Å images are shown at four different times and processed with four different methods. **(A–D)** Intensity images. **(E–H)** Difference images with fixed Δt = 12 h. **(I–L)** WPE-processed images. **(M–P)** MGN-processed images. Dimming and brightening regions are indicated with arrows (see text for details).

first being rather prominent and close to the northwestern limb and the second being more diffuse and culminating in the vicinity of the solar north pole, with faint loops reminiscent of a post-eruption arcade in between. These features start to develop around 12:00 UT on February 4. In non-differenced images, the westernmost ribbon appears significantly less prominent and the more diffuse one is not visible at all. The structure that we recognized as a post-eruption arcade based on difference images is somewhat visible, but less clearly attributable to a post-eruption arcade. Although all these coronal features can be observed in intensity images as well, their structure appears sharper in WPE- and MGN-processed data. Furthermore, all images reveal an especially faint dimming region close to the solar north pole (with onset around 06:00 UT on February 4 and indicated with arrows in **Figure 5D,L,P**. This darkening feature appears equally visible in intensity, MGN, and WPE images. **Supplementary Video S6** demonstrates that while it is not possible to establish with certainty whether a large-scale eruption occurred from

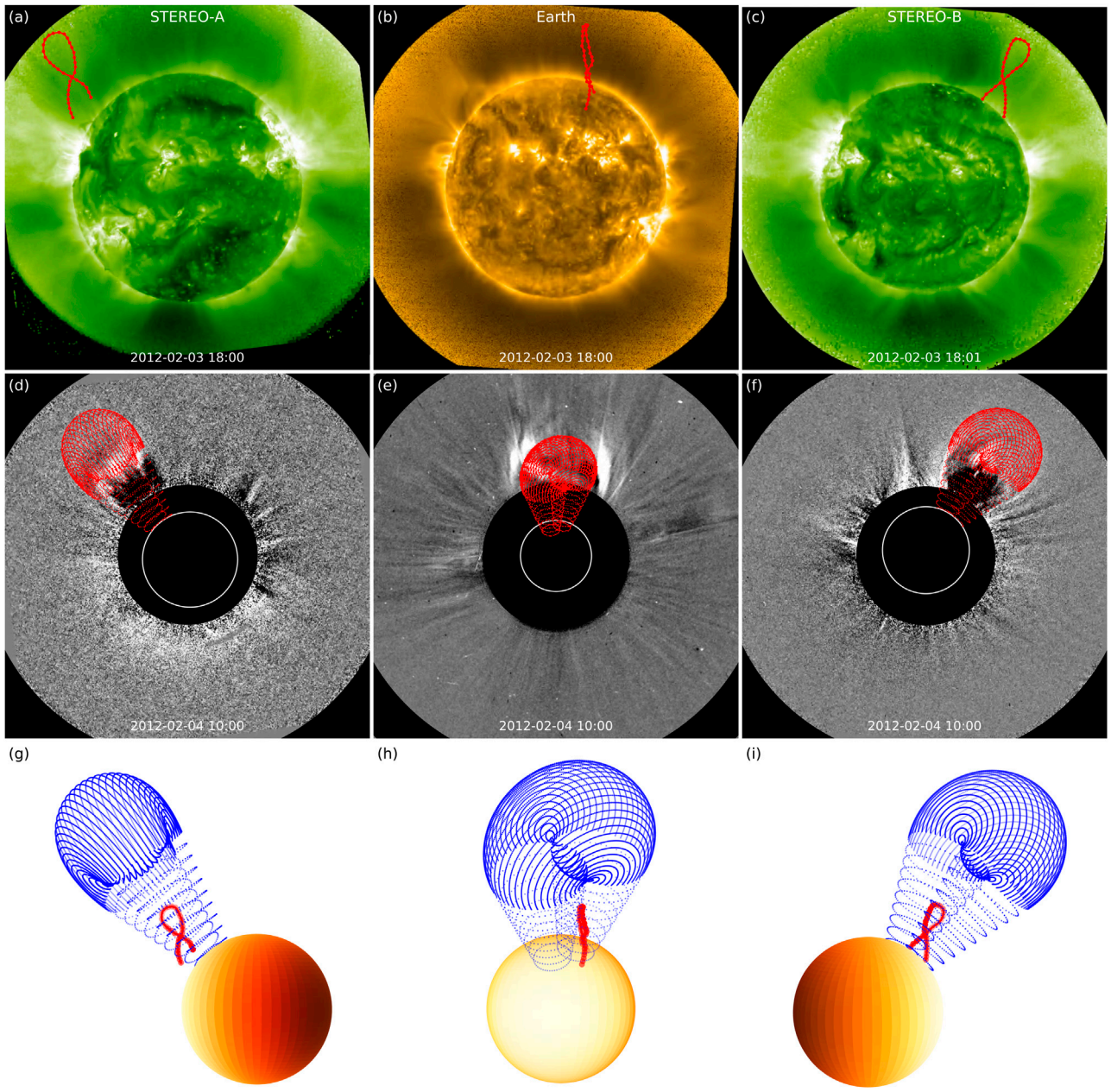

FIGURE 6 | Geometric techniques applied to the 2012 February 4 CME (Event 3). **(A–C)** Application of the TP technique to the pre-eruptive loop structure. The technique is applied to STEREO-A and STEREO-B images and then projected into the PROBA2 field of view. **(D–F)** GCS reconstruction applied to the white-light structure seen in STEREO-A, SOHO, and STEREO-B imagery. **(G–I)** Results of the TP and GCS reconstruction techniques displayed together in a 3D representation and shown from the viewpoints of STEREO-A, Earth, and STEREO-B.

intensity images alone, the development of the various brightening features in difference images unambiguously links the CME seen off limb from the twin STEREOs to a rather defined source region on the Earth-facing disc.

Figure 6 shows the results of the geometric techniques applied to Event 3. Being well-observed off limb from two different perspectives, the 2012 February 4 CME is well suited to be analyzed using the TP technique. Furthermore, the $\sim 135^{\circ}$ separation between the two STEREO spacecraft does not lead to the uncertainty issues that were encountered for Event 2. In the top row of **Figure 6**, a pre-eruptive loop (on 2012 February 3 at 18:00 UT) is traced with the TP technique in 195Å images from both STEREO spacecraft and then projected onto Earth's view, resulting in a structure rooted around N55°W30°. Note that the triangulated loop has been projected into a 174Å image from the Sun Watcher using Active Pixel System Detector and Image Processing (SWAP; Halain et al., 2013; Seaton et al., 2013) telescope onboard the Project for On Board Autonomy 2

(PROBA2; Santandrea et al., 2013) satellite, which has a larger field of view than SDO/AIA. The highest point in the reconstructed loop lies at 1.81 $R_\odot$ from the solar center, confirming that a high-altitude flux rope was involved in the eruption. The middle row of **Figure 6** shows the GCS technique applied to simultaneous images of the white-light CME from the SECCHI/COR2 coronagraphs onboard STEREO and the LASCO/C2 coronagraph onboard SOHO. The CME apex has direction N50°W03°, consistent with a high-latitude eruption. Results from the two reconstructions are combined in the bottom row of **Figure 6**. While the latitudes retrieved from the two methods are in agreement, larger differences are found in the longitudes, which is not surprising considering, for example, that the GCS precision is typically around $\pm 4°$ for latitude and $\pm 17°$ for longitude (Thernisien et al., 2009). Nevertheless, both techniques yield a source region that is (at least to some extent) consistent with the bright features indicated in **Figure 5H**.

3.4 Event 4: 2016 October 9

The fourth CME that we analyze in this work (Event 4) erupted on 2016 October 8 and was a stealth event as seen from Earth. This CME was first reported by Nitta and Mulligan. (2017) and was further analyzed by He et al. (2018). Having taken place in 2016, only the viewpoint from STEREO-A located 148° east of Earth is available since contact with STEREO-B was lost in October 2014. Observations from the EUVI and COR1 telescopes onboard STEREO-A are presented in **Supplementary Video S7**, where the eruption can be seen to originate close to the solar equator off the western limb, corresponding to an ejection off the Earth-facing disc. In addition, the CME cavity extended significantly beyond the central core early in the eruption, suggestive of a much larger-scale event. Loops corresponding to the outer CME rim can be observed to lift off $\sim 25°$ south of the equator around 16:00 UT on October 8, while structures to the north of the central core cannot be discerned with clarity in the EUVI field of view, most likely because of the presence of a bright helmet streamer. The resulting CME reached the COR2 field of view around 22:00 UT on October 8.

Images from SDO/AIA corresponding to the eruption period are shown in **Figure 7** and **Supplementary Video S8**. It is possible to discern signatures of two different eruptions in the presented data. The first can be noted clearly in the figure in difference images (indicated with an arrow in panel (E)) and in all panels in **Supplementary Video S8**, and corresponds to a small filament eruption from the northeastern quadrant. Despite the rather evident low-coronal signatures, this eruption does not correspond to the CME seen off limb in STEREO-A imagery (see **Supplementary Video S7**) because of its timing (~14:00 UT on October 8, several hours too early compared to its first appearance in COR1), its source region ($\sim 40°$ north of the equator), and its localized nature (in contrast to the large-scale CME observed by STEREO-A). Nevertheless, it is possible that this minor eruption destabilized the overlying field(s) and thus facilitated the onset of the subsequent, larger CME. Over the following hours, starting around 18:00 UT on October 8, a pair of coronal dimmings developed, marked by arrows in **Figure 7**D and evident in **Supplementary Video S8**. In the difference images in panels (F) and (G), it is evident that the eastern dimming appears deeper than the western one. In data processed with WPE or MGN in panels (A) to (L) and (M) to (P), respectively, the progressive darkening of these two areas over the presented interval shows that the dimmings developed over a remarkably long time span (i.e., even longer than the Δt = 12 h used here for difference images). We do not note differences in the appearance of the dimmings in the intensity, WPE, and MGN images. Their extent in latitude (from ~N02° to ~S22°) is in agreement with the location of the off-limb signatures observed from the STEREO-A viewpoint and shown in **Supplementary Video S8**.

Results from applying geometric techniques to Event 4 are shown in **Figure 8**. In the top row, the red line indicates the approximate latitude of the CME core as derived from STEREO-A observations (marked with an arrow in **Figure 8A**, see also **Supplementary Video S7**) projected onto the solar disc from both available viewpoints. The latitude of ~S02° is rather consistent with the dimming locations, but less compatible with the GCS reconstruction shown in the middle row of **Figure 8**, which gives a CME apex propagation direction of N12°E05°, indicating a significant deflection and/or non-radial propagation of the structure toward the north after eruption (this aspect can also be noted in **Supplementary Video S8**). The dimmings covered a longitudinal span of E44°–W22° at the time of the GCS reconstruction, highlighting the large-scale nature of the event, and were centered around E12°, i.e., well within the GCS uncertainties mentioned in **Section 3.3**. As was the case for Event 2 and Event 3, this eruption can be convincingly linked to low-coronal signatures (albeit weak), and as was the case for Event 1, relying uniquely on coronagraph imagery and GCS reconstructions would have resulted in a somewhat misleading estimated source region. The fact that this CME was a full halo as seen by SOHO and that only two viewpoints were available certainly contributed to the late reconstruction time, when the apex was already at $\sim 10\,R_\odot$. Hence, the geometric parameters were only determined after the CME had already experienced significant alterations to its trajectory.

4 DISCUSSION AND CONCLUSION

In this work, we have presented and analyzed four stealth CMEs that presented diverse characteristics: a classic streamer blowout (Event 1), a CME originating from an active region (Event 2), a flux rope lying at unusually high altitudes prior to eruption (Event 3), and a significantly large-scale event (Event 4). These case studies were also characterized by different viewing geometries between the "stealthy perspective" (on the solar disc) and the off-limb observer(s): Event 1 had STEREO-A $\sim 50°$ away from STEREO-B, Event 2 had the STEREOs nearly in quadrature with Earth, Event 3 had the STEREOs $\sim 110°$ away from Earth, and Event 4 had STEREO-A separated by $\sim 150°$ from Earth. We have investigated these CMEs using remote-sensing imaging and geometric techniques in order to determine their corresponding source region on the Sun. Our analysis was based

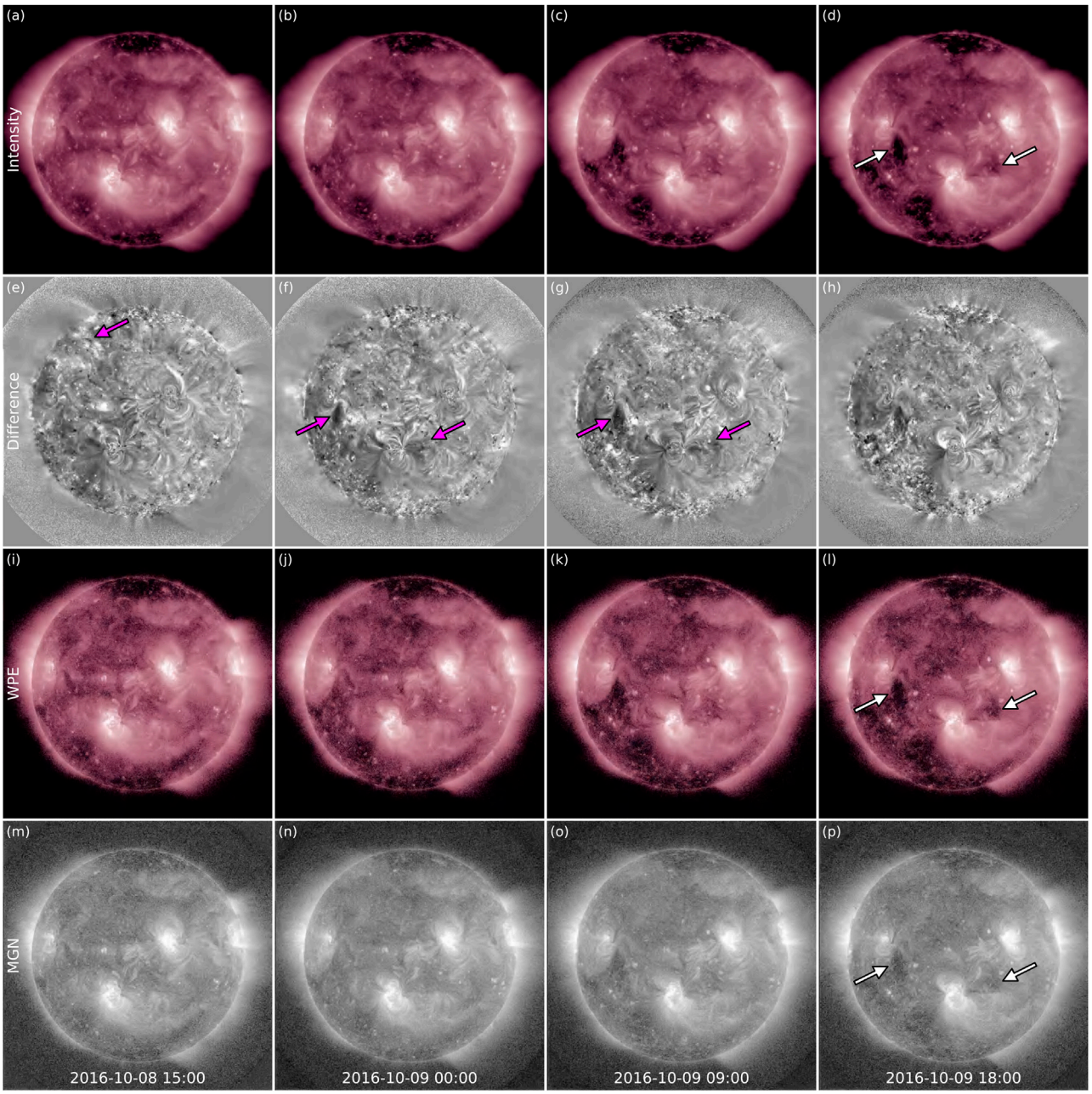

FIGURE 7 | Imaging techniques applied to the 2016 October 8 CME (Event 4). SDO/AIA 211Å images are shown at four different times and processed with four different methods. **(A–D)** Intensity images. **(E–H)** Difference images with fixed Δt = 12 h. **(I–L)** WPE-processed images. **(M–P)** MGN-processed images. Dimming and brightening regions are indicated with arrows (see text for details).

on EUV images of the solar disc in the 195 Å (STEREO) and 211 Å (SDO) channels, especially suited to detect dimming and brightening regions associated with low-coronal signatures of CMEs (e.g., Nitta and Mulligan, 2017), together with white-light images of the solar corona. Since for all events an approximate region of origin was known due to off-limb views from additional viewpoints, the motivation for our analysis was to test and demonstrate the effectiveness of the different techniques over a range of events with different properties and observation geometries. Our main findings are summarized in **Table 1**.

Analysis of solar disc imagery with various image processing techniques revealed the presence of signatures for all events, as shown in **Table 1**, albeit with different confidence levels. The most convincing evidence was found for Event 2 and Event 3, while Event 4 was associated with weak but reasonable signatures and Event 1 was characterized by the largest uncertainties. At least

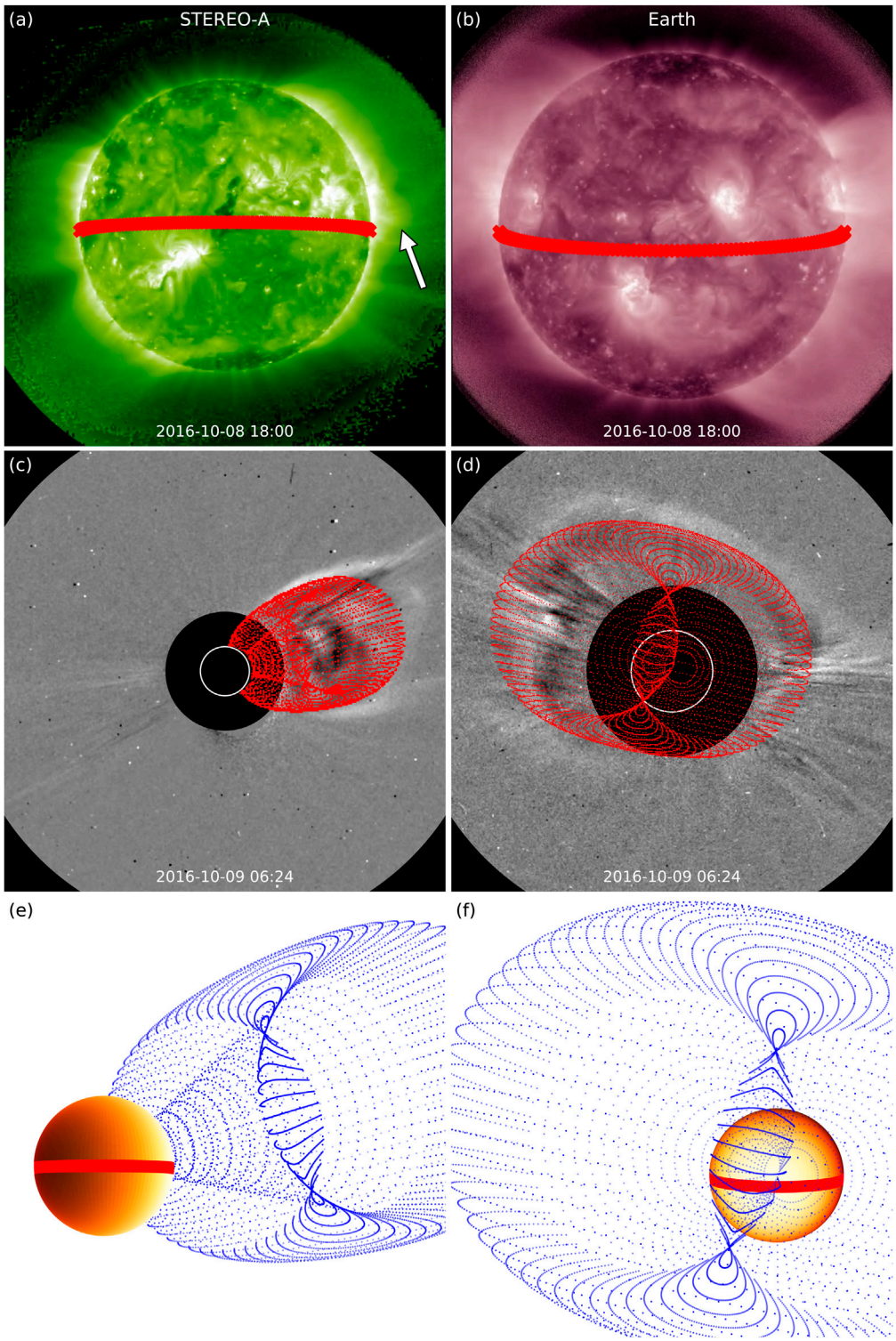

FIGURE 8 | Geometric techniques applied to the 2016 October 8 CME (Event 4). **(A–B)** Latitude (thick red line) of the CME core (indicated with an arrow) projected onto the solar disc as seen by STEREO-A and SDO. **(C–D)** GCS reconstruction applied to the white-light structure seen in STEREO-A and SOHO. **(E–F)** The GCS-reconstructed CME displayed together with the "source latitude" from **(A)** and **(B)** in a 3D representation and shown from the two viewpoints of STEREO-A and Earth.

TABLE 1 | Results from applying different imaging and geometric techniques to the events under study. For the imaging techniques, the observed eruption signatures are indicated, with A = arcade, B = brightening, and D = dimming. The upper cases denote strong signatures, while the lower cases denote only weak signatures. For the geometric techniques, it is indicated whether the TP method could be applied (N/A for events that only had one off-limb view available) and which features could be triangulated, as well as the radial distance from the Sun of the CME apex at which the earliest meaningful GCS reconstruction could be performed. The "latitude projection" scheme could in principle be applied to all events under study, since it only requires one off-limb viewpoint of the eruption, hence it is not shown here.

	—	Imaging				Geometric	
—	—	Intens	Diff	MGN	WPE	TP	GCS
E1	Streamer blowout	d	d	d	d	N/A	~ 7 $R_\odot$
E2	AR eruption	A,d	a,B,D	A,d	A,d	Lat only	~ 3 $R_\odot$
E3	High flux rope	b,d	A,B,d	b,d	b,d	Full loop	~ 4 $R_\odot$
E4	Large-scale CME	D	D	D	D	N/A	~ 10 $R_\odot$

according to the small sample investigated here, it seems that the main factor contributing to the level of "stealthiness" is the spatial extent of the eruption rather than the altitude from which a CME lifts off (in particular, compare the size of the on-disc signatures for Event 1 and Event 4 with those for Event 2 and Event 3, which are significantly more localised). Another aspect to note is that the eruption associated with the weakest signatures (Event 1) was also the only event that did not feature a nearby active region or area of strong magnetic fields. Regarding the image processing techniques used, it is evident that difference images with large temporal separations revealed the clearest eruptive signatures, as was also reported by Nitta and Mulligan. (2017). Moreover, we note that even if dimmings are often evident enough in intensity data, brightenings tend to appear overwhelmingly clearer in difference images (see Event 2 and Event 3). In this work, we have used a fixed $\Delta t = 12$ h for all events, but even longer separations may be explored in the case of eruptions that develop extremely slowly (as for Event 1 and Event 4), although artifacts at the solar limb would also become more prominent and problematic. In this regard, it should be noted that difference images are particularly prone to spurious effects due to spatio-temporal interference; i.e., dimming and brightening features may correspond to "true" dimmings and brightenings as well as moving structures over long time scales. Thus, difference images may be complemented with non-differenced data, which should be used to properly interpret the identified large-scale changes and connect them to well-defined activity on the Sun. Furthermore, we did not find substantial differences in the features revealed in "normal" intensity images and those produced by more advanced processing techniques for the cases that were only associated with (more or less defined) dimmings, i.e. Event 1 and Event 4. Since the main purpose of these methods is to sharpen coronal features and accentuate small-scale variations, it is not surprising that they are as powerful as non-processed images when such structures and alterations are missing in the first place, i.e. in the case of the most problematic events. This overall conclusion is in agreement with O'Kane et al. (2021a), who studied a stealth CME off limb (from a secondary viewpoint) using MGN, but found that this technique did not also reveal the corresponding signatures on disc, which were however completely elusive to other data sets as well. On the other hand, the events that were associated with more prominent structural changes in the corona, i.e. Event 2 and Event 3, showed significantly enhanced features in WPE and MGN imagery in comparison to intensity data. This allows for deeper analysis of the onset and signatures of these eruptions, which may in turn advance understanding of at least a subset of elusive events. Hence, this work demonstrates that advanced image processing techniques are also applicable to a portion of large-scale stealth CMEs observed against the solar disc, in addition to their usefulness for investigating small, short-lived activity and off-limb events that has been shown in previous studies (e.g., Alzate and Morgan, 2017; O'Kane et al., 2019; Liewer et al., 2021). In conclusion, our recommendation for identifying and analyzing the origins of stealth CMEs on the solar disc is a multi-step approach: 1) use difference images to easily single out large-scale changes, 2) use intensity data to properly interpret difference images and rule out artifacts, and 3) if coronal features such as brightenings, loops, and ribbons can be identified, use advanced image processing techniques such as WPE and MGN to analyze their fine structure in deeper detail.

Analysis of the events in this study with the aid of various geometric techniques has revealed that triangulation and reconstruction methods can help trace an eruption back to its source as long as they are used when the CME is as close as possible to the Sun. Given that most CME deflections and other non-radial propagation effects take place below a few solar radii (e.g., Kay et al., 2015; Kay and Opher, 2015; Liewer et al., 2015), it is crucial to determine the geometric parameters before the most dramatic evolution has occurred. In this sense, the CME propagation direction with respect to the observers plays a central role, as can be seen from the reconstructed CME apex heights shown in **Table 1**: among the cases investigated here, the best scenario was achieved for Event 2 and Event 3, in which the CMEs were propagating in directions well away from at least two viewpoints, enabling a meaningful GCS reconstruction to be made early on. The least favourable configuration happened for Event 4, where the CME was a full halo from one viewpoint and only a second observer was available, thus the apex was already at $\sim 10\,R_\odot$ at the time of the performed GCS fitting. In this case, the resulting CME reconstruction strongly hints at an eruption that originated from the northern hemisphere. Hence, without complementary observations from STEREO-A, the source of the white-light structure might have been erroneously attributed to the previous small filament eruption preceding the "main" event. Hence, our recommendation for tracing a CME observed in white light back to its elusive source is to take into consideration the viewing configuration of the event and to be more cautious the farther the reconstructed CME is from the Sun. The TP technique, on the other hand, is quite efficient in triangulating a pre-eruptive structure and/or tracing an eruption back to a source, but is more strongly dependent on the viewing geometry (see **Table 1**). Excluding cases in which a spacecraft separation of $\sim 180^\circ$ does not allow for a unique solution (see e.g. Event 2), the method requires two well-separated spacecraft to

observe a particular feature simultaneously, so it is not applicable to cases in which an eruption is behind the limb relative to at least one observer. Of course, being able to analyze a stealth CME with triangulation and reconstruction methods implies the availability of additional viewpoints to start with. Apart from helping to discern whether a CME is stealthy or simply far-sided, remote-sensing measurements away from the Sun–observer line may help identify the source of an elusive event in a more or less straightforward way, as was the case for the sample events analyzed in this study. Unfortunately after the loss of STEREO-B and with STEREO-A slowly approaching Earth, the capability to observe stealth CMEs from a viewpoint well-separated from the Sun–Earth line will be lost at least for a while. In the longer term, observations away from the Sun–Earth line, made for example by a STEREO-like, polar, or L4/L5 mission, would help to provide this capability (e.g., Vourlidas, 2015; Lavraud et al., 2016; Gibson et al., 2018; Bemporad, 2021).

The four events analyzed here took place during different stages of the solar cycle, with Event 1 happening at solar minimum, Event 2 and Event 3 close to solar maximum, and Event 4 in the midst of the descending phase of the cycle. Together with the different characteristics of each eruption summarized in **Table 1**, this indicates that stealth CMEs are not restricted to a particular set of source regions or solar activity period. Hence, although the long-standing question on the fundamental nature of stealth CMEs has not been officially answered yet, this study emphasizes that the characteristics of these events can be as diverse as those of "ordinary" eruptions. Other methods that may help advance current understanding of stealth CMEs include the study of the coronal environment from which these eruptions originate, as was done by O'Kane et al. (2021b) for Event 2 in this work. The authors concluded that flux emergence and magnetic reconnection episodes were observed in the CME source region prior to eruption, which led to the formation of the structure that later left the Sun as a stealth event, and that a high-altitude null point was revealed by photospheric magnetic field extrapolations of the pre-eruptive configuration. Moreover, images of the solar disc taken closer than 1 AU may more easily reveal the eruptive signatures of stealth CMEs. The Solar Orbiter (Müller et al., 2020) spacecraft, launched in February 2020 to orbit the Sun as close as ~ 0.3 AU and equipped with an EUV instrument as well as a coronagraph, will possibly be able to provide answers in this regard. Finally, it is worth remarking on the impact of stealth CMEs in the wider context of space weather. These events are occasionally capable of driving large geomagnetic disturbances (e.g., Nitta and Mulligan, 2017), so it is important to develop a framework in which they can be fully observed and forecast. One major issue in this sense is that the lack of well-defined low-coronal signatures does not allow for unambiguous analysis of the remote-sensing proxies that are necessary to determine the CME pre-eruptive structure and configuration (e.g., Palmerio et al., 2017). Nevertheless, successfully identifying the source region of a stealth CME represents a first step toward providing more reliable predictions.

DATA AVAILABILITY STATEMENT

All the solar data available in this study can be accessed at the Virtual Solar Observatory (http://sdac.virtualsolar.org/cgi/search). These data were visualised, processed, and analysed using Python's SunPy package (SunPy Community et al., 2020), IDL SolarSoft (Freeland and Handy, 1998), and the ESA JHelioviewer software (Müller et al., 2017). The original contributions presented in the study are included in the article/**Supplementary Material**, further inquiries can be directed to the corresponding author.

AUTHOR CONTRIBUTIONS

EP and NN selected the events examined in this study and organized the various aspects of the analysis. EP led the investigation and wrote the draft manuscript. All authors participated in the discussions, read and critically reviewed the manuscript, approved the final version, and agreed to be accountable for all aspects of the work.

FUNDING

EP was supported by the NASA Living With a Star Jack Eddy Postdoctoral Fellowship Program, administered by UCAR's Cooperative Programs for the Advancement of Earth System Science (CPAESS) under award no. NNX16AK22G. NN and TM acknowledge support from NASA grant no. NNX17AB73G. NN was partially supported by the NASA AIA contract no. NNG04EA00C and the NASA STEREO mission under NRL contract no. N00173-02-C-2035. MM and AZ thank the European Space Agency (ESA) and the Belgian Federal Science Policy Office (BELSPO) for their support in the framework of the PRODEX Programme. JO thanks the STFC for support via funding given in her PHD studentship. IR was supported by the STEREO mission and NASA program NNH17ZDA001N-LWS. SY would like to acknowledge NERC for funding via the SWIMMR Aviation Risk and Modelling (SWARM) Project, grant no. NE/V002899/1.

ACKNOWLEDGMENTS

The authors are pleased to acknowledge the International Space Science Institute (ISSI) for their support of International Team no. 415, "Understanding the Origins of Problem Geomagnetic Storms" (https://www.issibern.ch/teams/geomagstorm/), from which this work originated.

SUPPLEMENTARY MATERIAL

The Supplementary Material for this article can be found online at: https://www.frontiersin.org/articles/10.3389/fspas.2021.695966/full#supplementary-material

REFERENCES

Alzate, N., and Morgan, H. (2017). Identification of Low Coronal Sources of "Stealth" Coronal Mass Ejections Using New Image Processing Techniques. *Astrophys. J.* 840, 103. doi:10.3847/1538-4357/aa6caa

Attrill, G. D. R., Harra, L. K., van Driel-Gesztelyi, L., and Démoulin, P. (2007). Coronal "Wave": Magnetic Footprint of a Coronal Mass Ejection? *Astrophys. J.* 656, L101–L104. doi:10.1086/512854

Attrill, G. D. R., and Wills-Davey, M. J. (2010). Automatic Detection and Extraction of Coronal Dimmings from SDO/AIA Data. *Sol. Phys.* 262, 461–480. doi:10.1007/s11207-009-9444-4

Bemporad, A., Mierla, M., and Tripathi, D. (2011). Rotation of an Erupting Filament Observed by the STEREO EUVI and COR1 Instruments. *Astron. Astrophys.* 531, A147. doi:10.1051/0004-6361/201016297

Bemporad, A. (2021). Possible Advantages of a Twin Spacecraft Heliospheric Mission at the Sun-Earth Lagrangian Points L4 and L5. *Front. Astron. Space Sci.* 8, 627576. doi:10.3389/fspas.2021.627576

Brueckner, G. E., Howard, R. A., Koomen, M. J., Korendyke, C. M., Michels, D. J., Moses, J. D., et al. (1995). The Large Angle Spectroscopic Coronagraph (LASCO). *Sol. Phys.* 162, 357–402. doi:10.1007/BF0073343410.1007/978-94-009-0191-9_10

Burlaga, L. F., Klein, L., Sheeley, N. R., Howard, R. A., Koomen, M. J., et al. (1982). A Magnetic Cloud and a Coronal Mass Ejection. *Geophys. Res. Lett.* 9, 1317–1320. doi:10.1029/GL009i012p01317

Cane, H. V., and Richardson, I. G. (2003). Interplanetary Coronal Mass Ejections in the Near-Earth Solar Wind during 1996-2002. *J. Geophys. Res.* 108, 1156. doi:10.1029/2002JA009817

SunPy Community, Barnes, W. T., Bobra, M. G., Christe, S. D., Freij, N., Hayes, L. A., et al. (2020). The SunPy Project: Open Source Development and Status of the Version 1.0 Core Package. *Astrophys. J.* 890, 68. doi:10.3847/1538-4357/ab4f7a

D'Huys, E., Seaton, D. B., Poedts, S., and Berghmans, D. (2014). Observational Characteristics of Coronal Mass Ejections without Low-Coronal Signatures. *Astrophys. J.* 795, 49. doi:10.1088/0004-637X/795/1/49

Delaboudinière, J.-P., Artzner, G. E., Brunaud, J., Gabriel, A. H., Hochedez, J. F., Millier, F., et al. (1995). EIT: Extreme-Ultraviolet Imaging Telescope for the SOHO Mission. *Sol. Phys.* 162, 291–312. doi:10.1007/BF00733432

Demastus, H. L., Wagner, W. J., and Robinson, R. D. (1973). Coronal Disturbances. *Sol. Phys.* 31, 449–459. doi:10.1007/BF00152820

Domingo, V., Fleck, B., and Poland, A. I. (1995). The SOHO Mission: an Overview. *Sol. Phys.* 162, 1–37. doi:10.1007/BF00733425

Freeland, S. L., and Handy, B. N. (1998). Data Analysis with the SolarSoft System. *Sol. Phys.* 182, 497–500. doi:10.1023/A:1005038224881

Freiherr von Forstner, J. L., Dumbović, M., Möstl, C., Guo, J., Papaioannou, A., Elftmann, R., et al. (2021). Radial Evolution of the April 2020 Stealth Coronal Mass Ejection between 0.8 and 1 AU. Comparison of Forbush Decreases at Solar Orbiter and Near the Earth. *Astron. Astrophys.*. doi:10.1051/0004-6361/202039848

Gibson, S. E., Foster, D., Burkepile, J., de Toma, G., and Stanger, A. (2006). The Calm before the Storm: The Link between Quiescent Cavities and Coronal Mass Ejections. *Astrophys. J.* 641, 590–605. doi:10.1086/500446

Gibson, S. E., Vourlidas, A., Hassler, D. M., Rachmeler, L. A., Thompson, M. J., Newmark, J., et al. (2018). Solar Physics from Unconventional Viewpoints. *Front. Astron. Space Sci.* 5, 32. doi:10.3389/fspas.2018.00032

Gosling, J. T., Hildner, E., MacQueen, R. M., Munro, R. H., Poland, A. I., and Ross, C. L. (1974). Mass Ejections from the Sun: A View from Skylab. *J. Geophys. Res.* 79, 4581–4587. doi:10.1029/JA079i031p04581

Gosling, J. T. (1975). Large-scale Inhomogeneities in the Solar Wind of Solar Origin. *Rev. Geophys.* 13, 1053–1058. doi:10.1029/RG013i003p01053

Green, L. M., Kliem, B., Török, T., van Driel-Gesztelyi, L., and Attrill, G. D. R. (2007). Transient Coronal Sigmoids and Rotating Erupting Flux Ropes. *Sol. Phys.* 246, 365–391. doi:10.1007/s11207-007-9061-z

Halain, J.-P., Berghmans, D., Seaton, D. B., Nicula, B., De Groof, A., Mierla, M., et al. (2013). The SWAP EUV Imaging Telescope. Part II: In-Flight Performance and Calibration. *Sol. Phys.* 286, 67–91. doi:10.1007/s11207-012-0183-6

He, W., Liu, Y. D., Hu, H., Wang, R., and Zhao, X. (2018). A Stealth CME Bracketed between Slow and Fast Wind Producing Unexpected Geoeffectiveness. *Astrophys. J.* 860, 78. doi:10.3847/1538-4357/aac381

Howard, R. A., Michels, D. J., Sheeley, N. R. J., and Koomen, M. J. (1982). The Observation of a Coronal Transient Directed at Earth. *Astrophys. J.* 263, L101–L104. doi:10.1086/183932

Howard, R. A., Moses, J. D., Vourlidas, A., Newmark, J. S., Socker, D. G., Plunkett, S. P., et al. (2008). Sun Earth Connection Coronal and Heliospheric Investigation (SECCHI). *Space Sci. Rev.* 136, 67–115. doi:10.1007/s11214-008-9341-4

Howard, T. A., and Harrison, R. A. (2013). Stealth Coronal Mass Ejections: A Perspective. *Sol. Phys.* 285, 269–280. doi:10.1007/s11207-012-0217-0

Hudson, H. S., Acton, L. W., Hirayama, T., and Uchida, Y. (1992). White-light Flares Observed by YOHKOH. *Pub. Astron. Soc. Jpn.* 44, L77–L81.

Hudson, H. S., and Cliver, E. W. (2001). Observing Coronal Mass Ejections without Coronagraphs. *J. Geophys. Res.* 106, 25199–25214. doi:10.1029/2000JA90402610.1029/2000ja004026

Illing, R. M. E., and Hundhausen, A. J. (1985). Observation of a Coronal Transient from 1.2 to 6 Solar Radii. *J. Geophys. Res.* 90, 275–282. doi:10.1029/JA090iA01p00275

Inhester, B. (2006). Stereoscopy Basics for the STEREO mission. arXiv e-prints, astro-ph/0612649

Isavnin, A., Vourlidas, A., and Kilpua, E. K. J. (2014). Three-Dimensional Evolution of Flux-Rope CMEs and its Relation to the Local Orientation of the Heliospheric Current Sheet. *Sol. Phys.* 289, 2141–2156. doi:10.1007/s11207-013-0468-4

Kahler, S. W., and Hudson, H. S. (2001). Origin and Development of Transient Coronal Holes. *J. Geophys. Res.* 106, 29239–29247. doi:10.1029/2001JA000127

Kaiser, M. L., Kucera, T. A., Davila, J. M., St. Cyr, O. C. O. C., Guhathakurta, M., and Christian, E. (2008). The STEREO Mission: An Introduction. *Space Sci. Rev.* 136, 5–16. doi:10.1007/s11214-007-9277-0

Kay, C., Opher, M., and Evans, R. M. (2015). Global Trends of CME Deflections Based on CME and Solar Parameters. *Astrophys. J.* 805, 168. doi:10.1088/0004-637X/805/2/168

Kay, C., and Opher, M. (2015). The Heliocentric Distance where the Deflections and Rotations of Solar Coronal Mass Ejections Occur. *Astrophys. J.* 811, L36. doi:10.1088/2041-8205/811/2/L36

Kilpua, E. K. J., Mierla, M., Zhukov, A. N., Rodriguez, L., Vourlidas, A., and Wood, B. (2014). Solar Sources of Interplanetary Coronal Mass Ejections during the Solar Cycle 23/24 Minimum. *Sol. Phys.* 289, 3773–3797. doi:10.1007/s11207-014-0552-4

Koomen, M. J., Detwiler, C. R., Brueckner, G. E., Cooper, H. W., and Tousey, R. (1975). White Light Coronagraph in OSO-7. *Appl. Opt.* 14, 743–751. doi:10.1364/AO.14.000743

Lavraud, B., Liu, Y., Segura, K., He, J., Qin, G., Temmer, M., et al. (2016). A Small mission Concept to the Sun-Earth Lagrangian L5 point for Innovative Solar, Heliospheric and Space Weather Science. *J. Atmos. Solar-Terrestrial Phys.* 146, 171–185. doi:10.1016/j.jastp.2016.06.004

Lemen, J. R., Title, A. M., Akin, D. J., Boerner, P. F., Chou, C., Drake, J. F., et al. (2012). The Atmospheric Imaging Assembly (AIA) on the Solar Dynamics Observatory (SDO). *Sol. Phys.* 275, 17–40. doi:10.1007/s11207-011-9776-8

Liewer, P. C., Hall, J. R., Howard, R. A., De Jong, E. M., Thompson, W. T., and Thernisien, A. (2011). Stereoscopic Analysis of STEREO/SECCHI Data for CME Trajectory Determination. *J. Atmos. Solar-Terrestrial Phys.* 73, 1173–1186. doi:10.1016/j.jastp.2010.09.004

Liewer, P. C., Qiu, J., Vourlidas, A., Hall, J. R., and Penteado, P. (2021). Evolution of a Streamer-Blowout CME as Observed by Imagers on Parker Solar Probe and the Solar Terrestrial Relations Observatory. *Astron. Astrophys.* 650, A32. doi:10.1051/0004-6361/202039641

Liewer, P., Panasenco, O., Vourlidas, A., and Colaninno, R. (2015). Observations and Analysis of the Non-radial Propagation of Coronal Mass Ejections Near the Sun. *Sol. Phys.* 290, 3343–3364. doi:10.1007/s11207-015-0794-9

Lynch, B. J., Li, Y., Thernisien, A. F. R., Robbrecht, E., Fisher, G. H., Luhmann, J. G., et al. (2010). Sun to 1 AU Propagation and Evolution of a Slow Streamer-Blowout Coronal Mass Ejection. *J. Geophys. Res.* 115, A07106. doi:10.1029/2009JA015099

Lynch, B. J., Masson, S., Li, Y., DeVore, C. R., Luhmann, J. G., Antiochos, S. K., et al. (2016). A Model for Stealth Coronal Mass Ejections. *J. Geophys. Res. Space Phys.* 121 (10677–10), 697. doi:10.1002/2016JA023432

Ma, S., Attrill, G. D. R., Golub, L., and Lin, J. (2010). Statistical Study of Coronal Mass Ejections with and without Distinct Low Coronal Signatures. *Astrophys. J.* 722, 289–301. doi:10.1088/0004-637X/722/1/289

MacQueen, R. M., Eddy, J. A., Gosling, J. T., Hildner, E., Munro, R. H., Newkirk, G. A. J., et al. (1974). The Outer Solar Corona as Observed from Skylab: Preliminary Results. *Astrophys. J. Lett.* 187, L85. doi:10.1086/181402

Martin, S. F. (1979). Study of the Post-Flare Loops on 1973JULY29 - Part Three - Dynamics of the Hα Loops. *Sol. Phys.* 64, 165–176. doi:10.1007/BF00151125

McAllister, A. H., Dryer, M., McIntosh, P., Singer, H., and Weiss, L. (1996). A Large Polar crown Coronal Mass Ejection and a "Problem" Geomagnetic Storm: April 14-23, 1994. *J. Geophys. Res.* 101, 13497–13516. doi:10.1029/96JA00510

Michels, D. J., Howard, R. A., Koomen, M. J., Sheeley, J., and N, R. (1980). "Satellite Observations of the Outer corona Near sunspot Maximum,". *E. Gergely. Radio Physics of the Sun, IAS Symposium*. Editors M. R. Kundu and T. Kundu, 86, 439–442. doi:10.1017/S007418090003719010.1007/978-94-010-9722-2_62

Mierla, M., Davila, J., Thompson, W., Inhester, B., Srivastava, N., Kramar, M., et al. (2008). A Quick Method for Estimating the Propagation Direction of Coronal Mass Ejections Using STEREO-COR1 Images. *Sol. Phys.* 252, 385–396. doi:10.1007/s11207-008-9267-8

Mierla, M., Inhester, B., Antunes, A., Boursier, Y., Byrne, J. P., Colaninno, R., et al. (2010). On the 3-D Reconstruction of Coronal Mass Ejections Using Coronagraph Data. *Ann. Geophys.* 28, 203–215. doi:10.5194/angeo-28-203-2010

Mierla, M., Inhester, B., Marqué, C., Rodriguez, L., Gissot, S., Zhukov, A. N., et al. (2009). On 3D Reconstruction of Coronal Mass Ejections: I. Method Description and Application to SECCHI-COR Data. *Sol. Phys.* 259, 123–141. doi:10.1007/s11207-009-9416-8

Morgan, H., and Druckmüller, M. (2014). Multi-Scale Gaussian Normalization for Solar Image Processing. *Sol. Phys.* 289, 2945–2955. doi:10.1007/s11207-014-0523-9

Möstl, C., Farrugia, C. J., Temmer, M., Miklenic, C., Veronig, A. M., Galvin, A. B., et al. (2009). Linking Remote Imagery of a Coronal Mass Ejection to its *In Situ* Signatures at 1 AU. *Astrophys. J. Lett.* 705, L180–L185. doi:10.1088/0004-637X/705/2/L180

Müller, D., Cyr, St. O. C., Zouganelis, I., Gilbert, H. R., Marsden, R., Nieves-Chinchilla, T., et al. (2020). The Solar Orbiter MIssion: Science Overview. *Astron. Astrophys.* 642, A1. doi:10.1051/0004-6361/202038467

Müller, D., Nicula, B., Felix, S., Verstringe, F., Bourgoignie, B., Csillaghy, A., et al. (2017). JHelioviewer. Time-dependent 3D Visualisation of Solar and Heliospheric Data. *Astron. Astrophys.* 606, A10. doi:10.1051/0004-6361/201730893

Munro, R. H., Gosling, J. T., Hildner, E., MacQueen, R. M., Poland, A. I., and Ross, C. L. (1979). The Association of Coronal Mass Ejection Transients with Other Forms of Solar Activity. *Sol. Phys.* 61, 201–215. doi:10.1007/BF00155456

Nieves-Chinchilla, T., Gómez-Herrero, R., Viñas, A. F., Malandraki, O., Dresing, N., Hidalgo, M. A., et al. (2011). Analysis and Study of the *In Situ* Observation of the June 1st 2008 CME by STEREO. *J. Atmos. Solar-terr. Phys.* 73, 1348–1360. doi:10.1016/j.jastp.2010.09.026

Nieves-Chinchilla, T., Vourlidas, A., Stenborg, G., Savani, N. P., Koval, A., Szabo, A., et al. (2013). Inner Heliospheric Evolution of a "Stealth" CME Derived from Multi-View Imaging and Multipoint *In Situ* Observations. I. Propagation to 1 AU. *Astrophys. J.* 779, 55. doi:10.1088/0004-637X/779/1/55

Nitta, N. V., and Mulligan, T. (2017). Earth-Affecting Coronal Mass Ejections without Obvious Low Coronal Signatures. *Sol. Phys.* 292, 125. doi:10.1007/s11207-017-1147-7

Ogawara, Y., Takano, T., Kato, T., Kosugi, T., Tsuneta, S., Watanabe, T., et al. (1991). The SOLAR-A Mission: An Overview. *Sol. Phys.* 136, 1–16. doi:10.1007/BF00151692

O'Kane, J., Green, L., Long, D. M., and Reid, H. (2019). Stealth Coronal Mass Ejections from Active Regions. *Astrophys. J.* 882, 85. doi:10.3847/1538-4357/ab371b

O'Kane, J., Green, L. M., Davies, E. E., Möstl, C., Hinterreiter, J., von Forstner, J. L. F., et al. (2021a). Solar Origins of a strong Stealth CME Detected by Solar Orbiter. *Astron. Astrophys.* doi:10.1051/0004-6361/202140622

O'Kane, J., Mac Cormack, C., Mandrini, C. H., Démoulin, P., Green, L. M., Long, D. M., et al. (2021b). The Magnetic Environment of a Stealth Coronal Mass Ejection. *Astrophys. J.* 908, 89. doi:10.3847/1538-4357/abd2bf

Palmerio, E., Kilpua, E. K. J., James, A. W., Green, L. M., Pomoell, J., Isavnin, A., et al. (2017). Determining the Intrinsic CME Flux Rope Type Using Remote-Sensing Solar Disk Observations. *Sol. Phys.* 292, 39. doi:10.1007/s11207-017-1063-x

Palmerio, E., Kilpua, E. K. J., Witasse, O., Barnes, D., Sánchez-Cano, B., Weiss, A. J., et al. (2021). CME Magnetic Structure and IMF Preconditioning Affecting SEP Transport. *Space Weather* 19, e2020SW002654. doi:10.1029/2020SW002654

Panasenco, O., Martin, S. F., Velli, M., and Vourlidas, A. (2013). Origins of Rolling, Twisting, and Non-radial Propagation of Eruptive Solar Events. *Sol. Phys.* 287, 391–413. doi:10.1007/s11207-012-0194-3

Pesnell, W. D., Thompson, B. J., and Chamberlin, P. C. (2012). The Solar Dynamics Observatory (SDO). *Sol. Phys.* 275, 3–15. doi:10.1007/s11207-011-9841-3

Pevtsov, A. A., Panasenco, O., and Martin, S. F. (2012). Coronal Mass Ejections from Magnetic Systems Encompassing Filament Channels without Filaments. *Sol. Phys.* 277, 185–201. doi:10.1007/s11207-011-9881-8

Richardson, I. G., and Cane, H. V. (2010). Near-Earth Interplanetary Coronal Mass Ejections during Solar Cycle 23 (1996 - 2009): Catalog and Summary of Properties. *Sol. Phys.* 264, 189–237. doi:10.1007/s11207-010-9568-6

Robbrecht, E., Patsourakos, S., and Vourlidas, A. (2009). No Trace Left behind: STEREO Observation of a Coronal Mass Ejection without Low Coronal Signatures. *Astrophys. J.* 701, 283–291. doi:10.1088/0004-637X/701/1/283

Rust, D. M., and Bar, V. (1973). Magnetic fields, Loop Prominences and the Great Flares of August, 1972. *Sol. Phys.* 33, 445–459. doi:10.1007/BF0015243210.1007/bf00152391

Rust, D. M., and Kumar, A. (1996). Evidence for Helically Kinked Magnetic Flux Ropes in Solar Eruptions. *Astrophys. J. Lett.* 464, L199. doi:10.1086/310118

Rust, D. M., Nakagawa, Y., and Neupert, W. M. (1975). EUV Emission, Filament Activation and Magnetic Fields in a Slow-Rise Flare. *Sol. Phys.* 41, 397–414. doi:10.1007/BF00154077

Rust, D. M., and Webb, D. F. (1977). Soft X-ray Observations of Large-Scale Coronal Active Region Brightenings. *Sol. Phys.* 54, 403–417. doi:10.1007/BF00159932

Santandrea, S., Gantois, K., Strauch, K., Teston, F., Tilmans, E., Baijot, C., et al. (2013). PROBA2: Mission and Spacecraft Overview. *Sol. Phys.* 286, 5–19. doi:10.1007/s11207-013-0289-5

Schmidt, J. M., Cairns, I. H., Xie, H., Cyr, St. O. C., and Gopalswamy, N. (2016). CME Flux Rope and Shock Identifications and Locations: Comparison of white Light Data, Graduated Cylindrical Shell Model, and MHD Simulations. *J. Geophys. Res. Space Phys.* 121, 1886–1906. doi:10.1002/2015JA021805

Schwenn, R., dal Lago, A., Huttunen, E., and Gonzalez, W. D. (2005). The Association of Coronal Mass Ejections with Their Effects Near the Earth. *Ann. Geophys.* 23, 1033–1059. doi:10.5194/angeo-23-1033-2005

Seaton, D. B., Berghmans, D., Nicula, B., Halain, J. P., De Groof, A., Thibert, T., et al. (2013). The SWAP EUV Imaging Telescope Part I: Instrument Overview and Pre-flight Testing. *Sol. Phys.* 286, 43–65. doi:10.1007/s11207-012-0114-6

Sheeley, J., N. R., Bohlin, J. D., Brueckner, G. E., Purcell, J. D., Scherrer, V. E., Tousey, R., et al. (1975). Coronal Changes Associated with a Disappearing Filament. *Sol. Phys.* 45, 377–392. doi:10.1007/BF00158457

Shensa, M. J. (1992). The Discrete Wavelet Transform: Wedding the a Trous and Mallat Algorithms. *IEEE Trans. Signal. Process.* 40, 2464–2482. doi:10.1109/78.157290

Shi, T., Wang, Y., Wan, L., Cheng, X., Ding, M., and Zhang, J. (2015). Predicting the Arrival Time of Coronal Mass Ejections with the Graduated Cylindrical Shell and Drag Force Model. *Astrophys. J.* 806, 271. doi:10.1088/0004-637X/806/2/271

Srivastava, N., Inhester, B., Mierla, M., and Podlipnik, B. (2009). 3D Reconstruction of the Leading Edge of the 20 May 2007 Partial Halo CME. *Sol. Phys.* 259, 213–225. doi:10.1007/s11207-009-9423-9

Stenborg, G., and Cobelli, P. J. (2003). A Wavelet Packets Equalization Technique to Reveal the Multiple Spatial-Scale Nature of Coronal Structures. *Astron. Astrophys.* 398, 1185–1193. doi:10.1051/0004-6361:20021687

Stenborg, G., Vourlidas, A., and Howard, R. A. (2008). A Fresh View of the Extreme-Ultraviolet Corona from the Application of a New Image-Processing Technique. *Astrophys. J.* 674, 1201–1206. doi:10.1086/525556

Talpeanu, D. C., Chané, E., Poedts, S., D'Huys, E., Mierla, M., Roussev, I., et al. (2020). Numerical Simulations of Shear-Induced Consecutive Coronal Mass Ejections. *Astron. Astrophys.* 637, A77. doi:10.1051/0004-6361/202037477

Thernisien, A. F. R., Howard, R. A., and Vourlidas, A. (2006). Modeling of Flux Rope Coronal Mass Ejections. *Astrophys. J.* 652, 763–773. doi:10.1086/508254

Thernisien, A. (2011). Implementation of the Graduated Cylindrical Shell Model for the Three-Dimensional Reconstruction of Coronal Mass Ejections. *Astrophys. J. Suppl.* 194, 33. doi:10.1088/0067-0049/194/2/33

Thernisien, A., Vourlidas, A., and Howard, R. A. (2009). Forward Modeling of Coronal Mass Ejections Using STEREO/SECCHI Data. *Sol. Phys.* 256, 111–130. doi:10.1007/s11207-009-9346-5

Thompson, B. J., Cliver, E. W., Nitta, N., Delannée, C., and Delaboudinière, J.-P. (2000). Coronal Dimmings and Energetic CMEs in April-May 1998. *Geophys. Res. Lett.* 27, 1431–1434. doi:10.1029/1999GL003668

Thompson, B. J., Plunkett, S. P., Gurman, J. B., Newmark, J. S., Cyr, St. O. C., and Michels, D. J. (1998). SOHO/EIT Observations of an Earth-Directed Coronal Mass Ejection on May 12, 1997. *Geophys. Res. Lett.* 25, 2465–2468. doi:10.1029/98GL50429

Thompson, W. T. (2009). 3D Triangulation of a Sun-Grazing Comet. *Icarus* 200, 351–357. doi:10.1016/j.icarus.2008.12.011

Thompson, W. T., Kliem, B., and Török, T. (2012). 3D Reconstruction of a Rotating Erupting Prominence. *Sol. Phys.* 276, 241–259. doi:10.1007/s11207-011-9868-5

Tousey, R. (1977). Apollo-telescope Mount of Skylab: An Overview. *Appl. Opt.* 16, 825–836. doi:10.1364/AO.16.000825

Tousey, R. (1973). The Solar corona. *Space Res. Conf.* 2, 713–730.

Tripathi, D., Bothmer, V., and Cremades, H. (2004). The Basic Characteristics of EUV post-eruptive Arcades and Their Role as Tracers of Coronal Mass Ejection Source Regions. *Astron. Astrophys.* 422, 337–349. doi:10.1051/0004-6361:20035815

Tsuneta, S., Acton, L., Bruner, M., Lemen, J., Brown, W., Caravalho, R., et al. (1991). The Soft X-ray Telescope for the SOLAR-A mission. *Sol. Phys.* 136, 37–67. doi:10.1007/BF00151694

Vourlidas, A., Colaninno, R., Nieves-Chinchilla, T., and Stenborg, G. (2011). The First Observation of a Rapidly Rotating Coronal Mass Ejection in the Middle Corona. *Astrophys. J. Lett.* 733, L23. doi:10.1088/2041-8205/733/2/L23

Vourlidas, A., Lynch, B. J., Howard, R. A., and Li, Y. (2013). How Many CMEs Have Flux Ropes? Deciphering the Signatures of Shocks, Flux Ropes, and Prominences in Coronagraph Observations of CMEs. *Sol. Phys.* 284, 179–201. doi:10.1007/s11207-012-0084-8

Vourlidas, A. (2015). Mission to the Sun-Earth L Lagrangian Point: An Optimal Platform for Space Weather Research. *Space Weather* 13, 197–201. doi:10.1002/2015SW001173

Vourlidas, A., and Webb, D. F. (2018). Streamer-blowout Coronal Mass Ejections: Their Properties and Relation to the Coronal Magnetic Field Structure. *Astrophys. J.* 861, 103. doi:10.3847/1538-4357/aaca3e

Yurchyshyn, V., Abramenko, V., and Tripathi, D. (2009). Rotation of White-light Coronal Mass Ejection Structures as Inferred from LASCO Coronagraph. *Astrophys. J.* 705, 426–435. doi:10.1088/0004-637X/705/1/426

Zhang, J., Richardson, I. G., Webb, D. F., Gopalswamy, N., Huttunen, E., Kasper, J. C., et al. (2007). Solar and Interplanetary Sources of Major Geomagnetic Storms (Dst nT) during 1996-2005. *J. Geophys. Res.* 112, A10102. doi:10.1029/2007JA012321

Zhukov, A. N., and Auchère, F. (2004). On the Nature of EIT Waves, EUV Dimmings and Their Link to CMEs. *Astron. Astrophys.* 427, 705–716. doi:10.1051/0004-6361:20040351

Conflict of Interest: The authors declare that the research was conducted in the absence of any commercial or financial relationships that could be construed as a potential conflict of interest.

frontiers in Astronomy and Space Sciences

ORIGINAL RESEARCH
published: 13 September 2021
doi: 10.3389/fspas.2021.713999

Radial Sizes and Expansion Behavior of ICMEs in Solar Cycles 23 and 24

Wageesh Mishra [1], Urmi Doshi [2,3] and Nandita Srivastava [4]*

[1]Indian Institute of Astrophysics, Bengaluru, India, [2]Department of Physics, The M S University of Baroda, Vadodara, India, [3]M P Birla Institute of Fundamental Research, Bengaluru, India, [4]Udaipur Solar Observatory, Physical Research Laboratory, Udaipur, India

We attempt to understand the influence of the heliospheric state on the expansion behavior of coronal mass ejections (CMEs) and their interplanetary counterparts (ICMEs) in solar cycles 23 and 24. Our study focuses on the distributions of the radial sizes and duration of ICMEs, their sheaths, and magnetic clouds (MCs). We find that the average radial size of ICMEs (MCs) at 1 AU in cycle 24 is decreased by ~33% (~24%) of its value in cycle 23. This is unexpected as the reduced total pressure in cycle 24 should have allowed the ICMEs in cycle 24 to expand considerably to larger sizes at 1 AU. To understand this, we study the evolution of radial expansion speeds of CME-MC pairs between the Sun and Earth based on their remote and *in situ* observations. We find that radial expansion speeds of MCs at 1 AU in solar cycles 23 and 24 are only 9% and 6%, respectively, of their radial propagation speeds. Also, the fraction of radial propagation speeds as expansion speeds of CMEs close to the Sun are not considerably different for solar cycles 23 and 24. We also find a constant (0.63 ± 0.1) dimensionless expansion parameter of MCs at 1 AU for both solar cycles 23 and 24. We suggest that the reduced heliospheric pressure in cycle 24 is compensated by the reduced magnetic content inside CMEs/MCs, which did not allow the CMEs/MCs to expand enough in the later phase of their propagation. Furthermore, the average radial sizes of sheaths are the same in both cycles, which is also unexpected, given the weaker CMEs/ICMEs in cycle 24. We discuss the possible causes and consequences of our findings relevant for future studies.

Keywords: sun, coronal mass ejections, expansion speeds, solar cycle, heliosphere

OPEN ACCESS

Edited by:
Teimuraz Zaqarashvili, University of Graz, Austria

Reviewed by:
Manuela Temmer, University of Graz, Austria
Hui Li, National Space Science Center (CAS), China

****Correspondence:***
Wageesh Mishra
wageesh.mishra@iiap.res.in

Specialty section:
This article was submitted to Stellar and Solar Physics, a section of the journal Frontiers in Astronomy and Space Sciences

Received: *24 May 2021*
Accepted: *12 August 2021*
Published: *13 September 2021*

Citation:
Mishra W, Doshi U and Srivastava N (2021) Radial Sizes and Expansion Behavior of ICMEs in Solar Cycles 23 and 24. Front. Astron. Space Sci. 8:713999. doi: 10.3389/fspas.2021.713999

1 INTRODUCTION

Coronal mass ejections (CMEs) are the episodic release of large-scale magnetized plasma structures from the Sun into the heliosphere, and they are the primary drivers of space weather events (Hundhausen et al., 1984; Zhang et al., 2007; Webb and Howard, 2012). CMEs can be remotely observed in white-light observations close to the Sun by coronagraphs and by heliospheric imagers at large distances from the Sun (Brueckner et al., 1995; Eyles et al., 2009). They have also been observed in *in situ* observations at a certain location and time where they are often referred to as interplanetary coronal mass ejections (ICMEs) (Gosling et al., 1990). A CME propagating with speed high enough relative to ambient solar wind medium can drive a shock ahead of it. The ambient solar wind plasma piled-up and compressed between the shock and ICME front is termed the ICME sheath (Forsyth et al., 2006). A subset of ICMEs showing flux-rope structures in the *in situ* observations are classified as magnetic clouds (MCs) (Burlaga et al., 2002; Marubashi and Lepping, 2007). The kinematic and

morphological evolutions of different structures of ICMEs have been the focus of several studies in the last 2 decades (Schwenn, 2006; Webb and Howard, 2012; Harrison et al., 2018). However, the dynamic evolution of ICMEs under varying conditions of solar wind medium and/or preconditioned ambient medium is not yet completely understood (Temmer et al., 2011; Vršnak et al., 2013; Mishra et al., 2014; Gopalswamy et al., 2015a; Sachdeva et al., 2015).

Solar activity *via* episodic and quasi-steady outflows of magnetized plasma can modulate the state of the heliosphere starting close to the Sun to several AU from the Sun. The magnetic activity on the Sun varies over an almost 11 years period consisting of three phases, an ascending phase, maximum, and declining phase of solar activity, which altogether is termed a solar cycle (Wolf, 1861; Mathew et al., 2007; Pesnell, 2016). The progress of the Sun through different phases of the solar cycle and/or different cycles is manifested in sunspots number, the occurrence rate of CMEs, flares, the intensity of X-ray flux, strength of solar wind, etc., (Solanki et al., 2008; Lamy et al., 2017). The studies on understanding CMEs/ICMEs over solar cycles 23 and 24 gathered attention since it was reported that cycle 23 became extremely quiet and was in deep minimum phase for an unusually longer time (Ramesh, 2010; Janardhan et al., 2011). Solar cycle 23 began in August 1996 and ended in December 2008 with its maximum around 2002 (Joselyn et al., 1997; Temmer et al., 2006). Following the minimum of cycle 23, solar cycle 24 began in December 2008 and ended in December 2019 reaching its maximum around mid of 2014 (Pesnell, 2008; Bisoi et al., 2020). Cycle 24 is found to be weaker than the previous cycle in terms of disturbances that appeared on the solar surface and in the heliosphere (Antia and Basu, 2010; Richardson, 2013). However, several studies have confirmed that the CME rate in solar cycle 24 did not decrease as strongly as the sunspot number from the maximum of cycle 23 to the next maximum (Gopalswamy et al., 2015a; Mishra et al., 2019).

The reduction in the CMEs activity relative to sunspot number (i.e., an apparent increase in CME rate per sunspot number) in a weaker cycle 24 than that in cycle 23 has been explained using different primary and secondary factors in previous studies. Gopalswamy et al. (2015a) suggested that an apparent increased rate of halo CMEs over cycle 24 is a direct consequence of the reduced total pressure in the heliosphere which allowed the CMEs to expand considerably and appear as halos. Petrie (2015) found an increased rate of CMEs from higher latitudes since 2003 (middle of solar cycle 23) due to the weakening of polar photospheric magnetic field which allowed the eruptions from higher latitudes. A similar finding is also reported in Mishra et al. (2019). However, some studies suggested that an apparent increase in the CME rate in cycle 24 is due to some artifacts such as cadence and over-counting of narrow and faint ejections in different automated and manual CMEs catalogs (Wang and Colaninno, 2014; Lamy et al., 2017). Furthermore, a recent study by Gopalswamy et al. (2020) shows that the reduced total pressure in the heliosphere allows CMEs in cycle 24 to appear as halos at a shorter distance from the Sun and also at a lower speed than that in cycle 23. The study reveals that the increased rate of halo CMEs in cycle 24 is not due to eruption characteristics itself, but it is the effect of the weakened state of the heliosphere.

The lateral expansion of CMEs during their heliospheric journey is often measured close to the Sun using imaging observations and far from the Sun using *in situ* observations taken by several spacecraft at different heliocentric distances. Such an expansion of a CME is due to a faster speed of the CME leading edge compared to its trailing edge and/or the higher pressure inside the CME than that in the ambient heliospheric medium (Liu et al., 2006; Jian et al., 2008; Mishra and Srivastava, 2015). The expansion causes an increase in the sizes of ICMEs to hundreds of solar radii in interplanetary medium from a size of few solar radii in the outer corona. One way to measure radial expansion speeds (also referred as expansion speeds) is by exploiting *in situ* observations of the selected ICMEs by several spacecraft located at different heliocentric distances from the Sun (Good and Forsyth, 2016). The other way to understand such an expansion is to track specific ICMEs continuously from the Sun to several solar radii distances exploiting coronagraphic and heliospheric imaging observations (Davies et al., 2009; Mishra and Srivastava, 2015; Mishra and Wang, 2018). However, the continuous tracking of each individual CME in remote observations is cumbersome and extremely difficult to mark the leading and trailing edges of the ICMEs structures (Howard and DeForest, 2012; DeForest et al., 2013). On the other hand, it is also rare to observe the same ICME from multiple widely separated *in situ* spacecraft at different distances from the Sun (Reisenfeld et al., 2003). Apart from the aforementioned approaches, one can study the radial expansion, radial sizes, and duration of ICMEs using a statistical approach (Liu et al., 2006). In this approach, the properties of ICMEs/ambient medium estimated over a large number of events/intervals are assumed to represent the dominant properties of an individual case/local medium.

The study of evolution characteristics of ICMEs is of great significance and is one of the challenging problems in heliospheric physics. In fact, the expansion behavior of ICMEs is responsible for the dilution of magnetic and heat content inside the CMEs (Gopalswamy et al., 2014; Mishra and Wang, 2018). The more rapid dilution of density and magnetic field in ICMEs than the solar wind can be modeled taking into account the expansion of ICMEs (Wang and Richardson, 2004). The different expansion rates of ICMEs can lead to different rates of change in plasma parameters inside and outside ICMEs. In addition to the expansion effect, Li et al. (2017) have shown that the magnetic strength inside ICMEs decreases more for the regions which are rich in Alfvénic fluctuations (AF) than that for the AF-lacking region. Earlier studies have shown that the distribution, evolution, and dissipation of AF inside ICMEs can help in probing the thermodynamic evolution of ICMEs during their propagation (Liu et al., 2006; Li et al., 2017). The difference in the time interval for which solar wind and ICME material are observed at larger distances from the Sun may depend on the expansion rate of ICMEs as well as the phase of the solar cycle. The physical state of the heliosphere influences the expansion behavior of ICMEs which in turn also affects their dimensional (radial sizes and duration) and geoeffective characteristics (Liu

et al., 2006; Démoulin et al., 2016; Shen et al., 2017). The dimensional properties of both ICMEs and sheaths have been studied for the events observed near the Earth during solar cycle 23 (Zhang et al., 2008; Guo et al., 2010). In their study, the number of selected ICMEs was limited to ICMEs which gave rise to major geomagnetic storms. Kilpua et al. (2014) have found that ICMEs in minima and rising phase of cycle 24 are less geoeffective due to the lack of strong and long duration ICMEs. The study of mean magnetic field, proton temperature, speed, and duration of sheaths and ICMEs during cycle 23 is also discussed in Mitsakou and Moussas (2014). Recently, based on the statistical studies of ICMEs during the declining phase of cycles 23 and 24, Lawrance et al. (2020) have shown that the correlation between the ICMEs/sheaths sizes and storm strength is insignificant.

Thus, the earlier studies have focused on only a limited number of ICMEs due to the selection of either a particular cycle or a particular phase of either cycle, only geoeffective ICMEs, and/or only a particular feature (i.e., ICME, sheath, shock) of ICMEs. In this context, it would be an obvious next step to understand and compare the dimensional properties of different features of all the ICMEs identified at 1 AU during complete cycles of 23 and 24. It is known that ICMEs with different speeds may interact with ambient medium differently at different heliocentric distances (Manoharan, 2006; Sachdeva et al., 2015). This implies that some ICMEs may expand sufficiently close to the Sun itself while some ICMEs probably continue to expand upto larger distances from the Sun. Therefore, our study on ICMEs evolving into different heliospheric conditions over cycles 23 and 24 would provide insight into relative sizes of ICMEs and their expansion behavior.

Since the heliospheric state is found to change significantly over solar cycle 24, the expansion behavior of ICMEs in cycle 24 is expected to be different from those in the previous cycle 23. The relative distribution of ICMEs, sheaths of ICME, and MCs into different bins of radial sizes, duration, and speeds gives important information about their heliospheric evolution. In the present study, our focus is to estimate as well as compare the distribution of dimensional properties of Earth-arriving ICMEs and MCs over the last two solar cycles 23 and 24. Furthermore, we attempt to study the evolution of radial expansion speeds between the Sun and Earth for the associated CME-MC pairs to interpret their observed dimensional properties at 1 AU over both cycles. The selection of ICMEs/MCs from available *in situ* observations and the methodology of our approach are given in **Section 2**. The analysis and derived results are explained in **Section 3** followed by the summary and discussion in **Section 4**.

2 OBSERVATIONS AND METHODOLOGY

Our study focuses on understanding the duration and radial sizes of ICMEs at 1 AU near the Earth during solar cycles 23 and 24. The ICMEs have been routinely observed near the Earth by the *in situ* spacecraft *Wind* and *Advanced Composition Explorer (ACE)* (Ogilvie et al., 1995; Stone et al., 1998). However, the identification of ICMEs is based on several signatures, and there is often the situation that all of the signatures are not present in an individual ICME. Furthermore, even if several signatures are detected in an ICME, it is possible that the duration of these signatures is not the same, and also they are not coincident (Zurbuchen and Richardson, 2006). Therefore, the identification of ICMEs in the *in situ* observations is not straightforward. Due to this reason, different groups of researchers have considered some signatures as the primary and others as secondary identifiers of the ICMEs which resulted in several publicly available ICME catalogs (Richardson et al., 2000; Chi et al., 2016; Nieves-Chinchilla et al., 2018). Although these catalogs are broadly similar, differences in terms of the number of events, exact boundaries of ejecta have been noticed, due to subjective judgment in the identification of ICMEs. In the present study, we selected ICME catalog of Richardson and Cane (Richardson and Cane, 2010) (hereafter called RC catalog) (http://www.srl.caltech.edu/ACE/ASC/DATA/level3/icmetable2.htm), which has been extensively used in the literature (Zhang et al., 2007; Richardson, 2013; Li et al., 2018; Mishra et al., 2019). We find that the total number of ICMEs at 1 AU near the Earth is 520 during 1996 and 2019. There are 314 ICMEs listed in the catalog during 1996 and 2008 under solar cycle 23 while there are 206 ICMEs during 2009 and 2019 under solar cycle 24. Earlier studies have also found that ICME rate during cycle 24 decreased by 40% to that of the previous cycle except during the maximum of cycle 24 when it was the same as that in the cycle 23 (Li et al., 2018; Mishra et al., 2019).

The sizes of ICMEs are important to study as they can affect the performance and accuracy of several arrival time prediction methods. The ICMEs expand continuously during their heliospheric journey as they tend to achieve equilibrium with the surrounding solar wind plasma. Therefore, the radial sizes and duration of ICMEs are dictated by the expansion history of the ICMEs. Since the expansion speed of ICMEs is of the order of local Alfvén speed in the heliosphere (Jian et al., 2008), one can gain knowledge about the state of the heliosphere from their sizes at 1 AU. We attempt to understand the radial expansion speeds of ICMEs by comparing their dimensional properties, i.e., duration and radial sizes, in solar cycles 23 and 24. We estimate the radial size of each ICME by first estimating the time difference between the arrival of ICME leading and trailing edges, and then taking a product of this time difference with the average speed of the ICME. A similar approach has been followed in earlier studies (Mitsakou and Moussas, 2014; Lawrance et al., 2020). Other approaches involve integrating the solar wind speed with time during ICME passage through the spacecraft (Zhang et al., 2008; Jian et al., 2018). The start and end times of ICMEs leading and trailing boundaries, as listed in RC catalog, are based primarily on plasma and magnetic field observations. Importantly, the signatures of abnormally low proton temperatures are used for identifying ICMEs (Richardson and Cane, 1995). Such low-temperature plasma is identified by comparing, point by point, the *in situ* observed proton temperature (T_p) with the typical "expected" temperature (T_{ex}) found for solar wind with the speed (V_{sw}) (Neugebauer et al., 2003). The ICME boundaries are identified for the interval of solar wind having $T_p/T_{ex} < 0.5$ (Richardson and Cane, 1995). The arrival of shock and/or sheath region is based on the increase in the solar wind speed,

magnetic field strength, and density followed by the interval of turbulent plasma ahead of ICME (Kilpua et al., 2017).

Besides estimating the sizes and duration of sheaths and ICMEs individually, we have also studied the sizes and duration of compressed sheaths region preceding an ICME and following a CME-driven shock wave (Forsyth et al., 2006). However, sometimes there may be neither a shock wave nor a sheath region preceding an ICME (Kilpua et al., 2017). We note that ~16% and ~26% of the total number of ICMEs in cycles 23 and 24, respectively, have no sheath region ahead of them. Such events are not excluded from the chosen sample as it would be interesting to note the relative influence of such cases in the distribution of duration and radial sizes of the sheaths and ICMEs in both solar cycles 23 and 24. The duration of sheaths and their radial sizes are estimated in the same way as it is done for ICMEs. In addition to studying the region of sheaths and ICMEs individually, we also estimate the duration and radial sizes of the entire ejecta combining the sheaths and the ICMEs.

Furthermore, our analysis includes the magnetic clouds (MCs) which are a subset of ICMEs identified to have flux-ropes structures in the *in situ* observations. Earlier studies have shown that the geometrical selection effect is responsible for the absence of flux-rope structures in about two-thirds of the total number of ICMEs observed *in situ* at 1 AU (Riley et al., 2006; Chi et al., 2016). The flux-rope structures are not detected in the *in situ* observations if the *in situ* spacecraft passes through the flank of ICMEs. Thus, *in situ* spacecraft can observe different features of ICMEs depending on their trajectory along a different part of ICMEs. The radial sizes, duration, and expansion speeds of MCs are expected to be different than that of ICMEs (Marubashi and Lepping, 2007; Li et al., 2018). Therefore, it is important to study the dimensional properties of MCs and compare them with that of ICMEs over solar cycles 23 and 24.

We use the list of MCs compiled by Gopalswamy et al. (2015b) which includes the MCs observed during 1996–2015 covering solar cycle 23 and half of cycle 24. For including the list of MCs observed after 2015, we have analyzed the *in situ* observations of ICMEs listed in the RC catalog to examine if the ICMEs satisfy the criteria of MCs defined by Burlaga et al. (1981). These include the signatures of the enhanced magnetic field, plasma β less than unity, and smooth rotation of magnetic field vector to characterize the ICMEs as MCs. We find that the number of MCs identified at 1 AU in solar cycles 23 and 24 is 107 and 94, respectively. These numbers of MCs are ~34% and ~45% of the total number of ICMEs in cycles 23 and 24.

To understand the measured radial sizes of all the ICMEs in terms of expansion, we compare the expansion speeds of CMEs close to the Sun and that of MCs at 1 AU. Our plan to estimate the radial expansion speeds is limited for only MCs because they suffer the least from the geometric selection effect in the *in situ* observations. The *in situ* measured expansion speeds over large ICMEs sample would have been underestimated differently depending on the extent of leg-flanks encounter by the *in situ* spacecraft, i.e., how far from the nose of the ICME does the spacecraft intercepts the ICME structure. We assume that the distribution of radial expansion speeds of MCs over both cycles, and our interpretation based on this, would also be valid for ICMEs over both cycles. For examining the evolution of expansion speeds between Sun and Earth, only those MCs are selected for which a clear association of their solar sources (CMEs) is established. Such associated CME and MC pairs over solar cycles 23 and 24 are expected to mimic the behavior of CME-ICME pairs in general.

We estimate the average radial propagation and expansion speeds for all the identified CME and MC pairs. We approximate the CME shape by a full ice-cream cone, with its curved-front base representing the CME leading edge and apex of the cone subtends a cone angle at the center of the Sun (Xie et al., 2004). We first determine the half-cone angular widths of selected CMEs using the established empirical relations between cone angular widths (W) and projected speeds (V) of CMEs as $W = 0.11V + 24.3$ for solar cycle 23 and $W = 0.16V + 24.6$ for solar cycle 24 (Gopalswamy et al., 2014). The projected speeds of CMEs are taken from CDAW catalog (Yashiro et al., 2004) based on Spectrometric COronagraph (LASCO) observations onboard *Solar and Heliospheric Observatory* (SOHO) (Brueckner et al., 1995). Furthermore, following equation (1) in Gopalswamy et al. (2010), i.e., $V_{rad} = (\cos\omega + \sin\omega)V/(\cos\omega\cos\theta + \sin\omega)$, we derive the radial propagation speeds (also referred as radial speeds) of CMEs (V_{rad}) using their projected speeds (V), half angular widths (ω), and direction of propagation (θ) which is assumed to be 90° from the plane of the sky for the Earth-directed CMEs associated with MCs. Finally, the near-Sun lateral expansion speeds (V_{exp}) of the CMEs are calculated using their half-cone angular widths and radial propagation speeds relationship as expressed in equation (5) of Gopalswamy et al. (2009), i.e., $V_{rad} = (1/2)\ (1 + \cot\omega)V_{exp}$. The radial expansion speeds of MCs are calculated taking half of the difference between the propagation speeds at the leading and trailing edges of MCs observed in the *in situ* observations (Owens et al., 2005).

The average speeds of MCs passing the near-Earth *in situ* spacecraft are taken as their radial propagation speeds at 1 AU. Our approach to understand the evolution of propagation and expansion speeds of CME/MCs is based on only two-point measurements, one close to the Sun and the other close to the Earth. Using the above-mentioned formula of Gopalswamy et al. (2009), we can estimate lateral expansion speeds of CMEs close to the Sun but not their radial expansion speeds. We assume that CMEs observed in the coronagraphic field of view reveal a self-similar expansion which implies that the radial and lateral expansions increase at the same rate (Schwenn et al., 2005). Therefore, we use lateral expansion speeds of CMEs as a proxy of their radial expansion speeds close to the Sun. However, some studies on CME and cavity evolution in high-cadence EUV imagery have reported fast lateral expansion of CMEs low in the corona (Patsourakos et al., 2010). In the present study, for comparing the expansion of associated CME-MC pairs, we have taken the lateral expansion of CMEs while the radial expansion speeds of MCs. The distribution of relative values of radial expansion speeds with respect to radial propagation speeds of associated CME

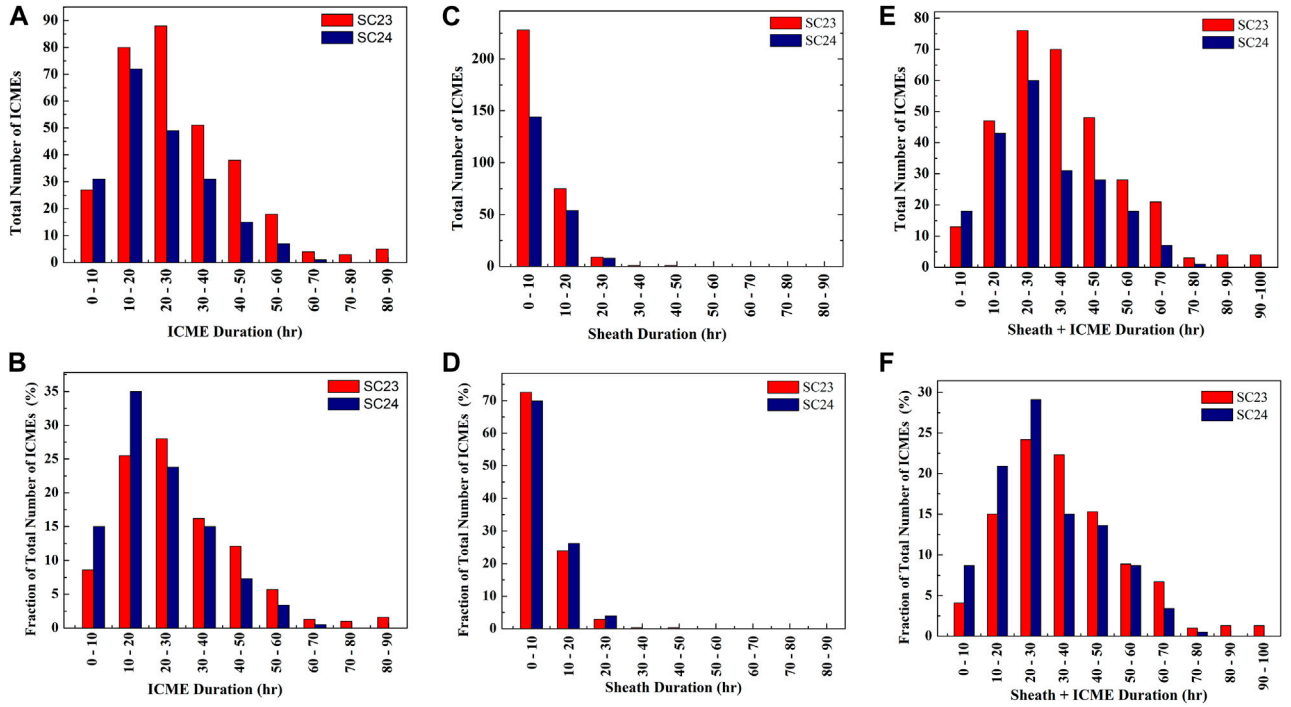

FIGURE 1 | The distributions of duration of ICME structures, i.e., ICMEs, sheath region preceding ICMEs, and ICMEs together with sheath (i.e., entire transients) are shown in **(A),(B), (C),(D)**, and **(E),(F)**, respectively, for both solar cycles 23 and 24. **(A),(C),(E)** and **(B),(D),(F)** show the distributions for the total number of ICMEs and the percentage fraction of the total number of ICMEs in each bin of duration, respectively.

and MC pairs over solar cycles 23 and 24 is examined to estimate the duration and radial sizes of ICMEs in both cycles.

3 ANALYSIS AND RESULTS

3.1 Duration of ICMEs, Sheaths, and ICMEs Combined With Sheaths

The duration of an ICME structure at 1 AU can be a proxy for its radial expansion history in the interplanetary medium before reaching the Earth. Furthermore, the duration of ICMEs and their sheaths can provide information about the state of the heliosphere. Estimation of these durations at 1 AU is important to know as it is the interval in which Earth's magnetosphere is likely to experience large perturbation responsible for geomagnetic storms (Zhang et al., 2008). The distributions of a fraction of ICMEs number with different duration of ICMEs, sheaths region, and entire transient (i.e., combined sheaths and ICMEs) region are shown in **Figure 1** for both solar cycles 23 and 24.

To examine the statistical significance of the differences in the duration of ICMEs over cycles 23 and 24, we performed the two-sample Kolmogorov-Smirnov (KS) test. The KS test is a nonparametric test that can compare two samples and determine whether or not the two samples are from the same distribution at a given confidence level, i.e., p-value. The test computes a KS statistic (D) which is the maximum distance between the empirical cumulative distribution functions of two samples. The two samples are considered to come from different distributions if the value of the KS statistic (D) is larger than the computed critical values (D_c). The critical value D_c can be computed at different p-value using the number of data points (i.e., sizes) of the first and second samples. It means for $D > D_c$, the null hypothesis that the two samples are drawn from the same distribution is rejected. For example, the number of ICMEs in solar cycles 23 and 24 is 314 and 206, respectively, i.e., m = 314 and n = 206, and this gives $D_c = 0.146$ at $p = 0.01$. The value of KS statistic $D = 0.159$ is found for the two samples of the duration of ICMEs, taking each sample for solar cycles 23 and 24. It is clear that $D > D_c$ which implies that the duration of ICMEs is different in cycles 23 and 24 with a 99% confidence level. This suggests that there remains only a very small probability of 1% that the difference between the two distributions of CMEs duration could have occurred just by random chance. However, we compute $D_c = 0.175$ at $p = 0.001$, and in this case, $D < D_c$, which implies that at the confidence level of 99.9%, the duration of ICMEs is not different in cycles 23 and 24. The minimum confidence level of 95% is often accepted in ICMEs research, and we will consider the same in concluding the findings from the two-sample KS test (Gopalswamy et al., 2015b).

We note that the duration of ICMEs identified at 1 AU over solar cycle 23 ranges between 3 and 90 h with an average of 28.8 h. The median of ICME duration is 26 h implying that half of the observed events last longer than 26 h, and half of all the events

have a duration below 26 h. To understand the degree of dispersion in the sample of ICMEs duration, we note that the standard deviation is around 16.2 h. From **Figure 1**, we clearly see that the distribution of ICMEs duration peaks at 20–30 h having ~28% (88 events) of the total number of ICMEs. We also note that there are around ~16% (51 events) of the total number of ICMEs which have the duration within 30–40 h and ~25% (80 events) of ICMEs with the duration within 10–20 h. On the other hand, in solar cycle 24, the duration of ICMEs ranges between 3 and 63 h with an average of 23.3 h. The median and standard deviation for ICMEs duration in cycle 24 are 20.5 and 13 h, respectively. A major fraction of ~35% (72 events) of the total number of ICMEs in cycle 24 has a duration within 10–20 h. In addition to this, there are ~24% (49 events) of events having duration within 20–30 h and 15% (31 events) corresponding to the duration within 10 h.

On comparing cycles 23 and 24, we note that the average duration of an ICME in cycle 24 is decreased by 19% of that in the previous cycle. Although the distribution for both the cycles is skewed right in the direction of longer duration values (i.e., positively skewed), the degree of skewness is stronger for cycle 23. We further note that ~10% (30 events) of ICMEs in cycle 23 have a duration larger than 50 h while only ~4% (8 events) of such ICMEs are present during cycle 24. Furthermore, the fractions of the total number of ICMEs over cycles 23 and 24 having a duration shorter (longer) than 20 h are ~34% (66%) and ~50% (50%), respectively. This suggests that the fraction of the total number of ICMEs in cycle 24 with larger duration decreased. The shorter duration of ICMEs in cycle 24 was attributed as a reason for their weaker geoeffectiveness (Kilpua et al., 2014).

The shorter duration of ICMEs at 1 AU may result either due to their smaller sizes or larger mean speeds which is defined as the radial propagation speed averaged over the entire duration of ICME. However, the mean ICME propagation speed at 1 AU in cycle 23 is 475 km s^{-1} which decreased by ~12% of its value to 420 km s^{-1} in cycle 24. The ranges of speeds in cycles 23 and 24 are 290–1,300 km s^{-1} and 270–680 km s^{-1}, respectively. Assuming that the total pressure is reduced in ICMEs and heliosphere in cycle 24 (Gopalswamy et al., 2015b), the possibility of smaller duration of ICMEs can be due to reduced ICME internal total pressure which may play a dominant role in governing the radial expansion/sizes of the ICMEs. This will be discussed in **Section 4** following the analysis of ICME sizes in **Section 3.2**.

The sheath regions of ICMEs are known to contribute ~30% of energy input in the magnetosphere during major geomagnetic storms (Zhang et al., 2008), and therefore, it is of interest as well. The value of KS statistic $D = 0.099$ is found for the two samples of the duration of sheaths, taking each sample for solar cycles 23 and 24. However, we compute $D_c = 0.122$ at $p = 0.05$, and in this case, $D < D_c$, which implies that at the confidence level of 95%, the duration of sheaths is not different in cycles 23 and 24. The duration of ICME sheaths in cycle 23 ranges from 0 to 43 h with an average value of 7 h. The median and standard deviation of the duration are 5.5 and 6.6 h, respectively. The distribution of sheaths duration peaks at 0–10 h having ~73% (228 events) of the total number of ICMEs. We further note that there are around ~24% (75 events) of the total number of ICMEs which have sheaths duration within 10–20 h and less than 1% (2 events) has sheaths duration larger than 30 h. However, the sheath duration for solar cycle 24 ranges from 0 to 28.5 h with an average value of 7 h. The median and standard deviation are noted to be 6 and 6.7 h, respectively. The distribution of sheaths duration for ICMEs in cycle 24 peaks at 0–10 h for ~69% (143 events) of the total number of events while only ~26% (54 events) of events have sheaths duration within 10–20 h.

Our analysis shows that ~16% (49 events) and ~25% (52) of the total number of ICMEs in solar cycles 23 and 24, respectively, have no sheath region, i.e., sheath duration is 0 h for these events. Interestingly, the distribution of sheath duration for ICMEs in cycle 23 is almost the same as in cycle 24, with only 2% smaller for the binning duration of 10–20 h and 4% larger for the duration bin of 0–10 h. A similar duration of sheaths for both the cycles is unexpected as ICMEs in cycle 24 were found to be slower and less geoeffective at 1 AU (Shen et al., 2017). If the sheaths ahead of ICMEs measured at 1 AU are a long-term effect during their complete journey, it is possible that both faster and slower ICMEs tending towards equalizing their speed to solar wind accumulate an equal amount of upstream solar wind plasma. This is consistent with recent studies of Salman et al. (2020a,b) who found that radial thickness of sheaths has no clear dependence on the initial speeds, measured *in situ* speeds, and associated Mach numbers of the CMEs. This suggests that accumulation of the solar wind is the dominant mechanism deciding the sizes of the sheaths at 1 AU rather than the compression which should depend on CME speed or shock Mach number (Russell and Mulligan, 2002). Also, Temmer et al. (2021) found that the sheath density does not depend on the CME propagation speed but rather depends on the ambient density and solar wind flow speed in the interplanetary space ahead of the CME. They suggested that the sheath region consists of piled-up ambient solar wind material and its magnitude is partially decided by the size of the CME. The discussion over different parameters dictating the duration and size of sheath at 1 AU is detailed in **Section 4**.

The energy transfer efficiency for sheaths and ICMEs is comparable, and their contribution to geomagnetic storms is decided by the relative duration of sheaths and ICMEs (Guo et al., 2010). The value of KS statistic $D = 0.163$ is found for the two samples of the duration of entire region of ICMEs, taking each sample for solar cycles 23 and 24. We compute $D_c = 0.146$ at $p = 0.01$, and in this case, $D > D_c$, which implies that at the confidence level of 99%, the duration of entire region of sheaths combined with ICMEs structure is different in cycles 23 and 24. The total duration of the entire region of sheaths combined with ICMEs structure over solar cycle 23 ranges from as low as 5 h to as high as 99.8 h with an average value of 35.8 h. The median and standard deviation of the duration are 33 and 17.6 h, respectively. From **Figure 1**, we see that the distribution of duration of combined regions of sheaths and ICMEs peaks at 20–30 h having ~24% (76 events) of the total number of ICMEs. We further note that there are around ~22% (70 events) of the total number of ICMEs which have a duration

TABLE 1 | The statistics of distributions of duration and radial sizes of different ICMEs structures at 1 AU for solar cycles 23 and 24 are listed. From the top: the distribution of the duration of ICMEs, sheaths, and entire transients (first panel); the radial sizes of ICMEs, sheaths, and entire transients (second panel); the duration of MCs (third panel); and the radial sizes of MCs (fourth panel). The ratio of radial expansion to radial propagation speeds of associated CMEs near the Sun and MCs at 1 AU is in the fifth and sixth panels, respectively. From the left: the solar cycle and structures (first column); the range, average, median, and standard deviation (second column); peak of the distribution having fraction of total number of events (third column); adjacent larger and smaller than the distribution peak having fraction of total number of events (fourth column).

Cycle (structures)	Range, average, median, standard deviation	Distribution peak (fraction of events)	Adjacent larger and smaller than peak (fraction of events)
Distributions of the duration of ICMEs, sheaths, and entire transients			
SC23 (ICMEs)	[3–90, 28.8, 26, 16.2] h	20–30 h (28%)	30–40 h (16%) and 10–20 h (25%)
SC24 (ICMEs)	[3–63, 23.3, 20.5, 13] h	10–20 h (35%)	20–30 h (24%) and 0–10 h (15%)
SC23 (Sheaths)	[0–43, 7, 5.5, 6.6] h	0–10 h (73%)	10–20 h (24%) and NA
SC24 (Sheaths)	[0–29, 7, 6, 6.7] h	0–10 h (69%)	10–20 h (26%) and NA
SC23 (ICMEs + Sheaths)	[5–100, 35.8, 33, 17.6] h	20–30 h (24%)	30–40 h (22%) and 10–20 (15%)
SC24 (ICMEs + Sheaths)	[5–72, 30.3, 27.6, 15.6] h	20–30 h (29%)	30–40 h (15%) and 10–20 (21%)
Distributions of the radial sizes of ICMEs, sheaths, and entire transients			
SC23 (ICMEs)	[0.03–1.34, 0.33, 0.29, 0.2] AU	0.1–0.2 AU (23%)	0.2–0.3 AU (23%) and 0–0.1 AU (18%)
SC24 (ICMEs)	[0.03–0.82, 0.24, 0.20, 0.14] AU	0–0.1 AU (34%)	0.1–0.2 AU (29%) and NA
SC23 (Sheaths)	[0–0.4, 0.07, 0.06, 0.07] AU	0–0.1 AU (85%)	0.1–0.2 AU (11%) and NA
SC24 (Sheaths)	[0–0.33, 0.07, 0.06, 0.07] AU	0–0.1 AU (86%)	0.1–0.2 AU (11%) and NA
SC23 (ICMEs + Sheaths)	[0.05–1.4, 0.4, 0.36, 0.23] AU	0.2–0.3 AU (24%)	0.3–0.4 AU (15%) and 0.1–0.2 AU (17%)
SC24 (ICMEs + Sheaths)	[0.06–0.99, 0.3, 0.27, 0.18] AU	0.2–0.3 AU (24%)	0.3–0.4 AU (12%) and 0.1–0.2 AU (23%)
Distributions of the duration of MCs			
SC23 (MCs)	[5–56, 19.8, 19, 9.4] h	10–20 h (44%)	20–30 h (28%) and 0–10 h (12%)
SC24 (MCs)	[4–46, 17.5, 16, 9.7] h	10–20 h (42%)	20–30 h (27%) and 0–10 h (23%)
Distributions of the radial sizes of MCs			
SC23 (MCs)	[0.05–0.63, 0.21, 0.21, 0.09] AU	0.2–0.3 AU (38%)	0.3–0.4 AU (11%) and 0.1–0.2 AU (36%)
SC24 (MCs)	[0.03–0.41, 0.16, 0.14, 0.08] AU	0.1–0.2 AU (44%)	0.2–0.3 AU (19%) and 0–0.1 AU (29%)
Distributions of the ratio of radial expansion to propagation speeds of CMEs			
SC23 (CMEs)	[48–127, 98, 110, 27.4] %	120–140% (34%)	NA and 100–120% (19%)
SC24 (CMEs)	[59–127, 103, 106, 26] %	120–140% (48%)	NA and 100–120% (10%)
Distributions of the ratio of radial expansion to propagation speeds of MCs			
SC23 (MCs)	[(–19)–29, 5, 5, 8] %	5–10% (33%)	10–15% (10%) and 0–5% (25%)
SC24 (MCs)	[(–10)–14, 3, 3, 5.7] %	0–5% (38%)	5–10% (21%) and (–20)-0% (31%)

ranging between 30 and 40 h and ~15% (47 events) of ICMEs with the duration within 10–20 h.

The distribution for cycle 23 shows a much wider peak than that for only ICME duration. In contrast, the duration for combined sheaths and ICMEs range for solar cycle 24 varies from 5 to 72 h with an average of 30.3 h. The median and standard deviation of the duration are 27.6 and 15.6 h, respectively. The distribution for cycle 24 peaks at 20–30 h having ~29% (60 events) of the total number of ICMEs. In addition, ~15% (31 events) of the total number of ICMEs have a duration ranging between 30 and 40 h and ~21% (43 events) of ICMEs with a duration ranging between 10 and 20 h. The fractions of the total number of ICMEs over cycles 23 and 24 having a duration shorter (longer) than 30 h are ~43% (57%) and ~58% (42%), respectively. This suggests that the fraction of events in cycle 24 having a duration shorter (longer) than 30 h is increased (decreased) by ~10% of its value in cycle 23. Since the duration of sheaths is equal in both cycles, the reason for shorter duration of ICMEs in cycle 24 will also hold good for the entire transients combining sheaths and ICMEs.

3.2 Radial Size of Interplanetary Coronal Mass Ejections, Sheath, and Entire ICMEs

We investigate the radial sizes of ICMEs, sheaths, and entire transients over solar cycles 23 and 24. The range, average, median, and standard deviation of the radial sizes of ICMEs over solar cycles 23 and 24 are noted in **Table 1**. The value of KS statistic $D = 0.247$ is found for the two samples of the radial sizes of ICMEs, taking each sample for solar cycles 23 and 24. We compute $D_c = 0.175$ at $p = 0.001$, and in this case, $D > D_c$, which implies that at the confidence level of 99.9%, the radial sizes of ICMEs are different in cycles 23 and 24. The average radial sizes of ICMEs in cycle 23 are 0.33 AU which decreased by 33% in

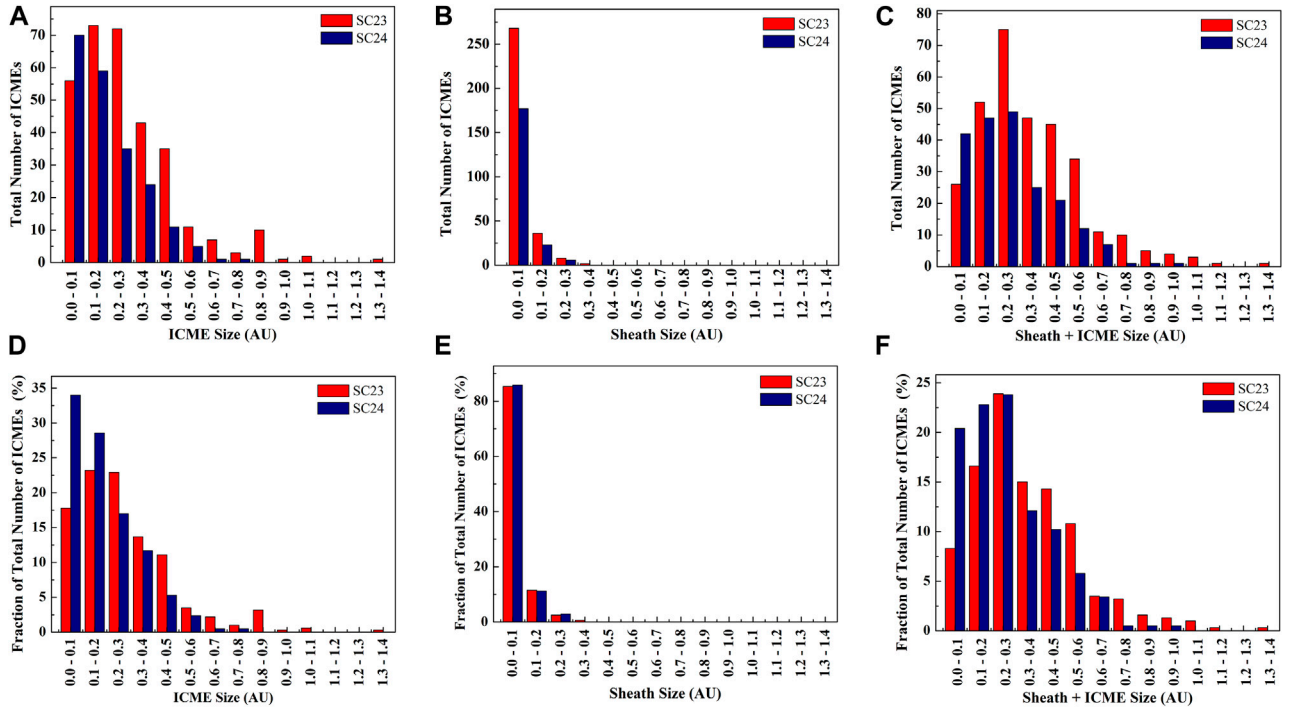

FIGURE 2 | The distributions of the radial sizes of ICMEs region, sheaths region preceding ICMEs, and the entire region of ICMEs together with sheaths (i.e., entire transients) for solar cycles 23 and 24 are shown. **(A),(B),(C)** and **(D),(E),(F)** show the distributions for the total number of ICMEs and the percentage fraction of the total number of ICMEs in each bin of duration, respectively.

cycle 24. From **Figure 2**, we see that the distribution of radial sizes for cycle 23 peaks at 0.1 to 0.2 AU having ~23% (73 events) of the total number of ICMEs. However, the distribution peak for solar cycle 24 is within 0.1 AU having ~34% (70 events) of the total number of ICMEs. For both cycles 23 and 24, the fraction of the total number of ICMEs corresponding to adjacent larger and smaller radial sizes than the distribution peak is also noted in **Table 1**. In addition to the distribution peak in cycle 23, there are ~23% (72 events) of the total number of ICMEs which have radial sizes within 0.2–0.3 AU while ~18% (56 events) of total ICMEs have radial sizes within 0.1 AU. However for cycle 24, in addition to the distribution peak, there are ~29% (59 events) of cases having radial sizes within 0.1–0.2 AU.

The distribution of radial sizes for both cycles is positively skewed, and the degree of skewness is stronger for cycle 23. The fractions of the total number of ICMEs over cycles 23 and 24 having radial sizes smaller (larger) than 0.2 AU are ~41% (59%) and ~63% (37%), respectively. The smaller fraction of the total number of ICMEs in cycle 24 at increasing radial sizes suggests that the sizes of ICMEs were relatively smaller than that in cycle 23. Earlier studies have confirmed the reduced heliospheric pressure in cycle 24 than that in previous cycle (Gopalswamy et al., 2020), and such reduced pressure should have allowed the CMEs to expand to larger sizes at 1 AU. Also, the anomalous lateral expansion of CMEs close to the Sun was confirmed by Gopalswamy et al. (2014). The possible reasons for smaller radial sizes of ICMEs in cycle 24 despite their propagation through the reduced pressure in the ambient medium will be discussed in **Section 4**. It is possible that ICMEs of cycle 23 are expanding at faster rate which does not cease even at larger distances from the Sun in contrast to ICMEs of cycle 24. We will also discuss our findings in comparison with earlier studies (Mitsakou and Moussas, 2014; Jian et al., 2018) on different chosen samples of ICMEs at 1 AU during different phases of cycles 23 and 24.

The range, average, median, and standard deviation of radial sizes of sheaths region of ICMEs in cycles 23 and 24 are listed in **Table 1**. The value of KS statistic $D = 0.116$ is found for the two samples of radial sizes of sheaths, taking each sample for solar cycles 23 and 24. We compute $D_c = 0.122$ at $p = 0.05$, and in this case, $D < D_c$, which implies that at the confidence level of 95%, the radial sizes of sheaths are not different in cycles 23 and 24. The distribution peak of sheaths radial sizes and the adjacent larger than the distribution peak is almost the same for both the cycles as shown in **Figure 1**. The distribution peak is within 0.1 AU for 85 and 86% for the total number of ICMEs in cycles 23 and 24, respectively. This suggests an equal degree of pile-up compression of the ambient medium, i.e., sheath accumulation region, ahead of ICMEs front. However, this is not expected as there are differences in the ICMEs speeds, sizes, and pressure in background solar wind medium between cycles 23 and 24 which should have resulted in a different rate of compression and lateral deflection of ambient medium plasma around the leading edge of ICMEs (Siscoe and Odstrcil, 2008).

The distribution of radial sizes of the entire transients, i.e., ICMEs combined with sheaths, is shown in the right panel

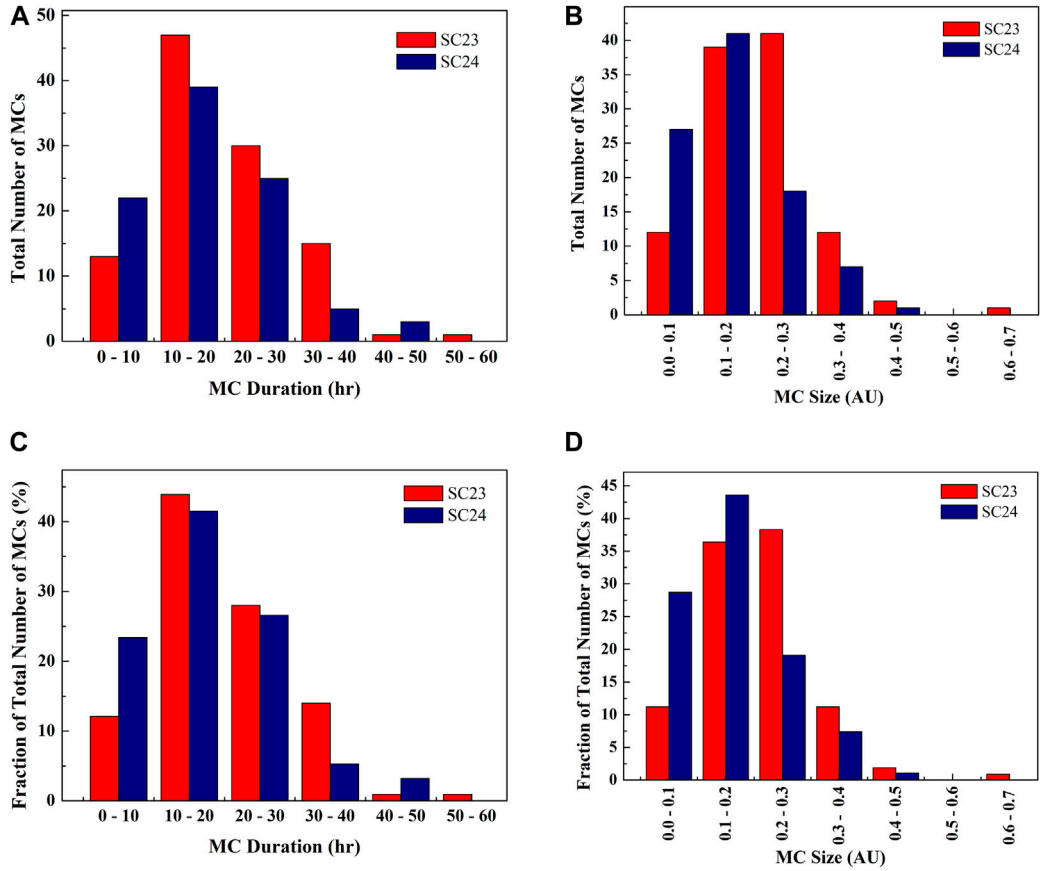

FIGURE 3 | The distributions of the duration and radial sizes of MCs for solar cycles 23 and 24 are shown. **(A),(B)** and **(C),(D)** show the distributions for the total number of MCs and the percentage fraction of the total number of MCs in each bin, respectively.

of **Figure 2** for both the cycles. The value of KS statistic $D = 0.248$ is found for the two samples of the radial sizes of entire region of ICMEs, taking each sample for solar cycles 23 and 24. We compute $D_c = 0.175$ at $p = 0.001$, and in this case, $D > D_c$, which implies that at the confidence level of 99.9%, the radial sizes of entire transient are different in cycles 23 and 24. The distribution for entire transients is slightly wider at peak than that for only ICMEs. The radial sizes at distribution peak, larger and smaller radial sizes than the peak with their corresponding fraction of the total number of events are listed in **Table 1**. The average radial size of the entire transients is 0.4 AU in cycle 23 which decreased by ~25% in cycle 24. The distribution of radial sizes of combined regions of sheaths and ICMEs peaks in the range 0.2–0.3 AU having ~24% of the total number of ICMEs in both cycles. We note that there are ~15% (47 events) and ~17% (52 events) of the total number of ICMEs in cycle 23 having radial sizes within 0.3–0.4 AU and 0.1-0.2 AU respectively. However, for cycle 24, there are ~12% (25 events) of the total number of ICMEs having radial sizes within 0.3–0.4 and ~23% (43 events) of ICMEs with sizes within 0.1–0.2 AU. We also note that the fractions of the total number of ICMEs over cycles 23 and 24 having radial sizes smaller (larger) than 0.3 AU are ~49% (51%) and ~67% (33%), respectively. It is obvious that the fraction of events in cycle 24 having radial sizes smaller (larger) than 0.3 AU is increased (decreased) by ~18% of its value in cycle 23 highlighting relatively larger sizes of transients in cycle 23.

3.3 Radial Sizes and Duration of Magnetic Clouds

The number of magnetic clouds (MCs) observed at 1 AU in solar cycles 23 and 24 is 107 and 94, respectively. These numbers of MCs are ~34% and ~45% of the total number of ICMEs in cycles 23 and 24. The abundance of MCs in cycle 23 is in agreement with earlier studies that MCs are about one-third of the total number of ICMEs (Richardson and Cane, 2010; Chi et al., 2016). However, there are more MCs per ICME in cycle 24 despite it was weaker in terms of sunspot number than cycle 23. The distribution of duration and radial sizes of MCs during both cycles are shown in **Figure 3**. For the samples of MCs in both cycles, the value of KS statistic $D = 0.143$ is found for the two samples of the duration of MCs, taking each sample for solar cycles 23 and 24. We compute $D_c = 0.192$ at $p = 0.05$, and in this case, $D < D_c$, which implies that at the confidence level of 95%, the duration of MCs is not different in cycles 23 and 24. But, for the two samples of the radial sizes of MCs, taking each sample for

solar cycles 23 and 24, $D = 0.269$. The value of $D_c = 0.230$ at $p = 0.01$, therefore, we find $D > D_c$ for the radial sizes. This implies that at the confidence level of 99%, the radial sizes of MCs are different in cycles 23 and 24.

For the distribution of duration and radial sizes, the range, average, median, and standard deviation for MCs observed in both cycles are listed in **Table 1**. We note that the average duration of MCs in cycle 23 is 19.8 h, and it decreased by ~12% in cycle 24. The average size of MCs in cycle 23 is 0.21 AU, and it decreased by ~24% in cycle 24. This implies that average speed of MCs at 1 AU in solar cycle 24 should have decreased by ~14% of that in the earlier cycle. From the *in situ* observations, we confirm that average speed of MCs in cycle 23 is 470 km s^{-1} which decreased by ~16% in cycle 24. However, the range of mean speeds is 315–1,315 km s^{-1} and 270–580 km s^{-1} for cycles 23 and 24, respectively. The smaller sizes of MCs in cycle 24 than in cycle 23 could also be due to diminished magnetic content inside MCs of cycle 24 which is also responsible for their reduced geoeffectiveness (Kilpua et al., 2014). The study by Gopalswamy et al. (2015b) found that the total pressure inside MCs of cycle 24 dropped by 41%, very similar to the drop in the ambient pressure by 38%, of its value in cycle 23. Lugaz et al. (2017) found that the average threshold of CME speed to drive a shock was lower in solar cycle 24 than that in solar cycle 23. Despite this, they found that the percentage of CMEs with shocks was the same for both cycles 23 and 24. The decrease in expected frequency shocks in cycle 24 was explained in terms of the slower expansion speed of CMEs in solar cycle 24 (Lugaz et al., 2017).

Although it has been confirmed that the total pressure in the heliosphere at 1 AU in cycle 24 is reduced by ~38% of its value in cycle 23 (Gopalswamy et al., 2015b), the reduced sizes of MCs in cycle 24 by ~24% of its value in cycle 23 are possible if the weakened ambient pressure in cycle 24 did not play a dominant role in shaping the radial expansion of MCs, especially during the later phase of their propagation. However, the possibility that the flux-ropes of cycle 24 were smaller in the beginning itself near the Sun cannot be ignored completely. The average duration of MCs in cycles 23 and 24 has decreased by ~25% of that for the ICMEs in the same cycle. The average radial sizes of MCs in cycles 23 and 24 have decreased by ~36% and ~33%, respectively, of that for the ICMEs in the same cycle. The smaller radial sizes and duration of MCs than non-MCs ICMEs, in both cycles, can arise due to the geometric selection effect, i.e., ICMEs nose pass through the observing spacecraft, and higher magnetic erosion of MCs in solar wind medium.

From **Figure 3**, we note that the distribution of duration of MCs for cycle 23 peaks at 10–20 h having ~44% (47 events) of the total number of MCs. The adjacent larger and smaller durations than distribution peak have ~28% (30 events) and ~12% (13 events) of the total number of MCs. The distribution for cycle 24 also peaks at the same 10–20 h with ~42% (39 events) of the total number of MCs, and the adjacent larger and smaller duration than distribution peak have ~27% 25) and ~23% (22 events) of the total number of MCs. The distribution peak of the duration of MCs has shifted towards a shorter duration having a larger fraction of events than that for ICMEs. The distribution peak of radial sizes for cycle 24 peaks at 0.1 to 0.2 AU having ~44% (41 events) of the total number of MCs while for cycle 23, it peaks at 0.2 to 0.3 AU having ~38% (41 events) of the total number of MCs.

We also note that the adjacent larger and smaller radial sizes than the distribution peak of radial sizes for cycle 23 have ~11% (12 events) and ~36% (39 events) of the total number of MCs, respectively. However, for cycle 24, the adjacent larger and smaller radial sizes than the distribution peak have ~19% (18 events) and ~29% (27 events), respectively, of the total number of MCs. Therefore, even taking the spread in the peak of the radial sizes, a majority of MCs in cycle 24 are found to be smaller than those in the earlier cycle. This is evident as the fractions of the total number of MCs over cycles 23 and 24 having a size shorter (longer) than 0.2 AU are ~48% (52%) and ~72% (28%), respectively. We also note that the degree of decrease in the sizes of MCs than that of ICMEs, in a fraction of events with radial sizes larger than 0.2 AU, is almost the same for both cycles. In **Section 4**, we discuss the reasons for our finding in the context of earlier studies.

3.4 Expansion Speeds of Magnetic Clouds

The RC catalog adopted for our analysis also lists the most probable coronal mass ejection (CMEs) associated with a few ICMEs/MCs. We find that there are 53 and 29 MCs in solar cycles 23 and 24, respectively, for which a clear association with their source CMEs is established. Although the total number of CME-MC pairs is relatively small, we examine the evolution of their radial expansion speeds from the Sun to 1 AU, in order to understand the role of the pressure difference between ICME and ambient medium, in their overall propagation. The average radial propagation speeds of CMEs close to the Sun are noted as 1,415 km s^{-1} in cycle 23 and 1,000 km s^{-1} in cycle 24, while its value for MCs near the Earth is noted as 510 km s^{-1} in cycle 23 and 410 km s^{-1} in cycle 24. Also, the average radial expansion speeds of CMEs close to the Sun are noted as 1,550 km s^{-1} in cycle 23 and 1,110 km s^{-1} in cycle 24, while its value for strictly expanding MCs near the Earth is noted as 45 km s^{-1} in cycle 23 and 25 km s^{-1} in cycle 24. Since the propagation speeds of CMEs and MCs are different close to the Sun and at 1 AU, one needs to estimate that what fraction of radial propagation speeds is the radial expansion speeds for CMEs and MCs in both cycles.

The methods to estimate the radial propagation and expansion speeds close to the Sun and Earth are described in **Section 2**. The distributions of the ratio of radial expansion to radial propagation speeds of CMEs and MCs are shown in **Figure 4** for both solar cycles 23 and 24. We performed the KS test on the two samples of the ratio of expansion to propagation speeds of CMEs, taking each sample for solar cycles 23 and 24. The value of KS statistic $D = 0.143$ is found while the computed $D_c = 0.314$ at $p = 0.05$ is noted. It is clear that $D < D_c$, which implies that at the confidence level of 95%, the ratio of expansion to propagation speeds of CMEs is not different in cycles 23 and 24. Similarly, the KS test on the two samples of the ratio of expansion to propagation speeds of MCs at 1 AU gives $D = 0.236$. It is clear that $D < D_c$ at $p = 0.05$, which implies that at the confidence level of 95%, the ratio of expansion to propagation speeds of MCs is not different in cycles

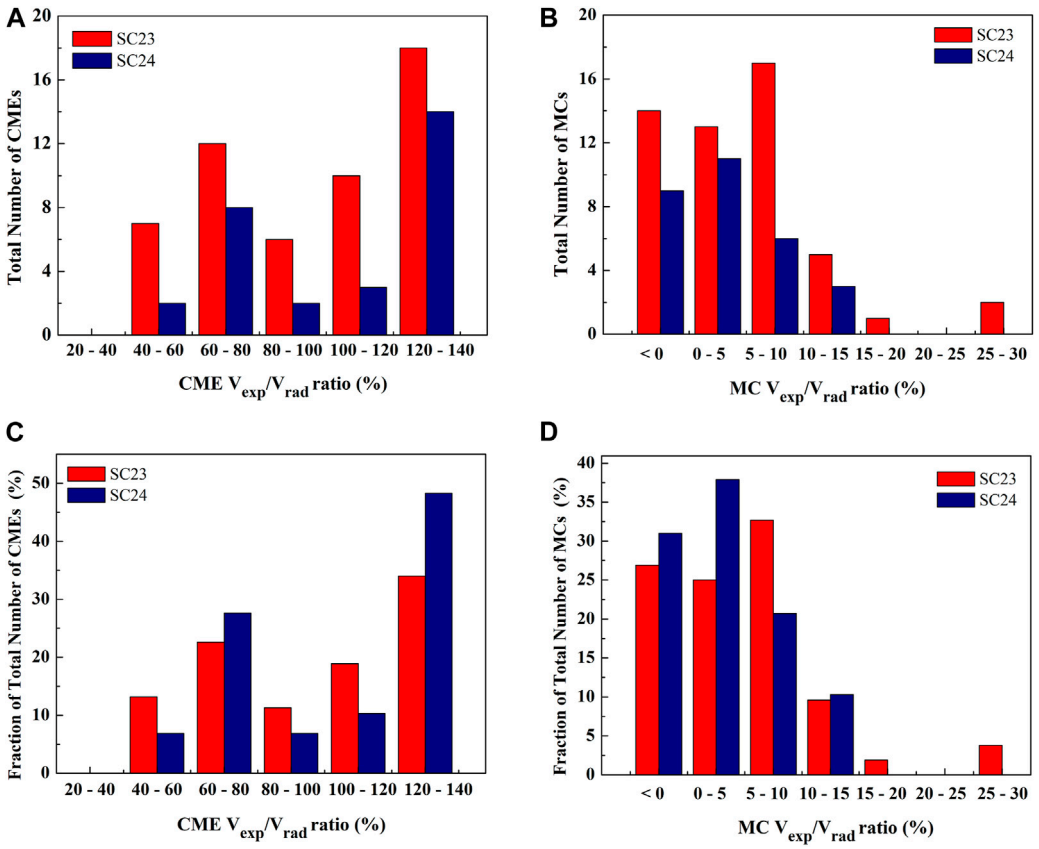

FIGURE 4 | The distributions of the ratio of radial expansion (V_{exp}) to radial propagation speed (V_{rad}) of CMEs near the Sun and associated MCs at 1 AU for solar cycles 23 and 24 are shown. **(A),(B)** and **(C),(D)** show the distributions for the total number of CMEs/MCs and the percentage fraction of the total number of CMEs/MCs in each bin, respectively.

23 and 24. The range, average, median, and standard deviation for the ratio of radial expansion to propagation speeds of the selected CMEs and MCs are listed in **Table 1**.

Our study assumes that under self-similar expansion, the radial and lateral expansion speeds of CMEs are equal when they are close to the Sun. We note that the average ratio of radial expansion to propagation speeds of CMEs in cycle 23 is 98%, and it increased to ~103% in cycle 24. However, the average ratio of radial expansion to propagation speeds of MCs in cycle 23 is 5%, and it decreased to ~3% in cycle 24. Excluding MCs with negative expansion speeds, i.e., taking only the strictly expanding MCs, we note that the average radial expansion speeds of MCs in cycle 23 are ~9% (45 km s^{-1}) of average radial propagation speeds (510 km s^{-1}) and become ~6% (25 km s^{-1}) of propagation speeds (410 km s^{-1}) in cycle 24. The statistics suggest that the radial expansion speeds of CMEs close to the Sun are only slightly larger fraction of their radial propagation speeds in cycle 24 than in cycle 23. Also, the radial expansion speeds of MCs at 1 AU in cycle 24 are only slightly smaller fraction of their radial propagation speeds than that in cycle 23. The decrease in the average radial expansion speeds measured at 1 AU for MCs in cycle 24 than that in cycle 23 is also noted in earlier studies (Gopalswamy et al., 2015b; Lugaz et al., 2017). Clearly, the distribution of expansion speeds of CMEs/MCs in cycles 23 and 24 is not significantly different which is also confirmed from the KS test.

From **Figure 4**, we note that the distribution of the ratio of expansion to propagation speeds of CMEs peaks at 120–140% for both the cycles with ~34% (18 events) and ~48% (14 events) of the total number of CMEs in cycles 23 and 24, respectively. The distribution for the range 100%–120% includes ~19% (10 events) and ~10% (3 events) of the total number of CMEs. Taking all the bins with the ratio of expansion to radial propagation speeds below 100% (i.e., when radial expansion speeds are smaller than the radial propagation speeds), the fraction of CMEs in cycle 23 is only ~5% larger than that in cycle 24. These statistics suggest that expansion of CMEs, in general, is not significantly larger in solar cycle 24 than that in the previous cycle. However, the overexpansion of CMEs of cycle 24 has been reported earlier and explained in terms of reduced ambient solar wind pressure (Gopalswamy et al., 2014, Gopalswamy et al., 2020). It is possible that such overexpansion occurred much closer to the Sun in the coronagraphic field of view than the height at which the speeds are estimated and used in our study.

From **Figure 4**, we note that the ratio of radial expansion to radial propagation speeds of MCs at 1 AU in cycle 24 peaks at 0–5% and has ~38% (11 events) of the total number of MCs while

only ~21% (6 events) of MCs have expansion speeds contribution in the range of 5–10% of the radial propagation speeds. On the other hand, the distribution for cycle 23 peaks at 5–10% and has ~33% (17 events) of the total number of MCs. About ~10% of events in both cycles have radial expansion speeds in the range of 10–15% of their radial propagation speeds. It is also noted that ~27% and ~31% of the total number of MCs have negative expansion speeds at 1 AU in solar cycles 23 and 24, respectively. The non-expansion of clouds is possible if they are compressed by the preceding and/or following large-scale solar wind structures. Such compression of CMEs by the following fast solar wind and faster CMEs has been reported earlier (Temmer et al., 2014; Mishra et al., 2017; Heinemann et al., 2019). Excluding the compressed MCs, the radial expansion speed of MCs is typically a small fraction (9% for cycle 23 and 6% for cycle 24) of their radial propagation speeds. Our statistics suggest that MCs in solar cycle 24 at 1 AU, on average, are expanding slightly slower than that in cycle 23. It is also found by Lugaz et al. (2017) that radial expansion speeds of CMEs in solar cycle 24 are smaller by about a factor of 2 than that in cycle 23. They also showed that reduced expansion speed is compensated by the decrease in the solar wind speeds and fast magnetosonic speeds. This resulted in a more or less equal probability of shock generation by CMEs in cycles 24 and 23.

In the present study, the radial expansion speeds of MCs are taken as half of the difference between the propagation speeds at the front and back of the MCs. However, Démoulin et al. (2008) have shown that the differences in the velocity at the front and back of MCs are just apparent, and larger differences do not necessarily imply their faster expansion rate. They showed that the velocity difference (ΔV) between the front and back of MC is the product of the mean velocity (V_c), the ratio of MC time duration (Δt) to its transit time ($\tau = D/V_c$) at a distance D from the Sun, and the expansion coefficient (ζ). This implies that the larger differences in the velocity at the front and back can arise due to a larger mean propagation velocity and acceleration of the MC. We note that Démoulin et al. (2008) had used the x-component (along the Sunspacecraft line) of MC speed and determined ΔV_x, but we can use the total speed of Earth-directed MC observed at L1 as the difference between ΔV_x and ΔV in our case would be insignificant. The dimensionless expansion rate, $\zeta = \frac{D}{V^2}\frac{\Delta V}{\Delta t}$, can be helpful in disentangling the internal causes of radial expansion from that of CMEs propagation speeds in a variable surrounding solar wind.

We computed the dimensionless expansion parameter of each MC in solar cycles 23 and 24 for which the CME-MC pair was established. We find that around 27% and 31% of MCs from the sample have a negative value of dimensionless expansion parameter implying that they are non-expanding MCs with ΔV less than zero. Taking only the expanding MCs with ΔV greater than zero, we find the average value of dimensionless expansion parameters as 0.64 and 0.62 in solar cycles 23 and 24, respectively. Therefore, we see that the average expansion rates in both cycles are almost equal. The constancy of the expansion parameter is expected as the decrease in the average value of ΔV in cycle 24 is compensated by the decrease in the mean velocity (V_c) of MC. Earlier studies have also shown that although MCs of different sizes and field strengths have a very broad range of velocity difference at their front and back, they have a narrow range ($\zeta = 0.8 \pm 0.2$) of dimensionless expansion parameter (Démoulin et al., 2008; Démoulin and Dasso, 2009; Gulisano et al., 2010).

Although the average value of the dimensionless expansion parameter is 0.63 ± 0.1 for MCs in both the cycles, it ranges from 0.1 to 1.57 for cycle 23 and 0.1 to 1.77 for cycle 24. The larger spread in the expansion parameter is expected due to different plasma parameters in each MCs, overtaking streams, and the ambient solar wind. The MCs compressed by following large-scale solar wind structures are expected to have a lower value of dimensionless expansion parameter, in general. If the compression is strong enough, it can indeed stop the expansion of MCs leading to ΔV less than zero. However, if the following structures/streams responsible for compression completely overtake through the preceding MC, then the MC would experience a lesser pressure at its back but higher internal pressure inside. This can cause the MC to overexpand, i.e., faster than the usual rate of expansion, and have a value of dimensionless expansion parameter greater than unity (Gulisano et al., 2010). It is obvious that the main driver of MC expansion is the rapid decrease of the total solar wind pressure with solar distance, but other factors such as pressure inside MC, its compression by following structures, and thereafter its temporal stage of evolution at the time of observations can influence the expansion rate of the MC.

4 SUMMARY AND DISCUSSION

In the present study, we have estimated the duration and radial sizes of ICMEs, sheaths preceding ICMEs, and MCs that arrived near the Earth at 1 AU during solar cycles 23 and 24. Taking CME-MC pairs associated with each other, we estimated radial propagation and expansion speeds of CMEs close to the Sun and MCs at 1 AU. The estimated dimensions of ICMEs/MCs are interpreted based on their radial expansion behavior between the Sun and Earth. The distribution of estimated characteristics of ICMEs and MCs is listed in **Table 1**. We compare our findings with those of earlier studies that have used a different sample of events during different phases/intervals of solar activity.

Our analysis finds the average duration of ICMEs, sheaths, entire region ICMEs, and MCs in cycle 23 at 1 AU as approximately 26, 7, 35, and 20 h, respectively. The average duration of ICMEs, entire ICMEs, and MCs in solar cycle 24 is decreased by ~19%, ~16%, and ~12%, respectively, of its value in the previous cycle 23. In contrast to ICMEs/MCs, the average duration of sheaths in cycle 24 is the same as in the previous cycle. Furthermore, the average radial sizes of ICMEs, sheaths, entire region of ICMEs, and MCs in cycle 23 are 0.33, 0.07, 0.4, and 0.21 AU, respectively. The average radial sizes of ICMEs, entire ICMEs, and MCs in solar cycle 24 decreased by ~33%, ~25%, and ~24%, respectively, of its value in the previous cycle 23. Similar to duration, the average radial sizes of sheaths of ICMEs remain the same in both cycles.

In general for both cycles, the dimensional characteristics (i.e., duration and radial sizes) of the ICMEs, entire region of

ICMEs, and MCs have wide distributions which range from around one-fifth of their average values to around three times their average values. In our study, radial sizes of MCs are around two-third of ICMEs radial sizes in both cycles. The possibility of erosion of ICMEs at the front during their propagation can be a reason for smaller and embedded MCs in the extended ICMEs structures (Ruffenach et al., 2012; Wang et al., 2018). The radial sizes of ICMEs, MCs, and their sheaths also depend on the trajectory of *in situ* spacecraft along the flanks or nose of the structures. In our study, the radial sizes of the sheaths at 1 AU range from as low as zero to as high as five times its average value. The average radial sizes of the sheaths are one-fifth and one-third of their following ICMEs radial sizes in cycles 23 and 24, respectively. Surprisingly, the radial sizes of sheaths in a weaker solar cycle 24 are a relatively larger fraction of their following ICMEs radial sizes than that in cycle 23. This suggests that there is almost no correlation between sheaths and ICME radial sizes at 1 AU. This is expected because the dynamic evolution of ICMEs is governed by expansion but the compression by CMEs or shocks is responsible for the sheaths (Russell and Mulligan, 2002). In a recent study, Temmer et al. (2021) have shown that the amount of sheath material depends on ambient solar wind density and speed ahead of the CME as well as on the angular width of the CME.

Our estimates of average duration and radial sizes of ICMEs in cycle 23 are slightly smaller by only 10% of that reported by Zhang et al. (2008). However, the average values of sheaths duration and sizes in our study are considerably smaller by 25% of those reported by them. Such a difference is possible as they have selected ICMEs responsible for intense geomagnetic storms which are expected to be stronger than the general population of ICMEs considered in the present study. Furthermore, the study of Forsyth et al. (2006); Mitsakou and Moussas (2014) found that average radial sizes of ICMEs (sheaths) in cycle 23 are 0.27 AU (0.1 AU) which are smaller by 20% (larger by 30%) of our estimates. Our findings of radial sizes and duration of ICMEs in cycle 23 are in agreement with the study of Richardson and Cane (2010). Furthermore, our study reports that the average radial sizes for ICMEs during cycles 23 and 24 are smaller by 10% and 25%, respectively, than that reported by Lawrance et al. (2020). The difference of our results from that in Lawrance et al. (2020) is expected as they have considered events only during the declining phase of cycles when one expects to have stronger ICMEs leading to intense geomagnetic storms than that over the rising phase of the solar cycle (Gonzalez et al., 2011).

Based on the *in situ* observations of MCs from *Helios* spacecraft, Gulisano et al. (2010) established a relation between the average radial size (S) of a MC and its distance (R) in AU from the Sun. They found that $S = (0.23 \pm 0.01) \times R^{0.78 \pm 0.12}$, and this result was consistent with the findings of Bothmer and Schwenn (1998) within error bars. However, using the *in situ* observations of MCs from several spacecraft located at different distances within 0.3 to 10 AU, Leitner et al. (2007) expressed the relation as $S = (0.20 \pm 0.02) \times R^{0.61 \pm 0.09}$. In the present study, the average radial size of MCs in solar cycle 23 is in good agreement with that derived from the expression of Gulisano et al. (2010) and Leitner et al. (2007). However, the average radial size of MCs in solar cycle 24 is 30% and 20% smaller than that obtained from expression by Gulisano et al. (2010) and Leitner et al. (2007), respectively. We also note that the estimated sizes of MCs included in our study agree with the typical sizes of MCs during 1974–1981 as reported in Bothmer and Schwenn (1998). Overall, our findings of radial sizes are reasonably consistent with earlier studies.

Furthermore, the average radial expansion speeds (V_{exp}) of MCs can be approximated as $V_{exp} = 0.18 \times V_{MC} \times D^{0.22}$ from the expression of Gulisano et al. (2010), where V_{MC} is the radial propagation speeds of MCs. The expansion speeds of MCs at 1 AU from this expression are 100% and 200% larger than that from *in situ* observations in solar cycles 23 and 24, respectively. Also, following the expression of Leitner et al. (2007), $V_{exp} = 0.12 \times V_{MC} \times D^{0.39}$, the expansion speeds of MCs at 1 AU are 30% and 100% larger than that from *in situ* observations in solar cycles 23 and 24, respectively. It is obvious that these established relations overestimate the expansion speeds of MCs at 1 AU. It is possible that the expressions of radial sizes as a function of distance from the Sun are biased due to the use of higher fraction of observations within 1 AU (such as from *Helios* at 0.3 to 0.7 AU). Furthermore, we also note that neither of the expressions used above was fitted using observations close to the Sun, it would be misleading to compare the expansion speeds of CMEs from the expressions that we obtained from coronagraphic observations. The differences in radial sizes/expansion speeds may be attributed to the preference in the selection of events from a different phase and interval of the solar cycle. The difference can also arise from the subjective identification criteria of ICMEs/MCs and also timings of front and rear boundaries of the events in the *in situ* observations.

In our chosen sample, around 70% of MCs are strictly expanding in both solar cycles 23 and 24. This is in agreement with Jian et al. (2018) who reported the same fraction of MCs with nonzero radial expansion speeds at *STEREO* (Kaiser et al., 2008). We find that the radial expansion speeds of MCs in cycles 23 and 24 are only 9% and 6%, respectively, of their radial propagation speeds at 1 AU. Wang et al. (2005) have found that typical speeds at which ICMEs expand at 1 AU are 12% of their radial speeds which is in good agreement with our values for cycle 23. It is expected that non-MC ICMEs have larger radial expansion speeds at 1 AU. We also note that the average radial expansion speed of MCs at 1 AU in cycle 24 is lower by about a factor of 2 as compared to cycle 23. We find that near the Sun in cycle 24, the fraction of radial speeds as expansion speeds of CMEs is increased by only ~5% of its value in cycle 23; however, a considerable anomalous lateral expansion of CMEs close to the Sun in cycle 24 was reported in Gopalswamy et al. (2014). It is possible that overexpansion of CMEs in cycle 24 happened much closer to the Sun than the height where expansion speeds are estimated and used in our study. We infer that the CMEs in cycle 24 observed as MCs in the *in situ* observations 1 AU have not expanded considerably during the later segment of their long journey.

The expansion of MCs is governed by the difference in the total pressure between MCs and the ambient medium. The ambient solar wind pressure at 1 AU has decreased in cycle 24 as compared to that in cycle 23. Despite this, the reduced average expansion speeds of MCs in cycle 24 are only possible if the total

pressure inside the MCs also decreased. In our analysis, the expansion speeds of CMEs in both cycles are almost similar fraction of their propagation speeds. However, the results of Gopalswamy et al. (2020) suggested that CMEs in solar cycle 24 become halos closer to the Sun and at lower speeds than that in cycle 23. We infer that the reduction in the heliospheric pressure in cycle 24 (Richardson, 2013; Gopalswamy et al., 2015a) seems to be balanced by the dilution of magnetic content inside the CMEs with or without their overexpansion close to the Sun. This can prevent them from expanding further as they evolve through interplanetary medium and reach 1 AU as *in situ* observed MCs. Our findings of radial sizes and expansion speeds at 1 AU suggest that the ratio of MCs to ambient medium total pressure at 1 AU should be slightly higher in cycle 23 than that in cycle 24 which is in agreement with Gopalswamy et al. (2015b). Furthermore, the limited radial expansion of ICMEs/MCs in the interplanetary medium in cycle 24 might have caused their crosssection to rapidly flatten, and this can also be partially responsible for their smaller radial sizes than that in cycle 23. However, the possibility of ejection of relatively smaller flux-ropes from the Sun itself in a weaker cycle 24 cannot be ignored, and further studies are required to rule out this possibility. We assume our findings from studying CME-MC pairs would also apply to CME-ICME (non-MC) pairs. This is because non-MC ICMEs are essentially the same as MCs but appear different due to the geometric selection effect in the *in situ* observations.

In our study, the dimensionless expansion parameter is the same ($\zeta = 0.63 \pm 0.1$) in both the cycles for MCs at 1 AU. This implies a constant expansion rate of MCs at 1 AU in cycles 23 and 24. Also, our analysis does not indicate that the ratio of expansion to propagation speeds of CMEs close to the Sun is considerably different between both cycles. However, the observed larger angular width of CMEs at a given speed in cycle 24 than that in cycle 23 is interpreted owing to overexpansion of CMEs in cycle 24 (Gopalswamy et al., 2014). It is possible that CMEs overexpanded much closer to the Sun than the average height at which speeds are estimated and used in the present study. If one assumes that the average value of dimensionless expansion parameter does not change beyond the distance where pressure balance is reached, this would suggest that CMEs in solar cycle 24 attain pressure balance with the ambient solar wind at a larger distance from the Sun. This can be confirmed in future studies taking limb CMEs and measuring the variation in their radial and lateral expansion speeds as well as angular widths. The sample of CMEs considered in the present study is Earth-directed halos, and their coronagraphic observations suffer from severe projection effects. Therefore, the estimation of radial propagation and expansion speeds of CMEs close to the Sun would have large uncertainties, and the findings based on this cannot be considered strong enough to make a solid conclusion.

Similar to the evolution of radial sizes of ICMEs, the sheaths preceding ICMEs also evolve as they propagate in the heliosphere. Several factors cause solar wind to deflect around an ICME and getting pile-up at its nose (Siscoe and Odstrcil, 2008; Takahashi and Shibata, 2017). The observed sizes of sheaths keeping compressed plasma of ambient medium accumulate gradually over long periods and range of distances from the Sun. The equal average dimension of sheaths in both cycles is unexpected because ICMEs in cycle 23 are of larger sizes, more geoeffective, faster radial propagation, and expansion speeds 1 AU than that in cycle 24. The unexpected result can be explained if the efficiency of these sheath accumulating factors, integrated over time of ICMEs journey from the Sun to 1 AU, is averaged to be equal in both cycles. In the present study, our sample has ~16% and ~26% of the total number of ICMEs without sheaths in cycles 23 and 24, respectively. This is not expected as the slower upstream solar wind speed and lower fast magnetosonic speed in interplanetary space in cycle 24 should have given a higher probability of the formation of shocks and sheaths in cycle 24. However, it was not the case as Lugaz et al. (2017) have shown for the slow CMEs with their reduced radial expansion speeds in cycle 24 compensated the effects of reduced solar wind speeds and fast magnetosonic speeds. Further studies are required in this direction to understand the heliospheric evolution of ICME sheath and its size in connection with the sizes of the ICME (Temmer et al., 2021). Our study did not analyze the sheaths sizes ahead of MCs separately instead focus on the general ICMEs sample including MCs. However, the sheaths preceding MCs observed due to the geometric selection effect are expected to have smaller sizes than the sheaths preceding non-MC ICMEs. This is because the compression ratio by CMEs-driven shock is higher near the nose of the CME front, and the separation between shock and ICME leading edge is larger at the flanks (Kwon and Vourlidas, 2018).

Based on the RC catalog, we find that the ICME number observed at 1 AU in the ecliptic plane in cycle 24 is decreased by 34% of its value in the previous cycle. This can be primarily due to a decrease in the CME rate itself from the Sun; however, other factors such as the launch of Earth-directed CMEs from higher latitudes, longitudes, and their deflection in cycle 24 can also contribute (Lamy et al., 2017; Mishra et al., 2019). The increased fraction of ICMEs as MCs (45% of ICMEs) in cycle 24 than that (24% of ICMEs) in cycle 23 might be an effect of reduced interaction of weaker ICMEs with the weaker ambient solar wind. Such reduced interaction did not disrupt the flux-rope structures and enabled them to be observed as MCs at 1 AU. The abundance of MCs in cycle 24 can also be due to bias in the Earth-arriving CMEs source regions towards the central meridian. In this scenario, one should find a decrease in the occurrence of complex ejecta in cycle 24 which can be explored in future studies. However, the increased abundance of MCs relative to ICMEs did not translate into an increase in the intensity of geomagnetic storms in cycle 24 Kilpua et al. (2014).

Overall, we find that size of ICMEs/MCs, their sheaths, and radial expansion speeds at 1 AU are difficult to be determined from their observations close to the Sun. These characteristics are governed primarily by their expansion and/or compression history with increasing distance from the Sun which is significantly decided by the decrease in the total pressure inside the ICMEs and also in the environment around them. Our study used expansion speeds of CMEs close to the Sun and MCs at 1 AU, and thus, the conclusion drawn here is based on the two-point measurements only. However, to better understand the evolution of radial sizes and expansion behavior of ICMEs, we need to observe them at different heliocentric distances. We point out that there is vast literature discussing the evolution of propagation speeds of CMEs from the Sun to 1 AU (Gopalswamy et al., 2001; Manoharan et al., 2004; Davies et al., 2009; Liu et al., 2010; Mishra et al., 2014;

Harrison et al., 2018); however, only limited efforts are made for understanding the evolution of radial expansion speeds (Liu et al., 2005; Démoulin and Dasso, 2009; Gulisano et al., 2010). Therefore, further studies in this direction are required for an in-depth understanding of the factors responsible for the observed sizes of ICMEs/MCs and especially their preceding sheaths structures.

DATA AVAILABILITY STATEMENT

Publicly available datasets were analyzed in this study. This data can be found here: CDAW CME catalog (https://cdaw.gsfc.nasa.gov/CME_list/), RC catalog of ICMEs (http://www.srl.caltech.edu/ACE/ASC/DATA/level3/icmetable2. htm), and CDAWeb (https://cdaweb.gsfc.nasa.gov/index.html/).

AUTHOR CONTRIBUTIONS

WM and NS contributed to the initial conception of the paper. The analysis was carried out primarily by UD under the guidance of WM and NS. The main draft was prepared by WM, and all of the authors have read the paper and approved its final version.

ACKNOWLEDGMENTS

We acknowledge the use of CDAW catalog of CMEs, RC catalog of ICMEs, and CDAWeb for providing *in situ* observations of solar wind at 1 AU. We also thank the referees for their helpful comments.

REFERENCES

Antia, H. M., and Basu, S. (2010). Solar Rotation Rate During the Cycle 24 minimum in Activity. *Astrophysical J.* 720, 494–502. doi:10.1088/0004-637X/720/1/494

Bisoi, S. K., Janardhan, P., and Ananthakrishnan, S. (2020). Another Mini Solar Maximum in the Offing: A Prediction for the Amplitude of Solar Cycle 25. *J. Geophys. Res. Space Phys.* 125, e27508. doi:10.1029/2019JA027508

Bothmer, V., and Schwenn, R. (1998). The Structure and Origin of Magnetic Clouds in the Solar Wind. *Ann. Geophys.* 16, 1–24. doi:10.1007/s00585-997-0001-x

Brueckner, G. E., Howard, R. A., Koomen, M. J., Korendyke, C. M., Michels, D. J., Moses, J. D., et al. (1995). The Large Angle Spectroscopic Coronagraph (LASCO). *Solar Phys.* 162, 357–402. doi:10.1007/BF00733434

Burlaga, L. F., Plunkett, S. P., and Cyr, St. O. C. (2002). Successive CMEs and Complex Ejecta. *J. Geophys. Res.* 107, 1266. doi:10.1029/2001JA000255

Burlaga, L., Sittler, E., Mariani, F., and Schwenn, R. (1981). Magnetic Loop Behind an Interplanetary Shock: Voyager, Helios, and IMP 8 Observations. *J. Geophys. Res.* 86, 6673–6684. doi:10.1029/JA086iA08p06673

Chi, Y., Shen, C., Wang, Y., Xu, M., Ye, P., and Wang, S. (2016). Statistical Study of the Interplanetary Coronal Mass Ejections From 1995 to 2015. *Sol. Phys.* 291, 2419–2439. doi:10.1007/s11207-016-0971-5

Davies, J. A., Harrison, R. A., Rouillard, A. P., Sheeley, N. R., Perry, C. H., Bewsher, D., et al. (2009). A Synoptic View of Solar Transient Evolution in the Inner Heliosphere Using the Heliospheric Imagers on STEREO. *Geophys. Res. Lett.* 36, a–n. doi:10.1029/2008GL036182

DeForest, C. E., Howard, T. A., and McComas, D. J. (2013). Tracking Coronal Features From the Low Corona to Earth: A Quantitative Analysis of the 2008 December 12 Coronal Mass Ejection. *Astrophysical J.* 769, 43. doi:10.1088/0004-637X/769/1/43

Démoulin, P., and Dasso, S. (2009). Causes and Consequences of Magnetic Cloud Expansion. *Astron. Astrophysics.* 498, 551–566. doi:10.1051/0004-6361/200810971

Démoulin, P., Janvier, M., Masías-Meza, J. J., and Dasso, S. (2016). Quantitative Model for the Generic 3D Shape of ICMEs at 1 AU. *Astron. Astrophysics.* 595, A19. doi:10.1051/0004-6361/201628164

Démoulin, P., Nakwacki, M. S., Dasso, S., and Mandrini, C. H. (2008). Expected *In Situ* Velocities From a Hierarchical Model for Expanding Interplanetary Coronal Mass Ejections. *Sol. Phys.* 250, 347–374. doi:10.1007/s11207-008-9221-9

Eyles, C. J., Harrison, R. A., Davis, C. J., Waltham, N. R., Shaughnessy, B. M., Mapson-Menard, H. C. A., et al. (2009). The Heliospheric Imagers Onboard the STEREO Mission. *Sol. Phys.* 254, 387–445. doi:10.1007/s11207-008-9299-0

Forsyth, R. J., Bothmer, V., Cid, C., Crooker, N. U., Horbury, T. S., Kecskemety, K., et al. (2006). ICMEs in the Inner Heliosphere: Origin, Evolution and Propagation Effects. *Space Sci. Rev.* 123, 383–416. doi:10.1007/s11214-006-9022-0

Gonzalez, W. D., Echer, E., Clúa de Gonzalez, A. L., Tsurutani, B. T., and Lakhina, G. S. (2011). Extreme Geomagnetic Storms, Recent Gleissberg Cycles and Space Era-Superintense Storms. *J. Atmos. Solar-Terrestrial Phys.* 73, 1447–1453. doi:10.1016/j.jastp.2010.07.023

Good, S. W., and Forsyth, R. J. (2016). Interplanetary Coronal Mass Ejections Observed by MESSENGER and Venus Express. *Sol. Phys.* 291, 239–263. doi:10.1007/s11207-015-0828-3

Gopalswamy, N., Akiyama, S., and Yashiro, S. (2020). The State of the Heliosphere Revealed by Limb-Halo Coronal Mass Ejections in Solar Cycles 23 and 24. *Astrophysical J.* 897, L1. doi:10.3847/2041-8213/ab9b7b

Gopalswamy, N., Akiyama, S., Yashiro, S., Xie, H., Mäkelä, P., and Michalek, G. (2014). Anomalous Expansion of Coronal Mass Ejections During Solar Cycle 24 and its Space Weather Implications. *Geophys. Res. Lett.* 41, 2673–2680. doi:10.1002/2014GL059858

Gopalswamy, N., Dal Lago, A., Yashiro, S., and Akiyama, S. (2009). The Expansion and Radial Speeds of Coronal Mass Ejections. *Cent. Eur. Astrophysical Bull.* 33, 115–124.

Gopalswamy, N., Lara, A., Yashiro, S., Kaiser, M. L., and Howard, R. A. (2001). Predicting the 1-AU Arrival Times of Coronal Mass Ejections. *J. Geophys. Res.* 106, 29207–29217. doi:10.1029/2001JA000177

Gopalswamy, N., Xie, H., Akiyama, S., Mäkelä, P., Yashiro, S., and Michalek, G. (2015a). The Peculiar Behavior of Halo Coronal Mass Ejections in Solar Cycle 24. *Astrophysical J.* 804, L23. doi:10.1088/2041-8205/804/1/L23

Gopalswamy, N., Yashiro, S., Xie, H., Akiyama, S., and Mäkelä, P. (2015b). Properties and Geoeffectiveness of Magnetic Clouds During Solar Cycles 23 and 24. *J. Geophys. Res. Space Phys.* 120, 9221–9245. doi:10.1002/2015ja021446

Gopalswamy, N., Yashiro, S., Michalek, G., Xie, H., Mäkelä, P., Vourlidas, A., et al. (2010). A Catalog of Halo Coronal Mass Ejections From SOHO. *Sun and Geosphere* 5, 7–16.

Gosling, J. T., Bame, S. J., McComas, D. J., and Phillips, J. L. (1990). Coronal Mass Ejections and Large Geomagnetic Storms. *Geophys. Res. Lett.* 17, 901–904. doi:10.1029/gl017i007p00901

Gulisano, A. M., Démoulin, P., Dasso, S., Ruiz, M. E., and Marsch, E. (2010). Global and Local Expansion of Magnetic Clouds in the Inner Heliosphere. *Astron. Astrophysics.* 509, A39. doi:10.1051/0004-6361/200912375

Guo, J., Feng, X., Zhang, J., Zuo, P., and Xiang, C. (2010). Statistical Properties and Geoefficiency of Interplanetary Coronal Mass Ejections and Their Sheaths During Intense Geomagnetic Storms. *J. Geophys. Res.* 115, a–n. doi:10.1029/2009JA015140

Harrison, R. A., Davies, J. A., Barnes, D., Byrne, J. P., Perry, C. H., Bothmer, V., et al. (2018). CMEs in the Heliosphere: I. A Statistical Analysis of the Observational Properties of CMEs Detected in the Heliosphere From 2007 to 2017 by STEREO/HI-1. *Sol. Phys.* 293, 77. doi:10.1007/s11207-018-1297-2

Heinemann, S. G., Temmer, M., Farrugia, C. J., Dissauer, K., Kay, C., Wiegelmann, T., et al. (2019). CME-HSS Interaction and Characteristics Tracked From Sun to Earth. *Sol. Phys.* 294, 121. doi:10.1007/s11207-019-1515-6

Howard, T. A., and DeForest, C. E. (2012). The Thomson Surface. I. Reality and Myth. *Astrophysical J.* 752, 130. doi:10.1088/0004-637X/752/2/130

Hundhausen, A. J., Sawyer, C. B., House, L., Illing, R. M. E., and Wagner, W. J. (1984). Coronal Mass Ejections Observed During the Solar Maximum Mission: Latitude Distribution and Rate of Occurrence. *J. Geophys. Res.* 89, 2639–2646. doi:10.1029/ja089ia05p02639

Janardhan, P., Bisoi, S. K., Ananthakrishnan, S., Tokumaru, M., and Fujiki, K. (2011). The Prelude to the Deep Minimum Between Solar Cycles 23 and 24: Interplanetary Scintillation Signatures in the Inner Heliosphere. *Geophys. Res. Lett.* 38, a–n. doi:10.1029/2011GL049227

Jian, L. K., Russell, C. T., Luhmann, J. G., and Galvin, A. B. (2018). STEREOObservations of Interplanetary Coronal Mass Ejections in 2007-2016. *Astrophysical J.* 855, 114. doi:10.3847/1538-4357/aab189

Jian, L. K., Russell, C. T., Luhmann, J. G., Skoug, R. M., and Steinberg, J. T. (2008). Stream Interactions and Interplanetary Coronal Mass Ejections at 5.3 AU Near the Solar Ecliptic Plane. *Sol. Phys.* 250, 375–402. doi:10.1007/s11207-008-9204-x

Joselyn, J. A., Anderson, J. B., Coffey, H., Harvey, K., Hathaway, D., Heckman, G., et al. (1997). Panel Achieves Consensus Prediction of Solar Cycle 23. *Eos Trans. AGU.* 78, 205. doi:10.1029/97EO00136

Kaiser, M. L., Kucera, T. A., Davila, J. M., St. Cyr, O. C. O. C., Guhathakurta, M., and Christian, E. (2008). The STEREO Mission: An Introduction. *STEREO Mission.* 136, 5–16. doi:10.1007/978-0-387-09649-0_2

Kilpua, E. K. J., Luhmann, J. G., Jian, L. K., Russell, C. T., and Li, Y. (2014). Why Have Geomagnetic Storms Been So Weak During the Recent Solar Minimum and the Rising Phase of Cycle 24?. *J. Atmos. Solar-Terrestrial Phys.* 107, 12–19. doi:10.1016/j.jastp.2013.11.001

Kilpua, E., Koskinen, H. E. J., and Pulkkinen, T. I. (2017). Coronal Mass Ejections and Their Sheath Regions in Interplanetary Space. *Living Rev. Sol. Phys.* 14, 5. doi:10.1007/s41116-017-0009-6

Kwon, R.-Y., and Vourlidas, A. (2018). The Density Compression Ratio of Shock Fronts Associated With Coronal Mass Ejections. *J. Space Weather Space Clim.* 8, A08. doi:10.1051/swsc/2017045

Lamy, P., Floyd, O., Quémerais, E., Boclet, B., and Ferron, S. (2017). Coronal Mass Ejections and Solar Wind Mass Fluxes Over the Heliosphere During Solar Cycles 23 and 24 (1996-2014). *J. Geophys. Res. Space Phys.* 122, 50–62. doi:10.1002/2016JA022970

Lawrance, M. B., Moon, Y.-J., and Shanmugaraju, A. (2020). Relationships Between Interplanetary Coronal Mass Ejection Characteristics and Geoeffectiveness in the Declining Phase of Solar Cycles 23 and 24. *Sol. Phys.* 295, 62. doi:10.1007/s11207-020-01623-1

Leitner, M., Farrugia, C. J., Möstl, C., Ogilvie, K. W., Galvin, A. B., Schwenn, R., et al. (2007). Consequences of the Force-Free Model of Magnetic Clouds for Their Heliospheric Evolution. *J. Geophys. Res.* 112, a–n. doi:10.1029/2006JA011940

Li, H., Wang, C., Richardson, J. D., and Tu, C. (2017). Evolution of Alfvénic Fluctuations inside an Interplanetary Coronal Mass Ejection and Their Contribution to Local Plasma Heating: Joint Observations from 1.0 to 5.4 au. *Astrophysical J.* 851, L2. doi:10.3847/2041-8213/aa9c3f

Li, Y., Luhmann, J. G., and Lynch, B. J. (2018). Magnetic Clouds: Solar Cycle Dependence, Sources, and Geomagnetic Impacts. *Sol. Phys.* 293, 135. doi:10.1007/s11207-018-1356-8

Liu, Y., Davies, J. A., Luhmann, J. G., Vourlidas, A., Bale, S. D., and Lin, R. P. (2010). Geometric Triangulation of Imaging Observations to Track Coronal Mass Ejections Continuously Out to 1 AU. *Astrophysical J.* 710, L82–L87. doi:10.1088/2041-8205/710/1/l82

Liu, Y., Richardson, J. D., and Belcher, J. W. (2005). A Statistical Study of the Properties of Interplanetary Coronal Mass Ejections From 0.3 to 5.4AU. *Planet. Space Sci.* 53, 3–17. doi:10.1016/j.pss.2004.09.023

Liu, Y., Richardson, J. D., Belcher, J. W., Kasper, J. C., and Elliott, H. A. (2006). Thermodynamic Structure of Collision-Dominated Expanding Plasma: Heating of Interplanetary Coronal Mass Ejections. *J. Geophys. Res.* 111, A01102. doi:10.1029/2005JA011329

Lugaz, N., Farrugia, C. J., Winslow, R. M., Small, C. R., Manion, T., and Savani, N. P. (2017). Importance of CME Radial Expansion on the Ability of Slow CMEs to Drive Shocks. *Astrophysical J.* 848, 75. doi:10.3847/1538-4357/aa8ef9

Manoharan, P. K. (2006). Evolution of Coronal Mass Ejections in the Inner Heliosphere: A Study Using White-Light and Scintillation Images. *Sol. Phys.* 235, 345–368. doi:10.1007/s11207-006-0100-y

Manoharan, P. K., Gopalswamy, N., Yashiro, S., Lara, A., Michalek, G., and Howard, R. A. (2004). Influence of Coronal Mass Ejection Interaction on Propagation of Interplanetary Shocks. *J. Geophys. Res.* 109, A06109. doi:10.1029/2003JA010300

Marubashi, K., and Lepping, R. P. (2007). Long-Duration Magnetic Clouds: a Comparison of Analyses Using Torus- and Cylinder-Shaped Flux Rope Models. *Ann. Geophys.* 25, 2453–2477. doi:10.5194/angeo-25-2453-2007

Mathew, S. K., Martínez Pillet, V., Solanki, S. K., and Krivova, N. A. (2007). Properties of Sunspots in Cycle 23. *Astron. Astrophysics.* 465, 291–304. doi:10.1051/0004-6361:20066356

Mishra, W., Srivastava, N., and Davies, J. A. (2014). A Comparison of Reconstruction Methods for the Estimation of Coronal Mass Ejections Kinematics Based on SECCHI/HI Observations. *Astrophysical J.* 784, 135. doi:10.1088/0004-637x/784/2/135

Mishra, W., and Srivastava, N. (2015). Heliospheric Tracking of Enhanced Density Structures of the 6 October 2010 CME. *J. Space Weather Space Clim.* 5, A20. doi:10.1051/swsc/2015021

Mishra, W., Srivastava, N., Wang, Y., Mirtoshev, Z., Zhang, J., and Liu, R. (2019). Mass Loss via Solar Wind and Coronal Mass Ejections during Solar Cycles 23 and 24. *Monthly Notices R. Astronomical Soc.* 486, 4671–4685. doi:10.1093/mnras/stz1001

Mishra, W., and Wang, Y. (2018). Modeling the Thermodynamic Evolution of Coronal Mass Ejections Using Their Kinematics. *Astrophysical J.* 865, 50. doi:10.3847/1538-4357/aadb9b

Mishra, W., Wang, Y., Srivastava, N., and Shen, C. (2017). Assessing the Nature of Collisions of Coronal Mass Ejections in the Inner Heliosphere. *Astrophysical J. Suppl. Ser.* 232, 5. doi:10.3847/1538-4365/aa8139

Mitsakou, E., and Moussas, X. (2014). Statistical Study of ICMEs and Their Sheaths During Solar Cycle 23 (1996 - 2008). *Sol. Phys.* 289, 3137–3157. doi:10.1007/s11207-014-0505-y

Neugebauer, M., Steinberg, J. T., Tokar, R. L., Barraclough, B. L., Dors, E. E., Wiens, R. C., et al. (2003). Genesis On-Board Determination of the Solar Wind Flow Regime. *SSRv.* 105, 661–679. doi:10.1023/A:1024478129261

Nieves-Chinchilla, T., Vourlidas, A., Raymond, J. C., Linton, M. G., Al-haddad, N., Savani, N. P., et al. (2018). Understanding the Internal Magnetic Field Configurations of ICMEs Using More Than 20 Years of Wind Observations. *Sol. Phys.* 293, 25. doi:10.1007/s11207-018-1247-z

Ogilvie, K. W., Chornay, D. J., Fritzenreiter, R. J., Hunsaker, F., Keller, J., Lobell, J., et al. (1995). SWE, A Comprehensive Plasma Instrument for the Wind Spacecraft. *Space Sci. Rev.* 71, 55–77. doi:10.1007/BF00751326

Owens, M. J., Cargill, P. J., Pagel, C., Siscoe, G. L., and Crooker, N. U. (2005). Characteristic Magnetic Field and Speed Properties of Interplanetary Coronal Mass Ejections and Their Sheath Regions. *J. Geophys. Res.* 110, A01105. doi:10.1029/2004JA010814

Patsourakos, S., Vourlidas, A., and Stenborg, G. (2010). The Genesis of an Impulsive Coronal Mass Ejection Observed at Ultra-High Cadence by AIA on SDO. *Astrophysical J.* 724, L188–L193. doi:10.1088/2041-8205/724/2/L188

Pesnell, W. D. (2008). Predictions of Solar Cycle 24. *Sol. Phys.* 252, 209–220. doi:10.1007/s11207-008-9252-2

Pesnell, W. D. (2016). Predictions of Solar Cycle 24: How Are We Doing?. *Space Weather.* 14, 10–21. doi:10.1002/2015SW001304

Petrie, G. J. D. (2015). On the Enhanced Coronal Mass Ejection Detection Rate Since the Solar Cycle 23 Polar Field Reversal. *Astrophysical J.* 812, 74. doi:10.1088/0004-637x/812/1/74

Ramesh, K. B. (2010). Coronal Mass Ejections and Sunspots-Solar Cycle Perspective. *Astrophysical J.* 712, L77–L80. doi:10.1088/2041-8205/712/1/L77

Reisenfeld, D. B., Gosling, J. T., Forsyth, R. J., Riley, P., and Cyr, St. O. C. (2003). Properties of High-Latitude CME-Driven Disturbances During Ulysses Second Northern Polar Passage. *Geophys. Res. Lett.* 30, 8031. doi:10.1029/2003GL017155

Richardson, I. G., Berdichevsky, D., Desch, M. D., and Farrugia, C. J. (2000). Solar-Cycle Variation of Low Density Solar Wind During More Than Three Solar Cycles. *Geophys. Res. Lett.* 27, 3761–3764. doi:10.1029/2000GL000077

Richardson, I. G., and Cane, H. V. (1995). Regions of Abnormally Low Proton Temperature in the Solar Wind (1965-1991) and Their Association With Ejecta. *J. Geophys. Res.* 100, 23397–23412. doi:10.1029/95JA02684

Richardson, I. G., and Cane, H. V. (2010). Near-Earth Interplanetary Coronal Mass Ejections During Solar Cycle 23 (1996 - 2009): Catalog and Summary of Properties. *Sol. Phys.* 264, 189–237. doi:10.1007/s11207-010-9568-6

Richardson, I. G. (2013). Geomagnetic Activity During the Rising Phase of Solar Cycle 24. *J. Space Weather Space Clim.* 3, A08. doi:10.1051/swsc/2013031

Riley, P., Schatzman, C., Cane, H. V., Richardson, I. G., and Gopalswamy, N. (2006). On the Rates of Coronal Mass Ejections: Remote Solar and *In Situ* Observations. *Astrophysical J.* 647, 648–653. doi:10.1086/505383

Ruffenach, A., Lavraud, B., Owens, M. J., Sauvaud, J.-A., Savani, N. P., Rouillard, A. P., et al. (2012). Multispacecraft Observation of Magnetic Cloud Erosion by Magnetic Reconnection during Propagation. *J. Geophys. Res.* 117, a–n. doi:10.1029/2012JA017624

Russell, C. T., and Mulligan, T. (2002). The True Dimensions of Interplanetary Coronal Mass Ejections. *Adv. Space Res.* 29, 301–306. doi:10.1016/s0273-1177(01)00588-9

Sachdeva, N., Subramanian, P., Colaninno, R., and Vourlidas, A. (2015). Cme Propagation: Where Does Aerodynamic Drag "Take Over"?. *Astrophysical J.* 809, 158. doi:10.1088/0004-637x/809/2/158

Salman, T. M., Lugaz, N., Farrugia, C. J., Winslow, R. M., Jian, L. K., and Galvin, A. B. (2020a). Properties of the Sheath Regions of Coronal Mass Ejections With or Without Shocks From STEREO *In Situ* Observations Near 1 au. *Astrophysical J.* 904, 177. doi:10.3847/1538-4357/abbdf5

Salman, T. M., Winslow, R. M., and Lugaz, N. (2020b). Radial Evolution of Coronal Mass Ejections Between MESSENGER, Venus Express , STEREO, and L1: Catalog and Analysis. *J. Geophys. Res. Space Phys.* 125, e27084. doi:10.1029/2019JA027084

Schwenn, R., dal Lago, A., Huttunen, E., and Gonzalez, W. D. (2005). The Association of Coronal Mass Ejections With Their Effects Near the Earth. *Ann. Geophys.* 23, 1033–1059. doi:10.5194/angeo-23-1033-2005

Schwenn, R. (2006). Space Weather: The Solar Perspective. *Living Rev. Solar Phys.* 3, 2. doi:10.12942/lrsp-2006-2

Shen, C., Chi, Y., Wang, Y., Xu, M., and Wang, S. (2017). Statistical Comparison of the ICME's Geoeffectiveness of Different Types and Different Solar Phases From 1995 to 2014. *J. Geophys. Res. Space Phys.* 122, 5931–5948. doi:10.1002/2016JA023768

Siscoe, G., and Odstrcil, D. (2008). Ways in Which ICME Sheaths Differ From Magnetosheaths. *J. Geophys. Res.* 113, a–n. doi:10.1029/2008JA013142

Solanki, S. K., Wenzler, T., and Schmitt, D. (2008). Moments of the Latitudinal Dependence of the Sunspot Cycle: a New Diagnostic of Dynamo Models. *Astron. Astrophysics.* 483, 623–632. doi:10.1051/0004-6361:20054282

Stone, E. C., Frandsen, A. M., Mewaldt, R. A., Christian, E. R., Margolies, D., Ormes, J. F., et al. (1998). The Advanced Composition Explorer. *Adv. Compost. Explorer Mission.* 86, 1–22. doi:10.1007/978-94-011-4762-0_1

Takahashi, T., and Shibata, K. (2017). Sheath-Accumulating Propagation of Interplanetary Coronal Mass Ejection. *Astrophysical J.* 837, L17. doi:10.3847/2041-8213/aa624c

Temmer, M., Holzknecht, L., Dumbović, M., Vršnak, B., Sachdeva, N., Heinemann, S. G., et al. (2021). Deriving CME Density From Remote Sensing Data and Comparison to In-Situ Measurements. *J. Geophys. Res. Space Phys.* 126, e28380. doi:10.1029/2020JA028380

Temmer, M., Rollett, T., Möstl, C., Veronig, A. M., Vršnak, B., and Odstrčil, D. (2011). Influence of the Ambient Solar Wind Flow on the Propagation Behavior of Interplanetary Coronal Mass Ejections. *Astrophysical J.* 743, 101. doi:10.1088/0004-637X/743/2/101

Temmer, M., Rybák, J., Bendík, P., Veronig, A., Vogler, F., Otruba, W., et al. (2006). Hemispheric sunspot Numbers ${R_{n}}$ and ${R_{s}}$ From 1945-2004: Catalogue and N-S Asymmetry Analysis for Solar Cycles 18-23. *Astron. Astrophysics.* 447, 735–743. doi:10.1051/0004-6361:20054060

Temmer, M., Veronig, A. M., Peinhart, V., and Vršnak, B. (2014). Asymmetry in the CME-CME Interaction Process for the Events From 2011 February 14-15. *Astrophysical J.* 785, 85. doi:10.1088/0004-637X/785/2/85

Vršnak, B., Žic, T., Vrbanec, D., Temmer, M., Rollett, T., Möstl, C., et al. (2013). Propagation of Interplanetary Coronal Mass Ejections: The Drag-Based Model. *Sol. Phys.* 285, 295–315. doi:10.1007/s11207-012-0035-4

Wang, C., Du, D., and Richardson, J. D. (2005). Characteristics of the Interplanetary Coronal Mass Ejections in the Heliosphere Between 0.3 and 5.4 AU. *J. Geophys. Res.* 110, A10107. doi:10.1029/2005JA011198

Wang, C., and Richardson, J. D. (2004). Interplanetary Coronal Mass Ejections Observed by Voyager 2 Between 1 and 30 AU. *J. Geophys. Res.* 109, A06104. doi:10.1029/2004JA010379

Wang, Y.-M., and Colaninno, R. (2014). Is Solar Cycle 24 Producing More Coronal Mass Ejections Than Cycle 23?. *Astrophysical J.* 784, L27. doi:10.1088/2041-8205/784/2/L27

Wang, Y., Shen, C., Liu, R., Liu, J., Guo, J., Li, X., et al. (2018). Understanding the Twist Distribution Inside Magnetic Flux Ropes by Anatomizing an Interplanetary Magnetic Cloud. *J. Geophys. Res. (Space Physics).* 123, 3238. doi:10.1002/2017ja024971

Webb, D. F., and Howard, T. A. (2012). Coronal Mass Ejections: Observations. *Living Rev. Solar Phys.* 9, 3. doi:10.12942/lrsp-2012-3

Wolf, R. (1861). Abstract of His Latest Results. *Monthly Notices R. Astronomical Soc.* 21, 77–78. doi:10.1093/mnras/21.3.77

Xie, H., Ofman, L., and Lawrence, G. (2004). Cone Model for Halo CMEs: Application to Space Weather Forecasting. *J. Geophys. Res.* 109, A03109. doi:10.1029/2003JA010226

Yashiro, S., Gopalswamy, N., Michalek, G., Cyr, St. O. C., Plunkett, S. P., Rich, N. B., et al. (2004). A Catalog of White Light Coronal Mass Ejections Observed by the SOHO Spacecraft. *J. Geophys. Res.* 109, A07105. doi:10.1029/2003JA010282

Zhang, J., Poomvises, W., and Richardson, I. G. (2008). Sizes and Relative Geoeffectiveness of Interplanetary Coronal Mass Ejections and the Preceding Shock Sheaths During Intense Storms in 1996-2005. *Geophys. Res. Lett.* 35, L02109. doi:10.1029/2007gl032045

Zhang, J., Richardson, I. G., Webb, D. F., Gopalswamy, N., Huttunen, E., Kasper, J. C., et al. (2007). Solar and Interplanetary Sources of Major Geomagnetic Storms (Dst≤ −100 nT) During 1996-2005. *J. Geophys. Res.* 112, a–n. doi:10.1029/2007JA012321

Zurbuchen, T. H., and Richardson, I. G. (2006). *In-Situ* Solar Wind and Magnetic Field Signatures of Interplanetary Coronal Mass Ejections. *SSRv.* 123, 31–43. doi:10.1007/s11214-006-9010-4

Conflict of Interest: The authors declare that the research was conducted in the absence of any commercial or financial relationships that could be construed as a potential conflict of interest.

Publisher's Note: All claims expressed in this article are solely those of the authors and do not necessarily represent those of their affiliated organizations, or those of the publisher, the editors, and the reviewers. Any product that may be evaluated in this article, or claim that may be made by its manufacturer, is not guaranteed or endorsed by the publisher.

Advantages of publishing in Frontiers

OPEN ACCESS
Articles are free to read for greatest visibility and readership

FAST PUBLICATION
Around 90 days from submission to decision

HIGH QUALITY PEER-REVIEW
Rigorous, collaborative, and constructive peer-review

TRANSPARENT PEER-REVIEW
Editors and reviewers acknowledged by name on published articles

Frontiers
Avenue du Tribunal-Fédéral 34
1005 Lausanne | Switzerland

Visit us: www.frontiersin.org
Contact us: frontiersin.org/about/contact

REPRODUCIBILITY OF RESEARCH
Support open data and methods to enhance research reproducibility

DIGITAL PUBLISHING
Articles designed for optimal readership across devices

FOLLOW US
@frontiersin

IMPACT METRICS
Advanced article metrics track visibility across digital media

EXTENSIVE PROMOTION
Marketing and promotion of impactful research

LOOP RESEARCH NETWORK
Our network increases your article's readership